Multiscale Micromechanical Modeling of the Thermal/Mechanical Properties of Polymer/Clay Nanocomposites

by

Nuo Sheng

B.S., Tsinghua University, China (2000)
M.S., Massachusetts Institute of Technology (2002)

Submitted to the Department of Mechanical Engineering
In partial fulfillment of the requirements for the degree of

Doctor of Philosophy in Mechanical Engineering

at the

MASSACHUSETTS INSTITUTE OF TECHNOLOGY

June 2006

Author .....
Department of Mechanical Engineering
May 19, 2006

Certified by .....
Mary C. Boyce
Professor of Mechanical Engineering
Thesis Supervisor

Certified by .....
David M. Parks
Professor of Mechanical Engineering
Thesis Supervisor

Accepted by .....
Lallit Anand
Chairman, Departmental Committee on Graduate Students

Multiscale Micromechanical Modeling of the Thermal/Mechanical Properties of Polymer/Clay Nanocomposites

by

Nuo Sheng

Submitted to the Department of Mechanical Engineering
on May 19, 2006, in partial fulfillment of the
requirements for the degree of
Doctor of Philosophy in Mechanical Engineering

Abstract

Polymer/clay nanocomposites have been observed to exhibit enhanced thermal/mechanical properties at low weight fractions (W_c) of clay. Continuum-based composite modeling reveals that the enhanced properties are strongly dependent on particular features of the second-phase "particles"; in particular, the particle volume fraction (f_p), the particle aspect ratio (L/t), and the ratio of particle thermal/mechanical properties to those of the matrix. These important aspects of as-processed nanoclay composites require consistent and accurate definition.

A multiscale modeling strategy is employed to account for the hierarchical morphology of the nanocomposite: at a lengthscale of thousands of microns, the structure is one of high aspect ratio particles within a matrix; at the lengthscale of microns, the clay particle structure is either (a) exfoliated clay sheets of nanometer level thickness or (b) stacks of parallel clay sheets separated from one another by interlayer galleries of nanometer level height, and the matrix, if semi-crystalline, consists of fine lamella, oriented with respect to the polymer/nanoclay interfaces. Here, quantitative structural parameters extracted from XRD patterns and TEM micrographs (the number of silicate sheets in a clay stack, N, and the silicate sheet layer spacing, $d_{(001)}$) are used to determine geometric features of the as-processed clay "particles", including L/t and the ratio of f_p to W_c. These geometric features, together with estimates of silica lamina elastic and thermal expansion properties obtained from molecular dynamics simulations, provide a basis for modeling effective thermal/mechanical properties of the clay particle. In the case of the semi-crystalline matrices (e.g., nylon 6), the transcrystallization behavior induced by the nanoclay is taken into account by modeling a layer of matrix surrounding the particle to be highly textured and therefore mechanically anisotropic. Micromechanical models (numerical as well as analytical) based on the "effective clay particle" were employed to calculate the overall anisotropic elastic constants, anisotropic coefficient of thermal expansion (CTE), and anisotropic yield surface of the amorphous and semi-crystalline polymer-clay nanocomposites and to compute their dependence on the matrix and clay properties as well as internal clay structural parameters.

The proposed modeling technique captures the strong modulus enhancements observed in elastomer/clay nanocomposites as compared with the moderate enhancements observed in glassy and semi-crystalline polymer/clay nanocomposites. For the case where the matrix is semi-crystalline, the enhancements of composite modulus and strength are

found to rely on different functions of the clay: while the modulus enhancement can be explained by the conventional role of "stiff filler", the strength enhancement of the nanocomposite mainly lies in the improvements of the matrix property achieved through the matrix transcrystallization induced by nanoclay the "nucleation sites". When the nanocomposite experiences a morphological transition from intercalated to completely exfoliated, an abrupt jump in the composite initial yield strength, as opposed to the moderate increase in the overall composite modulus, was predicted. The elastic moduli and anisotropic CTE for MXD6-clay and nylon 6-clay nanocomposites predicted by the micromechanical models are in excellent agreement with experimental data. In summary, continuum-based micromechanical models can provide robust predictions of the overall thermal/mechanical properties of polymer/clay nanocomposites, with the employment of a reliable method to account for the intrinsically hierarchical morphology of the nanoclay, and for the special matrix morphology and properties adjacent to the nanoclay.

Thesis Supervisor: Mary C. Boyce

Tile: Professor of Mechanical Engineering

Thesis Supervisor: David M. Parks

Tile: Professor of Mechanical Engineering

Nanotechnology

Nanotechnology is a field of applied science focused on the design, synthesis, characterization and application of materials and devices on the nanoscale. Nanotechnology is a sub classification of technology in colloidal science, biology, physics, chemistry and other scientific fields and involves the study of phenomena and manipulation of material at the nanoscale, **in essence an extension of existing sciences into the nanoscale.**

http://wikipedia.org/

Contents

Chapter 1

Introduction

Polymeric materials are often reinforced by stiff fillers to improve mechanical properties. The efficiency of reinforcement depends on the filler aspect ratio, the filler mechanical properties, and the adhesion between the matrix and the filler. Single clay layers were proposed to be an ideal reinforcing agent in 1974 (Maine and Shepherd, 1974) due to their extremely high aspect ratio and also due to the nanometer filler thickness being comparable to the scale of the polymer chain structure. Two decades later, the Toyota research group (Kojima, Usuki, Kawasumi, Okada, Fukushima, Kurauchi, and Kamigaito, 1993) revealed a major breakthrough in polymer/clay nanocomposite technology with the success of *in situ* polymerization of nylon 6/clay nanocomposites, a synthesis method economically suitable for industrial production. A 70% increase in the tensile modulus and a 40% increase in the tensile strength were achieved with as little as 4.7-weight percent clay; furthermore, the property enhancements extend to relatively high temperatures and, indeed, act to substantially increase "transition temperatures" over that of the parent homopolymer (an increase of 80C in the heat distortion temperature has been observed, Kojima, et al., 1993). Table 1.1 lists mechanical properties of nylon 6/clay nanocomposite with 4.7-weight percentage montmorillonite given in the original paper of the Toyota Central Lab.

Table 1.1: Mechanical properties of nylon 6/clay nanocomposite (Kojima, Usuki, Kawasumi, Okada, Fukushima, Kurauchi, and Kamigaito, 1993)

Properties		Nylon 6	Nylon 6/clay nanocomposite
Tensile strength (MPa)	23°C	68.6	97.2
	120°C	26.6	32.3
Tensile modulus (GPa)	23°C	1.11	1.87
	120°C	0.19	0.61
Flexural strength (MPa)	23°C	89.3	143
	120°C	12.5	32.7
Flexural modulus (GPa)	23°C	1.94	4.34
	120°C	0.29	1.16
Izod impact strength (J/m)		20.6	18.1
Charpy impact strength (kJ/m)		6.21	6.06
HDT (1.82 MPa) (°C)		65	152

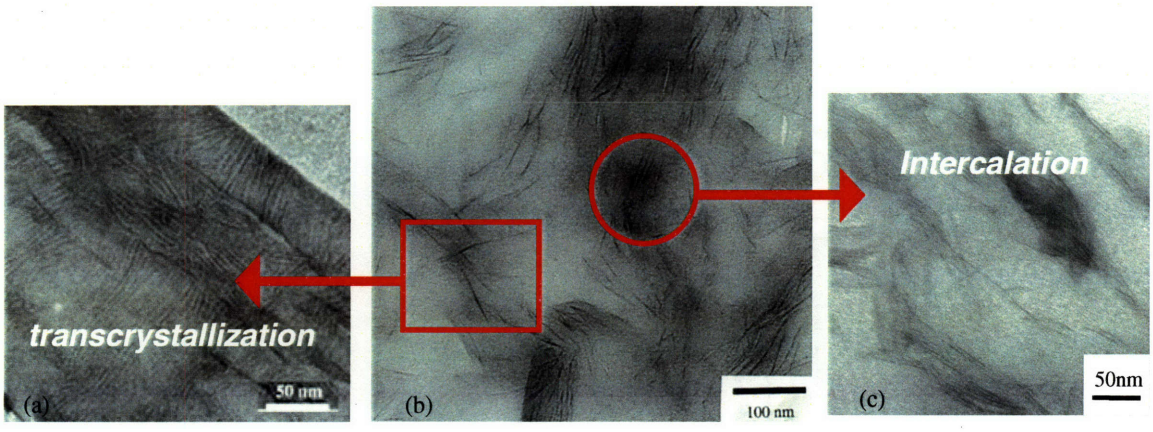

Figure 1.1: (a) Transcrystallized nylon6/clay nanocomposite (Li and Shimuzu, 2006). (b) Epoxy/clay nanocomposite with mixed exfoliated and intercalated morphology (Brown, et al., 2000). (c) Intercalted MXD6 nylon/clay nanocomposite (Lee and McKinley, 2002). Note that Figures (a), (b) and (c) are TEMs of different materials and from different group of researchers; the arrows are for illustration purposes only.

Polymer/clay nanocomposites have a hierarchical morphology. At a lengthscale of thousands of microns, the structure is one of high aspect ratio particles within a matrix; at the lengthscale of microns, the clay particle structure is either exfoliated sheets of nanometer thickness or stacks of parallel clay sheets separated from one another by interlayer galleries of nanometer level height (as shown in Fig. 1.1c), and the matrix, if semi-crystalline, consists of fine lamellae, often preferentially oriented with respect to the polymer/nanoclay interfaces (as demonstrated in Fig. 1.1a).

The prospect of polymer/clay nanocomposites to serve as a light-weight, low-cost alternative to conventional high-performance composites has led to extensive investigation into physical properties of various polymer/clay nanocomposite systems over the last decade, including thermal expansion (Okada and Usuki, 1995; Yoon, et al., 2002), barrier (Yano, et al., 1993; Messersmith and Giannelis, 1994, 1995), flammability resistance (Gilman, 1999), and ablation performance (Vaia, et al., 1999). The nanocomposite technology has also been extended to various polymer systems, including elastomers (Wang and Pinnavaia, 1998; Burnside and Giannelis, 2000) and epoxies (Triantafillidis, et al., 2002; Ratna, et al., 2003); different levels of property enhancement are achieved, depending on the chosen matrix polymer.

Although in general, polymeric nanocomposites have been found to possess improved thermal/mechanical properties over the matrix polymer, the efficiency of reinforcement appears to depend strongly on various factors including the morphology of the nanocomposite (intercalated or exfoliated particle structure), the orientation of the clay platelets, the crystallinity (amorphous or semi-crystalline), the thermophysical properties

(thermoplastic, epoxy or elastomer) of the matrix, and the adhesion between the matrix and the nanoclay. The overall mechanical behavior of a certain polymeric nanocomposite system is usually a comprehensive result of multiple factors described above. For example, with the same or similar clay dispersion, a compliant matrix exhibits a much more dramatic relative modulus increase than a stiffer matrix. Polymer/clay nanocomposite systems exhibit 200-300% increase in modulus (e.g., Burnside, et al., 2000; Triantafillidis, et al., 2002; Ratna, et al., 2003) when the matrix is a compliant epoxy or elastomer (or a thermoplastic above its glass transition temperature (T_g)), whereas a stiffer epoxy or thermoplastic matrix (below T_g) results in rather more modest improvement (less than 100%). Even more diversity arises when it comes to the yield and post-yield behavior of the nanocomposites — while the enhancement in tensile modulus for nanocomposites has been widely observed, the same does not necessarily hold for the composite strength. For instance, axial tension tests on amorphous polymer/clay nanocomposites with predominately intercalated morphology show little or no increase in initial yield strength over the matrix polymer (MXD6 nylon/clay nanocomposites, by the author; PC/clay nanocomposites by Hsieh, et al. 2004); in addition, elongation at break is observed to decrease with increasing clay content (in fact, composites of both PC and MXD6 nylon matrices, with ~5-wt% of clay behaved in a rather brittle manner). However, significant increases (50-100%) in yield strength have been reported for completely or partially exfoliated nanocomposites with semi-crystalline polymer matrices such as nylon 6 (Medellin-Rodriguez, et al., 2003) and polyethylene (Wang, et al., 2002). Furthermore, comparison between mechanical properties of exfoliated and heavily aggregated 4-wt% nylon 12/fluoromica (McNally, et al., 2003) shows that the exfoliated

composite exhibits significant enhancement in both tensile strength and elongation at break, whereas the poorly intercalated composite shows little or no improvement.

Presumably, matrix crystallinity and clay dispersion play important roles in the deformation behavior of polymer/clay nanocomposites. The presence of modifying particles (e.g., rubber or inorganic particles such as clay) is well known to influence directly the crystallization behavior of the polymer matrix (Chacko, et al. 1982; Muratoglu, et al. 1995). The change in the morphology of the semi-crystalline polymer matrix induced by the addition of modifying particles can cause remarkable differences in the composite mechanical properties (Muratoglu, et al. 1995). Over the past decade, there has been a rising interest in the impact of nanoclay on the crystallization behavior of semi-crystalline matrices. Addition of layered silicate has been observed to have profound influences on the matrix morphology, including special orientation of crystal lamellae with respect to the silicate surfaces (Kojima, et al., 1995; Kim, et al., 2001; Li and Shimizu, 2006; Weon, et al., 2005), alteration of the crystal fraction — preferred γ-form crystals in nylon 6 nanocomposites rather than the α-form as in bulk nylon 6 (Kojima, et al. 1993; Nam, et al. 2001; Lincoln, et al., 2001), and alteration of chain mobility (Nam, et al., 2001).

Another crucial contributor to efficient property enhancement is interfacial bonding between matrix and particle. Good interfacial adhesion up to the stress level when yield occurs is required if improvement on the initial yield strength is to be achieved. In fact, scanning electron micrographs (SEM) of a well-exfoliated and oriented polyethylene/clay nanocomposite after 30% tensile loading shows a homogeneous surface without any

voids (Wang, et al., 2002), indicating good adhesion between the silicate and the matrix, which is also consistent with the ~ 30% increase in the yield strength observed for the nanocomposite over the homopolymer.

Mechanics-based composite models have proved successful in predicting the enhanced mechanical properties of conventional polymer/fiber and flake composites, where the filler lengthscale is on the order of tens of microns or larger. The continuum mechanics-based composite models generally include parameters such as the particle volume fraction, particle aspect ratio and orientation, and particle/matrix property ratios. Researchers have recently begun applying some of these models to assess the thermal-mechanical properties of polymer nanocomposites (Nam, et al., 2001; van Es, et al., 2001; Brune and Bicerano, 2002; Yoon, et al., 2002). Concepts such as "matrix" and "particle", which are well-defined in conventional two-phase composites, can no longer be directly applied to polymer/clay nanocomposites due to the hierarchical nanometer lengthscale morphology of the particle structure and surrounding matrix, as recently emphasized by Brune and Bicerano (2002). Issues as basic as the proper description of the mechanical and thermal behavior of nanoparticles of atomic level thickness, as well as the proper conversion of filler weight fraction to particle volume fraction, require careful treatment if one is to understand the dependence of composite properties on nanoclay content and structure. In addition, the transcrystallization behavior of semi-crystalline matrix, induced by the presence of nanoclay, needs to be properly accounted for in order to achieve a comprehensive understanding of semi-crystalline polymer-clay nanocomposites.

In this work, mechanics-based model predictions of the dependence of the anisotropic elastic constants, anisotropic thermal expansion, and anisotropic yield surface of the composite material on plate-like filler content are presented. The hierarchical nature of the underlying structure of polymer/nanoclay composites is then detailed, and the applicability of well-established models to this new class of composite material is discussed. A multiscale modeling strategy accounts for the hierarchical morphology of the nanocomposite through use of an "effective particle", defined and employed to represent the inherently discrete nanoclay structure as a basic object in micromechanical modeling. Particular attention is given to the thermal/mechanical description of the clay sheets and incorporation of this description into an effective particle model. The potential for describing macroscopic thermal/mechanical property enhancements in terms of composite-level effects is explored, treating the nanocomposite as an appropriately-described matrix containing a suitable dispersion of the "effective particles". Model predictions of macroscopic modulus and coefficient of thermal expansion (CTE) are in excellent agreement with experimental data for various polymer (amorphous vs. semi-crystalline)-clay nanocomposites. In addition, the dual-role played by the nanoclay as conventional "stiff filler" and as a "nucleation site" for matrix transcrystallization in semi-crystalline polymer nanocomposites is examined; the effects of matrix texture on the composite modulus and strength are compared to the composite-level effects of stiff fillers.

This thesis consists of seven chapters. The fundamentals of the multiscale modeling approach are introduced in Chapter 2; modeling of the anisotropic elastic properties, the anisotropic thermal expansion, and anisotropic initial yielding behavior of the

nanocomposites are covered in Chapter 3, Chapter 4, and Chapter 5, respectively; Chapter 6 focuses on the special morphology in semi-crystalline polymer/clay nanocomposites and its impact on the mechanical properties; with Chapter 7, the thesis is concluded.

Chapter 2

Multiscale Modeling Approach

Polymer/clay nanocomposites have a hierarchical morphology. At a lengthscale of thousands of microns, the structure is one of high aspect ratio particles within a matrix; at the lengthscale of microns, the clay particle structure is either exfoliated sheets of nanometer thickness or stacks of parallel clay sheets separated from one another by interlayer galleries of nanometer level height, and the matrix, if semi-crystalline, consists of fine lamellae, often preferentially oriented with respect to the polymer/nanoclay interfaces.

A multiscale modeling strategy that accounts for such complex morphology has been proposed by the author in Sheng, et al., 2004, with emphasis on the continuum-level representation of the inherently discrete structure of intercalated nanoclay, defined as the 'effective particle'. In this thesis, this modeling approach is extended in order to account for the special matrix morphology induced by the addition of nanoclay, as well as to properly capture the deformation behavior of the nanoclay at larger strains. The modeling hierarchy is schematically illustrated in Fig. 2.1, where the composite-level micromechanical model (Fig 2.1b) is established upon proper structural/mechanical characterization of the nanoclay (Fig 2.1a) and the oriented crystalline material induced by the presence of the nanoclay when the matrix polymer is semi-crystalline (Fig 2.1c).

In this chapter, first a brief description of the hierarchical morphology of the nanocomposite is given in Section 2.1. Section 2.2 focuses on morphology

characterization and constitutive modeling of the nanoclay; structure and properties of a single silicate layer are determined from molecular dynamics (MD) simulations; two types of models are proposed to represent the intercalated nanoclay, each designed to suit different scales of deformation. The continuum-level micromechanical modeling details are described in Section 2.3.

Note that the special morphology of a semi-crystalline matrix, as demonstrated in Fig. 2.1(c), as well as its effects on the properties of the nanocomposite, are thoroughly discussed in Chapter 6 and will not be elaborated on here.

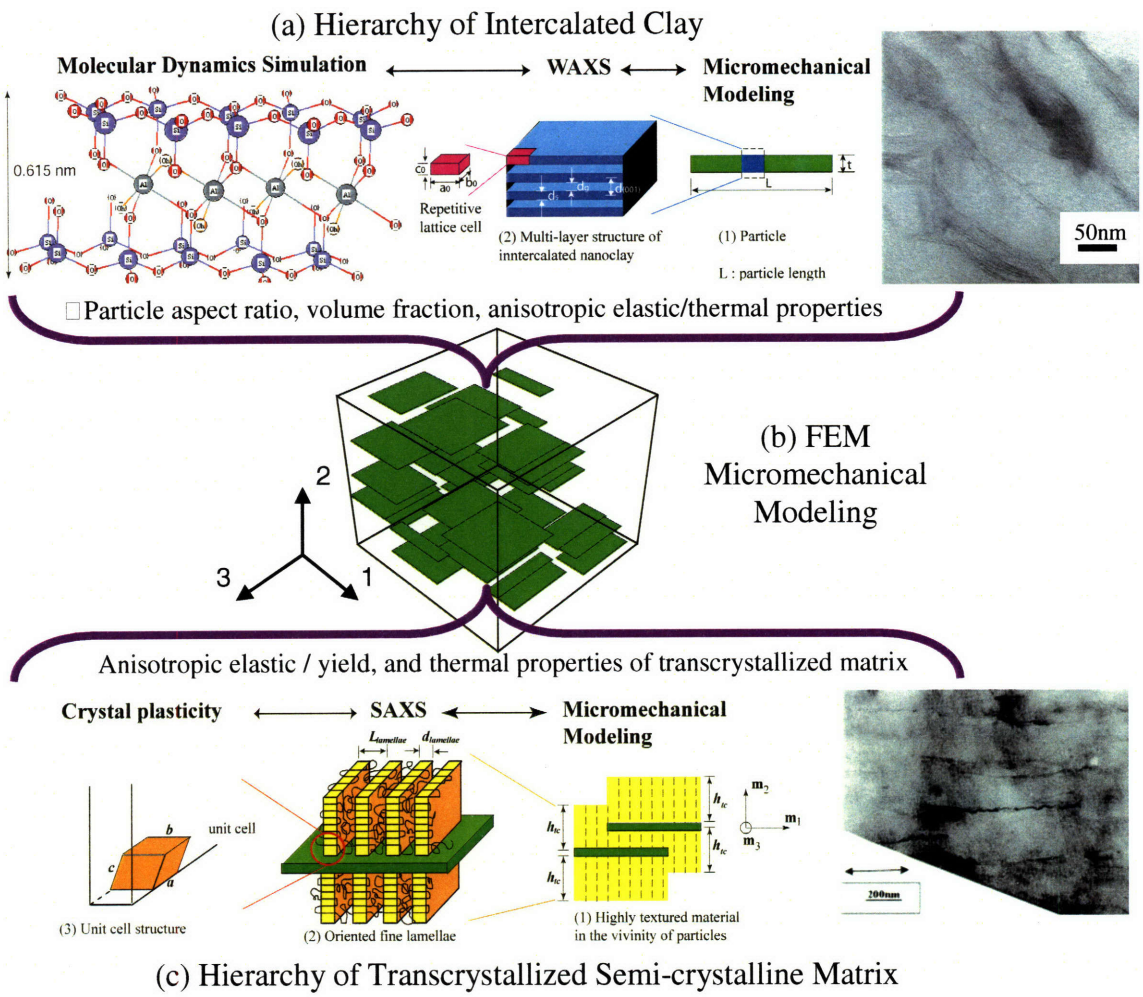

Figure 2.1: Illustration of the multiscale modeling approach: (a) hierarchical structure and homogenization of the intercalated nanoclay; (b) typical 3D RVE with randomly distributed particles used in finite element (FE)-based micromechanical modeling; (c) hierarchical structure and homogenization of oriented crystal lamellae induced by the presence of the nanoclay in semi-crystalline matrix.

2.1. Hierarchical Morphology of the Nanocomposite

The morphology of polymer/layered-silicate composites has a hierarchical structure. The dispersion of the clay in the matrix is typically described in terms of *intercalation* vs. *exfoliation*. In the *intercalated* structure, inter-layer domains of the primary clay particles are penetrated by polymer chains and consequently expand, with a typical inter-layer

spacing of the order of 1-4 nm; in contrast, the *fully-exfoliated* morphology consists of single silicate layers dispersed in a polymer matrix. In practice, however, many systems fall between these two idealized morphologies. Figure 2.2 shows a TEM image of a nanocomposite containing both exfoliated and intercalated structures (Brown, et al., 2000). Different synthesis and processing histories will produce positional and orientational correlations between the platelets. These histories contribute to the development of a hierarchical morphology exhibiting nano-, meso-, and micro-level features. A summary of the morphology of polymer/clay nanocomposites, and of corresponding microscopy and scattering techniques to determine such hierarchical morphology, was given by Vaia (2000).

Characteristic parameters of various length-scales are necessary in order to capture the special hierarchical morphology of nanocomposites. Nam and co-workers (2001) have ascertained key features of the hierarchical morphology of intercalated polypropylene/clay nanocomposites (PPCN) using WAXS, SAX, TEM, polarized optical microscopy and light scattering. Figure 2.3 shows a schematic of such a structure and illustrates the parameters of various hierarchies. The representative values of these parameters for a 4-wt% PPCN (Nam, et al., 2001) are listed in Table 1. In an intercalated structure, where the inter-layer spacing ($d_{(001)}$ in Figure 2.3) within a multi-layer stack of clay is usually 1-4 nm (Vaia, 2000), the intra-layer polymer chains have a highly confined morphology. In the exfoliated or partially exfoliated systems, the particle separation (ξ_p) is about 20-50 nm (Vaia, 2000), and is on the same order of crystal lamellae thickness. Such spacing, along with the detailed molecular interaction between clay and polymer, has an impact on the formation of crystallites in semi-crystalline

polymer matrices (in particular, transcrystallization behavior of the matrix can be induced by the presence of the silicate layers), as observed in morphology studies on clay-filled polymer (Kojima, et al., 1994; Kim, et al., 2001) as well as other micron-sized particle filled polymers (Chacko, et al., 1982; Muratoglu, et al., 1995; Bartczak, et al., 1999;).

Here, based on experimental observations together with modeling considerations, we identify two important sets of structural descriptors for the clay "particle": primary descriptors and intermediate descriptors. The primary descriptors are the characteristic clay structural parameters directly related to processing, including the clay weight fraction (W_c), the clay atomic structure, the silicate interlayer spacing ($d_{(001)}$), the average number of silicate layers per clay stack (N), and the inter-layer gallery material, if present. The intermediate descriptors are conventional composite material descriptors, including the particle volume fraction (f_p), the particle aspect ratio (L/t), and particle/matrix property ratio S_p/S_m, where "S" can be modulus (E), initial yield strength (σ_y), or thermal expansion coeffiencient (α), and is often anisotropic.

In order to develop predictive models of the macroscopic properties of polymer/nanoclay composites, a mapping of the primary descriptors to the intermediate descriptors of the nanoclay particle is needed, as presented next in Section 2.2. Micromechanical models (which are described in Section 2.3) are then constructed and utilized to compute the macroscopic thermal/mechanical properties of the polymer/clay nanocomposites in terms of the intermediate descriptors, as presented in Chapter 3 through Chapter 6.

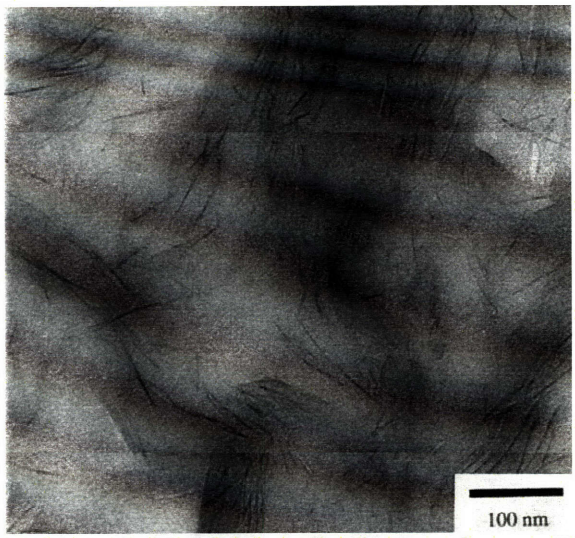

Figure 2.2: TEM image of 10 wt% Cloisite 30A in a diamine-cured epoxy (Brown, et al., 2000)

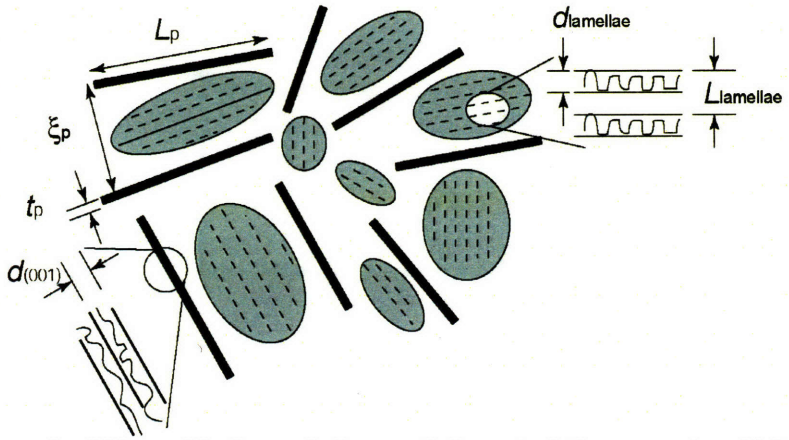

Figure 2.3: Schematic of hierarchical morphology and characteristic parameters (Adapted from Nam, et al., 2001).

Table 2.1 Characteristic values for hierarchical structure-describing parameters for 4-wt% PPCN, (Nam, et al., 2001) (see Figure 2.3 for schematic illustration).

Symbol	Characteristic parameter	Typical value (nm)
L_p	Length of the dispersed clay particles	130~180
ξ_p	Correlation between particles (inter-particle spacing)	40~60
t_p	Thickness of the clay particles	7~9
$d_{(001)}$	Inter-layer spacing of the (001) plane in intercalated clay	3
$d_{lamellae}$	Average lamellae thickness of polymer matrix crystallite	7
$L_{lamellae}$	Long-period lamellae thickness of polymer crystallite	15

2.2. Modeling of the Nanoclay

Continuum models for the macroscopic properties of composite materials operate on the 'particle' and the 'matrix'. The total spatial volume of the composite is well-partitioned into the 'particle domain' and the 'matrix domain'; each domain is then treated as a homogeneous material with its own properties: mechanical (elastic, plastic), thermal, permeability, etc. However, a clearly defined 'particle domain' does not exist in polymer/clay nanocomposites: the layered structure of intercalated nanoclay (single silicate layers separated by inter-layer galleries) can be distinctly identified in TEM images; even for exfoliated clay, there is ambiguity in the definition of the particle thickness, which is on the atomic level.

Here we propose two types of models for the intercalated nanoclay, depending on the scale of deformation: (a) a homogenized "effective particle", characterized by anisotropic elastic and thermal properties, is used in small-strain thermal/mechanical analysis, as shown in Fig. 2.4b; (b) a "sandwich"-like structure consisting of an hyper-elastic "effective gallery" and two stiff sheets at the exterior, as illustrated in Fig. 2.4c, is intended for proper characterization of the complex particle deformation under large strain, utilizing finite element tools. In addition, the structure and mechanical behavior of single-layer silicates are briefly discussed since they lay the foundation for further descriptions of the multi-layer intercalated clay.

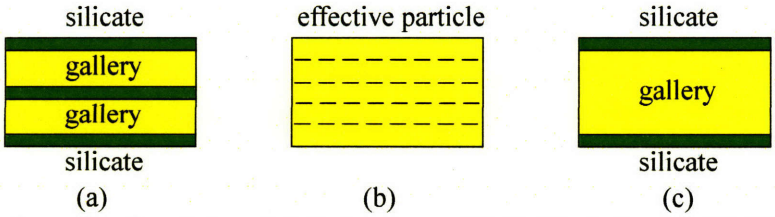

Figure 2.4: (a) schematic of an intercalated structure with 3 silicate layers. (b) 'Effective particle' model for small-strain analysis. (c) 'Sandwich'-like particle model for large deformation analysis.

2.2.1. Structure and Property of Single-layer Silicate

Fig 2.1b shows the crystal structure of montmorillonite (MMT). The single clay sheet of MMT is a lamella composed of one crystallographic unit cell in the thickness direction and an infinite number of unit cells in the two in-plane directions. Manevitch and Rutledge (2004) calculated the elastic properties of a single lamella of MMT by Molecular Dynamics (MD) simulations. The molecular characterization of the lattice cell is listed in Table 2.2.

The MD simulation results suggest that the clay layer may be represented approximately as a sheet with orthotropic symmetry, having in-plane membrane stiffness $E_{silicate}d_s$ = 250 ~ 260 N/m, and in-plane shear stiffness $G_{silicate}d_s$ = 166 N/m, where $E_{silicate}$ and $G_{silicate}$ are the in-plane Young's modulus and shear modulus of the silicate, respectively, and d_s is the "sheet thickness". In order to determine a value for the modulus $E_{silicate}$, one must divide the membrane stiffness by the sheet thickness. There is ambiguity in assigning a thickness to a particle of one atomic lattice unit thickness, since it is unclear how to assess the proper radius of influence of an atom in this regard.

This issue has been successfully addressed in the Carbon Nanotube (CNT) literature (Yakobson, et al., 1996), where a combination of atomistic simulations of membrane (where membrane stiffness is given by Et) and bending (where bending stiffness is given by Et^3) deformation act to identify an ***effective mechanical thickness*** (the thickness value that will provide accurate representation of the mechanical behavior of the atomic-thickness lamina, both stretching and bending, when using continuum-level models). Pantano, et al., (2003) have demonstrated that using the CNT wall (modulus, thickness)

pair computed in this manner, together with elastic shell theory, enables the prediction of a wide range of mechanical behaviors of single and multi-wall CNTs.

Manevitch and Rutledge follow an analogous approach to extract a (modulus, thickness) pair for the montmorillonite silicate sheet from their MD simulations, which sampled both membrane and bending behavior of the sheet. Their calculations of the membrane stiffness, together with the bending stiffness deduced from buckling behavior yield a (modulus, thickness) pair of d_s = 0.678 nm and $E_{silicate}$ = 369 ~ 383 GPa; note that the effective mechanical thickness of 0.678 nm is comparable to the distance between the outermost layers of atoms on either surface of the atomically thin sheet, i.e., the lattice thickness, c_0 (c_0 = 0.615 nm, as given in Table 2.2).

Note that in the remainder of the thesis, the thickness of a single layer (exfoliated) silicate is taken to be the **effective mechanical thickness**, d_s, if not otherwise stated.

Table 2.2: Molecular characterization of montmorillonite lattice cell (Manevitch and Rutledge, 2004)

	Unit	Symbol	Value
Chemical structure			$2\{Al_2Si_4O_{10}(OH)_2\}$
Planar dimensions	nm	(a_0, b_0)	(0.53, 0.92)
Planar Area	$(nm)^2$	$A_0 = a_0b_0$	0.49
Lattice thickness	nm	c_0 ($c_0 \sim d_s$)	0.615
Molecular Weight	g/mol	M_0	720

2.2.2. Structure Characterization of Intercalated Clay

The hierarchical structure of the intercalated nanoclay is well-illustrated in Fig. 2.5, where representations of the nanoclay at various lengthscales, such as 'particle', 'multi-layer stack', and 'repetitive lattice cell', in turn, are the fundamental elements of interest in analytical/numerical micromechanical modeling, WAXS, and molecular dynamics

simulations. While the 'particle' in micromechanical modeling is simply characterized by its aspect ratio (geometry) and thermal/mechanical properties, the underlying structure of the nanoclay must be characterized and approximated in order to obtain reasonable estimates of the effective geometry and properties of the 'particle'; indeed, both WAXS and MD simulation results provide indispensable assistance to micromechanical modeling of polymer/clay nanocomposites.

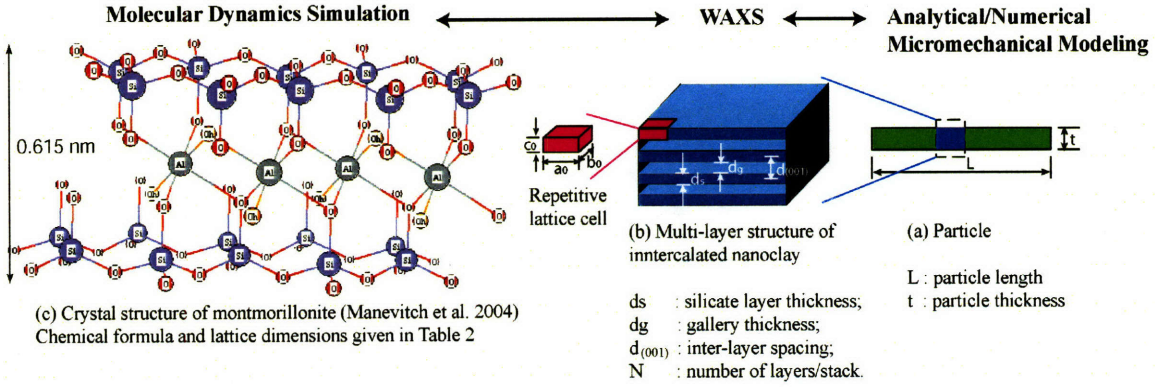

Figure 2.5: Hierarchical structure of intercalated clay.

- Idealized Multi-layer Structure

For simplicity, the internal structure of an intercalated clay particle is idealized as a multi-layer stack containing N single silicate sheets (each sheet has an area A, an effective thickness d_s and mass M) with uniform inter-layer spacing $d_{(001)}$, as illustrated in Figure 2.2b. Separating adjacent sheets is a so-called gallery layer comprising both surfactants and polymer matrix chains that have penetrated the inter-silicate layers during various stages of synthesis and processing. As mentioned in Section 2.2.1, there is some ambiguity in assigning a precise value to thickness for nanoparticles of atomic level thickness, especially with regard to providing accurate representation of mechanical

properties using continuum level models. Therefore, we choose to represent the effective particle thickness in terms of the measurable interlayer spacing $d_{(001)}$ and a single sheet thickness d_s, where d_s has been defined previously in Section 2.1.1 as the *mechanical thickness* of the sheet[1]. The particle thickness t can be related to the internal structural parameters N and $d_{(001)}$ through

$$t = (N-1)d_{(001)} + d_s . \tag{2.1}$$

This model framework will later be used to determine effective properties of the clay "particle", including determination of the particle aspect ratio, volume fraction of the particle (in terms of clay weight fraction), particle stiffness (which may be anisotropic), and coefficient of thermal expansion of the particle (which can also be highly anisotropic). Note that the subscripts *silicate* and *gallery* are used to denote properties attributed to the silicate sheet and the gallery, respectively. The subscripts p and m are used to denote the properties of the effective particle and the matrix, respectively.

An important parameter of the clay structure is the number of silicate sheets per unit particle thickness:

$$\chi_N \equiv \frac{N}{t} = \frac{N}{(N-1)d_{(001)} + d_s}, \tag{2.2}$$

which can be alternatively expressed in terms of the volume fraction of silicate in the effective particle as:

[1] Furthermore, immediately surrounding the exterior silicate layers is an interface region composed of some blend of surfactants and confined matrix polymer chains, which rapidly transitions to 100% matrix material with increasing distance from the particle. For present purposes, we neglect these special regions and features, and simply include them within the matrix volume and matrix properties. The proposed approach can be straightforwardly extended to account for these features within the definition of the "effective particle".

$$\chi \equiv \frac{V_{silicate}}{V_p} = \frac{N d_s}{(N-1)d_{(001)} + d_s} = \frac{1}{\left\{\left(1-\frac{1}{N}\right)\left(\frac{d_{(001)}}{d_s}\right)+\frac{1}{N}\right\}}, \tag{2.3}$$

where $V_{silicate}$ and V_p are the volumes assigned to the silicate sheets in a stack and to the effective particle, respectively. The dimensionless quantity χ is a function of two internal parameters of the nanoclay particle: its number of silicate sheets, N, and the relative inter-layer swelling, $d_{(001)}/d_s$. Figure 2.6 shows decreases in silicate volume fraction χ with increasing $d_{(001)}/d_s$ for different N-values; the observation that the case $N = 1$ stands out from the others ($N > 1$) suggests significant distinction in structure-related effective particle properties between exfoliated systems and intercalated systems.

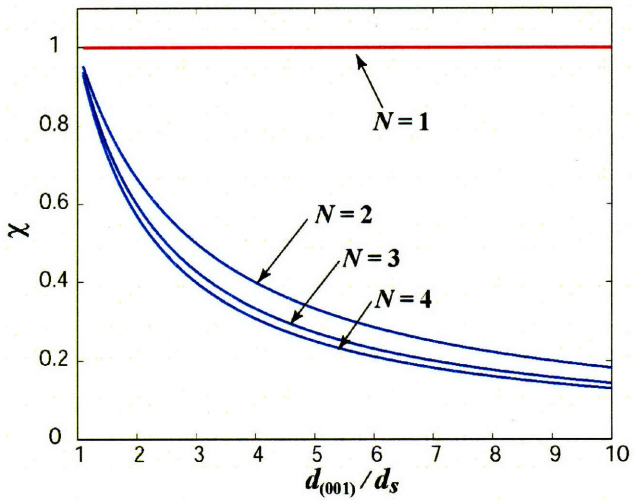

Figure 2.6: Dependence of particle silicate volume fraction χ on clay structural parameters N and $d_{(001)}/d_s$.

- Characterization by WAXD

Wide-angle X-ray diffraction (WAXD) experiments are widely performed for structure characterization of polymer/clay nanocomposites. In particular, WAX is used to monitor the peak position (2θ), full width at half maximum (*fwhm*), and intensity of the (001)

basal reflection corresponding to the repeat distance perpendicular to the silicate layers. The average interlayer spacing ($d_{(001)}$) and the average clay particle thickness (t) can be determined using the Bragg equation ($d_{(001)} = \lambda / 2\sin\theta$, where λ is the wave length of the Xray used, and θ is the angle between the beam and (001)-normal) and the Scherrer equation ($t = 0.9\lambda / b\cos\theta$; b is the *fwhm*), respectively. However, characterization of the clay structure in the above manner bares some uncertainty since both the peak position and the intensity will be affected by the presence of internal layer disorder, as well as numerous experimental factors (Vaia, 2000). Figure 2.7 shows exemplary XRD patterns of organo-clay and 5.1-wt % nylon/clay nanocomposite (see Fig. 2.8 for TEMs) (Lee and McKinley, 2002). Characteristic parameters determined from the peak position and the *fwhm* are given in Table 2.3.

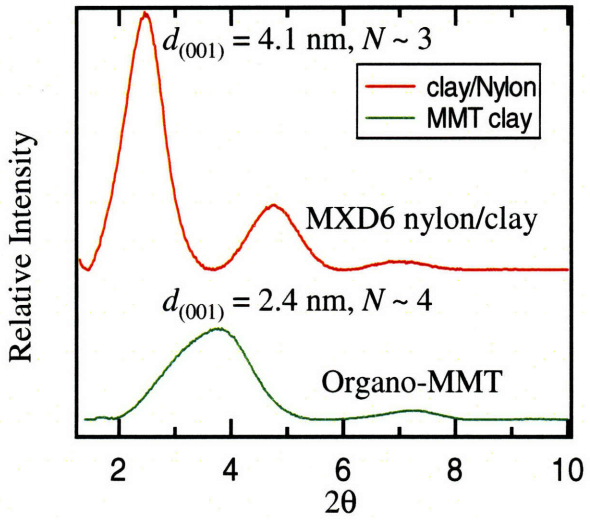

Figure 2.7: X-ray diffraction patterns for: 5.1-wt% MXD6/clay (see Fig. 2.7 for TEMs), 3-wt% PS solution/clay, and montmorrillonite (MMT). (Lee and McKinley, 2002)

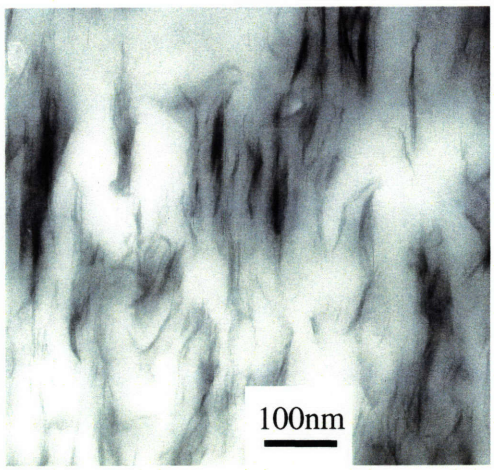

(a)

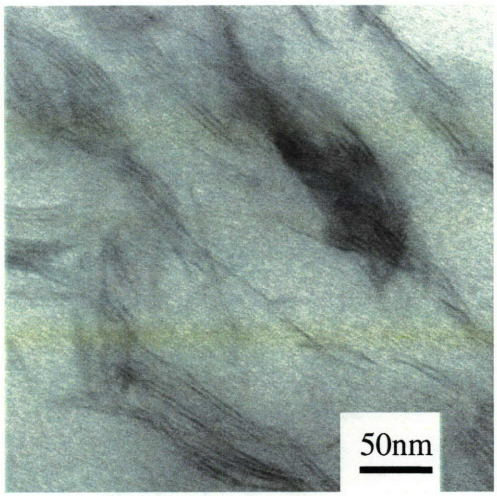

(b)

Figure 2.8: TEMs of 5.1-wt% MXD 6 nylon/clay nanocomposite, magnified by (a) 50,000, (b) 100,000 (Lee and McKinley, 2002).

Table 2.3 Structural characterization from XRD patterns in Figure 2.7 (Lee and McKinley, 2002).

Material	$d_{(001)}$ (nm)	t (nm)	N
Organo-MMT	2.4	8.74	~ 4
MXD6/MMT	4.1	10.3	~ 3

2.2.3. "Effective Particle" Model

The "effective particle", used as the basic element in continuum micromechanical models when assessing the effect of nanoclay on the overall properties of the nanocomposite, is identified by a well-defined spatial volume, occupied by both the silicate layers and the inter-layer galleries, as shown in Fig. 2.4(b). The homogeneous "effective particle" is equivalent to the multi-layer stack, shown in Fig. 2.4(a), in the sense that it possesses the same L/t, f_p, and the same homogenized elastic and thermal expansion properties as the discrete stack.

Here we pay special attention to the relationship between clay weight fraction and "particle" volume fraction; homogenization of overall thermal/mechanical properties (often anisotropic) of the "effective particle" and the dependence of "particle" properties on the clay structural parameters (N, $d_{(001)}$) are discussed later in Chapter 3 and Chapter 4, when assessing the anisotropic elastic and thermal expansion properties of the nanocomposite.

- **Volume Fraction / Weight Fraction Conversion**

Experimental studies often detail and plot property enhancement data in terms of weight fraction clay. Since the clay content is provided in terms of weight fraction W_c (ash weight), it is necessary to establish a quantitative connection between W_c and the volume fraction of the "effective particle" f_p, an important parameter in micromechanical models. First consider a two-phase composite consisting of matrix and particles (or "effective particles" in the case of a nanocomposite); the particle volume fraction f_p and particle weight fraction W_p are related according to

$$f_p = \frac{V_p}{V_p + V_m} = \frac{W_p/\rho_p}{W_p/\rho_p + (1-W_p)/\rho_m}, \tag{2.4}$$

where ρ_p and ρ_m are the mass densities of the particle and the matrix, respectively.

For an intercalated nanocomposite, the clay weight fraction W_c differs from the "particle" weight fraction W_p, since the "particle" consists of both silicate sheets and the inter-layer galleries. The two quantities are related through

$$\frac{W_p}{W_c} = \frac{\rho_p V_p}{\rho_{silicate} V_{silicate}} = \left(\frac{\rho_p}{\rho_{silicate}}\right) \Big/ \left(\frac{V_{silicate}}{V_p}\right) = \frac{\rho_p}{\rho_{silicate}} \cdot \frac{1}{\chi} \equiv \alpha, \tag{2.5}$$

where $\rho_{silicate}$ is the mass density of the silicate sheet, and the ratio W_p/W_c is defined as α.

Taking $W_p = \alpha W_c$ into Eq. (2.4), we can write f_p as a function of W_c:

$$f_p = \frac{W_c/\rho_p}{W_c/\rho_p + (1/\alpha - W_c)/\rho_m}. \tag{2.6}$$

When $W_c << 1$, as it often is for the nanocomposite, Eq. (2.6) can be linearized as

$$f_p \approx \left(\frac{\alpha\rho_m}{\rho_p}\right) W_c = \left(\frac{\rho_m}{\rho_p} \cdot \frac{\rho_p}{\rho_{silicate}} \cdot \frac{1}{\chi}\right) W_c = \left(\frac{\rho_m}{\rho_{silicate}} \cdot \frac{1}{\chi}\right) W_c. \tag{2.7}$$

The density $\rho_{silicate}$ can be calculated from the montmorillonite lattice parameters given in Table 1,

$$\rho_{silicate} = \rho_{lattice} = \frac{M_0}{A_0 d_s} = \left(\frac{2.44}{d_s}\right) nm \cdot g/(cm)^3. \tag{2.8}$$

Taking Eq. (2.8) and using an assumed value of ρ_m = 1.0 $g/(cm)^3$ into Eq. (2.7), we have

$$f_p = \left(\frac{0.41 d_s}{nm}\right) \frac{W_c}{\chi} = \left(\frac{0.41 nm^{-1}}{\chi_N} W_c\right). \tag{2.9}$$

The conversion ratio f_p/W_c given in Eq. (2.9) is plotted as a function of N and $d_{(001)}/d_s$ in Figure 2.9. Beall (2000) took N = 1 and d_s = 1 nm, and obtained f_p = 0.4 W_c, consistent

with the present result; however, other particle structures can lead to f_p/W_c ratios > 1, reflecting the increased spatial extent of swollen intercalated stacks.

Similarly, the anisotropic elastic and thermal expansion properties of the "effective particle" can be expressed in terms of the clay structural parameter χ (or χ_N) plus relevant properties of the silicate and the matrix polymer, as will be discussed in Chapter 3 (Section 3.1) and Chapter 4 (Section 4.1).

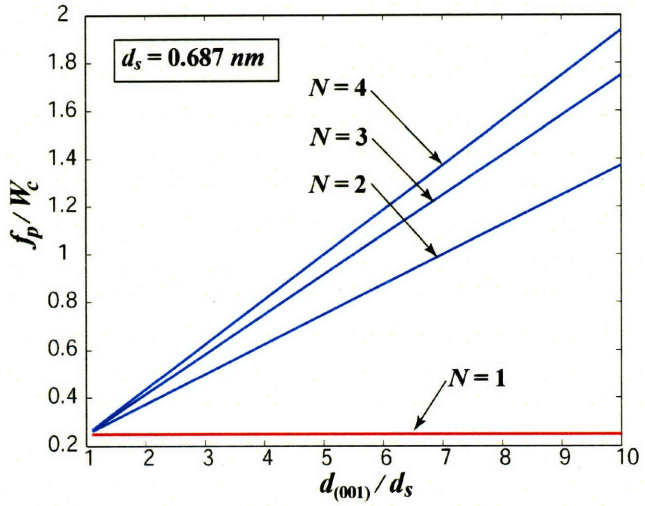

Figure 2.9: Dependence of f_p/W_c on clay structural parameters N and $d_{(001)}/d_s$.

2.2.4. Large Deformation Model

While the particle model as basic as the 'effective particle' elaborated previously proves sufficient in capturing the load transfer mechanism in elastic analysis, it may not be able to properly account for large-strain deformation modes of the particle, including bending of the atomic-level thick silicate layers and shearing of the inter-layer gallery material to large deformation, when the simple particle model is utilized in finite element tools.

In finite deformation analysis, a desired particle model is one that is capable of capturing the major deformation behaviors of the nanoclay without introducing further modeling complications. One strategy is to extend the usage of the small-strain "effective particle" model — modeling the 'particle' as an elastic entity with low transverse shear stiffness can properly accommodate the large shear deformation that is apt to occur in the inter-layer gallery. The homogenized "effective particle" as illustrated in Fig. 2.4b is modeled to be highly anisotropic; the transverse shear modulus ($G_{p,12}$) is taken to be substantially lower than the in-plane shear modulus ($G_{p,13}$) since the inter-layer gallery, consisting mainly of short surfactant molecules and oriented polymer chains that had penetrated and swollen the interlayers of the clay during the initial synthesis procedure, is speculated to be a highly shearable material.

However, a major drawback of an anisotropic 'elastic' particle is that, when implemented in many finite element simulations, the material direction vectors (needed to properly describe the direction-dependent anisotropic behavior of the particle) were found to erroneously rotate during simulation of large deformation, resulting in incorrect and unphysical particle behavior.

Therefore, a 'sandwich'-like particle model, as illustrated in Figure 2.4(c), is proposed to substitute for the homogeneous 'effective particle' in large deformation analysis, where a homogeneous "effective gallery" region, modeled to be hyper-elastic, is bound by stiff silicate sheets on its top and bottom interfaces. The hyper-elastic interior with very little compressibility compared to its shear flexibility is ideal for the mechanical characterization of the gallery material, while the much more rigid silicate sheets bound the "effective gallery" and put a proper constraint on its in-plane deformation.

Details of mechanical properties of the hyper-elastic "effective gallery" are not discussed since large scale deformation behavior of the composite is part of the ongoing work and is not presented in this thesis. However, such a model (the silicate-bonded effective gallery representation) certainly provides a physically realistic and computationally feasible approach to account for the primary deformation modes of the intercalated clay particle, when investigating behavior of the nanocomposite and underlying deformation mechanisms of the nanoclay under large scale compression.

2.3. Continuum-level Micromechanical Model Description

Micromechanical models of various representative volume elements (RVEs) of the underlying structure of the nanoclay-filled polymers are constructed for assessing the effects of the nanoclay on macroscopic thermal/mechanical properties of the nanocomposite. The continuum-level models operate on continuous 'matrix' and 'particle' phases; meso- and nano-scale features of the clay (as well as a semi-crystalline matrix, if applicable) are embedded in geometrical and material parameters of the composite components through proper procedures of homogenization, as illustrated in Fig. 2.1. The continuum-level model can be characterized by a set of geometrical and material parameters. The geometrical descriptors include particle volume fraction, particle aspect ratio, particle dispersion (random vs. regular), and particle orientation distribution. The material descriptors can be thought of in terms of clay exfoliation (exfoliated vs. intercalated), polymer/clay interface behavior, and polymer morphology (both in the vicinity and away from clay surfaces).

Periodic boundary conditions are applied to the RVEs to make them space-filling and thus mimic macroscopic material. RVEs are subjected to various types of loading in finite element simulations, depending on the specific property under investigation (e.g., uniaxial stretching for E and σ_y, temperature change for thermal expansion coefficient); macroscopic composite behavior can then be obtained by calculating the average RVE response. Standard RVE procedures for homogenized composite property extraction via micromechanics are given by Danielsson (Danielsson, et al., 2002; Danielsson, Ph.D. thesis, 2003) and the author in previous work (Sheng, M.S. thesis, 2002).

2.3.1. Representative Volume Elements (RVEs)

A schematic RVE of a general three-dimensional case of a particulate composite with random spatial distribution, as well as a random orientation distribution of high-aspect ratio, equi-axed particles is shown in Fig. 2.10a. We can simplify the representation to two-dimensions and also specialize to highly-oriented (aligned) dispersions. Furthermore, the random dispersion can be idealized to different types of regularly-patterned distributions such as stacked (Fig. 2.10e) and staggered (Fig. 2.10f and g) arrays.

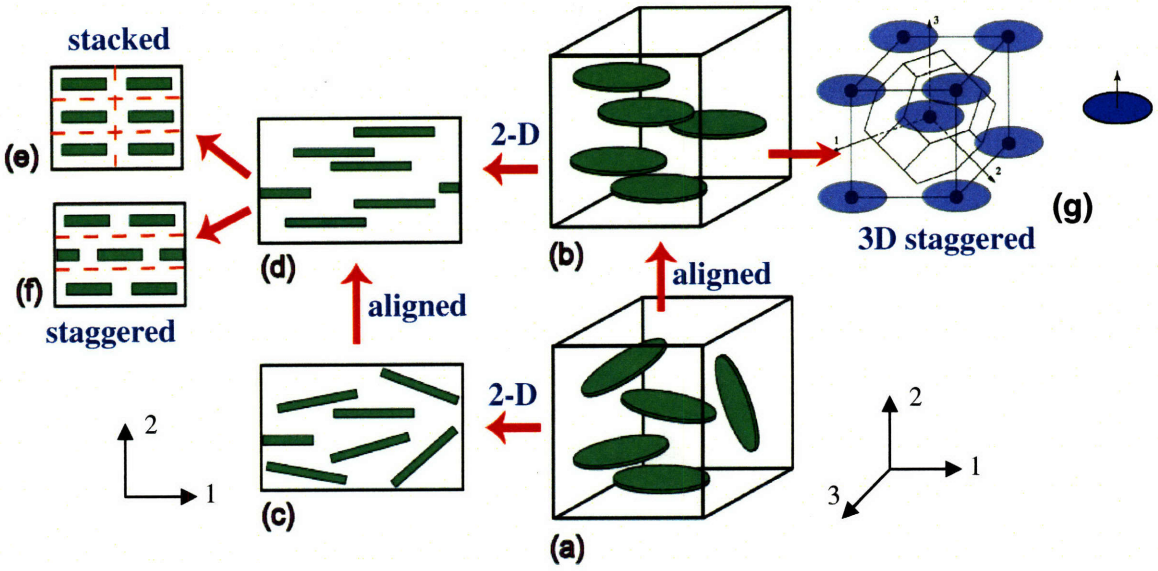

Figure 2.10: Schematics of 2D and 3D representative volume elements.

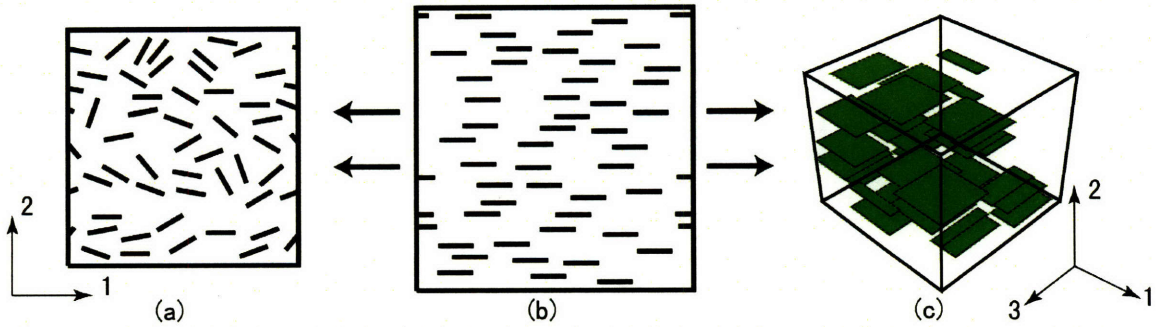

Figure 2.11: FEM realizations of RVEs: (a) 2D RVE with random particle orientation distribution; (b) 2D RVE with randomly-located particles aligned in 1-direction; (c) 3D RVE with particles aligned parallel to the 1-3 plane.

Fig. 2.11(c) and (b) show FEM realizations of 3D and 2D RVEs, respectively, with well-aligned, randomly-distributed particles. In the generation of such random spatial distributions of particles, a non-overlapping rule is imposed (i.e., no particle is allowed to be overlapped). Also, if one particle happens to cross the RVE boundary, the part extruding out of the RVE boundary "re-enters" the RVE in the corresponding position required by the periodic continuation constraint. 2D RVEs with misaligned particles, as shown in Fig. 11(a), are constructed to study the effect of particle orientation distribution on macroscopic composite properties. The automatic mesh-generating tool *Triangle*[2] (Shewchuk, 1996) has been utilized to assist mesh generation of the 2D configurations. Generations of 3D/2D RVEs, as demonstrated in Fig. 2.11, are automatically realized through MATLAB codes developed by the author, with convenient user input parameters such as particle aspect ratio, particle volume fraction, particle orientation distribution (if mis-aligned), etc. Representative MATLAB codes are included in Appendix A.

Note that the 2D plane strain model is only an approximation of the 3D geometry. In particular, the real platelet inclusions have finite dimensions in all directions; however, the 2D "particle" has an unbounded dimension in the plane strain direction (the 3-direction in Fig. 2.11a and b). Furthermore, the stress-strain state in a 2D plane strain analysis differs from that in a 3D case, given the same external loading condition, due to the plane strain constraint. Limits of the 2D plane strain analysis will be discussed in Chapters 5 and 6, when 2D RVEs are used to assess effects of particle orientation distribution on the stiffness and initial yield strength of the nanocomposites.

V-BCC like unit cell The 3D staggered RVE, as illustrated in Fig. 2.10(g) can be viewed as a simplification of the 3D random, aligned structure (Fig. 2.10b). Such a

[2] http://www.cs.cmu.edu/~quake/triangle.html

micromechanical unit cell model is constructed for polymeric nanocomposites with regularly distributed nanoclay particles. It is based on a Voronoi tessellation of aligned disc-shaped particles whose centers are arranged on a body-centered cubic (BCC) array, as illustrated in Figure 2.12(a). The geometry and meshing of an exemplary unit cell containing a tilted particle are shown in Figure 2.12(b) and (c), respectively. The surface facet meshes are generated with assistance of 2D mesh-generator *Triangle*; the cell itself is meshed with assistance of 3D mesh-generator *Tetgen*[3] (Si and Gaertner, 2005). While such a RVE considerably cut down computational cost, its regular geometry prohibits insightful investigations into many physics of the naturally randomly distributed nanocomposites. It is due to this reason that we choose not to present work based on the 3D unit cell in this thesis.

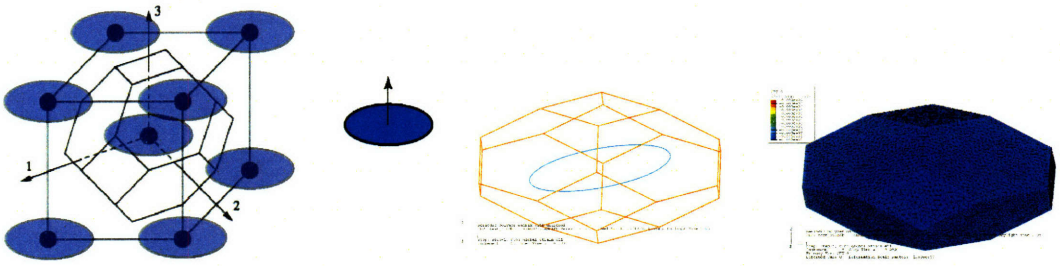

Figure 2.12: (a) Schematic of a 3D staggered spatial arrangement of disc-shaped particle, where the center of the particles are located on a BCC-type lattice. (b) Realization of a V-BCC like unite cell, containing a tilted particle. (c) Meshed unite cell ready to be used in FEM analysis.

[3] http://tetgen.berlios.de/index.html

2.3.2. Periodic Boundary Conditions and Macroscopic Response

The representative volume elements are space-filling and spatially periodic. When an RVE is subjected to a macroscopic loading, periodic boundary conditions must be applied to the surface of the RVE so that it deforms in a periodically repeating manner and so that no overlaps or cavities form. Fig. 2.13 shows a schematic of a periodically repeating RVE (adapted from Danielsson, 2003). Periodic boundary conditions expressed in terms of the macroscopic deformation gradient, **F**, are applied to the RVE. In particular, considering a periodically repeating point pair (A, B) located on the surface of the RVE, as shown in Fig. 2.13(a), the 'no overlapping, no cavity' requirement poses a constraint on the relative displacement of point-A with respect to point-B. The relative displacement is determined by the applied macroscopic displacement gradient, **H** (**H** = **F** – **1**), through

$$\mathbf{u}(B)-\mathbf{u}(A)=(\mathbf{F}-\mathbf{1})\{\mathbf{X}(B)-\mathbf{X}(A)\}=\mathbf{H}\{\mathbf{X}(B)-\mathbf{X}(A)\}, \tag{2.10}$$

where **u** denotes displacement, and **X** denotes position in the undeformed reference configuration. Each point pair on periodic surfaces of the RVE is constrained by Eq. (2.10). The macroscopic deformation of the RVE is imposed by prescribing the nine components of **F**.

When other variables such as temperature, T, (when investigating heat transfer properties) or concentration, c, (when investigating mass transfer properties) are of concern, similar constraints must be applied to {T(B)-T(A)} or to {c(B)-c(A)} to ensure the continuity and periodicy of the temperature or concentration field. General periodic boundary conditions are accordingly expressed in terms of the macroscopic temperature gradient (∇T), or concentration gradient (∇c). For example, the relative temperature of

the periodic pair (A, B) is related through the prescribed macroscopic temperature gradient ∇T:

$$T(B) - T(A) = (\nabla T' - \mathbf{1}) \cdot \{\mathbf{X}(B) - \mathbf{X}(A)\}. \tag{2.11}$$

The principle of virtual work has been used to calculate the overall mechanical response of the RVE. Danielsson, et al., 2002, derived the components of the macroscopic (RVE-average) first Piola-Kirchhoff stress tensor, **P,** in terms of the generalized reaction forces of three "imaginary nodes", the displacement components of which are related to the macroscopic deformation gradient **F**. The macroscopic Cauchy stress tensor **T** is then obtained from $\mathbf{T} = \mathbf{P}\mathbf{F}^T/J$, where $J = \det(\mathbf{F})$. In this work the same method is used for the calculation of the macroscopic cell response; such a procedure has also been adapted to the frame of small geometry change for the convenience of elastic analysis in previous work of the author (Sheng, 2002 MS thesis).

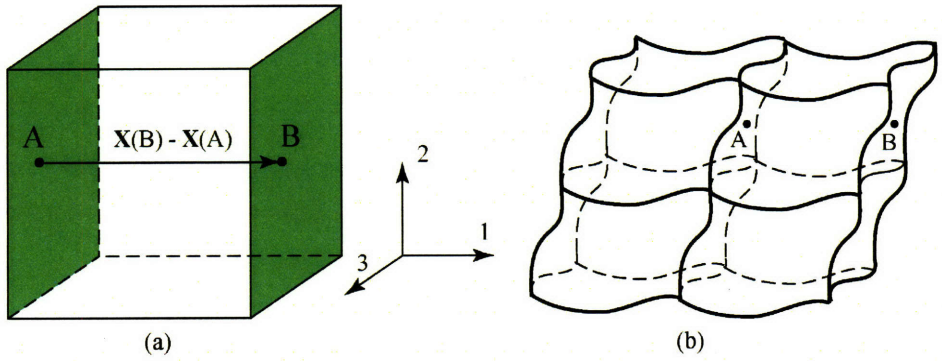

Figure 2.13: (a) Undeformed RVE; (b) deformed RVE with its periodic neighbors (adapted from Danielsson, 2003).

Chapter 3

Anisotropic Elastic Properties of Nanocomposites

Nanocomposites generally demonstrate improved axial modulus over the matrix polymer. The level of modulus increase with just a few weight percent of clay can vary from ~40% up to two or three fold, depending on a variety of morphological and material features. This chapter evaluates the complete set of elastic constants of the nanocomposite and parametrically studies the effects of the primary structural and morphological features of the nanoclay on the composite elastic properties. Underlying mechanisms governing the property enhancements are explored, including the load transfer mechanism, the strain shielding and the in-plane constraining effect of the clay platelets. In the end, the multi-scale modeling approach is applied to amorphous and semi-crystalline polymer/clay nanocomposites; the predicted composite moduli are in good agreement with experimental data.

3.1. Effective Elastic Properties of the Clay

Considering the multi-layer clay particle as a laminate (with isotropic silicate sheets and orthotropic polymeric galleries[1]), as illustrated in Figure 3.1, the overall elastic properties of the homogenized "effective particle" can be estimated as

$$E_{p,11} = E_{p,33} = \chi E_{silicate} + (1-\chi) E_{gallery,11} \approx \chi E_{silicate}, \text{ (assuming } E_{gallery,11} << E_{silicate}) \quad (3.1)$$

[1] Note that orthotropic material properties are denoted with index (e.g., $G_{gallery,12}$), whereas isotropic material properties do not need any index (e.g., $E_{silicate}$).

$$G_{p,13} = \chi G_{silicate} + (1-\chi)G_{gallery,13} \approx \chi G_{silicate}\text{, (assuming } G_{gallery,13} << G_{silicate}) \tag{3.2}$$

$$v_{p,12} = \chi v_{silicate} + (1-\chi)v_{gallery,12}\text{,} \tag{3.3}$$

$$E_{p,22} = \left\{ \frac{\chi}{E_{silicate}} + \frac{(1-\chi)}{E_{gallery,22}} + 2\left(\frac{v_{silicate}}{E_{silicate}} - \frac{v_{gallery,12}}{E_{gallery,11}} \right)(1-\chi)\varsigma \right\}^{-1}\text{, with}$$

$$\varsigma = \frac{\left[\frac{v_{gallery,21}}{E_{gallery,22}} - \frac{v_{silicate}}{E_{silicate}} \right]}{\left[\frac{(1-v_{silicate})}{E_{silicate}} \cdot \frac{(1-\chi)}{\chi} + \frac{(1-v_{gallery,13})}{E_{gallery,11}} \right]} \tag{3.4}$$

$$G_{p,12} = \frac{G_{silicate} G_{gallery,12}}{(1-\chi)G_{silicate} + \chi G_{gallery,12}}\text{.} \tag{3.5}$$

It should be noted that the particle properties refer to local orthogonal axes, where axis-1 and axis-3 lie in the particle plane and axis-2 is normal to the particle plane, as illustrated in Fig. 3.1. The "effective particle" is transversely isotropic about the axis normal to the particle plane (i.e., the 2-direction). Therefore the two Poisson's ratio v_{12} and v_{21} are generally different and are related by

$$\frac{v_{p,12}}{E_{p,11}} = \frac{v_{p,21}}{E_{p,22}}\text{.} \tag{3.6}$$

where v_{12} has the physical interpretation of the Poisson's ratio that characterize the transverse strain in the 2-direction resulting from uniaxial stress in the 1-direction, while v_{21} characterizes the strain in the plane of isotropy resulting from stress normal to it.

The in-plane shear modulus $G_{p,13}$, Young's modulus, $E_{p,11}$, and Poisson ratio, $v_{p,13}$, are related through

$$G_{p,13} = \frac{E_{p,11}}{2(1+v_{p,13})} \tag{3.7}$$

The elastic properties of the gallery have yet to be determined; however, it is reasonable to assume $E_{gallery,ii}/E_{silicate} << 1$ (no sum on repeated index i), and $G_{gallery,ij}/G_{silicate} << 1$. While the in-plane "particle" properties $E_{p,11}$ and $G_{p,13}$ are dominated by the stiff silicate sheets (Eq. 3.1, 3.2), the transverse properties $E_{p,22}$ and $G_{p,12}$ are much lower and are highly dependent on the gallery properties.

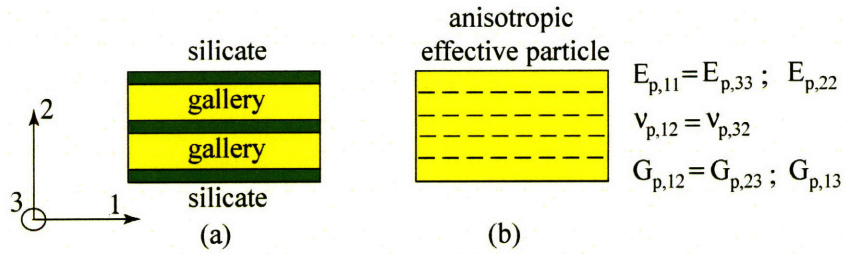

Figure 3.1: (a) Multi-layer structure of intercalated nanoclay; (b) homogenized "effective particle" with anisotropic elastic properties.

Modeling of the gallery material

The gallery material in a multi-layer silicate stack consists of both surfactants and matrix polymer chains that have penetrated the inter-silicate layers during various stages of synthesis and processing. The physical properties of the gallery material have yet to be clearly identified. However, the structure and dynamics of the nanoconfined polymer chains have been probed by various analytical techniques, such as DSC, NMR, scattering, dielectric spectroscopy (Giannelis, et al., 1999). The local dynamic behavior of the confined polymer chains in the nanocomposites are found to differ markedly from the bulk; particularly, local intercalated PEO chains exhibit greater flexibility along the chain backbone as compared to those in bulk (Giannelis, et al., 1999; Hackett, et al., 1998; Vaia, et al., 1995). In addition, the behavior of the confined inter-layer chains is expected

to depend on the thermophysical nature of the matrix polymer (thermoset vs. plastic). Based on available measurements and MD findings, the gallery material is expected to be more flexible and less dense than the bulk polymer; hence it is modeled with lowered mass density and shear modulus.

Presumably, the nano-confined (consequently, oriented) gallery material is mechanically highly anisotropic. Here we model the inter-layer gallery with relatively low transverse shear ($G_{gallery,12} = G_{gallery,23} \sim G_m/10$), but neglect the anisotropy in the axial moduli or the Poisson ratios ($E_{gallery,11} = E_{gallery,22} \sim E_m$, $\nu_{gallery,12} = \nu_{gallery,22} \sim \nu_m$) since this stiffness contribution to the overall particle stiffness will be small compared to that of the silicate sheets in any event.

Modeling of the single layer silicate

As mentioned in Chapter 2 (Section 2.2.1), Manevitch and Rutledge (2004) extracted a (modulus, thickness) pair for the montmorillonite silicate sheet from their MD simulations, which sampled both membrane and bending behavior of the sheet. Their calculations of the membrane stiffness together with the bending stiffness deduced from buckling behavior yield a (modulus, thickness) pair of $d_s = 0.678$ nm and $E_{silicate} = 369 \sim 383$ GPa; the effective mechanical thickness of 0.678 nm is comparable to the distance between the outermost layers of atoms on either surface of the atomically thin sheet (0.615 nm).

Fig. 3.2 and Fig. 3.3 depict the effect of clay structural parameters (N, $d_{(001)}$) on the longitudinal ($E_{p,11}$) and transverse ($E_{p,22}$) particle/matrix stiffness ratios, respectively,

assuming $E_{gallery,11} = E_{gallery,22} = E_m = 4$ GPa and $\nu_{gallery,12} = \nu_{gallery,13} = \nu_m = 0.35$. For a given micro-structure of intercalated clay ($N > 2$), $E_{p,11} >> E_{p,22} \sim E_m$. An abrupt jump in the "particle" stiffness occurs as the morphology the nanoclay transits from *intercalation* ($N \geq 2$) to *complete exfoliation* ($N = 1$).

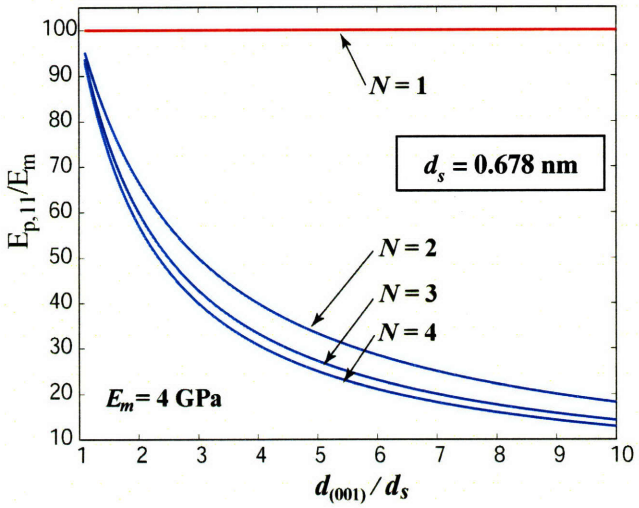

Figure 3.2: Dependence of longitudinal particle modulus $E_{p,11}/E_m$ on clay structural parameters N and $d_{(001)}/d_s$ (E_m = 4 GPa).

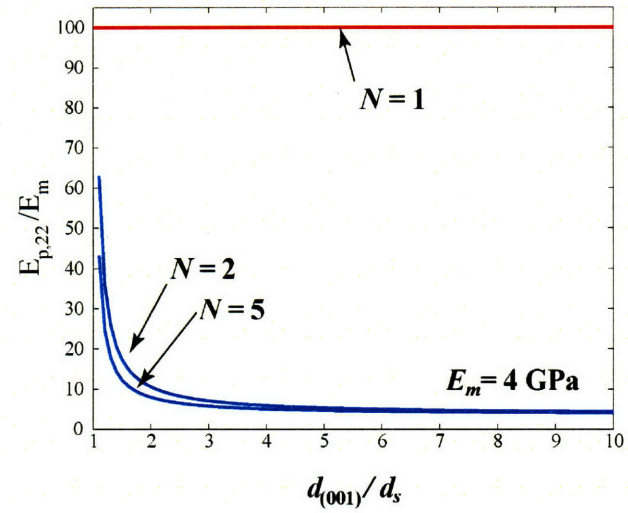

Figure 3.3: Dependence of longitudinal particle modulus $E_{p,22}/E_m$ on clay structural parameters N and $d_{(001)}/d_s$ (E_m = 4 GPa).

3.2. Continuum-level Prediction of Anisotropic Elastic Properties of Composites

Prediction of the mechanical properties of discontinuous fiber/flake composite materials has been a subject of extensive study. The composite of interest is considered to consist of two homogeneous phases: matrix and high-aspect-ratio particles. Here both analytical and numerical predictions of the overall composite stiffness are presented. These models can be readily applied to polymer/clay nanocomposites with reasonable homogenization of the "effective particle" geometry and properties.

- Mori-Tanaka Type Model (analytical)

Numerous micromechanical models (e.g., Eshelby, 1957; Hill, 1965; Mori and Tanaka, 1973; Halpin, 1969, 1976) have been proposed to predict the elastic constants of well-aligned discontinuous fiber/flake composites, as shown in Fig. 3.4a. These models generally depend on parameters including particle/matrix stiffness ratio E_p/E_m, particle volume fraction f_p and particle aspect ratio L/t. Tucker (Tucker and Liang, 1999) provides a good review of the application of several classes of micromechanical models to discontinuous fiber-reinforced polymers. They note that, of the existing models, the Mori-Tanaka type models (Mori and Tanaka, 1973; Tandon and Weng, 1984) give the best results for large-aspect-ratio fillers. Here we employ a closed-form analytical solution for the complete set of anisotropic elastic properties of the composite derived by Tandon and Weng (1984) by combining the Eshelby theory and the Mori-Tanaka model. For a composite material reinforced with disc-like fillers aligned along direction 1, as illustrated in Fig. 3.4a, the Tandon-Weng prediction of the moduli E_{11}, E_{22}, and the in-plane shear modulus, G_{13}, of the composite are:

$$\frac{E_{11}}{E_m} = \frac{1}{1+f_p[-2v_m A_3 + (1-v_m)A_4 + (1+v_m)A_5 A]/2A}, \tag{3.6}$$

$$\frac{E_{22}}{E_m} = \frac{1}{1+f_p(A_1 + 2v_m A_2)/A}, \tag{3.7}$$

$$\frac{G_{13}}{G_m} = 1 + \frac{f_p}{G_m/(G_p - G_m) + 2(1-f_p)H_{1313}}, \tag{3.8}$$

where A and A_i are constants depending on the components of the Eshelby tensor and the matrix/particle properties, and H_{ijkl} are the Cartesian components of the Eshelby tensor (Eshelby, 1957).

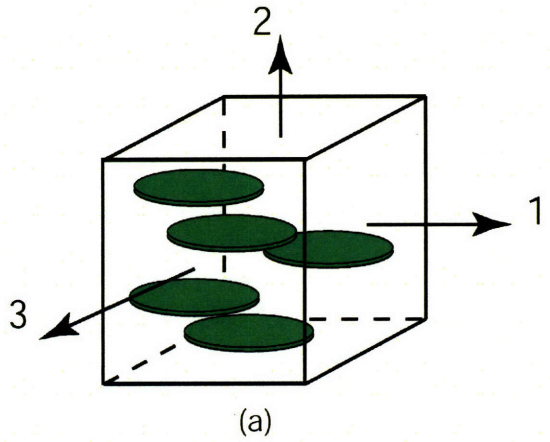

(a)

Figure 3.4: Aligned disc-shape ellipsoidal particles assumed by theoretical models.

- Finite Element (FE)-Based Numerical Simulation

Figure 3.5 shows an exemplar 3D RVE used in FE simulations to calculate the anisotropic elastic properties of composites with aligned plate-shaped fillers. The particle is characterized by its aspect ratio (L/t) and elastic properties. The particle can be modeled to be isotropic or transversely isotropic, depending on the state of clay morphology (exfoliation vs. intercalation) of the specific nanocomposite under investigation. Ideally, the RVE size is desired to be large compared to the particle

dimension so that a sufficient amount of particles are modeled for an accurate statistical representation of the nanocomposite miscrostructure; however, due to computational limit (3D simulations are in general costly in terms of computational time and resource occupation), we choose to construct RVEs of smaller scale (usually the dimension of the cubic RVE shown in Fig. 3.5 is 3 ~ 5 times the in-plane dimension of the embedded particle, and the number of particles inside the RVE, varying with volume fraction, is no less than 10) and obtain the overall composite property by averaging over results of 8 ~ 10 random RVE realizations. In fact, Danielsson (2003) has shown that overall properties averaged over results of small-size RVEs can efficiently equate those obtained from a RVE of much larger scale, satisfying statistical homogeneousness.

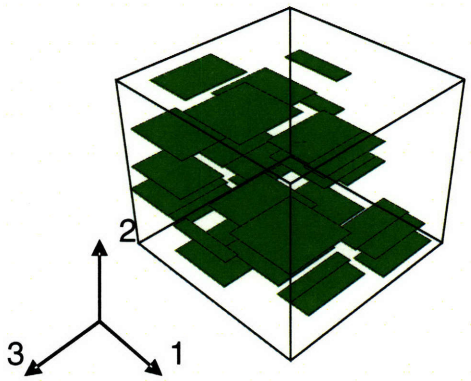

Figure 3.5: 3D RVE with aligned plate-like particles.

Here we assign isotropic elastic properties to the particle in order to draw comparison between the analytical (Mori-Tanaka) and numerical (FE-based simulation) predictions of the anisotropic elastic properties of the composite. Fig. 3.6 compares the Mori-Tanaka and the FE predictions of E_{11}, E_{22}, ν_{12}, and ν_{13} of a composite with L/t = 50, E_p/E_m = 100; the close agreement between Mori-Tanaka and FE results in all four elastic constants indicates that the Mori-Tanaka type models can serve as an excellent tool for the

prediction of the elastic properties of composites filled with isotropic particles (for instance, exfoliated polymer/clay nanocomposites).

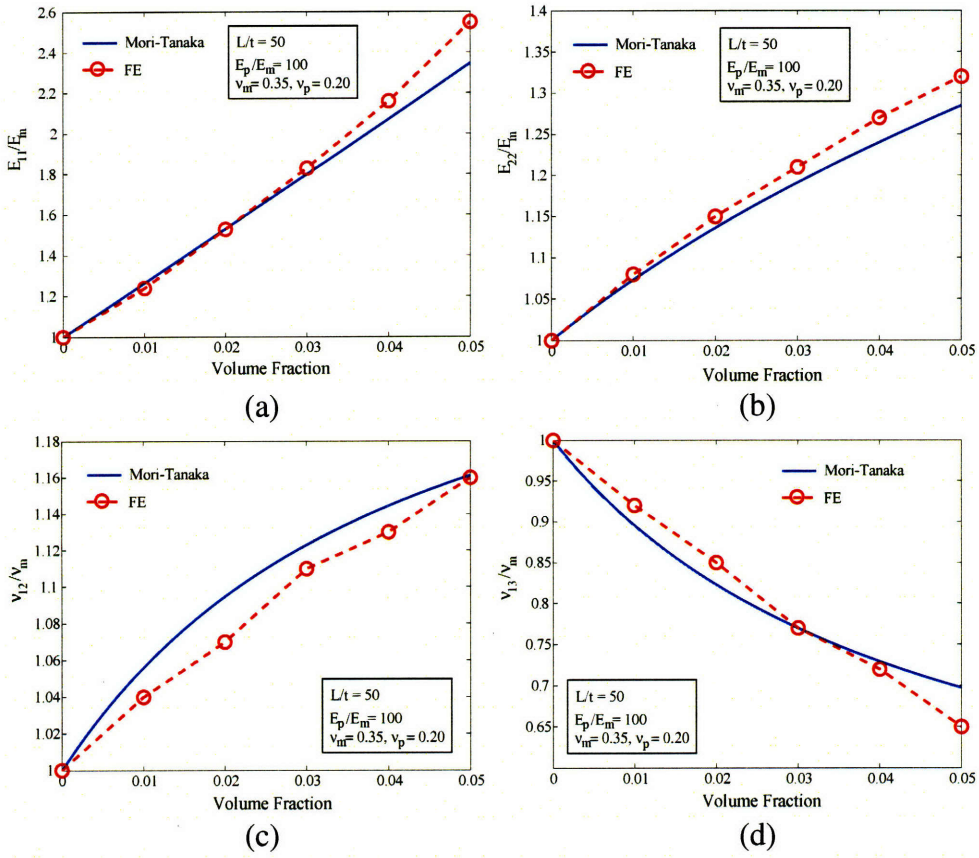

Figure 3.6: Comparison of Mori-Tanaka and 3D FE predictions of the composite elastic properties (L/t = 50, E_p/E_m = 100, ν_m = 0.35, ν_p = 0.20): (a) E_{11}; (b) E_{22}; (c) ν_{12}; (d) ν_{13}. Each FE data point is averaged over 10 simulations.

- Results

Fig. 3.7(a), (b) and (c) depict the Mori-Tanaka predictions of the normalized anisotropic elastic properties (E_{11}, E_{22}, G_{12}, G_{13}, ν_{12}, ν_{13}) of the composite as functions of the particle aspect ratio (L/t) and the particle volume fraction (f_p) for fixed matrix and particle isotropic elastic properties: E_p/E_m = 100, ν_p = 0.20, ν_m = 0.35. As shown in Fig. 3.7(a) and (b), the in-plane properties, E_{11} (E_{11}= E_{33}) and G_{13}, are well reinforced by the stiff

filler aligned in the 1-3 plane, whereas the influence on the transverse (out-of-plane) counterparts, E_{22} and G_{12} (especially G_{12}), are rather limited. For a given f_p, while the particle aspect ratio has significant impact on the reinforcing efficiency of composite moduli, E_{11} and G_{13}, its effect on E_{22} or G_{12} is nearly negligible.

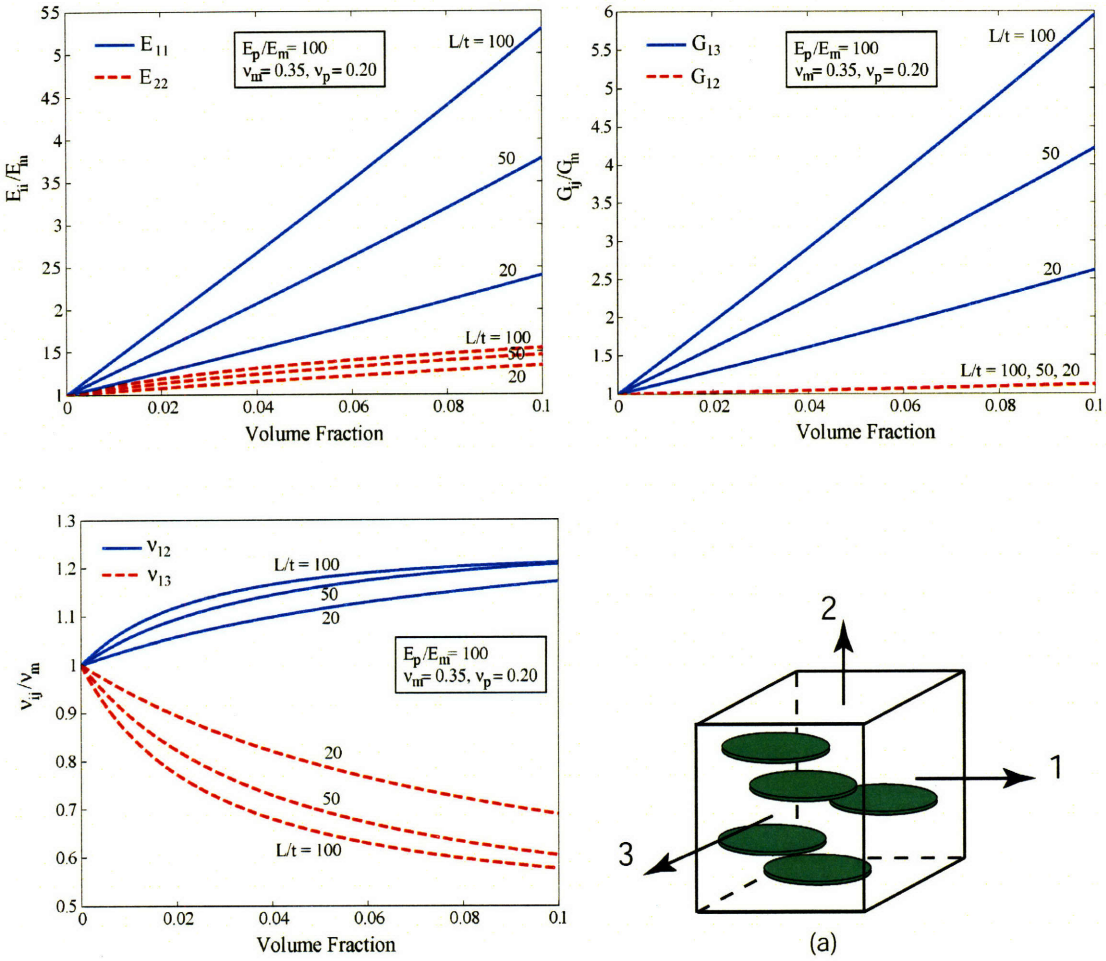

Figure 3.7: Effect of particle aspect ratio (L/t = 20, 50, 100) on the anisotropic elastic properties of composites filled with aligned disc-shape particles (refer to Fig. 3.1a for definition of axes), using Mori-Tanaka. (a) E_{11} and E_{22}, normalized by E_m; (b) G_{12} and G_{13}, normalized by G_m; (c) ν_{12}, ν_{13}, normalized by ν_m.

The dependency of the axial modulus E_{11} on the particle f_p, L/t and E_p/E_m has been thoroughly studied in previous work of the author (Sheng, 2002, MS thesis; Sheng, et al.,

2004). In summary, the governing mechanism is the load transfer mechanism: when a composite containing discontinuous high-aspect-ratio particles is subjected to tensile loading, the load is transferred from the surrounding matrix to the particle mainly through interface shear stress. As an example, Fig. 3.8 demonstrates simulation results of the distribution of the interface shear stress, τm, and the axial tensile stress in the particle, σp, with distance along the particle axis; the shear-distorted mesh surrounding the particle is shown in Fig. 3.8b (note that the undeformed mesh is a rectangular gird). Simple shear lag analysis (Cox 1952) reveals that large particle aspect ratio, L/t, and high relative matrix shear modulus, G_m/E_p, are desired for efficient stiffness enhancement; the former provides a relatively long central portion for effective load carrying, while the latter provides high load transfer efficiency through the high matrix shear modulus. Fig 3.9 shows the axial strain contour in a 2D RVE loaded in uniaxial 1-direcion stress to ε_{11} = 0.005; the typical axial stress build-up in a particular "isolated" particle is depicted in Figure 3.9(a). The stress distributions in particles partly or completely "overlapped" by other particles, as shown in Figures 3.9(b) and (c), demonstrate the negative effects of particle interaction on load transfer efficiency: high-aspect-ratio particles shield the matrix from straining, and thus reduce the efficiency of load transfer to neighboring particles. For a given f_p, particles with large L/t have a high tendency to cluster during a computer-generated "random" seeding process, which will result in a significantly lower macroscopic E_{11} when the clustering is dominated by the kind of particle "overlapping" shown in Figure 3.9(c).

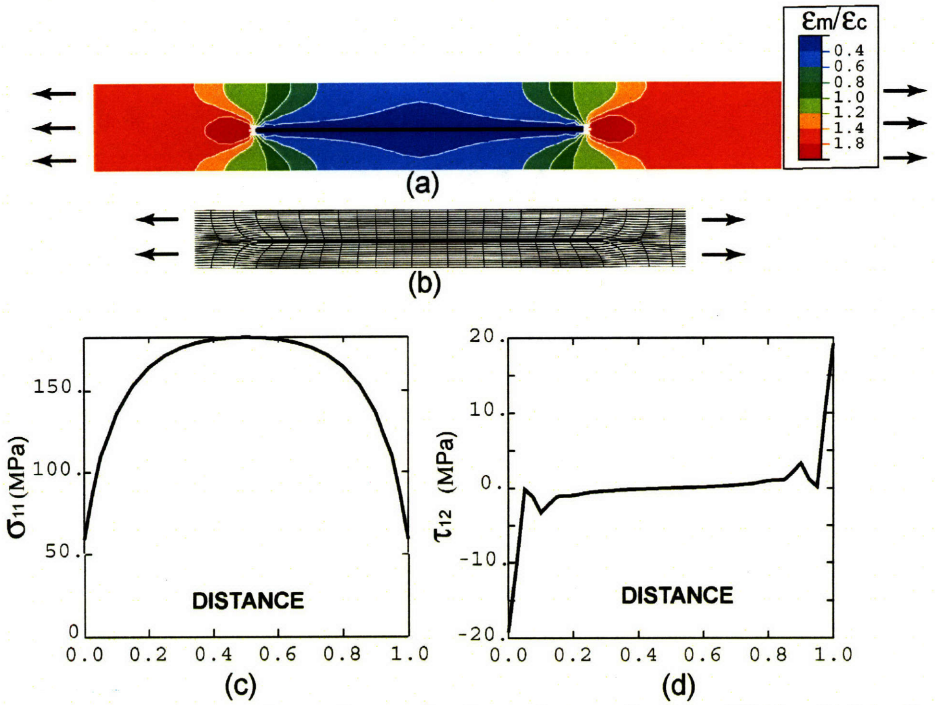

Figure 3.8: Illustration of the load transfer mechanism using results from 2D simulation of a unit cell representing the regular "stacked"-array distribution of particles (see Fig. 2.10e, f_p = 0.02, L/t = 100, macroscopic axial strain ~ 0.005): (a) normalized matrix axial strain contour; (b) shear deformation in the matrix adjacent to the particle; (c) axial tensile stress in the particle; (d) shear stress in the particle.

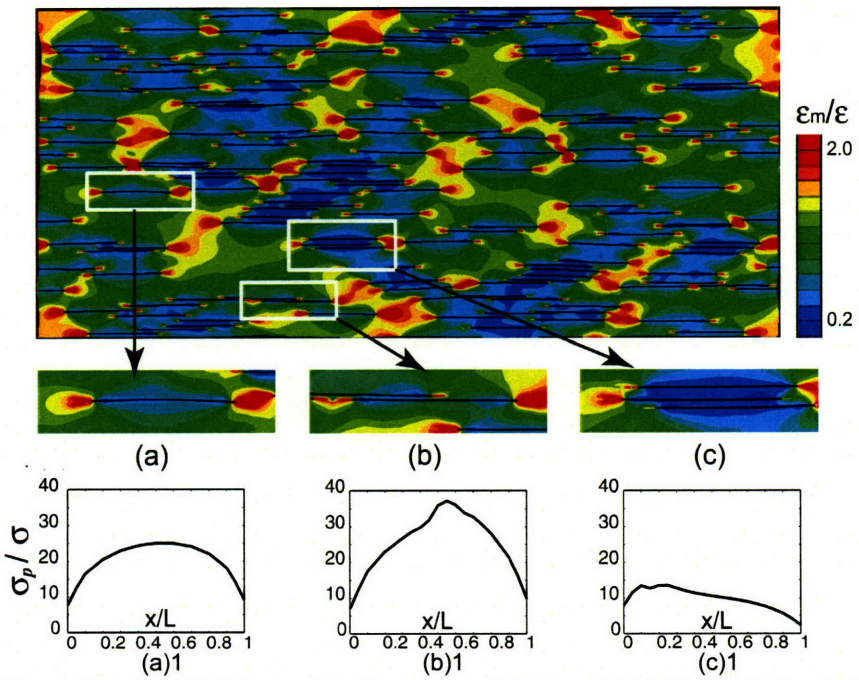

Figure 3.9: Effect of strain shielding on load transfer efficiency (2D RVE with f_p = 0.03, L/t = 100, E_p/E_m = 100). (a) "Isolated" particle; (b) partly "overlapped" particle; (c) completely "overlapped" particle. (a), (b), (c)1: Normalized stress distributions in particle (a), (b), and (c), respectively; σ_p is the axial stress in the particle, σ is the macroscopic axial stress (σ = 11.5 MPa), x/L is the fractional distance along the particle, from left to right.

The enhancement in E_{22} is far less prominent than the enhancement in E_{11}; however, nearly 50% increase in the composite E_{22} can be achieved with 10% volume faction of high stiffness, high aspect ratio particles, as shown in Fig. 3.7(a). The increase in E_{22} is mainly attributed to the in-plane constraint of the plate-like fillers with extremely high stiffness and high aspect ratio. The existence of such fillers creates a nearly plane-strain constraint in the matrix. When the composite is subjected to axial tensile loading in the 2-direction, the stiff particle constrains in-plane contraction in adjacent matrix material, resulting in in-plane tensile stress in the matrix, which, in turn, reduces in the strain in the transverse direction due to the Poisson effect. Larger particle aspect ratios or higher matrix Poisson ratios (e.g, elastomer matrix) will further enhance this effect.

It is also interesting to note the plane-strain-like effect of the fillers on the Poisson ratios of the composite. The nearly plane-strain constraint in the matrix yields $\nu_{12} > \nu_m > \nu_{13}$ (refer to Section 3.1 for conventions). The fact that the particle is much stiffer than the matrix places a high lateral constraint on the contraction of polymer that would occur in the 3-direction when stressed in the 1-direction, which reduces overall contraction in the 3-direction (hence decreases in ν_{13}, $\nu_{13} \equiv - \varepsilon_{33}/\varepsilon_{11}$, under uniaxial stress in direction-1), but promotes contraction in the 2-direction due to the Poisson effect (hence increases in ν_{12}, $\nu_{12} \equiv - \varepsilon_{22}/\varepsilon_{11}$, under the same uniaxial stress state). For a given f_p, this plane strain effect becomes more manifest when the particle aspect ratio increases.

3.3. Application of Multiscale Modeling

The multi-scale micromechanical modeling approach of the polymer/clay nanocomposite has been established in Chapter 2. In summary, clay structural parameters (L, N, $d_{(001)}$) extracted from XRD and/or TEM are mapped into effective "particle" properties (L/t, f_p/W_c, $E_{p,ii}/E_m$, $G_{p,ij}/G_m$, $\nu_{p,ij}$), which are then used as model parameters in analytical or numerical micromechanical composite models to calculate macroscopic stiffness of the nanocomposite. Here this modeling scheme is applied to various polymer-clay nanocomposite systems; FEM predictions of the composite modulus based on the "effective particle" are compared with a series of experimental data.

3.3.1. Parametric study of the effect of (N, $d_{(001)}$, and E_m) on composite properties

3.3.1.1. Composite E_{11}

Figure 3.11 depicts the influence of internal clay structural parameters (N, $d_{(001)}$) on the macroscopic modulus of the nanocomposite; the calculation of the micromechanical model parameters are based on the multi-scale approach established in Section 2.1.2 ~ 2.1.4; the particle length L is assumed to be 200 nm in (a)~(c), and 100 nm in (d). The Mori-Tanaka model (Eq. (2)) is used to predict E_{11} of the composite. The effects of (N, $d_{(001)}$) on (L/t, f_p/W_c, E_p/E_m) corresponding to Figure 3.11 are summarized in Table 2.

E_{11}/E_m is plotted as a function of W_c and N at a fixed $d_{(001)}$ in Figure 3.11(a). The strong dependence of E_{11}/E_m on N is clearly demonstrated; at a fixed W_c, E_{11}/E_m increases with decreasing N; the amount of increase gradually expands as $N \rightarrow 1$; however, no dramatic change occurs in this limit. At a given W_c, as N decreases, L/t and E_p increase, which both act to increase E_{11}, whereas f_p decreases, which acts to decrease E_{11}. The increases in L/t

and E_p have a stronger effect than the decrease in f_p. Figure 3.11(b) depicts the effect of $d_{(001)}/d_s$ on the macroscopic modulus for two different values of N: $N = 2$ and $N = 5$. Compared with N, the influence of $d_{(001)}/d_s$ on E_{11}/E_m is rather small, and depends on the specific value of N. In general, for a fixed N and W_c, E_{11}/E_m increases with increasing $d_{(001)}$ (note that a maximum $d_{(001)}$ of 5 nm is studied; values larger than this are not considered to be of interest); this increase is rather negligible when N is small; however, when the nanocomposite is highly intercalated (e.g., $N = 5$), the increase of a few nanometers in $d_{(001)}$ can cause a considerable increase in E_{11}/E_m. At a given W_c, as $d_{(001)}$ increases, both L/t and E_p decrease, acting to decrease E_{11}, whereas f_p increases, acting to increase E_{11}. The increase due to f_p prevails over the decreases from L/t and E_p.

Note that here we have assumed a matrix modulus of $E_m = 4$ GPa, which leads to modulus ratio of $E_{silicate}/E_m = 92$ (taking $d_s = 0.678$ nm, $E_{silicate} = 370$ GPa). However the modulus of different polymers vary from order MPa (elastomers; amorphous thermoplastic polymers above their glass transition temperature) to order GPa (semi-crystalline polymers, glassy polymers, and stiff epoxies) and thus $E_{silicate}/E_m$ for different polymer-clay nanocomposite systems has a wide range, from ~10^5 down to ~10^2. To emphasize the strong effect of E_p/E_m on composite modulus, we plot in Figure 3.11(c) the effect of N for two types of matrices. For a given exfoliated and well-aligned clay content W_c, the stiffness enhancement is much more dramatic for a compliant matrix where E_p/E_m is of order 10^5 (i.e., elastomers or thermoplastics at temperatures above T_g) than in a stiff matrix where $E_p/E_m = 10^2$. In particular, if we examine the case of 4 wt% clay, under fully exfoliated and fully aligned conditions, the elastomer nanocomposite modulus is over **3** times that of its matrix, whereas the glassy polymer nanocomposite modulus is only ~

50% higher than its matrix. This prediction is fully consistent with literature data (e.g., Burnside and Giannelis, 2000; Triantafillidis, et al., 2002; Ratna, et al., 2003). The effect of intercalated stacks ($N = 2$) vs. exfoliated layers ($N = 1$) is shown to be modest for the glassy polymer nanocomposites, but more dramatic for the elastomer nanocomposites. This is also consistent with experimental data on intercalated elastomeric polyurethane/clay nanocomposites (Wang and Pinnavaia, 1998). Another direct consequence of the strong E_p/E_m effect on soft matrices is the much improved Heat Distortion Temperature[2] (HDT) of thermoplastic polymer nanocomposites — as depicted in Fig. 3.10, E_m decreases monotonically with increasing temperature, while E_p changes negligibly, resulting in a much higher composite modulus E_c, compared to E_m at the same temperature — the Toyota pioneers (Kojima, et al., 1993) observed that with 4.7-Wt% nanoclay the HDT of nylon 6 increased from 65°C to 152°C.

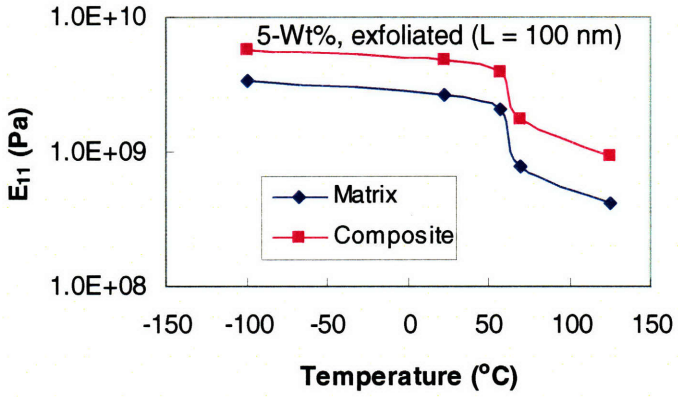

Figure 3.10: Modulus of nylon 6 as a function of temperature (van Es, et al., 2001) and corresponding modulus of nylon 6 nanocomposite with 5-Wt% exfoliated clay (L = 100 nm) , predicted by the Mori-Tanaka formula.

[2] The heat distortion temperature (HDT) is a measure of the resistance of polymer to distortion under a given load at elevated temperatures. Common test standard for the HDT of plastics is prescribed by ASTM D648.

Specific comparisons between the proposed model and much of the literature data are not possible because most authors have not provided enough detail regarding the underlying microstructure of the materials in their studies, such as L/t, silicate sheet orientation, N, $d_{(001)}$, and weight fraction. As seen in our model results, all of these factors are contributory to the end composite modulus.

The impact of multiple factors (e.g., L/t, E_p/E_m, N) on the composite modulus is emphasized by Figure 3.11(d), where all model parameters are exactly those used in Figure 3.11(c), except L = 100 nm rather than 200 nm. The effect of L/t is rather significant, comparing Figure 3.11(c) and (d). The exfoliated elastomer nanocomposite still exhibits a dramatic modulus enhancement relative to that observed in the glassy polymer nanocomposite, but the intercalated elastomer nanocomposite ($N \geq 2$) does not distinguish in as dramatic a manner from the glassy polymer nanocomposite enhancement.

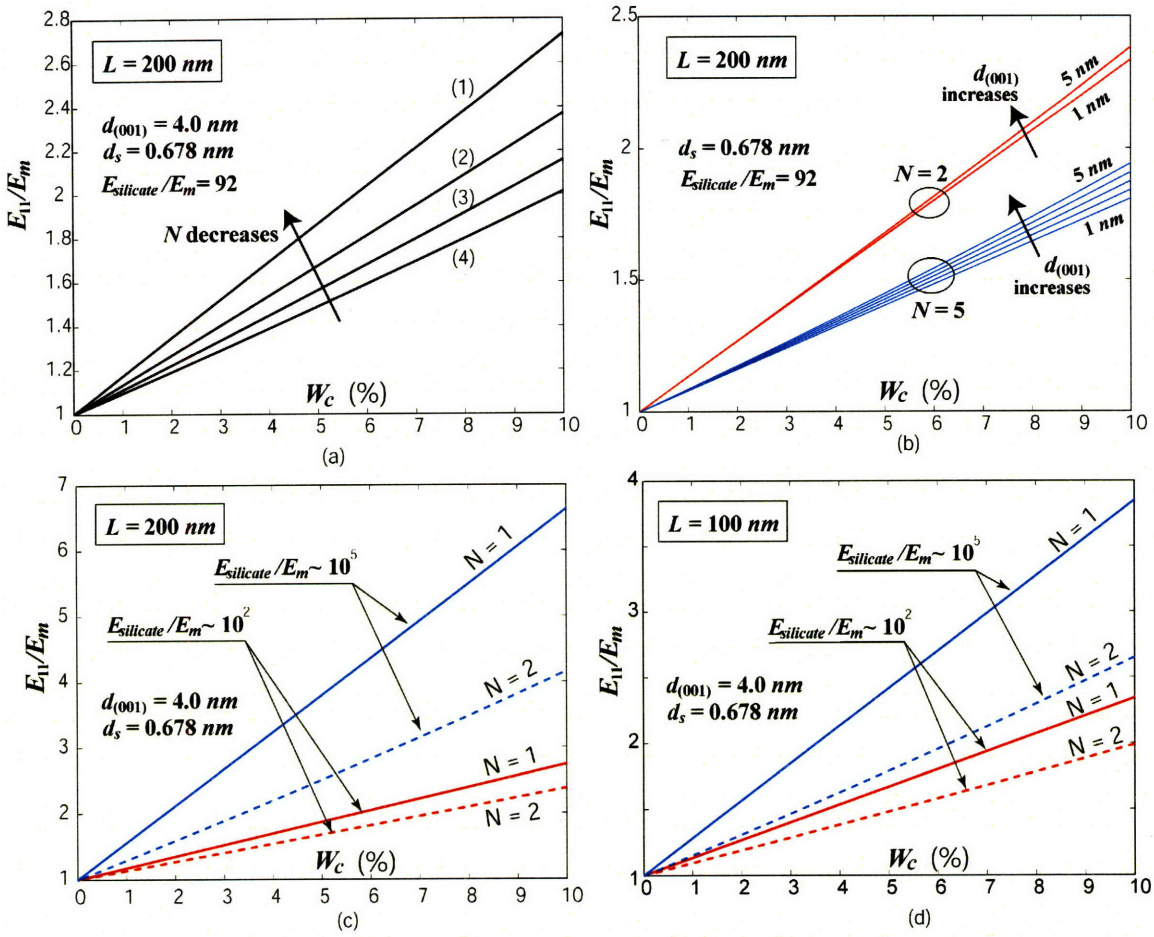

Figure 3.11: Effect of clay structural parameters (N, $d_{(001)}$) on the macroscopic modulus, as predicted by the Mori-Tanaka model; d_s = 0.678 nm, L = 200 nm for (a), (b) and (c), L = 100 nm for (d). (a) Effect of N at fixed $d_{(001)}$ = 4.0 nm. (b) Effect of $d_{(001)}$ at two fixed values N = 2 and N = 5. (c) Effect of matrix stiffness for exfoliated (N = 1) and intercalated (N = 2, $d_{(001)}/d_s$ = 4/0.678) systems, with L = 200 nm. (d) Effect of matrix stiffness for exfoliated and intercalated systems, with L = 100 nm.

Table 3.1 Effect of primary descriptors (N, $d_{(001)}$) on intermediate particle model descriptors (L/t, f_p/W_c, E_p/E_m) (see also Fig. 3.2 and Fig. 2.9).

N	$d_{(001)}/d_s$	L/t	f_p/W_c	E_p/E_m
Effect of N on model parameters				
4	6.5	16	1.28	19.5
3	6.5	23	1.17	21.4
2	6.5	43	0.94	26.7
1		325	0.25	100
Effect of $d_{(001)}/d_s$ on model parameters				
2	1.6	124	0.328	76.2
2	8.1	36	1.14	21.9
5	1.6	43	0.375	66.6
5	4.9	16	1.03	24.4
5	8.1	10	1.68	14.9

3.3.1.2. Complete set of elastic constants of the nanocomposite

The effect of clay *exfoliation* vs. *intercalation* on the complete set of elastic constants of a nanocomposite is studied for two types of matrices: a thermoplastic polymer, with E_m = 3.0 GPa, ν_m = 0.35 and an elastomer with E_m = 3.0 MPa, ν_m = 0.45. For each matrix polymer, we sample a low (2-wt %) and a high (6-wt %) filler content; at each fixed W_c, we compare the anisotropic elastic properties corresponding to N = 1 (exfoliated) and N = 2, 3 (intercalated). The length of the clay platelet is fixed to be 100 nm, and the inter-layer spacing $d_{(001)}$ is taken to be 4 nm. The gallery material is modeled with low transverse shear: $G_{gallery}/G_m = 0.1$.

The effects of N and matrix properties (E_m, ν_m) on the properties of the "effective particle" are listed in Table 3.2. The intercalated "effective particle" exhibits high anisotropy: $E_{p,11} \sim E_{silicate} >> E_{p,22} \sim E_m$, $G_{p,13} \sim G_{silicate} >> G_{p,12}$; $\nu_{p,12} \sim \nu_m > \nu_{p,13} \sim \nu_{silicate}$; this anisotropy in "particle" elasticity is especially severe when the matrix is an elastomer, where $E_{p,11}/E_{p,22}$ (also $G_{p,13}/G_{p,12}$) is as high as 10^5 due to the low modulus of the elastomer.

Table 3.3 summarizes the anisotropic elastic properties of the composites predicted by 3D FE-based simulations (the intercalated cases) and Mori-Tanaka[3] model (the exfoliated cases). The composite demonstrates some degree of anisotropy, but nothing as distinct as the anisotropy exhibited by the intercalated "effective particle", as listed in Table 3.3. For thermoplastic matrix, with 6-wt % addition of exfoliated clay, the composite is predicted to exhibit significant enhancements in E_{11} ($E_{11}/E_m \sim 1.9$) and G_{13} ($G_{13}/G_m \sim 2.0$), modest

[3] As demonstrated in Section 3.2, the Mori-Tanaka predictions of the elastic properties of composites with isotropic fillers are in excellent agreement with the FE-based simulations. Thus the Mori-Tanaka model can be used as substitute for FE simulations when modeling exfoliated polymer/clay nanocomposites, where the exfoliated clay sheet can be modeled as isotropic.

increases in E_{22} ($E_{22}/E_m \sim 1.2$), ν_{12} ($\nu_{12}/\nu_m \sim 1.1$), modest decreases in ν_{13} ($\nu_{13}/\nu_m \sim 0.8$), and an almost unchanged G_{12} ($G_{12}/G_m \sim 1.0$); these enhancements in composite properties over the matrix polymer are much more manifest, when the matrix is elastomer ($E_p/E_m \sim 10^5$), except for the negligibly-changing G_{12}. When the clay morphology transits from exfoliation ($N = 1$) to intercalation ($N \geq 2$), the enhancements in the composite properties over the homopolymer are in general weakened, due to the reduced aspect ratio and lowered stiffness of the "particle". However, this effect is not dramatic (as opposed to the abrupt decrease in $E_{p,11}$ and $E_{p,22}$ of the "effective particle" when N increases from 1 → 2, as shown in Fig. 3.2 and Fig. 3.3); in fact, the value of N has almost no or rather limited impact on E_{22}, ν_{12}, ν_{13}, and G_{12} of the composite (even with an elastomer matrix, the effect of N on these properties are small).

Fig. 3.11a, b and c demonstrate the impact of N on E_{11}, E_{22}, and G_{13} of the composite, respectively. For comparison purposes (thermoplastic vs. elastomer matrix), the composite properties are normalized with respect to corresponding property of the homopolymer. The normalized composite property decreases monotonically with increasing N; the decreasing slope depends on the clay weight fraction and the property of the matrix: for a given matrix, the value of N has a larger impact on the properties of composites with higher W_c (6-wt %).

Table 3.2: Overall properties of the "effective particle", using L = 100 nm, $d_{(001)}$ = 4.1 nm, $d_{silicate}$ = 0.678 nm, and $E_{silicate}$ = 370 GPa

N	L/t	f_p/W_c	$E_{p,11}$ (GPa)	$E_{p,22}$ (GPa)	$\nu_{p,12}$	$\nu_{p,13}$	$G_{p,12}$ (GPa)	$G_{p,13}$ (GPa)
a. *thermoplastic* $E_{gallery} = E_m$ = 3.0 GPa, $\nu_{gallery} = \nu_m$ = 0.35, $G_{gallery} = G_m/10$								
1		0.25	370	370	0.20	0.20		
2	21	0.98	105	6.64	0.31	0.20	0.155	44
3	11	1.21	85	6.18	0.32	0.20	0.144	35
b. *elastomer* $E_{gallery} = E_m$ = 0.003 GPa, $\nu_{gallery} = \nu_m$ = 0.45, $G_{gallery} = G_m/10$								
1		0.25	370	370	0.20	0.20		
2	21	0.98	105	0.016	0.38	0.20	1.44×10^{-4}	44
3	11	1.21	85	0.015	0.39	0.20	1.34×10^{-4}	35

Table 3.3: Anisotropic elastic properties of composites with (a) thermoplastic matrix and (b) elastomer matrix (refer to Table 3.2 for corresponding properties of the "effective particle"). Bold results for exfoliated particle (N = 1) from Mori-Tanaka model; intercalated (N = 2, 3) results from 3D FE RVE simulations.

Wc (%)	N	E_{11}/E_m	E_{22}/E_m	ν_{12}/ν_m	ν_{13}/ν_m	G_{12}/G_m	G_{13}/G_m
a. *thermoplastic matrix* E_m = 3.0 GPa, ν_m = 0.35							
2	**1**	**1.28**	**1.08**	**1.06**	**0.89**	**1.01**	**1.32**
	2	1.20	1.06	1.04	0.92	0.94	1.20
	3	1.18	1.05	1.04	0.92	0.95	1.18
6	**1**	**1.92**	**1.20**	**1.13**	**0.76**	**1.02**	**2.05**
	2	1.74	1.16	1.12	0.77	0.84	1.69
	3	1.57	1.14	1.10	0.81	0.85	1.54
b. *elastomer matrix* E_m = 0.003 GPa, ν_m = 0.45							
2	**1**	**1.53**	**1.23**	**1.15**	**0.82**	**1.01**	**1.62**
	2	1.34	1.16	1.10	0.88	0.95	1.31
	3	1.28	1.12	1.10	0.88	0.95	1.25
6	**1**	**2.72**	**1.64**	**1.30**	**0.65**	**1.01**	**3.06**
	2	2.37	1.47	1.29	0.65	0.86	2.17
	3	1.96	1.38	1.23	0.71	0.87	1.81

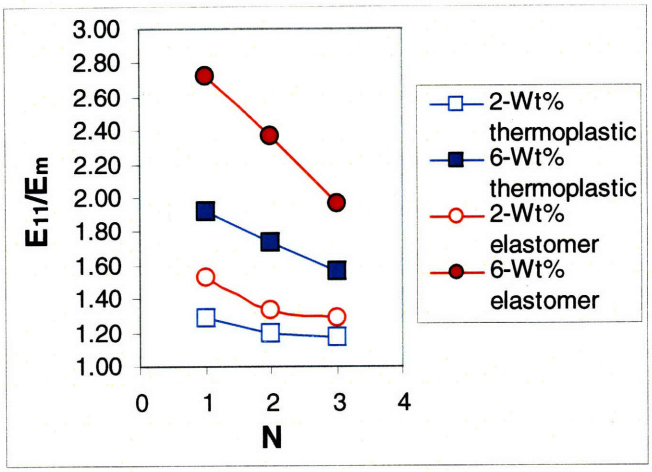

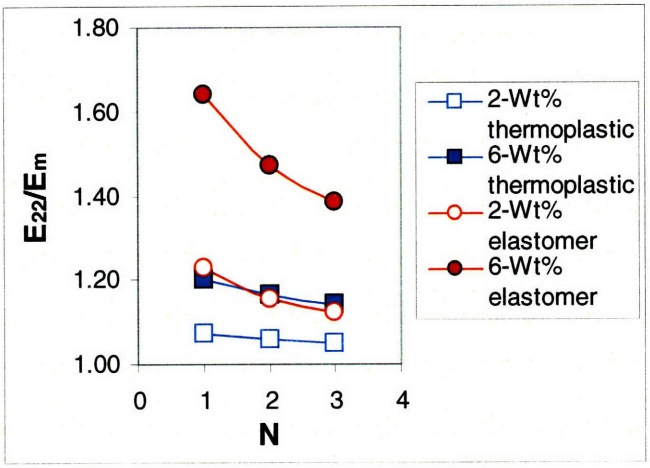

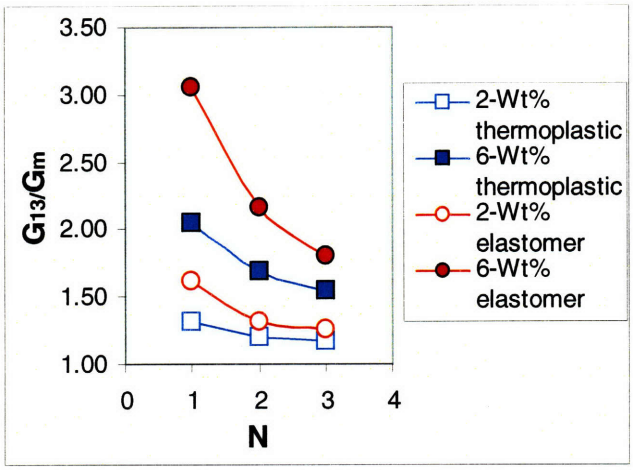

Figure 3.12: Effect of clay morphology (intercalation vs. exfoliation), characterized by N, on the overall E_{11}, E_{22}, and G_{13} of thermoplastic and elastomer polymer/clay nanocomposites. Refer to Table 3.3 for specific simulation data and to Table 3.2 for the effect of N on the properties of the "effective particle".

3.3.2. Amorphous polymer matrix (MXD6 nylon)

Eastman Chemical provided injection-molded MXD6/clay nanocomposites with various montmorillonite (MMT) clay weight fractions ranging from 0% to 5.27%. The chemical structure of the polymer matrix is primarily MXD6-6007 polyamide, an amorphous polymer with high barrier properties, produced by Mitsubishi Gas and Chemical Company. The layered montmorillonite clay is I.34MN organoclay from Nanocor Inc.

Material Characterization. TEM micrographs of MXD6-clay nanocomposite with various clay contents are shown in Figure 3.12. Intercalated multi-layer stacks with length ~ 200 nm are well aligned in the flow direction. X-ray scattering reveals that the fine structure of intercalated clay stacks is independent of clay content; in particular, the average number of silicate sheets per stack is $N \sim 3$, and the average inter-layer spacing is $d_{(001)} = 4.1$ nm (Lee and McKinley, 2003).

Experimental Description. Uniaxial tensile tests are conducted on various clay content specimens with a Model-5582 Instron at room temperature and strain rate of ~ 0.05/s; dog-bone-shaped plate tensile specimens with gage length of 12.7 mm and thickness of 3 mm were prepared according to *ASTM D638*. For each clay content, 4 to 6 tests were performed. During each test, an extensometer was used to measure the axial strain; the tensile modulus of the composites was obtained from the initial slope of true stress-strain curves.

Simulation. Three-dimensional RVEs with perfect particle alignment and random particle locations were used to model the nanocomposites. Key effective particle

parameters, using L = 200 nm[4], $d_{(001)}$ = 4.1 nm, (d_s, E_s) = (0.678 nm, 370 GPa), N = 3, are determined through Eqs. (3.1)-(3.6) as follows: L/t = 23, f_p/W_c = 1.20, and E_p/E_m = 21, where χ is calculated to be 0.23 . We compare the experimental data with both simulation results and predictions from the Mori-Tanaka model. Predicted results for the overall composite modulus are depicted in Figure 3.14. Results of Mori-Tanaka model and 3D FE simulation using the "effective particle" concept are in good agreement with the experimental data. The FE models give closer predictions than the Mori-Tanaka model, but the latter provides a reasonably accurate analytical estimate for the nanocomposite modulus.

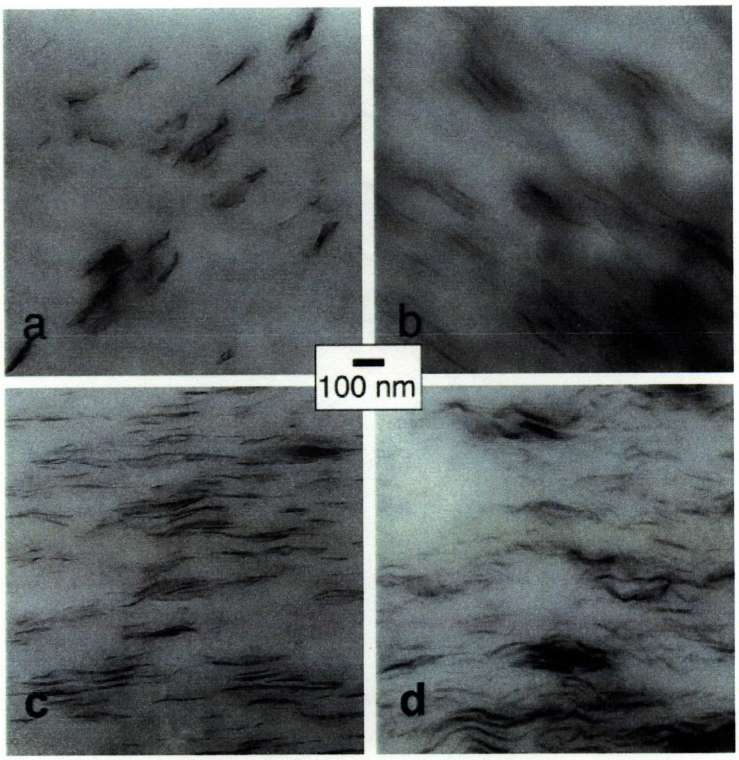

Figure 3.13: TEMs of MXD6 nylon/clay nanocomposites: (a) 1.1 wt%, (b) 3.67 wt%, (c) 4.17 wt%, (d) 5.27 wt%.

[4] Lateral dimension of montmorillonite can vary from ~100 to ~200 nm. For I.34MN organoclay, L ~ 200 nm.

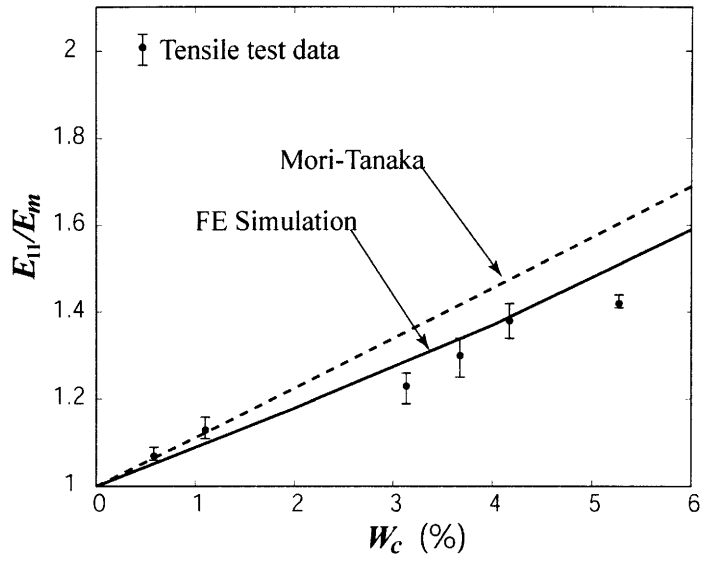

Figure 3.14: Predictions of the effective longitudinal modulus for MXD6/clay nanocomposites. (L/t = 23, E_p/E_m = 21, f_p/W_c = 1.20, N = 3, d_s = 0.678 nm, $d_{(001)}$ = 4.1 nm). FE results are based on 3D RVEs.

3.3.3. Semi-crystalline matrix (nylon 6)

In semi-crystalline polymer-clay nanocomposite systems, the crystallization behavior of the matrix can be directly influenced by the presence of nanoclay particles. Both TEM and X-ray studies (Kim, et al., 2001; Kojima, et al., 1994) of injection-molded nylon 12-clay and nylon 6-clay nanocomposites reveal that the fine lamella are oriented with their planes perpendicular to the polymer/clay interface, while the silicate sheets are aligned in the flow direction. In addition, the degree of orientation of polymer crystallites is found to increase linearly with increasing clay content, while the degree of crystallization remains constant (Kojima, et al., 1994). A TEM of nylon 12-clay (Fig. 3.15, Kim, et al., 2001) shows that this transcrystallized morphology has percolated throughout the entire matrix at a clay content of W_c = 2%. Based on the above observations, it is necessary to include in the FEM simulation a third "phase" (in addition to the effective particle and isotropic matrix) extending from the particle/polymer interfaces in order to model the transcrystallized matrix. In this section we do not take into account the textured matrix;

we first model the nanocomposite with matrix properties unvaried from the bulk state and assess the contribution of the nanoclay alone on the composite modulus. The modeling of the special matrix morphology induced by the addition of nanoclay in semi-crystalline polymer matrix and its effect on the composite modulus as well as initial yielding will be elaborated later in Chapter 6.

Room temperature modulus of exfoliated nylon 6-clay nanocomposites with clay contents varying from 0.2 to 7.2 wt% are obtained from van Es, et al.[5] (2001) and Fornes, et al. (2001). Both groups claim nearly complete exfoliation and good particle alignment for partial (up to 5 wt% for van Es, et al.) or complete ranges of the clay content. The Mori-Tanaka formula with well-aligned, isotropic particles (L = 100 nm, d_s = 0.678 nm, E_s = 370 GPa, E_m = 3.6 GPa) is used to model the fully-exfoliated systems. Model predictions of the composite axial moduli are plotted together with experimental data in Figure 3.16. The micromechanical model without any special treatment of the matrix gives results in good agreement with experimental data, indicating that clay acting as a stiff filler is the primary source of reinforcement for the composite modulus. As will be discussed in Chapter 6, modeling the matrix to be highly textured (hence highly anisotropic) does not have much effect on the composite modulus; however, its impact on the initial yield strength of the composite is significant, as will be shown in Chapter 6.

[5] van Es et al. performed DMTA tests and extracted storage modulus from the DMTA data at fixed temperatures. Here we analyze their data at T = 23 °C.

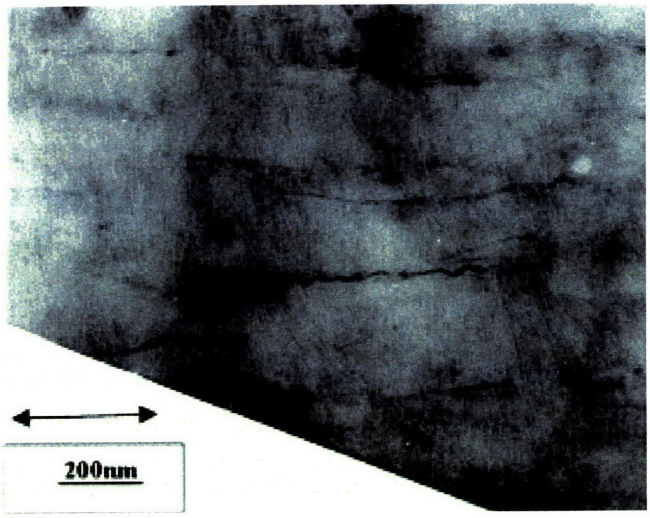

Figure 3.15: TEM of Nylon-12/clay nanocomposite, showing a lamellar structure perpendicular to the aligned clay particles (Kim, et al., 2001).

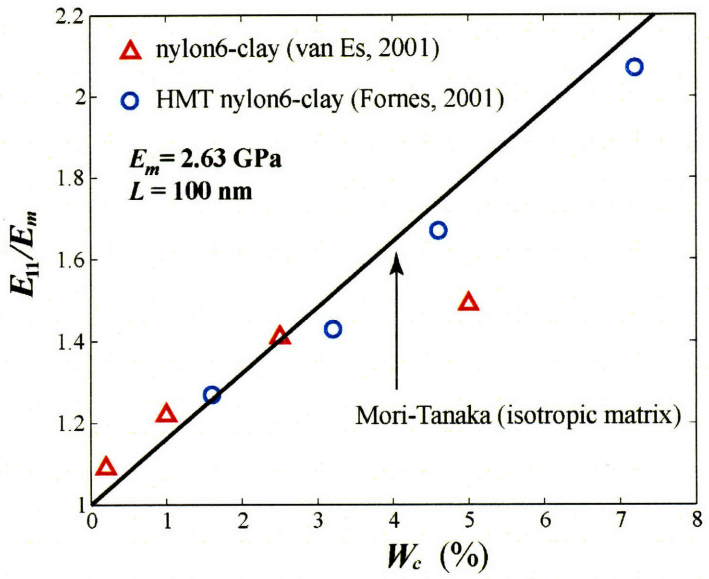

Figure 3.16: Mori-Tanaka predictions (with isotropic matrix) in comparison with experimental data for exfoliated nylon 6-clay nanocomposites at room temperature (van Es, et al., 2001, and Fornes, et al., 2001).

3.4. Summary

The elastic behavior of polymer/clay nanocomposite (with clay particles aligned in the 1-direction) is rather anisotropic. While the in-plane properties, E_{11} (E_{11}= E_{33}) and G_{13}, are

well reinforced by the stiff fillers, the influence of clay on the out-of-plane counterparts, E_{22} and G_{12} (especially G_{12}), are rather limited. Two mechanisms are found to be important players in the property enhancement of the nanocomposite: the load transfer mechanism and the "plane-strain"-constraint of the particle. Load transfer from surrounding matrix to the particle through interface shearing is the governing mechanism for the well-observed enhancement in the composite axial modulus E_{11}; large particle aspect ratio and high relative matrix shear modulus are desired for efficient load transfer. On the other hand, the high aspect ratio high stiffness particle creates a nearly plane-strain constraint on the in-plane deformation of surrounding matrix; such constraint acts to increase the composite transverse modulus (E_{22}) and the out-of-plane Poisson ratio (ν_{12}), but to decrease the in-plane Poisson ratio (ν_{13}). There is a strong dependence of the overall elastic property on the degree of particle exfoliation (which can be characterized by the number of silicate sheets in a primary "particle", N): at a fixed W_c, exfoliated clay is found to be most efficient in the composite stiffness enhancement; however, no dramatic transition occurs as N goes from 2 → 1 (intercalated → exfoliated) due to the counteracting effects of increased particle aspect ratio and decreased particle volume fraction. The stiffness enhancement efficiency also depends on the base matrix modulus: elastomer nanocomposites in general see much more dramatic improvement in the stiffness compared to thermoplastic nanocomposites, due to the large particle/matrix stiffness ratio (E_p/E_m). A direct consequence of the E_p/E_m effect on soft matrices is the much improved Heat Distortion Temperature (HDT) of thermoplastic polymer nanocomposites.

Chapter 4

Anisotropic Thermal Expansion

The low coefficient of thermal expansion (CTE) of clay makes it a good agent for the reduction of the composite CTE as compared to the matrix polymer. However, experimental data in the literature for the CTE of polymer/clay nanocomposites are rather limited in comparison to the reported composite mechanical properties. Available measurements of the thermal expansion of injection-molded nylon 6/clay nanocomposites (Okada and Usuki, 1995; Yoon, et al., 2002) reveal considerable anisotropy: the composite is found to have decreased CTE in the flow direction and increased CTE in the transverse direction.

The goal of this chapter is to assess the effect of nanoclay on the anisotropic thermal expansion behavior of the composite through the employment of the multiscale modeling strategy established in Chapter 2. First, the homogenized CTE of the "effective particle" is derived; the effects of clay structural parameters (N, $d_{(001)}$) as well as the matrix thermal/mechanical properties on the "particle" CTE are discussed (Section 4.1). Section 4.2 investigates the composite-level effects of particle volume fraction, particle aspect ratio, and particle/matrix property ratios on the composite CTE, using both theoretical model and finite element simulations. Finally, the effects of underlying structural and material parameters on the anisotropic composite CTE are assessed through multiscale micromechanical modeling. Model predictions of the anisotropic thermal expansion of

MXD 6/clay nanocomposites and nylon 6/clay nanocomposites are compared to experimental measurements.

4.1. Effective CTE (anisotropic) of the clay

The coefficient of thermal expansion (CTE) of the "effective particle" (defined in Chapter 2) representing the intercalated nanoclay is highly anisotropic; the effective CTE of the particle depends not only on the silicate volume fraction χ (refer to Eq. 2.3 for reference) and the CTEs of the silicate and the gallery, but also on the elastic properties of these two components as well.

$$\alpha_{p,ii} = \hat{\alpha}_{p,ii}\left(\alpha_{silicate}, E_{silicate}, v_{silicate}, \alpha_{gallery}, E_{gallery}, v_{gallery}, \chi\right), \quad i = 1,2,3$$

Treating the multi-layer structure of the intercalated clay as a laminate, we can obtain the anisotropic CTE of the particle ($\alpha_{p,ii}$) in terms of the silicate/gallery CTE ratio and the silicate/gallery modulus ratio:

$$\alpha_{p,11} = \alpha_{p,33} = \alpha_{silicate}\left\{1 + \frac{\left(\frac{\alpha_{gallery}}{\alpha_{silicate}} - 1\right)}{1 + \frac{\chi}{1-\chi}\cdot\frac{(1-v_{gallery})}{(1-v_{silicate})}\cdot\frac{E_{silicate}}{E_{gallery}}}\right\}, \text{ and} \tag{4.1}$$

$$\alpha_{p,22} = 2\chi\beta(\alpha_{gallery} - \alpha_{silicate}) + \chi\alpha_{silicate} + (1-\chi)\alpha_{gallery}, \text{ with} \tag{4.2}$$

$$\beta = \frac{v_{gallery} - v_{silicate}\cdot\frac{E_{gallery}}{E_{silicate}}}{(1-v_{silicate})\cdot\frac{E_{gallery}}{E_{silicate}} + \frac{\chi}{(1-\chi)}\cdot(1-v_{gallery})} \tag{4.3}$$

Approximating the properties of the gallery with those of the bulk matrix polymer, typical values of E and α for the silicate sheet and polymer systems with different

thermophysical properties as well as corresponding silicate/gallery CTE ratios and modulus ratios are listed in Table 4.1; $\alpha_{silicate}/\alpha_{gallery}$ varies from 10^{-1} to 10^{-3}, while $E_{silicate}/E_{gallery}$ varies from 10^{2} to 10^{5} as the matrix polymer changes from *thermoplastic* to *elastomer*.

Table 4.1 Typical values of E and α for silicate and different polymers

		α (10^{-5}/C)	$\alpha_{silicate}/\alpha_{gallery}$	E (GPa)	$E_{silicate}/E_{gallery}$	ν
Silicate		0.5		400		0.2
Matrix (gallery)	*thermoplastic*	5.2	1.0×10^{-1}	3.0	1.3×10^{2}	0.3
	epoxy	3.0	1.7×10^{-1}	5.0	0.8×10^{2}	0.3
	elastomer	200	2.5×10^{-3}	4.0×10^{-3}	1.0×10^{5}	0.45

With the assistance of Table 4.1, simple dimensional analysis of Eq. (4.1) reveals that the in-plane CTE of the particle, $\alpha_{p,11}$, is largely determined by $\alpha_{silicate}$. Since in general $E_{gallery}/E_{silicate} << 1.0$ ($E_{gallery}/E_{silicate}$ ranges from 10^{-2} to 10^{-5} according to Table 4.1), Eq. (4.3) can be approximated as

$$\beta \approx \frac{\nu_{gallery}}{(1-\nu_{gallery})}\cdot\frac{(1-\chi)}{\chi} \tag{4.4}$$

Taking Eq. (4.4) into (4.3), we have

$$\alpha_{p,22} \approx \alpha_{gallery}\left\{(1-\chi)\cdot\left(\frac{2\nu_{gallery}}{1-\nu_{gallery}}+1\right)+\frac{\alpha_{silicate}}{\alpha_{gallery}}\left[\chi-2(1-\chi)\frac{\nu_{gallery}}{(1-\nu_{gallery})}\right]\right\} \tag{4.5}$$

Taking into consideration $\alpha_{silicate}/\alpha_{gallery} << 1$ ($\alpha_{silicate}/\alpha_{gallery}$ varies from 10^{-1} to 10^{-3} according to Table 4.1), we can see from Eq. (4.5) that the transverse CTE of the particle relies more on $\alpha_{gallery}$ and $\nu_{gallery}$ rather than $\alpha_{silicate}$. The effect of the gallery Poisson ratio, $\nu_{gallery}$, on $\alpha_{p,22}$ is essentially a result of the in-plane constraint posed by the stiff, low expansion silicate. Specifically, the silicate acts as a relatively rigid substrate,

constraining the in-plane expansion; on heating, such constraint leads to in-plane compressive stress in the gallery, which, in turn, results in more expansion in the transverse direction due to the Poisson effect, as illustrated in Fig. 4.1.

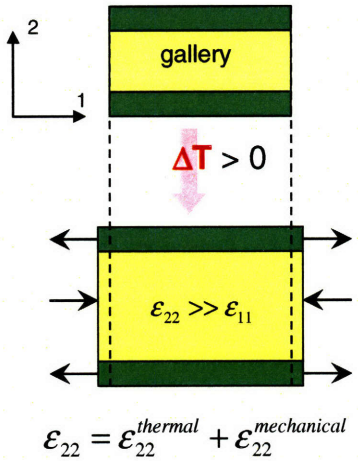

Figure 4.1: schematic of the effect of gallery Poisson ratio on the transverse CTE of the "particle".

Figure 4.2 depicts the effective in-plane ($\alpha_{p,11}$) and transverse ($\alpha_{p,22}$) CTE of intercalated clay as functions of the clay structural parameters $d_{(001)}/d_s$ and N, assuming the matrix to be thermoplastic. The high anisotropy of the effective particle CTE is self-evident; while the effective in-plane CTE is dominated by $\alpha_{silicate}$, a sudden jump in the transverse CTE of the particle occurs when N increases from 1 to 2 (the clay morphology changes from exfoliated to intercalated, correspondingly); furthermore, $\alpha_{p,22}$ of the intercalated clay is of the same order of magnitude as $\alpha_{gallery}$ and increases with increasing $d_{(001)}$ or N.

We also calculated the anisotropic effective particle CTE, employing Table 4.1 and Eq. (4.1)-(4.3), for various polymer systems, as shown in Fig. 4.3. The degree of anisotropy exhibited in the effective CTE of intercalated clay is of the highest level when the matrix polymer is taken to be an elastomer, due to the higher Poisson ratio of the gallery (~ 0.5

as opposed to 0.35 of thermoplastic polymer or epoxy); in fact, $\alpha_{p,22}/\alpha_{p,11}$ can be as high as 100 for clay-filled elastomer "effective particles".

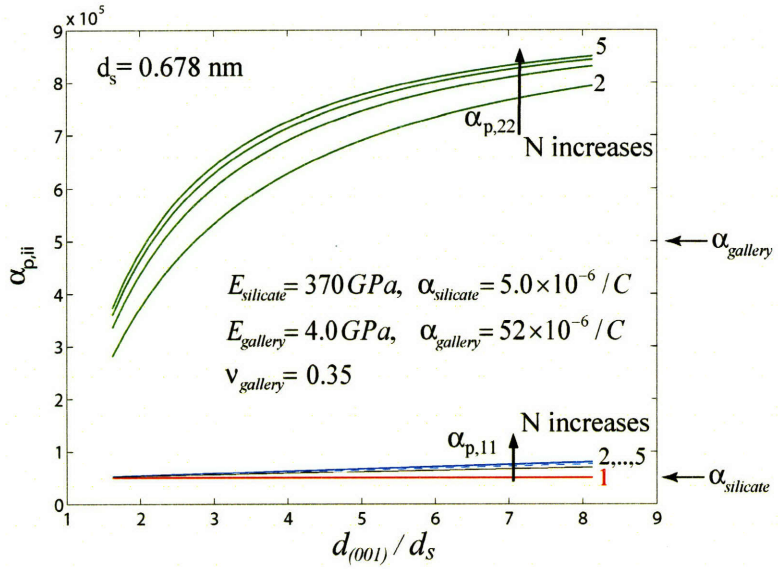

Figure 4.2: Dependence of the anisotropic particle CTE $\alpha_{p,ii}$ (i = 1,2) on clay structural parameters N and $d_{(001)}/d_s$. $\alpha_{silicate}$ and $\alpha_{gallery}$ are marked by arrows as references, assuming thermoplastic matrix.

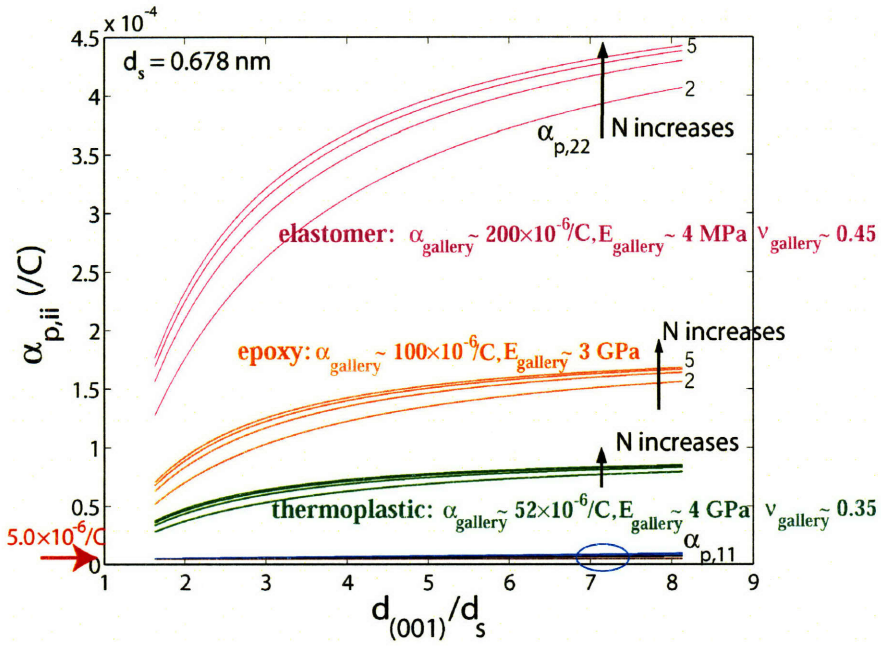

Figure 4.3: Anisotropic effective CTE of intercalated nanoclay with different polymer systems. Gallery properties for thermoplastic polymer: $\alpha_{gallery}$ = 5.2×10^{-5}/C, $E_{gallery}$ = 4.0 GPa; for epoxy polymer: $\alpha_{gallery}$ = 10×10^{-5}/C, $E_{gallery}$ = 3.0 GPa; for elastomer: $\alpha_{gallery}$ = 20×10^{-5}/C, $E_{gallery}$ = 4.0×10^{-3} GPa;

4.2. Continuum-level Prediction of the Composite CTE

- **Theoretical models**

The prediction of effective thermal expansion of a filled polymer in terms of the filler geometry and the material properties of each constituent has been a subject of interest since the 1940's; among available theoretical models, Chow's closed-form formula is capable of capturing the anisotropy of the composite CTE and is relatively easy to apply (Chow, 1978). Chow derived relations for the linear and volumetric thermal expansion coefficients of a filled polymer containing aligned ellipsoidal inclusions at finite concentrations, following a previous procedure developed for elastic moduli by application of a generalized approach of Eshelby; the particle shape is characterized by the particle aspect ratio, defined as the ratio of major to minor axes of the ellipsoidal inclusion. For a composite comprised of perfectly-aligned ellipsoidal particles, the longitudinal CTE (α_L, in the direction parallel to the major axis of the particles) and transverse CTE (α_T, in the direction parallel to the minor axis) of the composite are given by:

$$\alpha_L = \alpha_{11} = \alpha_{33} = \alpha_m + \frac{K_p}{K_m} \cdot \frac{(\gamma_p - \gamma_m) f_p B_3}{(2A_1 B_3 + B_1 A_3)}, \tag{4.7}$$

$$\alpha_T = \alpha_{22} = \alpha_m + \frac{K_p}{K_m} \cdot \frac{(\gamma_p - \gamma_m) f_p B_1}{(2A_1 B_3 + B_1 A_3)}, \text{ with} \tag{4.6}$$

$$\begin{cases} A_i = 1 + (K_p / K_m - 1) \cdot [(1 - f_p) a_i + f_p] \\ B_i = 1 + (G_p / G_m - 1) \cdot [(1 - f_p) b_i + f_p] \end{cases} (i = 1, 3),$$

where α, γ are the linear and volumetric CTE values, respectively; K and G are the bulk and shear moduli; subscripts p and m denote the particle and the matrix, respectively; a_i

and b_i are parameters directly related to the particle aspect ratio and the matrix Poisson ratio:

$$a_1 = \frac{4\pi}{3}Q - 2(2\pi - I)R$$

$$a_3 = \frac{4\pi}{3}Q + 4(\pi + I)R$$

$$b_1 = \left\{\frac{4\pi}{3} - \frac{(4\pi - 3I)}{(1-\eta^2)}\right\}Q - 4(I - 2\pi)R$$

$$b_3 = \left\{\frac{4\pi}{3} - \frac{(4\pi - 3I)\eta^2}{(1-\eta^2)}\right\}Q + (4\pi - I)R$$

where $\eta \equiv t/L$ is the inverse of the particle aspect ratio, I, Q, R are constants given in the following:

$$I = \frac{2\pi\eta}{(1-\eta^2)^{3/2}\left[\cos^{-1}(\eta) - \eta(1-\eta^2)^{3/2}\right]}$$

$$Q = \frac{3}{8\pi(1-\nu_m)}$$

$$R = \frac{(1-2\nu_m)}{8\pi(1-\nu_m)}$$

The dependences of the longitudinal and transverse CTE of composites with aligned disc-shaped inclusions (as illustrated in Fig 4.4) on the particle volume fraction (f_p), particle aspect ratio (L/t), particle/matrix CTE ratio (α_p/α_m), and particle/matrix stiffness ratio (E_p/E_m) are depicted in Fig. 4.4a, b, c and d, respectively; for the reference of later application to the polymer/clay nanocomposites, the disc-shaped particles are modeled to have large aspect ratio, higher stiffness and a lower value of CTE, compared to the matrix. As is evidenced in Fig 4.4, the effect of particles on the anisotropy of the composite CTE is profound: while the longitudinal CTE of the composite is sufficiently reduced by the addition of the high aspect ratio particles ($\alpha_p << \alpha_m$), the transverse CTE of the

composite is increased substantially; in fact, the amount of increase in α_T over α_m almost equals the decrease in α_L. Such effects can be elaborated by simple analysis of the upper-bound laminate model, as shown in Fig 4.5, where the high aspect ratio particle is approximated to be continuous throughout the matrix in the longitudinal direction; on heating ($\Delta T > 0$) the thermal mismatch between the particle and the matrix ($\alpha_p/\alpha_m < 0.1$) creates considerable in-plane compressive stress in the matrix surrounding the particle, which, in turn, leads to substantial expansion in the transverse direction due to the Poisson effect. Fig. 4.5 depicts the matrix compressive stress for a given temperature increase of 10°C as functions of α_p/α_m as well as f_p, based on the laminate model; the magnitude of σ_m is observed to increase almost linearly with decreasing α_p/α_m.

- **Finite Element Based Micromechanical Simulation**

Figure 4.6 shows an exemplary 3D RVE used in FE simulations to calculate the thermal expansion of composites with aligned plate-shaped fillers. The particle is characterized by its aspect ratio (L/t) and the elastic and thermal properties. A major advantage of the FE approach over Chow's theoretical model lies in its capacity to account for the material anisotropy of the particle, in the elastic properties as well as in the linear CTE.

Fig. 4.7 compares the composite CTE predicted by Chow's model and the FE simulation for (a) particles with isotropic CTE, and (b) particles with anisotropic CTE (specifically, $\alpha_{p,11} = \alpha_{p,33} = \alpha_{p,22}/10$ and $\alpha_{p,11} = \alpha_{p,33} = \alpha_{p,22}/20$). It is clear that while Chow's model gives predictions that agree well with the FE results when the particle is modeled to be isotropic, it tends to underestimate the transverse composite CTE (as shown in Fig. 4.6b) once the particle anisotropy is introduced. Nevertheless, Chow's formula serves as

a good tool for quick estimation and trend studies of the CTE of composites with aligned fillers.

Note that in FE simulations, the effect of anisotropy of the particle elastic property on the end composite CTE value is almost negligible. Hence the particles can be modeled with anisotropic CTE, but isotropic elasticity, as in case (b) of Fig. 4.7.

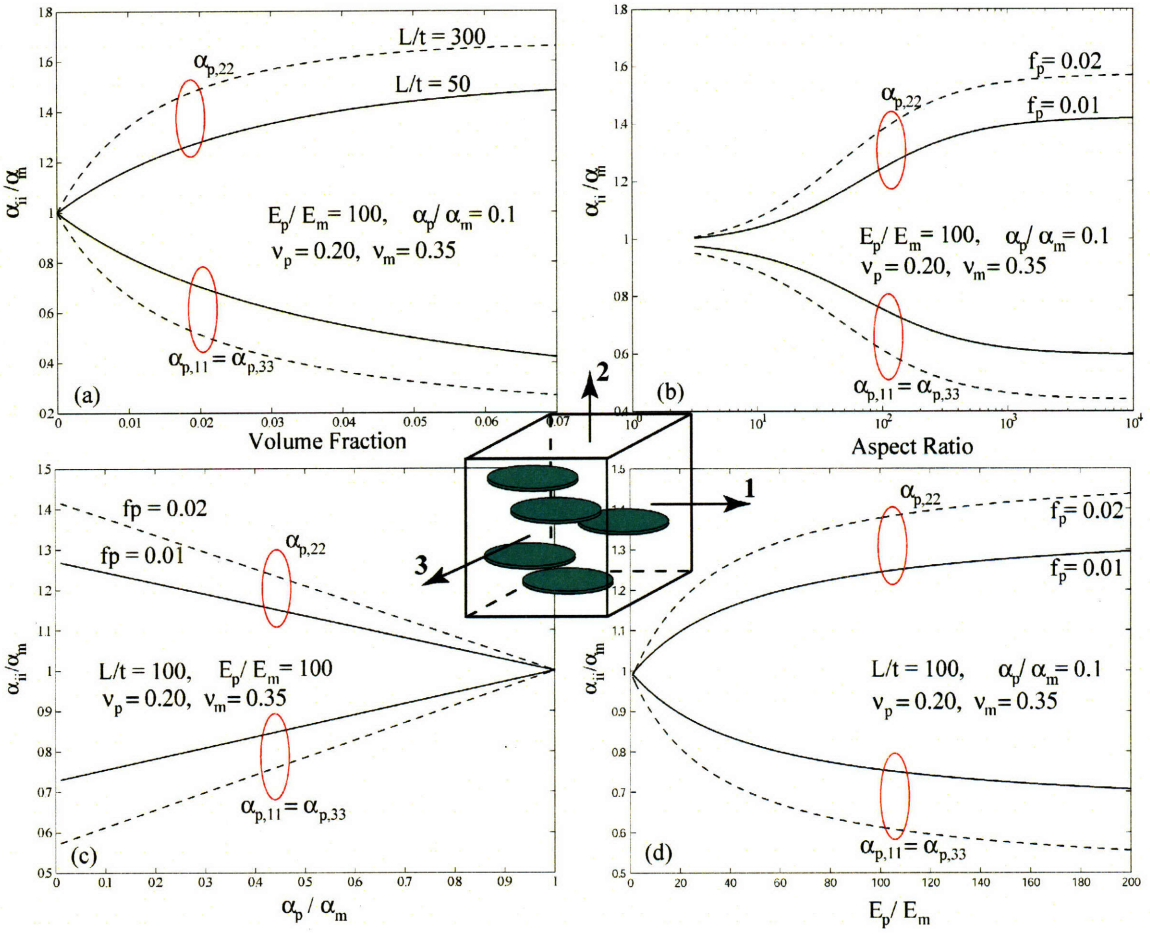

Figure 4.4: Anisotropic CTE of ellipsoidal particle reinforced composite material predicted by Chow's model: (a) effect of particle volume fraction; (b) effect of particle aspect ratio; (c) effect of particle/matrix CTE ratio; (d) effect of particle/matrix stiffness ratio. Particles have isotropic elastic properties and isotropic thermal expansion.

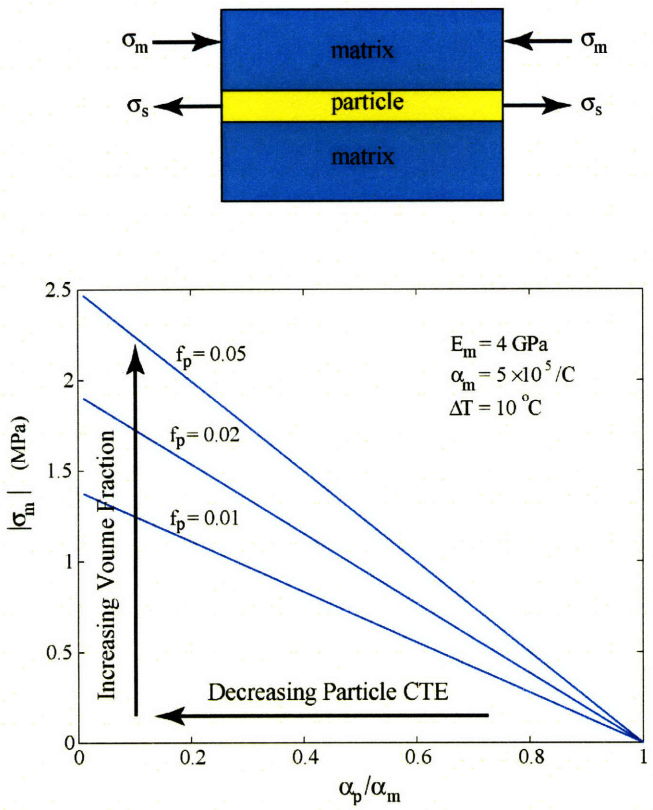

Figure 4.5: The in-plane compressive stress in the matrix, caused by thermal mismatch between the matrix and the filler, illustrated by the upper-bound laminate model.

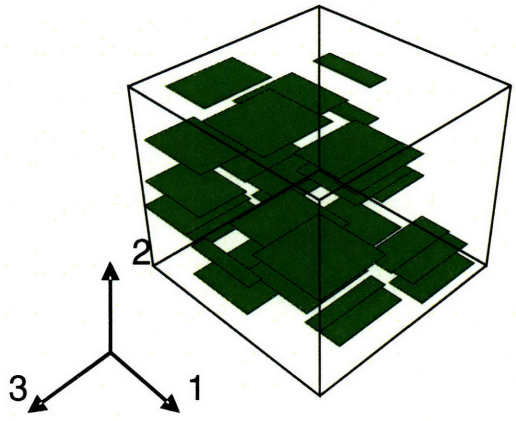

Figure 4.6: Typical 3D RVE used in FE simulations for the prediction of the composite CTE.

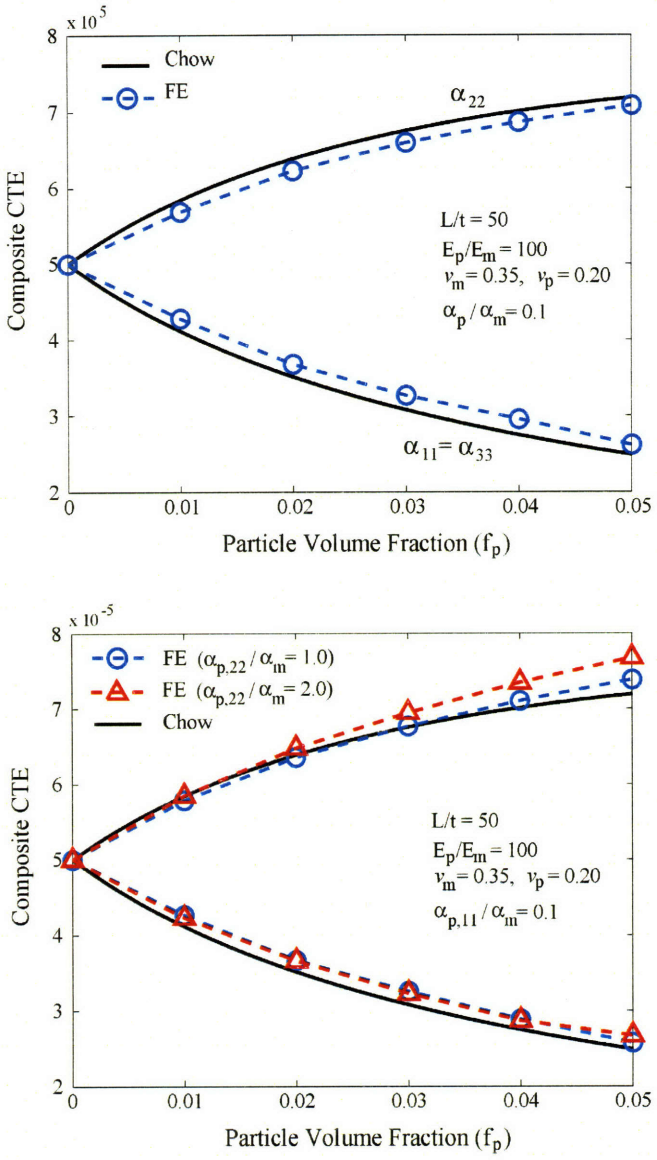

Figure 4.7: Chow's and FEM comparison (a) isotropic particle CTE: α_p/α_m = 0.1; (b) anisotropic particle CTE: $\alpha_{p,11}/\alpha_m = \alpha_{p,33}/\alpha_m$ = 0.1; $\alpha_{p,22}/\alpha_m$ = 1.0 and $\alpha_{p,22}/\alpha_m$ = 2.0. Note that the particles are modeled to be thermally anisotropic but mechanically isotropic, since the effect of mechanical anisotropy on the composite overall CTE is almost negligible.

4.3. Application of Multiscale Modeling

A multiscale micromechanical modeling approach has been developed in Chapter 2; particularly, the clay structural parameters (L, N, $d_{(001)}$) extracted from XRD and TEM are mapped into effective "particle" properties (L/t, f_p/W_c, E_p/E_m, α_p/α_m, etc), which are then used in analytical or numerical micromechanical models to calculate macroscopic thermal/mechanical properties of the nanocomposite. Here this approach is employed to investigate the CTE of polymer/clay nanocomposites with different morphologies (intercalated vs. exfoliated); model predictions exhibit good agreement with experimental data.

4.3.1. Parametric study of the effects of (N, $d_{(001)}$) on composite CTE

Fig. 4.8 depicts the influence of internal clay structural parameter N on the macroscopic CTE of the nanocomposite. The calculation of the micromechanical model parameters are based on the multi-scale approach established in Section 2.1.2 ~ 2.1.4. Table 4.2 summarizes the effect of N on micromechanical model particle descriptors (L/t, f_p/W_c, α_p/α_m, E_p/E_m), where fixed particle geometry parameters are: L = 200 nm, $d_{(001)}$ = 4.1 nm, d_s = 0.678 nm, properties of the silicate sheet are (it is assumed that the gallery possesses the same material properties as the bulk matrix): E_s = 370 GPa, ν_s = 0.20, α_s = 5.0×10^{-6}/C, and properties of the thermoplastic matrix material are: E_m = 4 GPa, ν_m = 0.35, α_m = 5.2×10^{-5}/C. The Chow formula is used to estimate the overall CTE of the composite; since this formula does not account for anisotropy, only the particle in-plane CTE ($\alpha_{p,11} = \alpha_{p,33}$) is used to characterize the thermal expansion behavior of the clay particle when

dealing with an intercalated morphology[1]. For cases N > 1, the FE results (marked with triangles) are also plotted, due to the inherent deficiency of the Chow model to capture the anisotropy of intercalated clay particles.

The influence of the degree of clay exfoliation, characterized by N, on the overall composite CTE is manifest: as N increases, for a fixed clay weight fraction, the composite CTE decreases in the longitudinal direction but increases in the transverse direction, as N decreases (i.e., the degree of anisotropy in composite CTE increases with improving degree of clay exfoliation); however, no dramatic change occurs as $N \rightarrow 1$ (which corresponds to the morphology transition from intercalation to exfoliation). The effect of N on the end composite property can be viewed as a comprehensive result of competing micromechanical model descriptors as listed in Table 4.2: at a given W_c, as N decreases, L/t and E_p increase, while α_p decreases, which all act to elevate the anisotropy of the composite CTE, whereas $f_p \downarrow$, which acts to considerably counteract the reinforcing effect of the remaining model parameters (refer to Fig. 4.4 for the influence of f_p, L/t, E_p/E_m, and α_p/α_m, each, on the overall CTE of the composite).

We also studied the effect of N on elastomeric polymer/clay nanocomposites, as shown in Fig 4.9; Chow's model is used for the prediction of the composite CTE; the primary model descriptors are exactly the same as used for the thermoplastic matrix, except for the matrix properties: E_m = 4 MPa, ν_m = 0.45, $\alpha_m = 20 \times 10^{-5}$/C; the curves depicted in Fig. 4.8 for thermoplastic matrix are plotted as well for comparison purposes. We can see that the effect of N on the composite CTE is far more distinct when the matrix is an elastomer, which can be mainly attributed to the high Poisson ratio and low stiffness of

[1] Such approximation gives good prediction of the composite in-plane CTE, but tends to underestimate the transverse CTE, as will be shown later.

the elastomer (refer to discussion regarding the transverse CTE of the "effective particle" in Section 4.1, Fig. 4.1). It should be noted that these predictions are based on Chow's formula, which tends to underestimate the transverse composite CTE. The actual degree of anisotropy of an intercalated elastomer/clay nanocomposite can be even more prominent.

Table 4.2 Effect of N on the intermediate model descriptors of the "effective particle"; L = 200 nm, $d_{(001)}$ = 4.1 nm, d_s = 0.678 nm; silicate properties E_s = 400 GPa, v_s = 0.20, α_s = 5.0×10-6/C; matrix properties E_m = 4 GPa, v_m = 0.35, α_m = 5.2×10-5/C

N	L/t	f_p/W_c	$\alpha_{p,ii}/\alpha_m$		E_p/E_m
			i = 1, 3	i = 2	
3	24	1.20	0.14	1.54	22
2	44	0.97	0.13	1.46	27
1	325	0.25	0.10	0.10	100

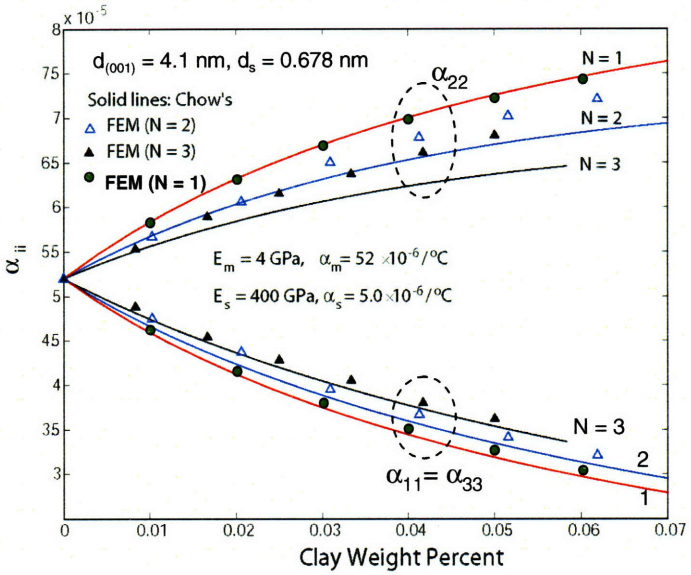

Figure 4.8: Parametric study of the effect of N on the anisotropic composite CTE, using both the Chow's formula (solid lines) and FE simulation (triangular markers).

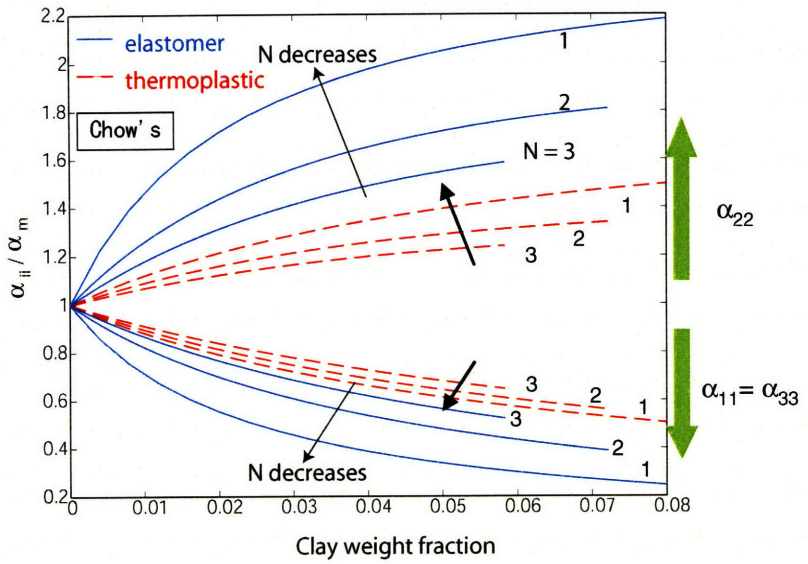

Figure 4.9: Parametric study of the effect of *N* on the anisotropic composite CTE: contrasting *thermoplastic* matrix and *elastomer* matrix. For the elastomer, E_m = 4 MPa, ν_m = 0.45, $\alpha_m = 20\times10^{-5}$/C; for the thermoplastic, E_m = 4 GPa, ν_m = 0.35, $\alpha_m = 5.2\times10^{-5}$/C.

4.3.2. Intercalated MXD6 nylon/clay

Injection-molded MXD6 nylon/clay nanocomposites with clay weight fraction varying from 0% to 5.27% were investigated for their anisotropic thermal expansion behaviors. The nanoclay are found to be aligned intercalated multi-layer stacks with in-plane dimension of ~ 200 nm (in the flow direction), average number of silicate per stack N ~ 3, and average inter-layer spacing d(001) ~ 4.1 nm (Lee and McKinley, 2002). Refer to Chapter 3 (Section 3.3.2) for detailed material characterization, including TEMs for nanocomposites with various clay fractions (Fig. 3.11).

- **Thermal Expansion Measurement**

Thermal expansion tests were conducted according to ASTM D696 using a Perkin-Elmer Thermomechanical Analyzer (Pyris Diamond TMA). Rectangular specimens were prepared in order to measure the anisotropic CTE of the nanocomposites; the two in-plane dimensions are 8 mm (Flow Direction) and 6 mm (orthogonal to FD), the

transverse dimension is 3 mm, as illustrated in Fig. 4.10. The specimens were stored in a desiccator in order to minimize water absorption. Thermal expansion tests were performed at a heating rate of 5°C/min and under a compressive force of 100 mN. A typical displacement-temperature curve of the homopolymer is shown in Fig. 4.11; the glass transition temperature (T_g) of MXD6 nylon measured by the TMA test is ~ 50 °C; two linear CTE slopes can be identified before and after T_g: the glassy state CTE, α_g, and the rubbery state CTE, α_r ($\alpha_g << \alpha_r$). Our major interest here lies in the glassy state nanocomposites; accordingly the TMA tests were performed over a temperature range from -40 → 35 °C. The linear CTE of pure MXD6 nylon is measured to be 5.2×10^{-5}/C, in good agreement with the value 5.1×10^{-5} /C reported by MITSUBISHI GAS (*Superior performance in barrier packaging*[2]).

The measured anisotropic CTE of MXD6 nylon/clay nanocomposites with a variety of clay contents are listed in Table 4.3; each data is the average of six tests. The CTE of the nanocomposites is observed to be transversely isotropic ($\alpha_{11} \approx \alpha_{33} < \alpha_{22}$); therefore we do not distinguish the two in-plane directions. Typically the composite, with clay particles aligned in the 1-3 planes, exhibit substantial anisotropy in thermal expansion; schematics of TMA test displacement-temperature curves of the composite in the in-plane (1-3) and the transverse (2) directions, together with that of the homopolymer, are plotted in Fig. 4.12.

[2] http://mgc-a.com/Pages/MXD6/media/Mxd6bro.pdf

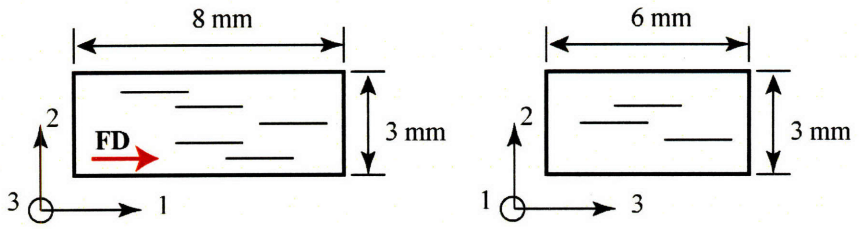

Figure 4.10: Dimensions of the TMA specimen; Axis-1 coincides with the flow direction (FD). Note that particles are not to scale and are shown for illustration and axes reference purposes only.

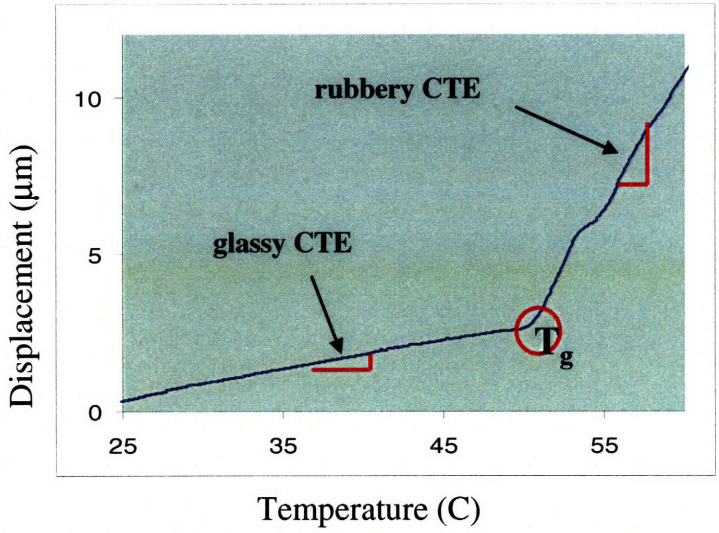

Figure 4.11: Typical TMA measurement curve, cover both glassy regime and rubbery regime.

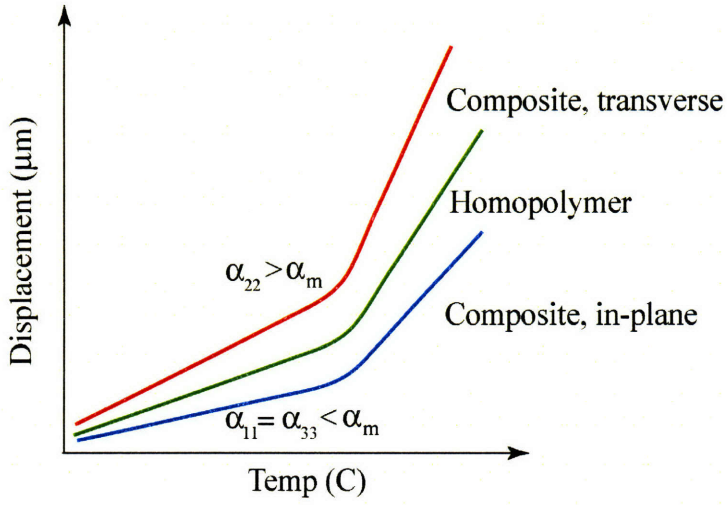

Figure 4.12: Schematics of TMA test curves of isotropic homopolymer, and composite (as illustrated in Fig. 4.10) in the in-plane (plane 1-3) and the transverse directions (2-direction). Composite exhibits high substantial anisotropy in thermal expansion due to the existence of clay platelets aligned normal to the 2-direction: $\alpha_{11} = \alpha_{33} < \alpha_m < \alpha_{22}$.

Table 4.3 TMA test data of the anisotropic linear CTE of MXD6 nylon/clay nanocomposites

W_c (%)	0	0.58	1.10	3.13	3.67	4.17	5.27
$\alpha_{11}=\alpha_{33}$ (10^{-5}/C)	5.20	5.10	4.93	4.97	4.56	4.29	4.09
α_{22} (10^{-5}/C)	5.20	5.39	5.83	6.02	6.46	6.58	6.75

- **Micromechanical Modeling (Chow & FE)**

Both FE simulations and Chow's formula are used to predict the anisotropic CTE of the nanocomposites. Structural parameters of the intercalated nanoclay are found to be $N = 3$, $d_{(001)} = 4.1$ nm; thermal and mechanical properties of the pure MXD6 nylon matrix are measured to be $\alpha_m = 5.2\times10^{-5}$ /C (TMA), $E_m = 4$ GPa (refer to previous work by the author for experiments and modeling of the tensile modulus of the MXD 6 nylon/clay nanocomposites, Sheng, et al., 2004; and MS thesis, 2002); here the CTE of single layer silicate is taken to be $\alpha_{silicate} = 1.0\times10^{-5}$ /C, employing the result of MD simulations performed by Manevitch, et al. (in press, 2006). Key micromechanical modeling parameters for the "effective particle" are summarized in Table 4.4.

Fig. 4.13 depicts the experimental data (TMA measurements) together with FE simulation results and predictions by the Chow model. The transverse composite CTEs (α_{22}) predicted by the FE simulations well match the experimental data, whereas the Chow predictions of α_{22} are generally lower, as the anisotropy in the thermal expansion of the intercalated clay is not accounted for in Chow's model (the particle thermal expansion is characterized only by $\alpha_{p,11}$). Both FE simulation and Chow's formula give approximately the same results for the longitudinal composite CTE (α_{11}), which are in relatively good agreement with test data at low clay contents ($W_c < 3\%$), but tend to over-exaggerate the efficiency of the nanoclay at reducing thermal expansion at higher clay

weight fractions. This discrepancy between experiments and model predictions can be attributed to the progressive changes that take place in the clay morphology as W_c increases; as evidenced by the TEMs shown in Fig. 3.11, the degree of waviness of the clay platelets increases substantially with increasing amount of clay; such waviness hinders the silicate from effectively reducing the CTE in the longitudinal direction. The micromechanical models (both FE and Chow's) assume particles to be perfectly aligned in the longitudinal direction, which yields a 'lower-bound' prediction of the composite α_{11}, considering the inevitable existence of imperfections in reality.

Table 4.4 Key parameters of the "effective particle" for micromechanical modeling of MXD6 nylon/clay nanocomposites (clay structure N = 3, $d_{(001)}$ = 4.1 nm; clay properties d_s = 0.678 nm, E_s = 370 GPa, $\alpha_s = 1.0\times10^{-5}$/C; matrix properties E_m = 4.0 GPa, ν_m = 0.35, $\alpha_m = 1.0\times10^{-5}$/C).

L/t	f_p/W_c	$E_{p,11}$ (GPa)	$\alpha_{p,11} = \alpha_{p,33}$ (10^{-5} /C)	$\alpha_{p,22}$ (10^{-5} /C)
23	1.20	87	$\nu_{gallery} = 0.35$	
			1.19	7.72
			$\nu_{gallery} = 0.45$	
			1.22	9.45

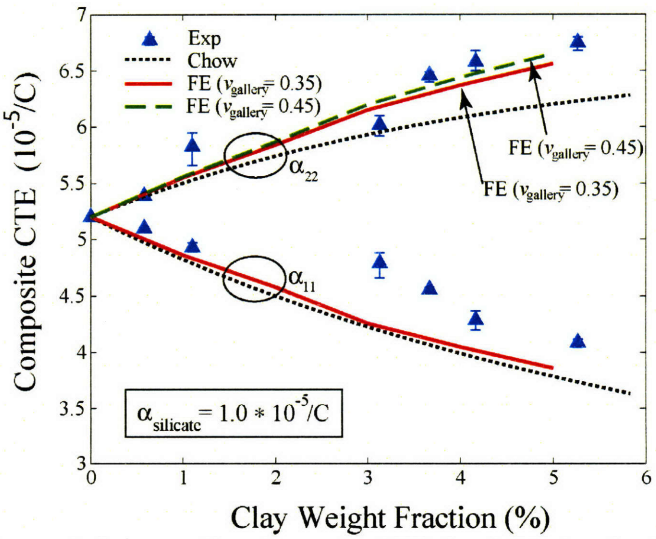

Figure 4.13: Predictions of the overall anisotropic CTE for MXD6 nylon/clay nanocomposites, together with TMA measurements; solid lines — FE results with $\nu_{gallery}$ = 0.35, dashed lines — FE results with $\nu_{gallery}$ = 0.45, dotted lines — Chow's predictions.

4.3.3. Partially Exfoliated Nylon 6 Nanocomposites

Yoon, et al. (2002), measured the anisotropic CTE of injection-molded nylon 6 nanocomposites; in addition they tried to compare the test data with Chow's theory. However, a systematic methodology of determining the model parameters (for instance, the proper conversion from clay weight fraction to particle volume fraction) is lacking in their work (Yoon, et al., 2002). Here we apply the multi-scale modeling strategy established in Chapter 2 to the nylon 6/clay nanocomposites described in their work, and compare the model predicted composite CTE with reported experimental data. Only Chow's formula is employed to model the nylon 6 nanocomposites since their clay particles are claimed to be exfoliated, and therefore no particle anisotropy is involved.

- **Material Characterization**

Fig. 4.14 shows the TEMs of the nylon 6 nanocomposites viewed from different perspectives (Yoon, et al., 2002). Well-exfoliated silicate plates are well-aligned in the flow direction; however, occasional aggregation of the platelets can also be observed. Yoon, et al., found the in-plane dimension of the clay platelet to be in the range of 70 ~ 90 nm.

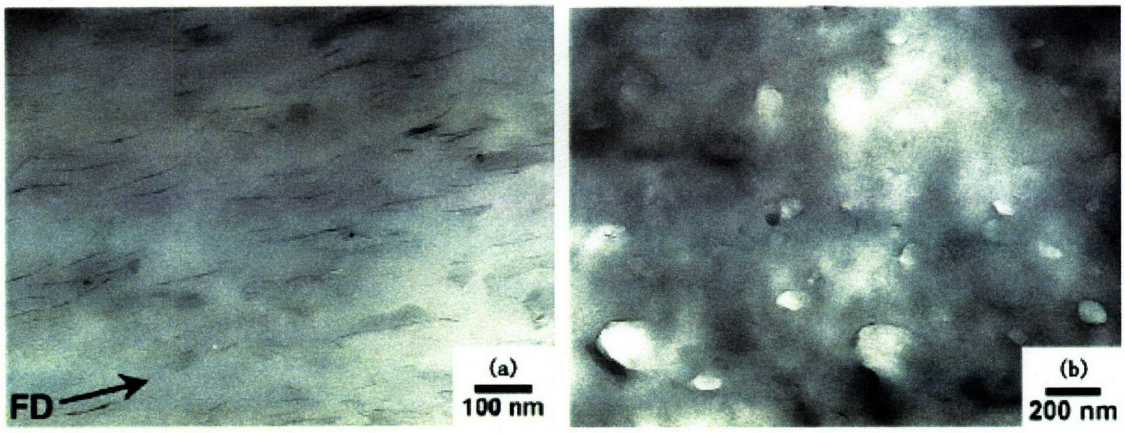

Figure 4.14: TEMs of the nylon 6 nanocomposites: (a) in-plane perspective; (b) transverse perspective (Yoon et al. 2002).

- **Micromechanical Modeling**

Chow's model is used to model the thermal expansion of the nylon 6 nanocomposites. We consider two cases: $N = 1$ and $N = 2$, since the exfoliation of the clay appears to be partial as shown in the TEM ($N = 1$ corresponds to complete exfoliation). Yoon, et al., measured the thermal/mechanical properties of pure nylon 6 to be $E_m = 2.75$ GPa and $\alpha_m = 7.9\times10^{-5}$ /C. Taking $L = 80$ nm, $d_s = 0.678$ nm, $\alpha_{silicate} = 1.0\times10^{-5}$/C and $d_{(001)} = 4.1$ nm for the intercalated case, we can calculate the key model parameters through the multi-scale modeling approach developed in Chapter 2; Table 4.5 lists these parameters corresponding to $N = 1$ and $N = 2$, respectively.

TMA-based test results of the anisotropic CTE of the nylon 6 nanocomposites are plotted in Fig. 4.15 together with predictions using Chow's model for complete exfoliation ($N = 1$) and intercalation ($N = 2$). The transverse experimental data α_{22} are well bounded by the two sets of model predictions using $N = 1$ and $N = 2$, each, indicating the coexistence of exfoliated and intercalated nanoclay, as seen in the TEM; the longitudinal experimental data α_{11} tend to be slightly higher than the predicted values, which can be due to some degree of particle misalignment and waviness, as mentioned in Yoon, et al.'s work.

Table 4.5 Key parameters of the "effective particle" for micromechanical modeling of nylon 6/clay nanocomposites (L = 80 nm; d_s = 0.678 nm, E_s = 370 GPa, $\alpha_s = 5.0\times10^{-6}$/C; E_m = 2.75 GPa, $\alpha_m = 7.9\times10^{-5}$/C)

N	L/t	f_p/W_c	$E_{p,11}$ (Gpa)	$\alpha_{p,11} = \alpha_{p,33}$ (10^{-5} /C)	$\alpha_{p,22}$ (10^{-5} /C)
1	130	0.25	400	1.0	1.0
2	17	0.97	106	1.16	11.4

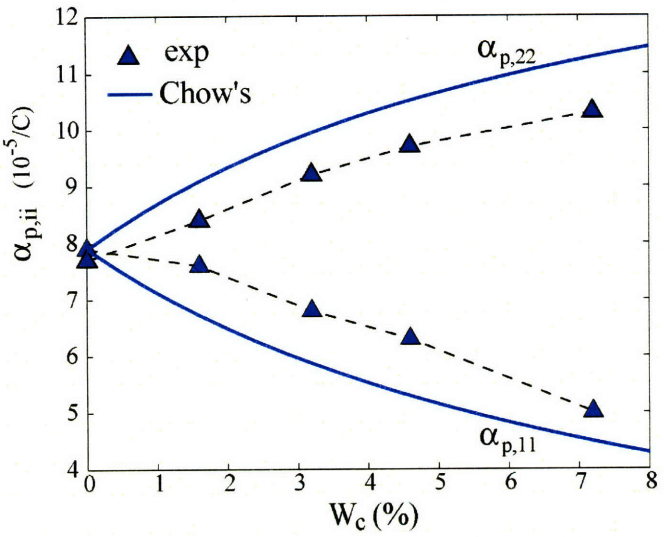

Figure 4.15: Micromechanical modeling of the CTE of partially exfoliated nylon 6 nanocomposites superposed with experimental data (Yoon et al. 2002).

4.4. Summary

Thermal expansion of well-aligned polymer/clay nanocomposite is highly anisotropic — while the in-plane CTE of the composite is sufficiently reduced by the addition of the nanoclay, the transverse CTE of the composite is increased substantially due to the in-plane constraint imposed by the low-CTE, planar-shaped nanoclay inclusion, giving an additional Poisson-effect expansion normal to the particle plane. For a given clay weight fraction, the effect of exfoliation vs. intercalation on CTE is found to be rather trivial for thermoplastic polymer nanocomposites. When the matrix is elastomeric, the degree of anisotropy in the composite thermal expansion is enhanced due to the high Poisson ratio and low stiffness of the elastomer polymer. Multscale micromechanical modeling (based on the "effective particle" concept) of the anisotropic thermal expansion behavior of intercalated MXD6 nylon/clay nanocomposites and exfoliated nylon 6/clay nanocomposites are in good agreement with TMA experimental data.

Chapter 5

Initial Tensile Yield Strength of the Nanocomposite

While the enhancement in tensile modulus for nanocomposites has been widely observed, the same does not hold for composite strength. Presumably, matrix crystallinity, clay dispersion, and interface adhesion also play important roles in the deformation behavior of polymer/clay nanocomposites. For instance, axial tension tests by the author on amorphous MXD6 nylon/clay nanocomposites (Fig. 5.1) with predominately intercalated morphology show little or no increase in initial yield strength over the matrix polymer[1]; however, significant increases (50-100%) in yield strength have been reported for completely or partially exfoliated nanocomposites with semi-crystalline polymer matrices such as nylon 6 (Medellin-Rodriguez, et al., 2003) and polyethylene (Wang, et al., 2002). This chapter aims to assess the contribution of nanoclay to the yield strength of the composite in the absence of any alteration of the matrix morphology (for instance, when the matrix is an amorphous polymer such as polycarbonate), rendering the separate contribution of 'stiff filler' to the composite mechanical properties. First, the axial yield strength of an idealized nanocomposite structure (with perfect orientation and complete exfoliation) is evaluated; effects of clay weight fraction and matrix yield strength are examined (Section 5.1). Then the influences of clay orientation distribution and degree of

[1] In fact, with 5.37-Wt% clay the composite breaks at a tensile strain as small as 2%, exhibiting only a small increase in strength and dramatic decrease in tensile ductility.

exfoliation on the composite axial yield strength are explored in Sections 5.2 and 5.3, respectively. The complete set of Hill ratios which describe the anisotropic yield surface of the composite is determined in Section 5.4. Finally, idealized micromechanical modeling predictions of composite modulus and initial tensile yield strength are compared to a range of collected experimental data. Comparisons reveal that while model predicted composite moduli well-bound the test data, the predictions on composite strength can not always explain the remarkable enhancement observed for nylon 6/clay nanocomposites, which leads to further study in Chapter 6 on the change of the crystal texture of semi-crystalline polymers due to the addition of nanoclay, as well as the effect of such special matrix morphology on the composite modulus and yield strength.

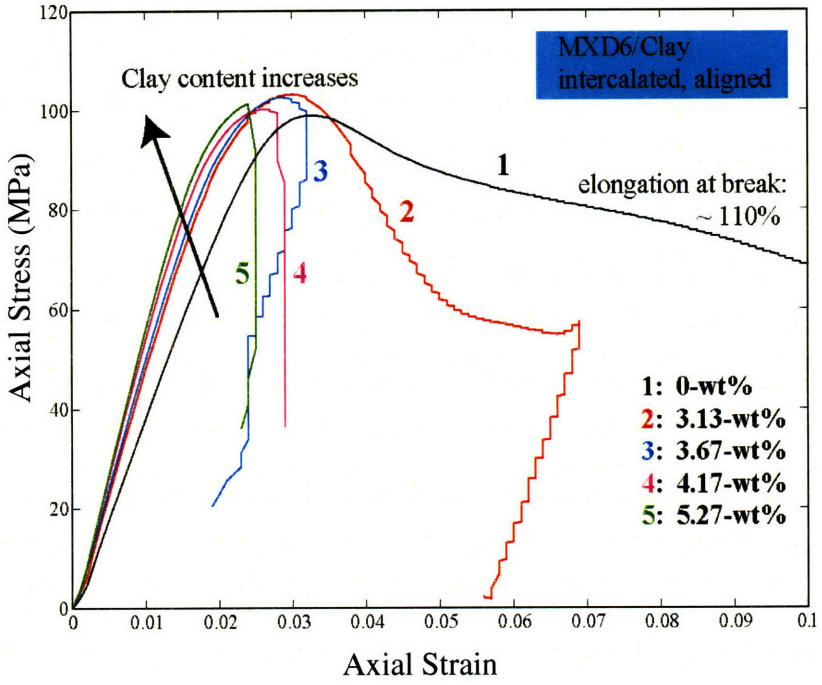

Figure 5.1: Uniaxial tensile curves (nominal stress and strain) of pure MXD6 nylon and nanoclay-reinforced MXD6 nylon/clay nanocomposites.

5.1. "Upper-bound" of the Composite $\sigma_{y,11}$

The goal of this section is to assess the maximum capacity of the nanoclay in improving the initial tensile yield strength (σ_y) of the matrix for a given clay content, and to explore the dependence of this capacity ($\sigma_y/\sigma_{y,m}$) on the matrix initial yield strength and the clay weight fraction. For such purposes, we idealize the critical micromechanical features which contribute to the highest reinforcing efficiency — perfect particle exfoliation, perfect particle alignment, and perfect matrix/particle interface bonding — yielding a composite structure whose tensile properties in the axial direction (the direction parallel to the aligned particle planes) essentially become **upper-bounds** for nanocomposites (of the given L/t, f_p, E_m, and $\sigma_{y,m}$), and provide the high stiffness of the exfoliated clay as the only source of reinforcement. Note that while the composite is highly anisotropic (the complete anisotropic elastic properties have been investigated in Chapter 3), the primary concern here are the in-plane tensile properties E_{11} and $\sigma_{y,11}$.

5.1.1. Model Description

Finite element-based micromechanical modeling

Three-dimensional RVEs with perfectly aligned particles, as shown in Fig. 5.2(a), are subjected to uniaxial tension in the direction parallel to the particle planes. The overall composite modulus and initial yield strength are then extracted from the macroscopic stress strain responses of the RVEs (refer to Chapter 2 for the detailed procedure).

Constitutive Modeling of the matrix

The matrix is modeled with isotropic elasticity, characterized by E_m and ν_m, and non-hardening, isotropic yielding (von Mises) (as illustrated in Fig. 5.2b), characterized by

the initial tensile yield strength, $\sigma_{y,m}$. A slight softening is introduced after initial yielding; typically the yield strength of the polymer drops from 70 MPa (initial yield strength of a thermoplastic) to ~ 61 MPa over a 10% strain increase, giving an average softening slope of -86 MPa. In this finite element analysis, 3D solid elements (specifically, 8-node linear brick elements) are used for the matrix material.

Constitutive Modeling of the exfoliated clay

The structure and properties of the nanoclay have been discussed in Chapter 2. For exfoliated clay, we adopt the modulus-thickness pair of (E_s = 370 GPa, d_s = 0.678 nm) determined by Manevitch and Rutledge (2004), and derive an f_p/W_c ratio of 0.25. In this finite element analysis, shell elements (specifically, 4-node linear shell elements) are used to model the thin plate-like exfoliated clay.

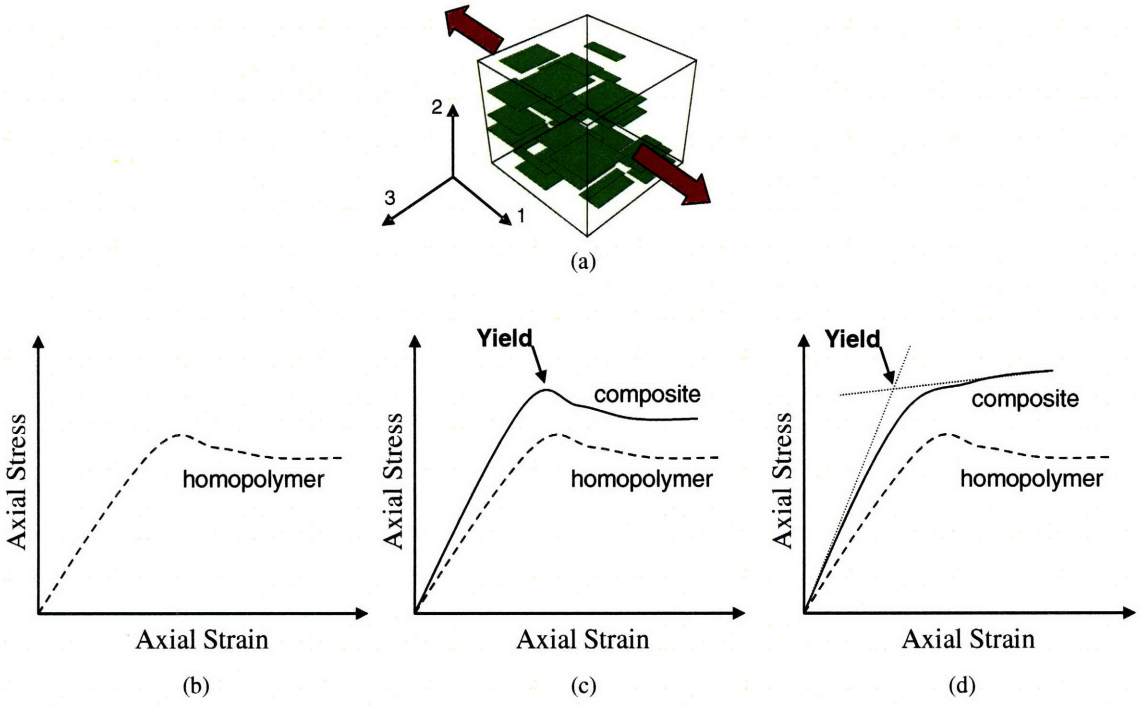

Figure 5.2: (a) Three-dimensional RVE with perfectly aligned platelet particles subjected to uniaxial tension in 1-direction. (b) Schematics of the uniaxial stress-strain curve of a matrix polymer with slight strain softening after yield. (c) Definition of the initial yield strength for a composite with observable softening. (d) Schematic definition of the initial yield strength for a composite without apparent strain softening.

Definition of the initial yield strength of the composite

We take care to define the uniaxial tensile behavior of the matrix to have slight strain softening after initial yield for clear identification of the yield point, as schematically shown in Fig. 5.2b; however, the true stress-strain behavior of the composite may or may not maintain the softening feature, depending on the filler content. For a composite with observable strain softening, the initial yield strength is defined to be the maximum stress in the true stress-strain curve, as illustrated in Fig. 5.2c. For a composite without apparent softening, the yield point is taken to be the intersection of the first elastic part and the final fully-plastic part of the stress-strain curve, as illustrated in Fig. 5.2d.

5.1.2. Model Results

Uniaxial tensile curves of composites filled with 2, 4, and 6-Wt% exfoliated clay are plotted in Fig. 5.3(a), together with the tensile behavior of the homopolymer; particle length is fixed to be 100 nm, giving L/t = 147; the matrix properties are E_m = 3.0 GPa, $\sigma_{y,m}$ = 70 MPa. Fig. 5.3(b) depicts E/E_m and $\sigma_y/\sigma_{y,m}$ of the composites, extracted from tensile curves in Fig. 5.3(a), as functions of the clay weight fraction. Both E_{11} and $\sigma_{y,11}$ increase linearly with increasing W_c, although the enhancement in $\sigma_{y,11}$ is not as significant as in E_{11}. In addition, the macroscopic yield strain ($\varepsilon_{y,11}$) is observed to decrease with increasing W_c. In the next few paragraphs, we will study the yielding process of the composites and identify the role of the nanoclay during deformation.

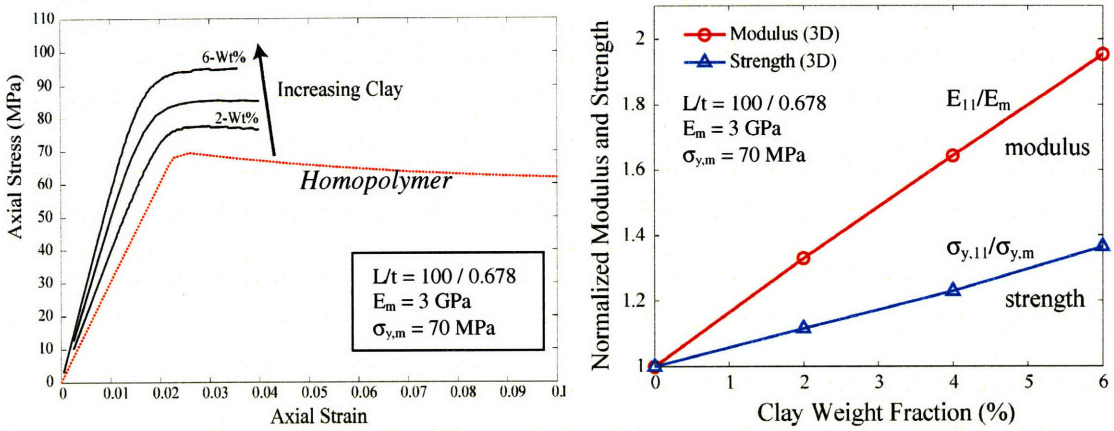

Figure 5.3: (a) Uniaxial tension curves of composites with 2, 4, and 6-Wt% exfoliated clay (L = 100 nm, t = 0.678 nm); dotted line depicts the tensile behavior of the homopolymer with E_m = 3.0 GPa, and $\sigma_{y,m}$ = 70 MPa (note that the matrix is modeled to have slight post-yield softening for clear identification of the yield point). (b) Composite E_{11} and $\sigma_{y,11}$ extracted from tensile curves in (a), normalized by E_m and $\sigma_{y,m}$, respectively.

5.1.2.1. Tensile Yielding of the Composite

The tensile yielding of the composite is a gradual process, as shown in Fig. 5.4 (**A→ B→ C**), where the tensile stress-strain curve of 6-Wt% clay nanocomposite and contours of the plastic strain rate at different stages of deformation are demonstrated[2]. At stage-**A** (ε_{11} ~ 0.014) plasticity initiates at particle ends due to stress concentration; accordingly, the macroscopic stress-strain curve begins to deviate from the linear elastic response. As the macroscopic strain increases to stage-**B**, (ε_{11} ~ 0.017), these local deformation sources interconnect with each other and form into shear bands; macroscopically, the stress-strain curve has further rolled away from the initial slope and is ready to enter macroscopic yield. As the deformation proceeds into stage-**C** (ε_{11} ~ 0.026), local deformation pathways have fully established and percolated through the entire RVE, resulting in overall macroscopic yielding of the composite.

[2] Contours from two-dimensional plane-strain simulations are used here for illustrative purposes.

Fig. 5.5 zooms in on contours of the Mises stress (Fig. 5.5a and b), the transverse shear stress (Fig. 5.5c and d) and the axial stress (Fig. 5.5e and f) in the matrix, at the onset (Stage-**A**) and at the fully-developed stage (Stage-**C**) of yielding, respectively. When plasticity initiates in the matrix, the Mises stress at the particle ends reaches $\sigma_{y,m}$ (Fig. 5.5a, $\sigma_{y,m}$ = 70 MPa) ; meanwhile the particle-tip shear stress reaches the value of the matrix shear yield strength, $\tau_{y,m}$ (Fig. 5.5c, $\tau_{y,m} = \sigma_{y,m}/\sqrt{3} \cong 40$ MPa). At the post-yield stage, the plastic deformation pathways have fully percolated in the matrix, bypassing the particles (Fig. 5.5b), and the matrix shear stress at particle tips has saturated at $\tau_{y,m}$ (Fig. 5.5d). The axial stress in regions adjacent to the particles is low, due to the deformation constraint of the stiff particles.

The reinforcing mechanisms of clay particles during tensile deformation can be summarized as:

- *Load transfer*

During tensile deformation, the clay particles first act as reinforcing agents (highly efficient load carriers) for the enhancement of composite axial modulus. Particularly, when the composite is subjected to axial tensile loading, the load is transferred to the particles mainly through interface shearing (refer to Chapter 3 for discussion regarding the "load transfer" mechanism of the particles).

Fig. 5.6c depicts the axial strain distribution along a particular particle in a 2-wt% composite (exfoliated clay with L = 100 nm, t = 0.678 nm; matrix E_m = 3 GPa, $\sigma_{y,m}$ = 70 MPa) and its evolution with increasing macroscopic axial strain $\bar{\varepsilon}_{11}$; the average particle

axial strain[3], $\bar{\varepsilon}_{p,11}$, is plotted as a function of $\bar{\varepsilon}_{11}$ in Fig. 5.6d. It is observed that $\bar{\varepsilon}_{p,11}$ increases linearly with increasing $\bar{\varepsilon}_{11}$ throughout the elastic regime; once the composite has undergone macroscopic yielding, $\bar{\varepsilon}_{p,11}$ stays constant and continues to bear load.

The constant post-yield value of $\bar{\varepsilon}_{p,11}$ (and correspondingly, the average particle axial stress) directly results from matrix yielding — once the composite has fully yielded, the magnitude (and axial extent along the particle length) of the matrix shear stress at particle ends saturates at the value of $\tau_{y,m}$, as demonstrated in Fig. 5.5(d), and therefore can not transfer additional axial stress to the particle.

- *Strain shielding*

The stiff particles constrain the matrix material in their vicinity from undergoing axial deformation adjacent to the particle plane, resulting in low-strain zones surrounding the interior portions of the clay particles. Compatibility requires that the axial strain in the matrix adjacent to the particle plane equals that in the stiff particle (generally less than 1/5 of the macroscopic $\bar{\varepsilon}_{11}$ for this particular matrix stiffness, as shown in Fig. 5.6a and b). Consequently, the elastic state of the matrix material within such constrained regions extends well into post-yielding stages. Materials in these regions bear load, but remain elastically stiff and not plastically deforming; the shear bands percolate around these regions, finding a continuous path across a net section, giving macroscopic yield.

Comparison of the matrix strain in 2-wt% and in 6-wt% nanocomposites (Fig. 5.6a and b) reveals that addition of clay particles raises the proportion between the volume of the constrained elastic regions and the volume of matrix with the plastically deforming shear

[3] $\bar{\varepsilon}_{p,11}$ is defined to be the volume average of the axial strain in the particle: $\bar{\varepsilon}_{p,11} = \int_V \varepsilon_{11} dv \Big/ V$, where V is the particle domain.

bands, which, together with the increased amount of load-carrying particles, act to increase the macroscopic composite yield strength (Fig. 5.3b shows linear increase in the composite $\sigma_{y,11}$ with increasing W_c). Also note that in the 6-Wt% case, the axial strain in the shear bands are higher compared to the 2-Wt% case at a given macroscopic axial strain, because there is less matrix deforming to accommodate the macroscopic strain.

- *Tortuous deformation pathway*

As local plastic deformation pathways inter-connect with each other in the matrix, the existence of non-deforming particles also hinders the development of local shear deformations into percolating shear bands, consequently forcing the formation of tortuous deformation pathways, as shown in Fig. 5.4(c).

Fig. 5.7 compares the axial tensile behavior of the discontinuous particle composite schematically with those of two extreme cases: the parallel model (upper-bound) and the serial model (lower-bound). The upper-bound model yields $\varepsilon_{y,u} = \varepsilon_{y,m}$ and $\sigma_{y,u}/\sigma_{y,m} = E_u/E_m$, the lower bound model gives $\sigma_{y,l} = \sigma_{y,m}$ and $\varepsilon_{y,l}/\varepsilon_{y,m} = E_m/E_l$, where subscripts 'l' and 'u' stand for 'lower' and 'upper' bound, respectively. The modulus and initial tensile yield strength of the discontinuous particle composite is bounded by these two extreme cases; due to the gradual yielding process (**A→ B→ C,** as illustrated in Fig. 5.4), the enhancement in σ_y is not as prominent as in E: $\varepsilon_y < \varepsilon_{y,m}$, $\sigma_y/\sigma_{y,m} < E/E_m$, which explains the lower slope of the $\sigma_y/\sigma_{y,m}$–W_c curve compared to the E/E_m – W_c curve, as depicted in Fig. 5.3(b).

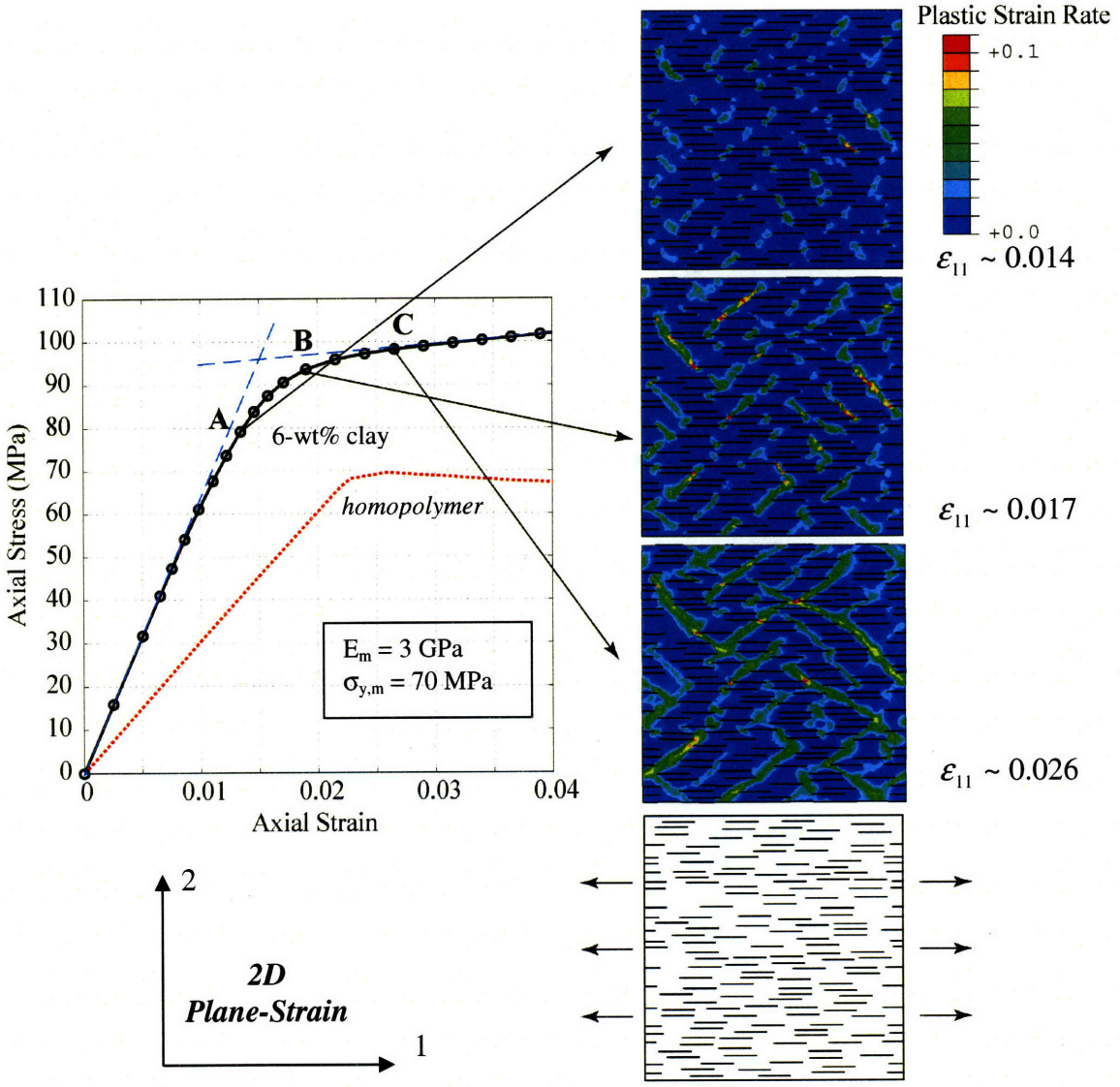

Figure 5.4: Stress-strain curve of 6-Wt% nanocomposite and contours of the plastic strain rate at stage (A) 0.014 axial strain, (B) 0.017 axial strain, and (C) 0.026 axial strain. Matrix E_m = 3 GPa, $\sigma_{y,m}$ = 70 MPa. Exfoliated clay L = 100 nm, t = 0.678 nm. Results are from 2D plane-strain simulations.

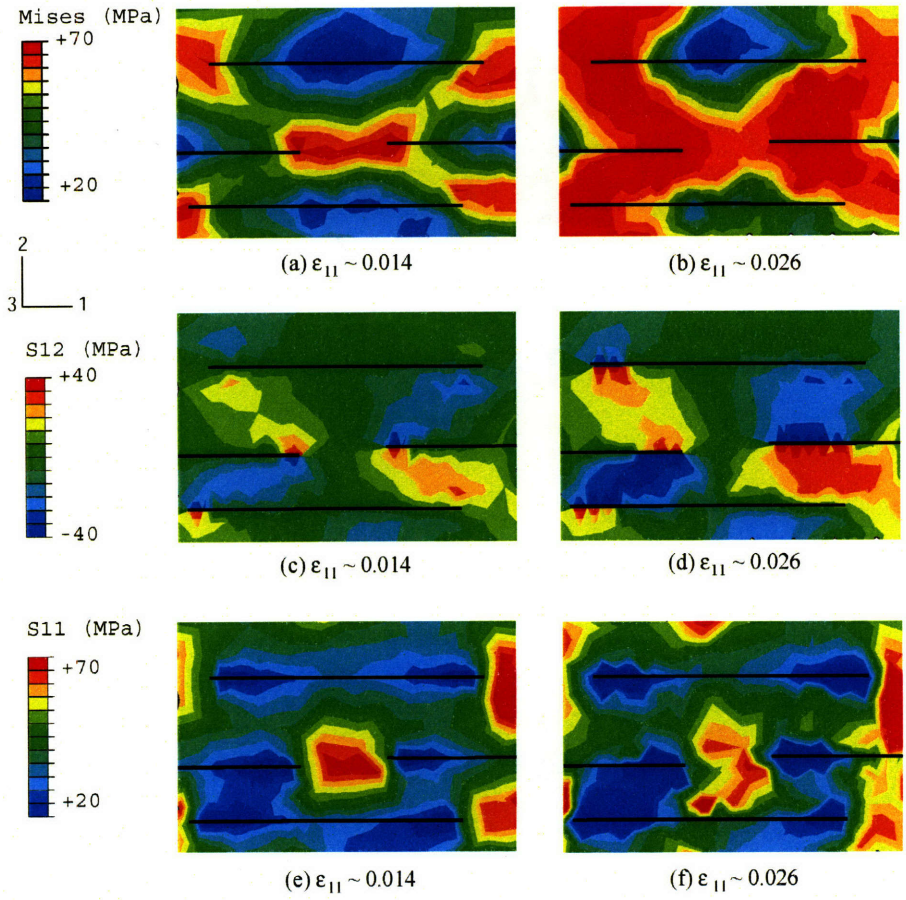

Figure 5.5: Local details of evolution of various stress components in the matrix of a 6-wt% nanocomposite (see Fig. 5.4 for stress-strain behavior and contours of the plastic strain rate; results are from a 2D plane-strain simulation). Contours of the Mises stress: (a) macroscopic axial strain of ~ 0.014 (Stage-A, as denoted in Fig. 5.4), (b) axial strain ~ 0.026 (Stage-C, as denoted in Fig. 5.4). Contours of the transverse shear stress: (c), (d). Contours of the axial stress: (e), (f). Dark lines mark the particles.

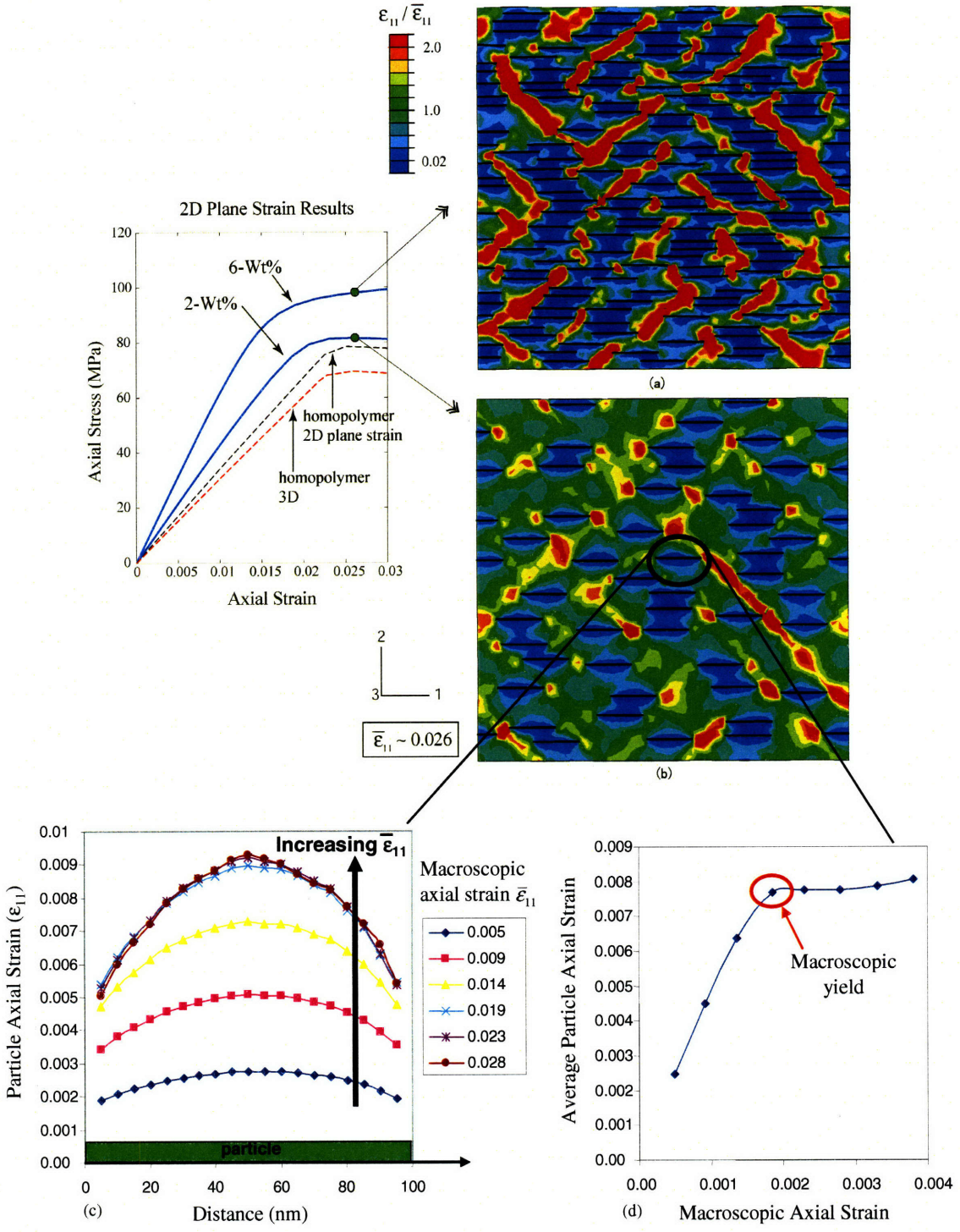

Figure 5.6: Contours of the matrix axial strain of (a) 6-wt% and (b) 2-wt% nanocomposites at macroscopic axial strain of ~ 0.026 (Stage-C in Fig. 5.4). Matrix E_m = 3 GPa, $\sigma_{y,m}$ = 70 MPa. Exfoliated clay L = 100 nm, t = 0.678 nm. Black lines mark the particles. Regions in the vicinity of particles experience axial strain less than 1/5 of the macroscopic axial strain. (c) Evolution of the axial strain distribution along one particle chosen from the 2-wt% composite; (d) average particle axial strain as a function of macroscopic axial strain.

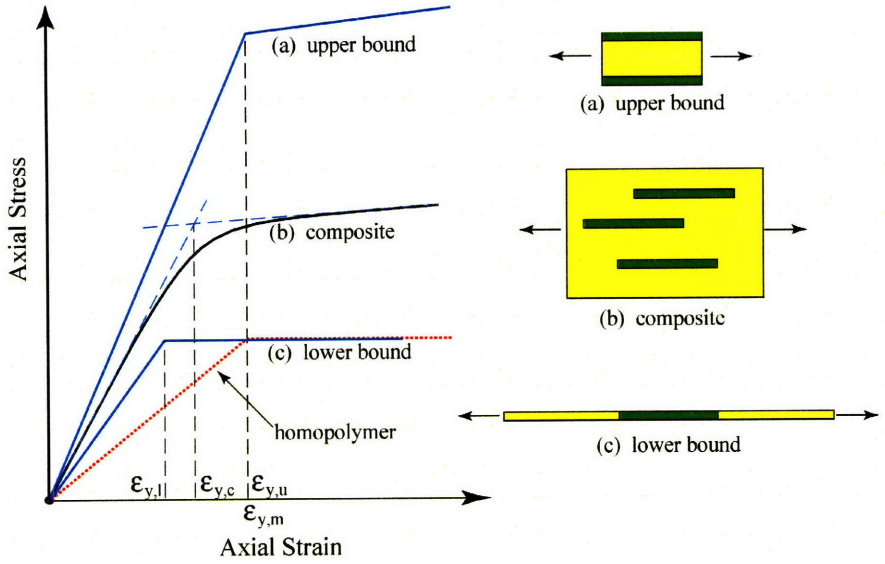

Figure 5.7: Schematics of the axial tensile behaviors of (a) parallel model, (c) serial model, and (b) discontinuous particle model, where (a) and (c) give upper and lower bounds for composite modulus and yield strength.

5.1.2.2. Effect of Matrix Yield Strength

The effect of matrix yield strength, $\sigma_{y,m}$, on the composite axial yield strength, $\sigma_{y,11}$, is demonstrated in Fig. 5.8. Again, three-dimensional RVEs filled with perfectly-aligned, exfoliated clay particles (L/t = 100 nm/ 0.678 nm) are subjected to uniaxial tensile loading in the 1-direction, as shown in Fig 5.2(a). Three sets of matrix properties are assigned: (a) E_m = 3.0 GPa, ν_m = 0.35, $\sigma_{y,m}$ = 70 MPa; (b) E_m = 1.5 GPa, ν_m = 0.45, $\sigma_{y,m}$ = 50 MPa; and (c) E_m = 0.5 GPa, $\sigma_{y,m}$ = 24 MPa.

Fig. 5.8(b) plots the yield strength enhancements for composites with 2, 4, and 6-Wt% exfoliated clay as functions of the matrix yield strength. For a given clay weight fraction, $\sigma_{y,11}/\sigma_{y,m}$ decreases monotonically with increasing $\sigma_{y,m}$; the influence of $\sigma_{y,m}$ is more manifest at higher clay content (6-Wt% as opposed to 2-Wt%).

The fact that composites with low $\sigma_{y,m}$ see more enhancement in the yield strength can be explained through a simple analysis utilizing the concept of "constrained matrix volume". As revealed earlier in Section 5.1.2.1, once overall yielding is established, the entire composite volume can be partitioned into two types of domains: (a) the particle-constrained elastic regions, and (b) the percolated shear bands, undergoing plastic flow. The overall composite yield strength can hence be approximately decomposed into contributions from these two types of regions:

$$\sigma_{y,11} = f_{elastic}\overline{\sigma}_{elastic} + f_{plastic}\sigma_{y,m}, \tag{5.1}$$

where $f_{elastic}$ and $f_{plastic}$ are the volume fraction of the constrained regions and the volume fraction of the plastic shear bands, respectively; $\overline{\sigma}_{elastic}$ is the average axial stress of the constrained region, which depends on particle volume fraction, particle aspect ratio, and particle/matrix stiffness ratio:

$$\overline{\sigma}_{elastic} = \hat{\overline{\sigma}}_{elastic}\left(f_p, L/t, E_p/E_m\right). \tag{5.2}$$

For given clay weight fraction and clay morphology (exfoliated, fixed in-plane dimension), $f_{elastic}$, $f_{plastic}$, and $\overline{\sigma}_{elastic}$ can be considered to be approximately constant. As an example, Fig. 5.8 (d) and (e) compares the contours of the matrix axial strain of two composites with identical morphology parameters (W_c = 6%, N = 1, L/t = 100 nm/0.678 nm) and particle distribution, but possessing different matrix yield strength ($\sigma_{y,m}$ = 70 MPa in Fig. 5.8 d, $\sigma_{y,m}$ = 24 MPa in Fig. 5.8 e), at macroscopic axial strain of ~ 0.365. The fact that they have nearly the same amount of constrained regions and shear banding regions (actually, even the strain levels in each region are similar, comparing d and e) further validates our constant ($f_{elastic}$, $f_{plastic}$, and $\overline{\sigma}_{elastic}$) assumption.

Therefore the relative enhancement in the composite yield strength can be expressed as:

$$\frac{\sigma_{y,11}}{\sigma_{y,m}} = \frac{a}{\sigma_{y,m}} + b, \qquad a \equiv f_{elastic}\overline{\sigma}_{elastic}, \quad b \equiv f_{plastic} \tag{5.3}$$

Eq. (5.3) shows that for fixed clay fraction and morphology, the composite yield strength enhancement $\sigma_{y,11}/\sigma_{y,m}$ increases with decreasing $\sigma_{y,m}$. Fig. 5.8(c) demonstrates curve-fits of the data points in Fig. 5.8(b) to Eq. 5.3. The fitting parameters *a*, *b* for each clay weight fraction are listed in Table 5.1. Note that although parameter *b* is defined to be the volume fraction of plastically deformed regions, $f_{plastic}$, in Eq. 5.3, it should only be viewed as an indicator for $f_{plastic}$ since the derivations presented here are fairly primitive. For given clay morphology (well-aligned and exfoliated with fixed L/t = 100/0.678, as in this case), the value of *b*, proportional to the volume fraction of the plastically deformed regions, increases linearly with increasing W_c, indicating more tortuous deformation pathways with higher clay content.

Table 5.1: Parameters for curve-fits of data-points in Fig. 5.8b to Eq. 5.3 (dash-lines in Fig. 5.8c).

W_c (%)	*a* (MPa)	$b \equiv f_{plastic}$
2	1.20	1.10
4	2.64	1.19
6	4.32	1.30

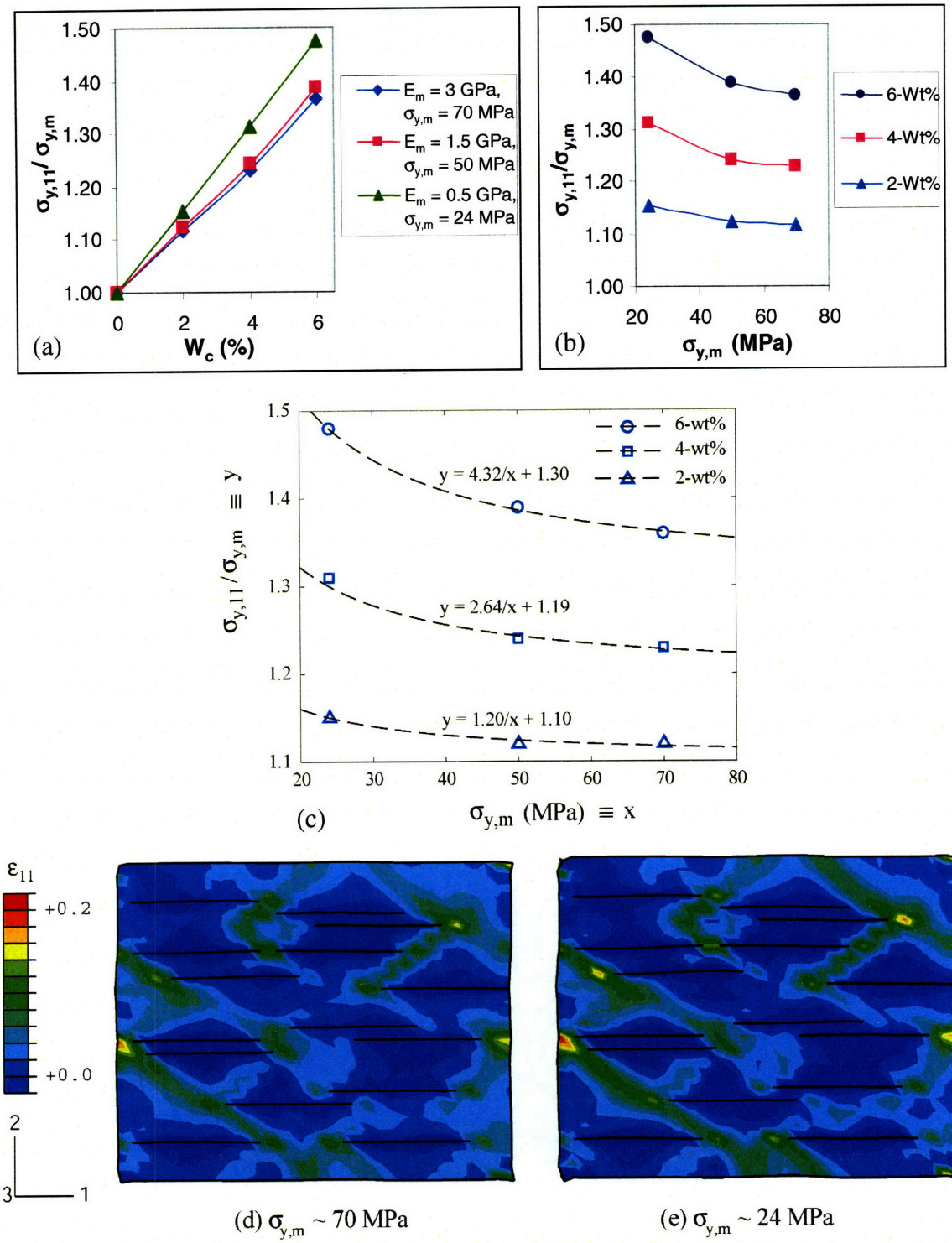

Figure 5.8: (a) 3D FE-based micromechanical prediction of the $\sigma_{y,11}$ of well-aligned, exfoliated nanocomposites (L = 100 nm, t = 0.678 nm) with three sets of matrix elasto-plastic properties: (E_m , $\sigma_{y,m}$) = (3.0 GPa, 70 MPa), (1.5 GPa, 50 MPa), and (0.5 GPa, 24 MPa). (b) The effect of $\sigma_{y,m}$ on $\sigma_y/\sigma_{y,m}$ for a given clay content. (c) Curve-fits of data points in (b) to equation y = a/x + b (Eq. 5.3), where a and b are constants for given (W_c, L/t). (d), (e) Contours of the matrix axial strain at macroscopic uniaxial tensile strain of ~ 0.365 (in the 1-direction) for the case $\sigma_{y,m}$ = 70 MPa (d) and $\sigma_{y,m}$ = 24 MPa (cross-section view from 3D FE simulations).

5.2. Effect of Particle Orientation Distribution

As shown in most TEMs of nanocomposites in the literature, perfect particle alignment is rare. Although injection-molding and compression molding both tend to align the clay platelets in the flow direction, particle misalignment is an inevitable result in the microstructure of the nanocomposites, the degree of which depends on processing conditions as well as the thermophysical nature of the matrix polymer. It is the goal of this sub-section to explore the impact of particle orientation on the composite modulus and strength, hence testing the robustness of the 3D model featuring fully aligned particles.

2D plane strain vs. 3D simulation

To simplify the construction of micromechanical models containing misaligned particles, we use 2D models to carry out the study of the influence of particle orientation on composite modulus and yield strength. Note that the 2D plane-strain approximation bears certain inherent limitations: in terms of loading, "uniaxial" tension is essentially equal to plane strain tension due to the plane strain constraint; in terms of particle geometry, the particle is essentially a continuous inclusion (with infinite dimension) in the 3-direction (the direction perpendicular to the modeled two-dimensional plane), as illustrated in Fig. 5.9. The plane strain modulus, E^*, and plane strain initial yield strength, σ_y^*, are related to E and σ_y as: $E^* = \frac{E}{(1-\nu^2)}, \sigma_y^* = \frac{\sigma_y}{\sqrt{1-2\nu+\nu^2}}$. Given ν = 0.35 (thermoplastic), E^*/E ~ 1.14, σ_y^*/σ_y ~ 1.14; given $\nu = 0.45$, E^*/E ~ 1.25, σ_y^*/σ_y ~ 1.15.

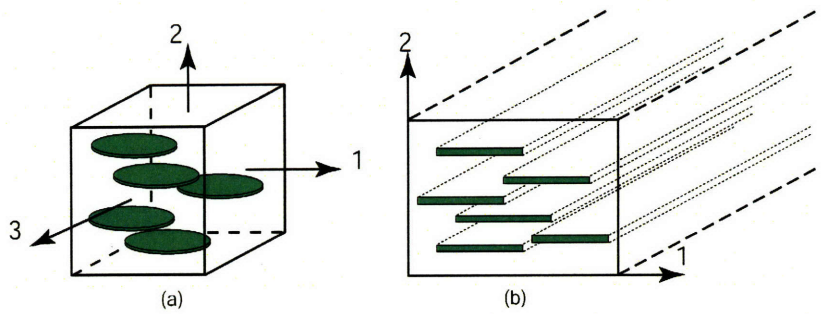

Figure 5.9: Schematics of (a) 3D model and (b) 2D plane strain model.

Fig. 5.10 compares results of the normalized composite modulus (E/E_m) and strength ($\sigma_y/\sigma_{y,m}$) predicted by 2D and 3D FE simulations. Identical matrix and particle properties are assigned to 2D and 3D models: uniform particle length of 100 nm, perfect exfoliation, perfect particle alignment in the loading direction, with matrix E_m = 3 GPa and $\sigma_{y,m}$ = 70 MPa. The 2D plane strain simulations give slightly higher predictions of composite modulus and strength compared to the 3D ones, due to the plane strain nature of the simulations. At zero-percent clay, the results are essentially the plane strain properties of the matrix ($E_m^*/E_m \sim \sigma_{y,m}^*/\sigma_{y,m} \sim 1.14$, as introduced in the previous paragraph). Actually, the extremely high stiffness and aspect ratio of the planar-shaped nanoclay tend to create a nearly 'plane-strain' situation through its constraint on matrix strain tangential to the particle plane. This effect has been elaborated in Chapter 3, when discussing the overall composite transverse modulus and the in-plane and transverse Poisson ratios, as depicted in Fig. 5.10.

Orientation Distribution

The particle orientation angle θ, defined as the angle between the particle plane and the loading direction, is introduced in order to quantify the degree of particle orientation. Particles clockwise away from the loading axis are considered to have the positive angle,

as illustrated in Fig. 5.11(a). A normal distribution of the orientation angle with an average value centered at 0 degree, as depicted in Fig. 5.11(b), is generated to approximate clay misalignment in nanocomposites. Note that the average particle orientation coincides with the loading direction. The degree of misalignment is characterized by the standard deviation (SDV) of the normal distribution. During the construction of the 2D RVE, particles with length L, thickness t, and orientation angle θ, are randomly placed inside the rectangular boundary of the RVE, as long as no particle intercepting/overlapping occurs. Such a treatment of the particle orientation distribution is justified by a study of the clay orientation in nylon6/clay nanocomposite films conducted by Loo and Gleason (2004) through a combination of infrared (FTIR) trichroid and TEM image analysis, who found that the clay orientation in these nylon 6 nanocomposite films can be described by a Gaussian function having a standard deviation of 15°. However, this distribution is three dimensional — as illustrated in Fig. 5.11(c), the deviation of the particle normal directions lie in an axisymmetric "cone" centered about the axis perpendicular to the film surface — there are not only particles tilted about axis-3 (as assumed in the 2D simulations), but also those tilted about axis-1, which do not impair the enhancement in the composite stiffness or strength when loaded in the 1-direction. Therefore the 2D simulations tend to overestimate the effect of clay orientation distribution on the composite E_{11} or $\sigma_{y,11}$.

To study the effect of particle orientation distribution on the nanocomposite properties, we construct three RVEs possessing the same material and geometrical parameters (L = 100 nm, E_m = 3 GPa, $\sigma_{y,m}$ = 70 MPa) except the degree of orientation distribution: one has perfect particle alignment, the other two have orientation distributions with SDVs of

14^{o} (relatively well aligned) and 32^{o} (nearly random), each. The tensile stress-strain curves of these three cases are depicted in Fig. 5.12(a) together with the 3D and 2D-plane-strain tensile behaviors of the matrix homo-polymer. Predicted results of the composite strength and modulus, normalized with respect to the corresponding plane strain property of the matrix ($E_m^* = 3.4$ GPa, $\sigma_{y,m}^* = 78$ MPa), are reported in Fig. 5.12(b) according to the clay content. Contours of the plastic strain rate right after yielding (at about 4% macroscopic strain) are shown in Fig. 5.12(d).

The influence of particle orientation distribution on the composite modulus and initial yield strength is well demonstrated in Fig. 5.12(c), where E/E_m^* and $\sigma_y/\sigma_{y,m}^*$ are plotted as functions of the SVD of the orientation distribution. Using the properties of composites filled with perfectly aligned particles as reference, we can see that the reduction in E and σ_y caused by particle misalignment is almost negligible with SDV of ~ 14^{o}; it is only when the orientation distribution widens and approaches randomness (SDV of 32^{o}) that the efficiency of reinforcement becomes considerably impaired. Therefore the model with perfect particle alignment bears rather high tolerance to the disturbance of particle misalignment. Such sensitivity to mis-orientation is assumed to apply to 3D cases as well.

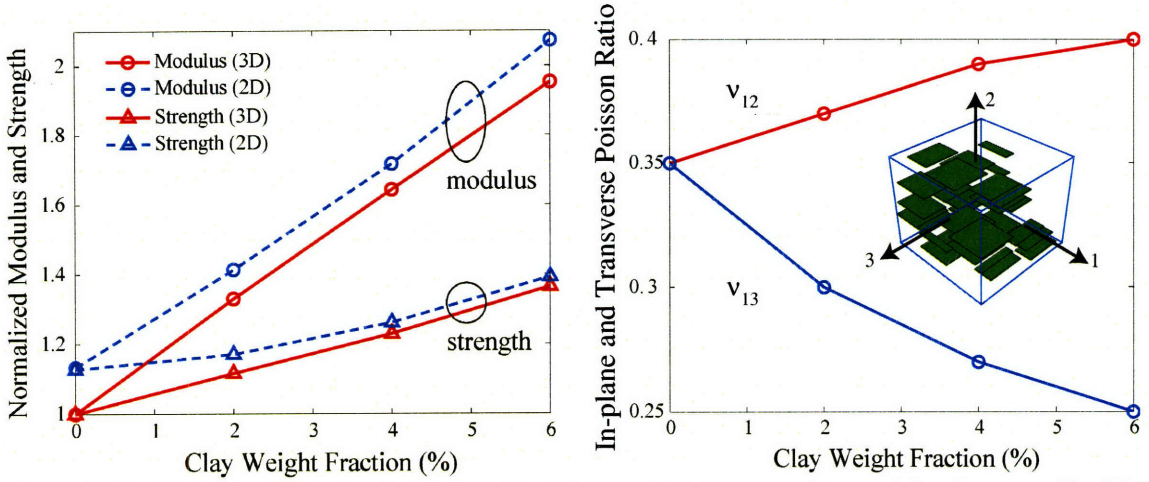

Figure 5.10: (a) 2D and 3D simulation results. The predicted composite modulus is normalized by matrix modulus of 3.0 GPa, the predicted composite strength normalized by matrix strength of 70 MPa. (b) In-plane (ν_{13}) and transverse (ν_{12}) Poisson ratios. It should be noted that the 2D results here are normalized by E_m and $\sigma_{y,m}$, while results in Fig. 5.12(b) are normalized by the plane-strain equivalents E_m^* and $\sigma_{y,m}^*$.

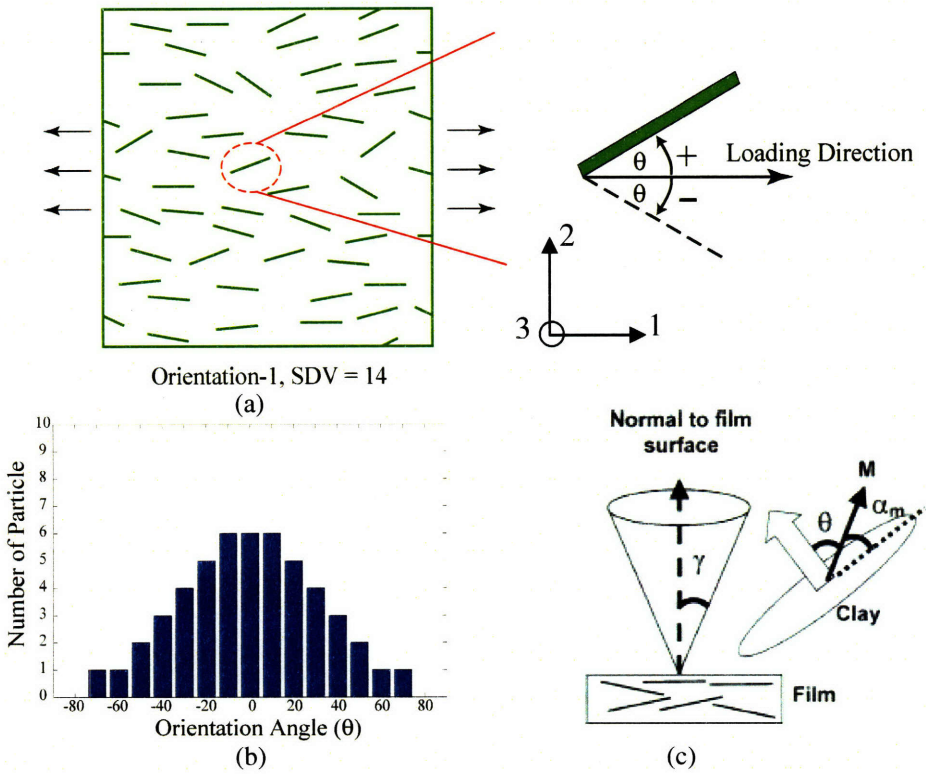

Figure 5.11: (a) Definition of the particle orientation angle and sign convention in 2D RVE. (b) Histogram of the particle orientation angle (total number of particles in the 2D RVE = 50). (c) Schematic of the 3D orientation distribution of the clay platelets in a nylon6/clay nanocomposite flim, where the deviation of the normal directions lies within an axisymmetric cone centered about the axis perpendicular to the film surface (Loo and Gleason, 2004).

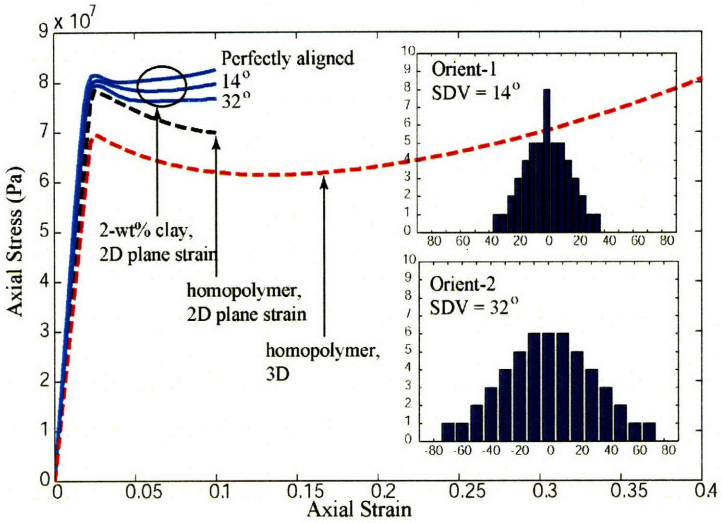

(a)

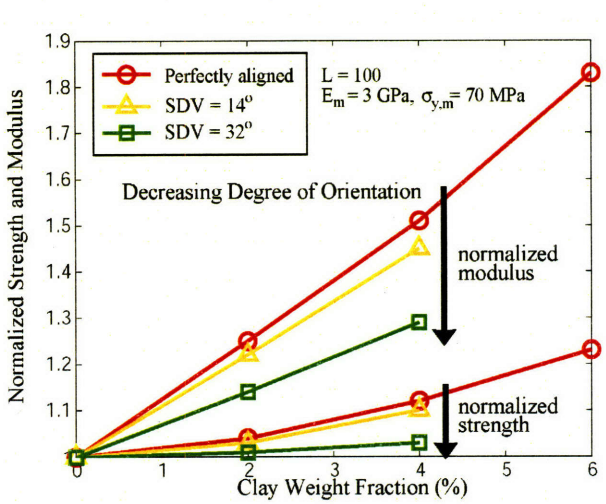

(b)

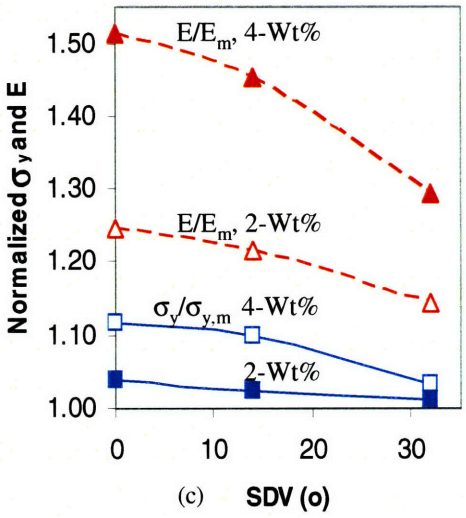

(c)

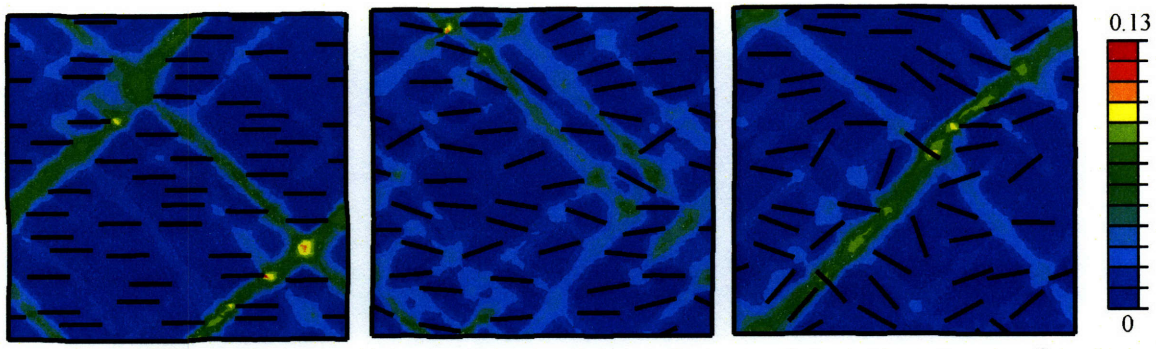

(d)

Figure 5.12: Effect of clay orientation on the composite tensile modulus and strength. (a) Tensile curves of the homo-polymer and nanocomposites with various degrees of orientation distribution characherized by the SDV of the orientation angle. (b) Model predicted composite modulus and strength, normalized by the plane-strain modulus and strength of the matrix homo-polymer, respectively. (c) Normalized E and σ_y plotted as functions of the SDV of the particle orientation distribution. (d) Contours of the plastic strain rate at about 4% macroscopic strain.

5.3. Effect of Clay Morphology: Exfoliation vs. Intercalation

The effect of clay *exfoliation* vs. *intercalation* on the composite yield strength is studied for two types of matrices: (a) thermoplastic polymer, with E_m = 3.0 GPa, ν_m = 0.35, $\sigma_{y,m}$ = 70 MPa and (b) low yield strength polymer, with E_m = 0.5 MPa, ν_m = 0.45, $\sigma_{y,m}$ = 24 MPa. For each matrix polymer, at a fixed clay content of 6-wt%, we calculate the axial composite initial yield strength corresponding to N = 1 (exfoliated) and N = 2, 3 (intercalated) by stretching 3D RVEs filled with well-aligned particles slightly beyond initial yielding, as illustrated in Fig. 5.2. The in-plane dimension of the clay platelets is fixed to be 100 nm, and the inter-layer spacing $d_{(001)}$ is taken to be 4 nm.

- **Effect of N on "Particle" Properties**

The homogenization of the multi-layer intercalated clay into an anisotropic homogeneous "effective particle", as elaborated in Chapter 2, is again employed here. We model the "effective particle' to be elastic, since the "particle" undergoes much smaller deformation compared to the macroscopic strain (the macroscopic axial strain is less than 10%), due to the strain shielding effect of the stiff silicate platelets.

The effects of N on the overall geometric and elastic properties of the "effective particle" (L/t, f_p/W_c, $E_{p,ii}$, $G_{p,ij}$, $\nu_{p,ij}$) are listed in Table 5.2, for the thermoplastic polymer matrix and for the low-yield strength polymer matrix, respectively. As shown earlier when examining the effect of clay morphology on the composite elastic properties in Section 3.3.1, the exfoliated clay particle (N = 1) possesses extremely high stiffness and aspect ratio, but rather low volume fraction for a given weight fraction, compared to intercalated clay ($N \geq 2$); in addition, the intercalated clay exhibits a high degree of anisotropy. The impact exhibited by the clay morphological features (e.g., N, $d_{(001)}$) on the overall

composite properties is, indeed, a comprehensive result of interplays among these intermediate "particle"-level parameters.

- **Effect of *N* on Composite Axial Yield Strength and Modulus**

Fig 5.13a and b depict the effect of *N* on the normalized composite axial yield strength and modulus, respectively; the results are calculated from 3D FE simulations for two types of polymer matrices.

Modulus As discussed in Section 3.3.1.1, despite the extremely high stiffness and aspect ratio of exfoliated single layer silicate, there is no abrupt jump in the composite axial modulus when the morphology transits from intercalation (N = 2) to exfoliation (N = 1), due to the counteracting effect of low particle volume fraction of the exfoliated clay at a given weight fraction. Recall that the load carrying clay particles are the primary source for composite stiffness enhancement; large particle/matrix stiffness ratio, large particle aspect ratio, and high volume fraction/weight fraction ratio act as crucial contributors to a highly efficient stiffness reinforcement.

Yield Strength Unlike for the composite modulus, the impact of clay exfoliation on composite $\sigma_{y,11}$ is rather significant: when *N* decreases from 2 → 1 (i.e., from intercalation → exfoliation), the composite $\sigma_{y,11}$ experiences a steep jump for both types of matrices; whether the intercalated structure contains 2 or 3 layers of silicate sheets makes little difference. Such advantage of the exfoliated clay over intercalated in reinforcing the composite axial yield strength can be mainly attributed to increased volume of elastic "constrained regions" in the matrix associated with exfoliation (and corresponding decrease in volume of matrix available for shear band percolation). As introduced earlier in Section 5.1.2.1, the stiff particles constrain surrounding matrix from

in-plane straining, resulting in the formation of cone-shaped[4] low-strain zones on either side of the particle. Matrix material within these "constrained regions" remains elastic and thus the creation of percolated sets of shear bands requires a more tortuous path in order to find material that can plastically deform.

In addition to the load-carrying particles, the constrained regions play an important role in the enhancement of the composite yield strength (more important than for the stiffness enhancement). When N goes from $2 \rightarrow 1$, although the particle volume fraction is much reduced (for 6-wt% clay, $f_p = 0.015$ when $N = 1$; $f_p = 0.059$ when $N = 2$), the volume of the elastic constrained regions is considerably increased, as illustrated by the schematics shown in Fig 5.15, acting to provide additional enhancement to the composite yield strength. Comparison of the contours of the equivalent plastic strain in Fig. 5.14 shows that the plastic deformation pathway developed in the exfoliated composite (Fig. 5.14a) is more tortuous than that in the intercalated (Fig. 5.14b).

This gives rise to another important parameter (in addition to the f_p or W_c) — the "particle" number density, ρ_p, defined as the number of "effective particles" within a unit volume. For the same (L, E_m, σ_m), while f_p is crucial in determining the overall composite modulus, the composite yield behavior is more or less dictated by the value of ρ_p, which directly impacts the volume fraction of the *particle-shielded regions* in a composite and thus the *degree of tortuosity* of the percolating deformation pathway. Additionally, unlike for the composite modulus, which relies comprehensively on f_p, as well as L/t and E_p/E_m (see previous discussion on the effect of N on the composite modulus), the composite yield strength depends less on the particle elastic property E_p, since the amount of axial

[4] This is assuming the particle to have a round planar shape. If instead, the particle adopts polygon planar shape, the constrained regions should be more like pyramids.

load carried by the particle ceases increasing once the surrounding matrix has yielded, as evidenced by Fig. 5.6(d). In fact, for a given W_c, the value of ρ_p for the intercalated morphology with $N = 2$ is only one-half of that for the exfoliated morphology, resulting in the severe drop in the composite yield strength when N increases from 1 ($\sigma_{y,11}/\sigma_m$ = 1.36 for the thermoplastic matrix in Fig. 5.13a) to 2 ($\sigma_{y,11}/\sigma_m = 1.18$).

To further elucidate the important role of ρ_p in the composite yield behavior, let's now consider two cases: (a) a composite with clay weight fraction $W_c = 6\%$, and a two-layer intercalated structure ($N = 2$, L = 100 nm), and (b) a composite with exfoliated morphology ($N = 1$, L = 100 nm), but only with a clay fraction half as much as in case (a), $W_c = 3\%$; matrix properties are the same for both cases, $E_m = 3$ GPa, $\sigma_{y,m} = 70$ MPa. According to Fig. 5.14, composite-(a) and composite-(b) bear the same ρ_p of "particles" with identical L (L = 100 nm), and consequently, the same volume fraction of the "shielded" matrix regions, neglecting possible overlapping. Presumably, the axial yield strengths of composite (a) and (b) should be close, if not identical. Fig. 5.16 depicts the uniaxial tensile curves of composite (a) and (b), together with that of 6-Wt%, exfoliated composite as reference. Indeed, the macroscopic yield behaviors of these two systems under investigation are nearly identical (in fact, the contours of the equivalent plastic strain shown in Fig. 5.14b and c reveal approximately the same shear band density for the two cases), which verifies our theory regarding the influence of the matrix shielding on the composite yield behavior, as well as the governing role of the parameter ρ_p in the enhancement of the composite yield strength for fixed particle dimension, L, and matrix properties, provided that alteration of the matrix morphology is not a governing factor.

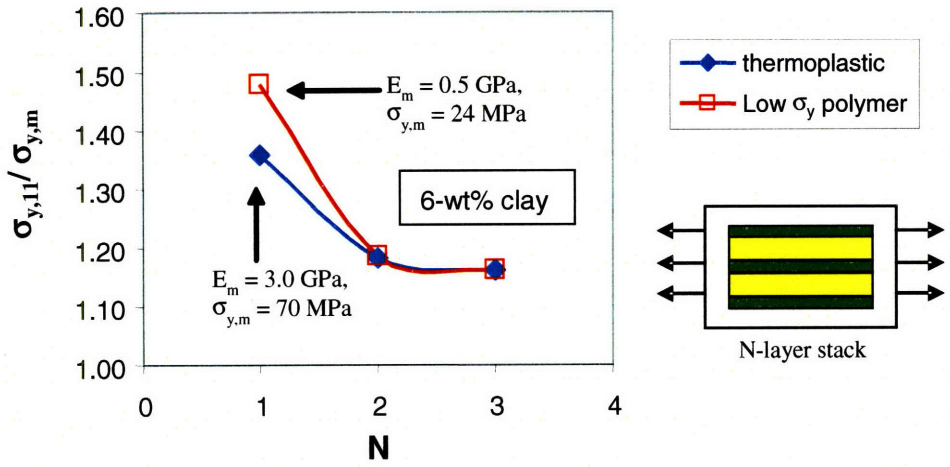

(a)

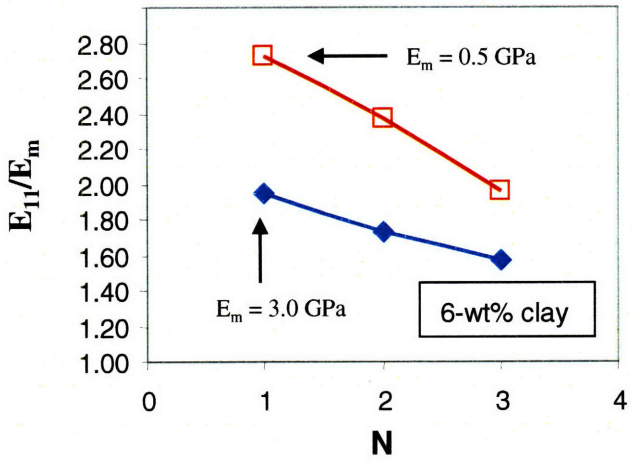

(b)

Figure 5.13: Effect of N on (a) composite axial yield strength $\sigma_{y,11}$ and (b) composite axial modulus E_{11} (6-wt% clay). Matrix properties: thermoplastic E_m = 3.0 GPa, $\sigma_{y,m}$ = 70 MPa; low-yield-strength polymer E_m = 0.5 GPa, $\sigma_{y,m}$ = 24 MPa. Particle properties: L = 100 nm, $d_{(001)}$ = 4.1 nm.

Table 5.2 Overall properties of the "effective particle", using L = 100 nm, $d_{(001)}$ = 4.1 nm, $d_{silicate}$ = 0.678 nm, and $E_{silicate}$ = 370 GPa

N	L/t	f_p/W_c	$E_{p,11}$ (GPa)	$E_{p,22}$ (GPa)	$\nu_{p,12}$	$\nu_{p,13}$	$G_{p,12}$ (GPa)	$G_{p,13}$ (GPa)
a. *thermoplastic* $E_{gallery,ii} = E_m$ = 3.0 GPa, $\nu_{gallery,ij} = \nu_m$ = 0.35, $G_{gallery,ij} = G_m/10$								
1	148	0.25	370	370	0.20	0.20	154	154
2	21	0.98	105	6.64	0.31	0.20	0.155	44
3	11	1.21	85	6.18	0.32	0.20	0.144	35
b. *low-yield-strength polymer* $E_{gallery,ii} = E_m$ = 0.5 GPa, $\nu_{gallery,ij} = \nu_m$ = 0.45, $G_{gallery,ij} = G_m/10$								
1	148	0.25	370	370	0.20	0.20	154	154
2	21	0.98	105	2.73	0.38	0.20	0.025	44
3	11	1.21	85	2.54	0.39	0.20	0.023	35

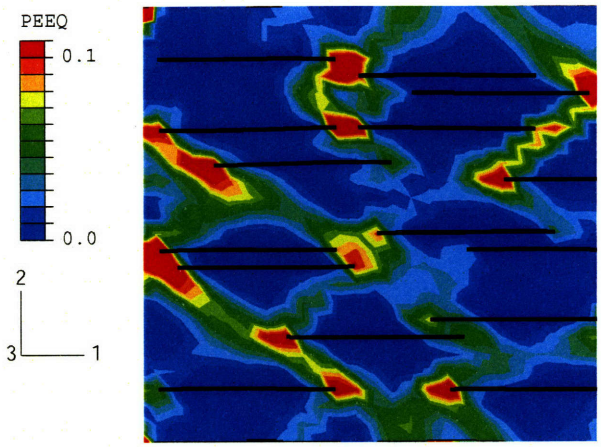

(a) 6-Wt%, N = 1

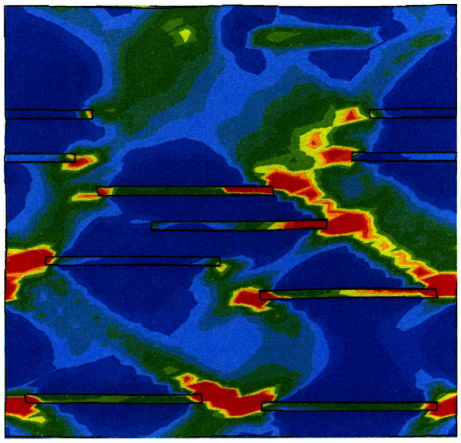

(b) 6-Wt%, N = 2

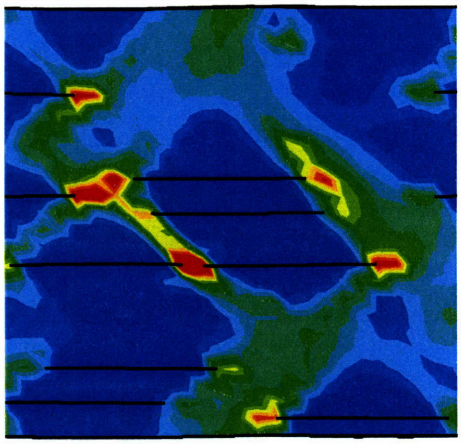

(c) 3-Wt%, N = 1

Figure 5.14: Contours of the equivalent plastic strain for nanocomposites at macroscopic axial strain in the 1-direction, $\varepsilon_{11} \sim 0.365$ (cross-section views from 3D FE-based simulations); particle in-plane dimension L = 100 nm; matrix properties E_m = 3 GPa, $\sigma_{y,m}$ = 70 MPa. (a) 6-wt% exfoliated clay, N = 1; dark lines mark the exfoliated particles with t = 0.678 nm. (b) 6-wt% intercalated clay, N = 2; rectangular boxes mark the "effective particles" with t = 4.8 nm. (c) 3-wt% exfoliated clay, N = 1. See Fig. 5.12 for composite elastic and yield properties and Table 5.2 for particle properties. Corresponding macroscopic stress-strain curves are plotted in Fig. 5.16.

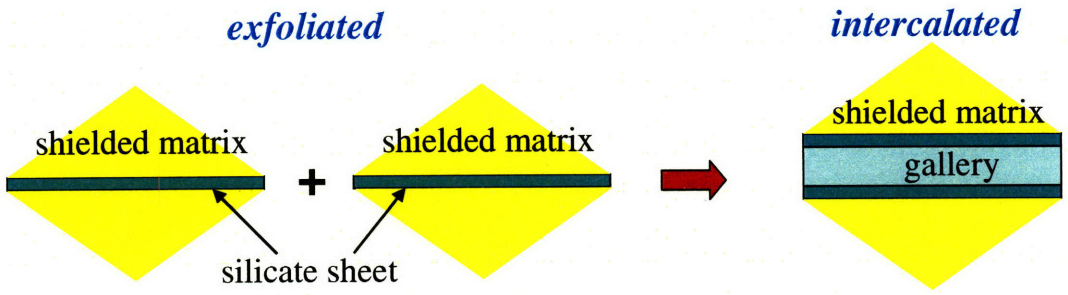

Figure 5.15: Schematics of the effect of clay morphology (exfoliation vs. intercalation) on the volume of shielded matrix regions by the clay platelet.

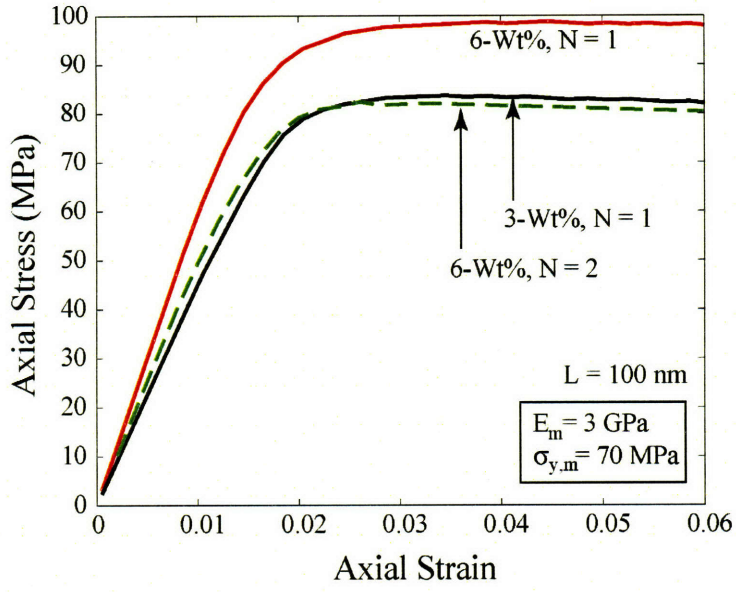

Figure 5.16: Uniaxial tensile behaviors of 3 and 6-Wt% exfoliated composites (N = 1) and 6-Wt% intercalated composite (N = 2). Fixed particle in-plane dimension L = 100 nm. Matrix properties E_m = 3 GPa, $\sigma_{y,m}$ = 70 MPa. View contours of the equivalent plastic strain at macroscopic axial strain of ~ 0.365 in Fig. 5.14.

5.4. Anisotropic Yield Surface of the Composite

Hill (1947) developed an anisotropic yield criterion for metals of orthotropic symmetry and defined so-called Hill ratios (R_{ij}) as descriptors for yield anisotropy. In a local frame aligned with the principal axes of anisotropy, the Hill yield surface can be written as:

$$\left[F(T_{22}-T_{33})^2+G(T_{33}-T_{11})^2+H(T_{11}-T_{22})^2+2LT_{23}^2+2MT_{31}^2+2NT_{12}^2\right]^{1/2}-\sigma_{BY}=0, \quad (5.4)$$

where F, G, H, L, M, N are constants calculated from Hill ratios:

$$F=\frac{1}{2}\left(\frac{1}{R_{22}^2}+\frac{1}{R_{33}^2}-\frac{1}{R_{11}^2}\right),\quad G=\frac{1}{2}\left(\frac{1}{R_{33}^2}+\frac{1}{R_{11}^2}-\frac{1}{R_{22}^2}\right),\quad H=\frac{1}{2}\left(\frac{1}{R_{11}^2}+\frac{1}{R_{22}^2}-\frac{1}{R_{33}^2}\right),$$
$$L=\frac{3}{2R_{23}^2},\quad M=\frac{3}{2R_{13}^2},\quad N=\frac{3}{2R_{12}^2}. \quad (5.5)$$

The Hill ratios are constants characteristic of the state of anisotropy. Specifically, R_{ii} (i = 1,2,3) is the ratio of the tensile yield strength of the textured material in direction-i to the reference tensile yield strength, σ_{BY}, here taken to be that of the bulk isotropic material; similarly, R_{ij} ($i \neq j$) is the ratio of the ij-shear yield strength to the corresponding yield strength of reference-isotropic material, τ_{BY} ($\tau_{BY}=\sigma_{BY}/\sqrt{3}$).

Here we can determine the anisotropic yielding behavior of the composite by stretching and shearing the RVE in all three orthogonal directions, as illustrated in Fig 5.17, and calculate the "Hill ratios" of the composite:

$$R_{ii}=\frac{\sigma_{y,ii}}{\sigma_{y,m}},\ i=1,\ 2,\ 3;\quad R_{ij}=\frac{\tau_{y,ij}}{\tau_{y,m}},\ i\neq j \quad (5.6)$$

We focus on nanocomposites filled with well-aligned, exfoliated clay, since for a given clay fraction they not only possess the highest reinforcing efficiency but also exhibit the highest degree of anisotropy. There are only 4 independent Hill ratios due to transverse isotropy: $\sigma_{y,11}=\sigma_{y,33}$, $\tau_{y,12}=\tau_{y,23}$. Table 5.3 summarizes the Hill ratios of composites with

6-Wt% exfoliated clay for two types of matrices: (a) thermoplastic polymer, with E_m = 3.0 GPa, ν_m = 0.35, $\sigma_{y,m}$ = 70 MPa and (b) low-yield-strength polymer, with E_m = 0.5 MPa, ν_m = 0.45, $\sigma_{y,m}$ = 24 MPa.

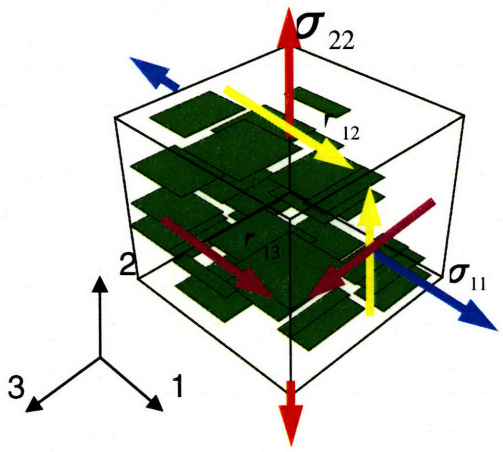

Figure 5.17: Stretching and shearing the RVE for the determination of the anisotropic yield surface of the composite.

Table 5.3: Anisotropic yield properties of composites filled with well aligned exfoliated clay (see Fig. 5.10 for the definition of orientations). L = 100 nm, W_c = 6%.

Matrix	$(\sigma_{y,11}= \sigma_{y,33})/ \sigma_{y,m}$	$\sigma_{y,22}/ \sigma_{y,m}$	$(\tau_{y,12}= \tau_{y,23})/ \tau_{y,m}$	$\tau_{y,13}/ \tau_{y,m}$
E_m = 3 GPa, $\sigma_{y,m}$ = 70 MPa	1.38	1.22	1.0	1.39
E_m = 0.5 GPa, $\sigma_{y,m}$ = 24 MPa	1.48	1.38	1.0	1.54

Recall the evaluation of the complete set of elastic constants of the composite carried out in Section 3.1.2, the axial modulus, E_{11}, and in-plane shear modulus, G_{13}, are well-reinforced by the clay particle (90% increase in E_{11} and 100% increase in G_{13} are achieved with 6-wt% exfoliated clay); the transverse modulus, E_{22}, is also slightly increased (20% increase with 6-wt% exfoliated clay) mainly due to the in-plane constraint effect of the clay platelets; whereas the transverse shear modulus, G_{12}, is not

affected by the addition of clay since the clay platelets, oriented with their planes normal to the 2-direction, essentially translate with the transverse matrix shear deformation. Similarly, for the anisotropic yield properties of the composite, the axial tensile yield strength, $\sigma_{y,11}$, and the in-plane shear yield strength, $\tau_{y,13}$, are well-enhanced due to the existence of the load-carrying and matrix-constraining clay particles, and also due to the strain-shielding (constraining) effect of these particles, as discussed in Section 5.1.2.1. The transverse shear yield strength, $\tau_{y,12}$, stays the same. The enhancement in $\sigma_{y,22}$ is less compared to the enhancement in $\sigma_{y,11}$; however, the gap between $\sigma_{y,22}$ and $\sigma_{y,11}$ is not as distinct as that between E_{22} and E_{11}, due to the stronger impact of particle in-plane constraint on the composite $\sigma_{y,22}$ than on the composite E_{22}. Figure 5.18(c) and (d) show the contours of local σ_{22} and σ_{11} in the matrix of a composite with 6-wt% exfoliated clay under transverse macroscopic tensile strain of ~ 0.03 (slightly after macroscopic yield) in the 2-direction; the contours of the equivalent plastic strain at transverse macroscopic strain of ~ 0.03 and 0.04 are plotted in Fig. 5.18(e) and (f), respectively. The matrix material in the vicinity of the clay particles is subjected to tensile in-plane strain due to the constraint of the nearly rigid particles (Fig. 5.18d); as a result, σ_{22} in the constrained matrix regions can be well above the matrix yield strength (70 MPa), as shown in Fig. 5.18c. Actually, simple analysis of a material subjected to uniaxial strain condition ($\varepsilon_{11} = \varepsilon_{33} = 0, \varepsilon_{22} \neq 0$) yields modulus and yield strength[5] as

$$E^{**} = E \cdot \frac{1-\nu}{1-\nu-2\nu^2}, \tag{5.7}$$

$$\sigma_y{}^{**} = \sigma_y \cdot \frac{1-\nu}{1-2\nu}, \tag{5.8}$$

[5] according to the Mises yield criterion.

where '**' marks the uniaxial strain properties. Taking $\nu = 0.35$, we have $E^{**} = 1.6\ E$, and $\sigma_y^{**} = 2.2\ \sigma_y$; therefore the in-plane constraint effect of the particles has a greater impact on the composite transverse yield strength than on the transverse modulus.

Note that the compressive yielding behaviors of the composite do not differ from the tensile yielding behaviors[6] (in fact, the uniaxial tensile and compressive stress-strain curves remain identical well into the post-yield stage, loaded either in the 1-direction or the 2-direction, as shown in Fig. 5.19a and b) despite the suspicion that these thin clay platelets might undergo local buckling by the strain at which macroscopic yield is reached, when the composite is macroscopically compressed in the 1-direction or stretched in the 2-direction. The value of the stress levels required to create the percolating shear bands throughout the matrix is not sufficient to trigger buckling of the clay. As will be shown in Chapter 6, for the case of textured semi-crystalline matrix, whose axial yield strength can be much higher than that of the bulk polymer, the stress levels are greater and can trigger local instability events; additionally, the impacts of transverse tensile vs. compressive loading on the relative particle positioning (transverse tension → particles approaching each other in the in-plane direction; transverse compression → particles spreading the in-plane direction) can result in considerable difference in the development of plastic deformation pathways under each loading condition, which, acting upon the highly anisotropic yield properties of the textured matrix (high axial slip resistances and low transverse slip resistance), can lead to rather distinct composite tensile and compressive yield properties.

[6] It should be noted that here we have not accounted for any pressure-dependent yield of the matrix polymer, which would have a slightly higher compressive yield strength than tensile strength, and is a feature of most polymer materials.

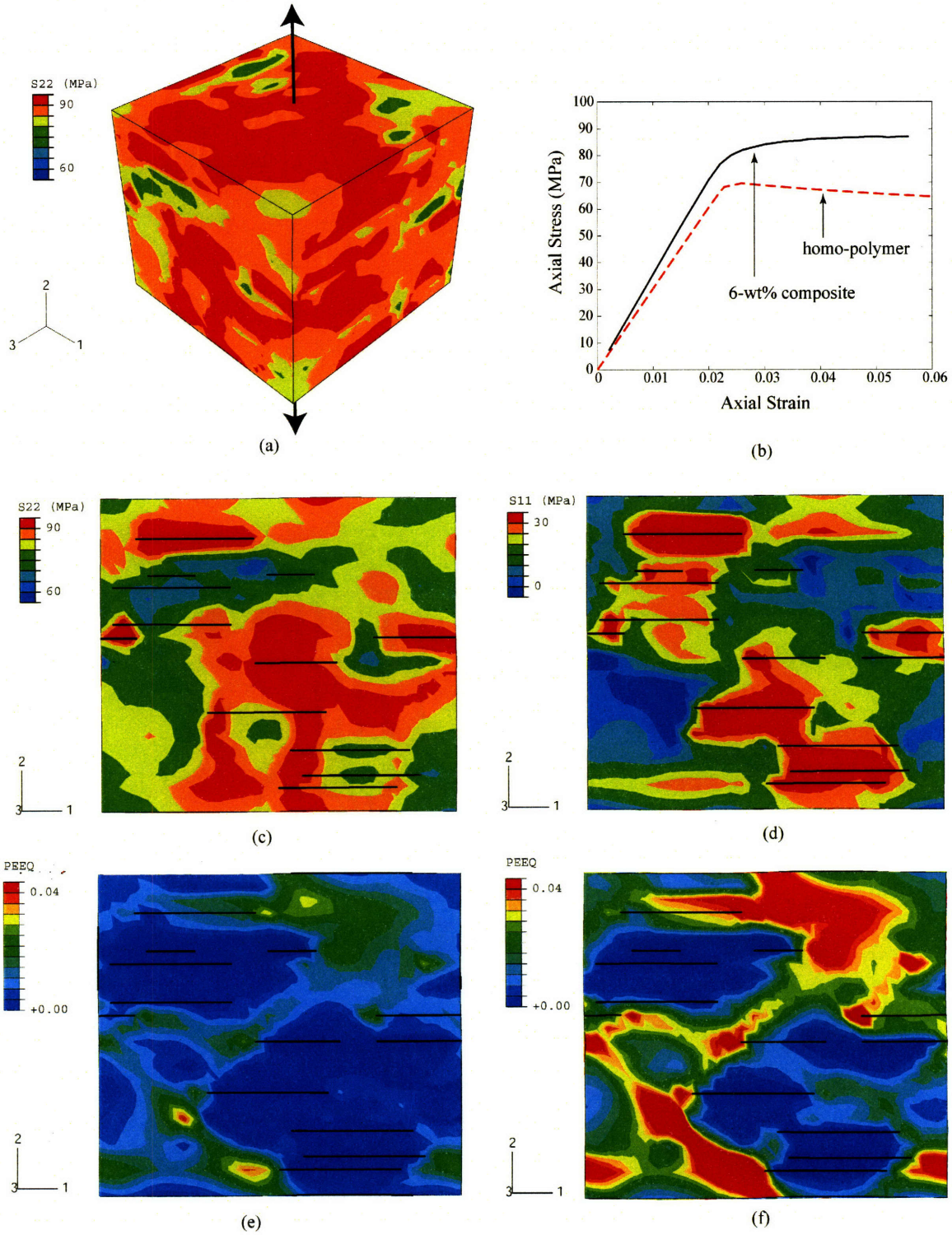

Figure 5.18: (a) 3D RVE of composite with 6-wt% clay under tensile load in the 2-direction (macroscopic ε_{22} ~ 0.03); (b) axial stress-strain curves of the composite and the homo-polymer; (c) contour of σ_{22} in the matrix, viewing perpendicular to the 1-2 plane (macroscopic ε_{22} ~ 0.03); (d) contour of σ_{11} in the matrix (macroscopic ε_{22} ~ 0.03). (e) contour of the equivalent plastic strain at macroscopic ε_{22} ~ 0.03; (f) contour of the equivalent plastic strain at macroscopic ε_{22} ~ 0.04.

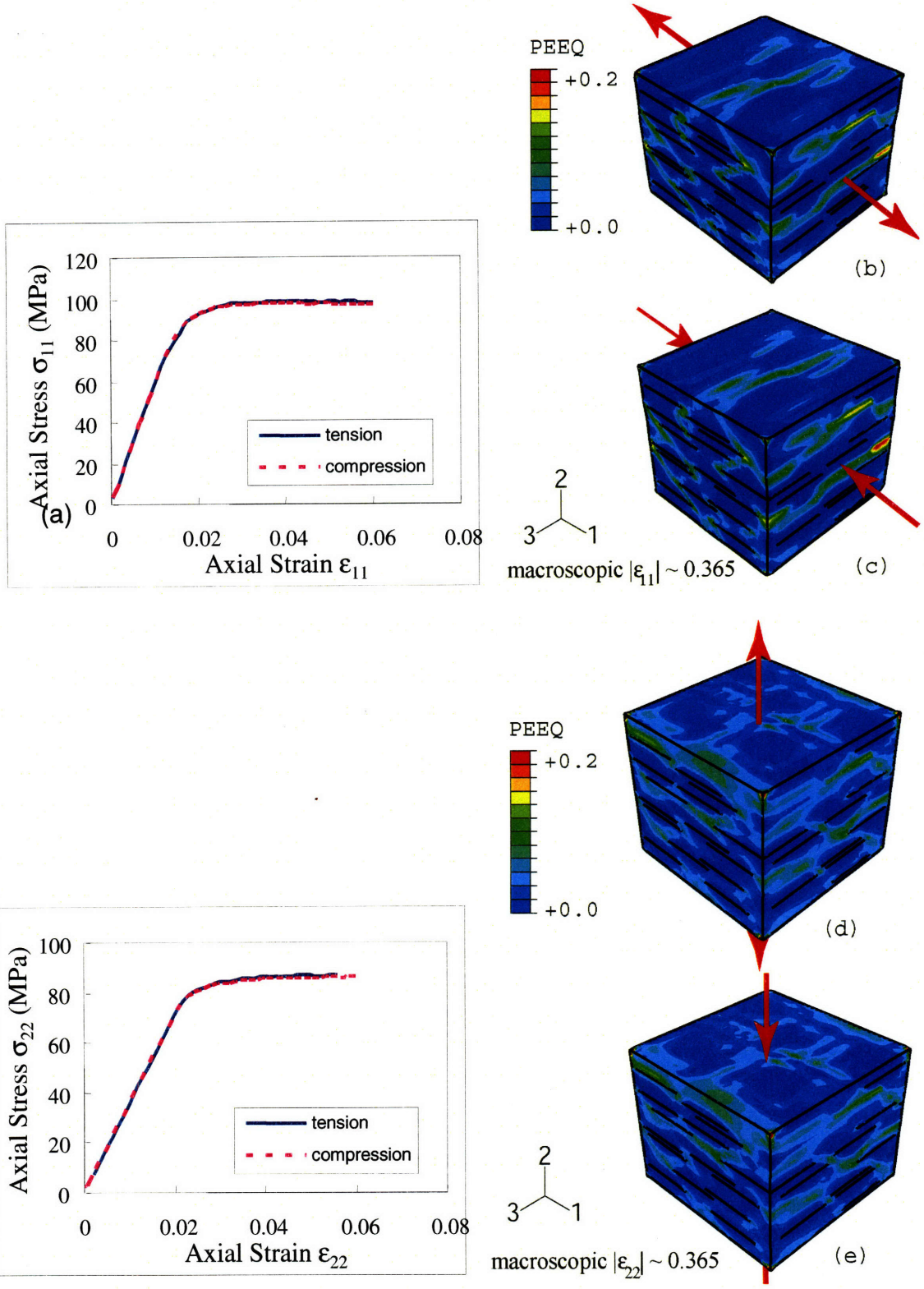

Figure 5.19: Uniaxial tension and compression stress-strain curves of 6-Wt%, exfoliated composites, loaded in (a) the 1-direction, and (d) the 2-direction. L = 100 nm, t = 0.678 nm. Em = 3 GPa, σm = 70 MPa. Particles planes normal to the 2-direction, as illustrated in Fig. 5.17. (b), (c) Contours of the equivalent plastic strain at macroscopic $|\varepsilon_{11}| \sim 0.365$. (d), (e) Contours of equivalent plastic strain at macroscopic $|\varepsilon_{22}| \sim 0.365$.

5.5. Comparison with Collected Experimental Data

For comparison purposes, experimental data of yield strength and modulus for nylon/clay nanocomposites reported in the literature by different authors are collected and depicted as functions of the clay weight fraction in Fig. 5.20 and Fig. 5.21, respectively (morphology and properties of the referred data are summarized in Table 5.4). Considering the fact that the composite property is really a comprehensive result of various material and morphological factors, we try to convey some of the crucial characteristics along with each data point ($\sigma_{y,11}$, W_c) or (E_{11}, W_c). Three key quantities that are normally provided by most authors[7] are chosen to classify the nanocomposites under investigation: the in-plane particle size (L), the degree of exfoliation, and the corresponding property of the matrix homo-polymer. In Fig. 5.20(a) and Fig. 5.21(a), each composite strength/modulus data point is tied to its homo-polymer property marked with a '*'; exfoliated (including partially exfoliated) morphology and intercalated morphology are marked by circles and triangles, respectively; the average particle length is distinguished by color spectrum; data points with unknown particle length are left as open circles/triangles. The composite strength and modulus values are then normalized with respect to the matrix property and plotted in Fig. 5.20(b) and Fig. 5.21(b), respectively.

Observations:

- In general, given similar material parameters (W_c, E_m, L), the modulus and strength property improvements exhibited by the fully or partially exfoliated nanocomposites

[7] The degree of orientation of the clay platelets is hard to quantify. In addition, in most cases where the composites are press-molded or injection molded, the clay platelets are preferably aligned in the flow direction.

are more significant than the intercalated ones. The advantage of clay exfoliation over intercalation is especially distinct when examining the composite strength.

- The plots (Fig. 5.20b and Fig. 5.21b) of normalized data show the strength data to be far more scattered than the modulus data. While the normalized composite moduli appear to increase monotonically with increasing clay content, there is no obvious correlation between the normalized composite strength and W_c. Quite the contrary, dramatic strength improvements tend to occur at lower clay contents (for instance, an increase of about 50% over the matrix polymer is achieved with as little as 2-wt% clay, reference point-6 in Fig. 5.21a and b).

Based on the above observations, we speculate that the respective mechanisms responsible for the increase in the nanocomposite modulus and strength can bear fundamental differences.

Simulation Results

3D RVEs with perfectly-aligned particles, as shown in Fig. 5.2(a), are subjected to uniaxial tension in the direction parallel to the particle planes. We idealize the critical micromechanical features which contribute to the highest reinforcing efficiency — perfect particle exfoliation, perfect particle alignment, and perfect matrix/particle interface bonding — yielding a composite structure whose tensile properties in the longitudinal direction (the direction parallel to the aligned particle planes) essentially become **upper-bounds** for nanocomposites.

Initial Matrix Property In order to make meaningful comparisons between the model predictions and experimental data, one needs to recognize the importance of the parent matrix property, since the particle/matrix property ratio directly affects the

ultimate composite properties. Close observation of Fig. 5.20(a) and Fig. 5.21(a) reveals that the apparently dispersed matrix properties (marked with '*') are more or less scattered around three reference values: a high value (H), an intermediate value (I), and a low value (L). Specifically, for matrix strength, σ_{y,m_H} ~70 MPa, σ_{y,m_I} ~ 50 MPa, σ_{y,m_L} ~ 24 MPa; for matrix modulus, E_{m_H} ~ 2.75 GPa, E_{m_I} ~ 1.5 GPa, E_{m_L} ~ 0.5 GPa. These values are used as starting matrix properties in 3D simulations to generate property versus W_c curves shown as solid lines in Fig. 5.20(a) and Fig. 5.21(a).

Modulus Three sets of modulus-W_c curves predicted by 3D FE simulations using high, intermediate, and low matrix modulus (E_{m_H} = 2.75 GPa; E_{m_I} = 1.5 GPa; E_{m_L} = 0.5 GPa), respectively, are superposed with collected experimental data in Fig. 5.20a and b. Particle in-plane dimension is set to be 100 nm in all cases; additional simulation results using in-plane particle size L = 80 nm are plotted for E_{m_H} = 2.75 GPa in order to demonstrate the effect of particle aspect ratio. Overall, the FE-predicted composite moduli well bound the test data except for occasional violations. Although the effect of special matrix morphology is not taken into account here, the stiff clay alone proves capable of providing sufficient reinforcement to explain the enhanced composite modulus.

Strength Three sets of strength-W_c curves predicted by 3D FE-based micromechanical simulations using high, intermediate, and low matrix properties (E_{m_H} = 3 GPa, σ_{y,m_H} = 70 MPa; E_{m_I} = 1.5 GPa, σ_{y,m_I} = 50 MPa; E_{m_L} = 0.5 GPa, σ_{y,m_L} = 24 MPa), respectively, are superposed with collected experimental data in Fig. 5.21a and b. A particle length of 100 nm is applied in all cases. It is quite surprising to notice that these FE results, which are expected to serve as theoretical 'upper-bounds', in general under-predict the composite strength. For the few cases where they do serve as upper-

bounds, the clay morphology is intercalated instead of exfoliated; the discrepancy between predicted and measured data is especially substantial for nanocomposites with intermediate and low matrix properties. Such model-experiment discrepancy leads to an important conclusion: the exfoliated clay alone can not account for the dramatic improvement in the strength of the nanocomposites. The failure of nanoclay as the 'stiff filler' to account for experimental observation suggests that the nanoclay-induced special matrix morphology, which has not been taken into account here, plays a critical role in the strength enhancement mechanism.

In summary, comparison between a range of experimental data and FE-based micromechanical model predictions based on idealized models ignoring any induced matrix texture reveals that the stiff nanoclay alone is sufficient in accounting for reinforcing the modulus, but not in providing the strength of the nanocomposites. This further indicates that the essential mechanism for the strength enhancement of the semi-crystalline-polymer nanocomposites[8] lies in the existence of the special matrix material induced by the addition of the nanoclay, whose morphology as well as properties can vary dramatically from those of the bulk polymer, as will be discussed next in Chapter 6.

[8] Note that the data points plotted in Figure 5.20 and 5.21 are all for semi-crystalline (mostly, nylon 6) polymer/clay nanocomposites.

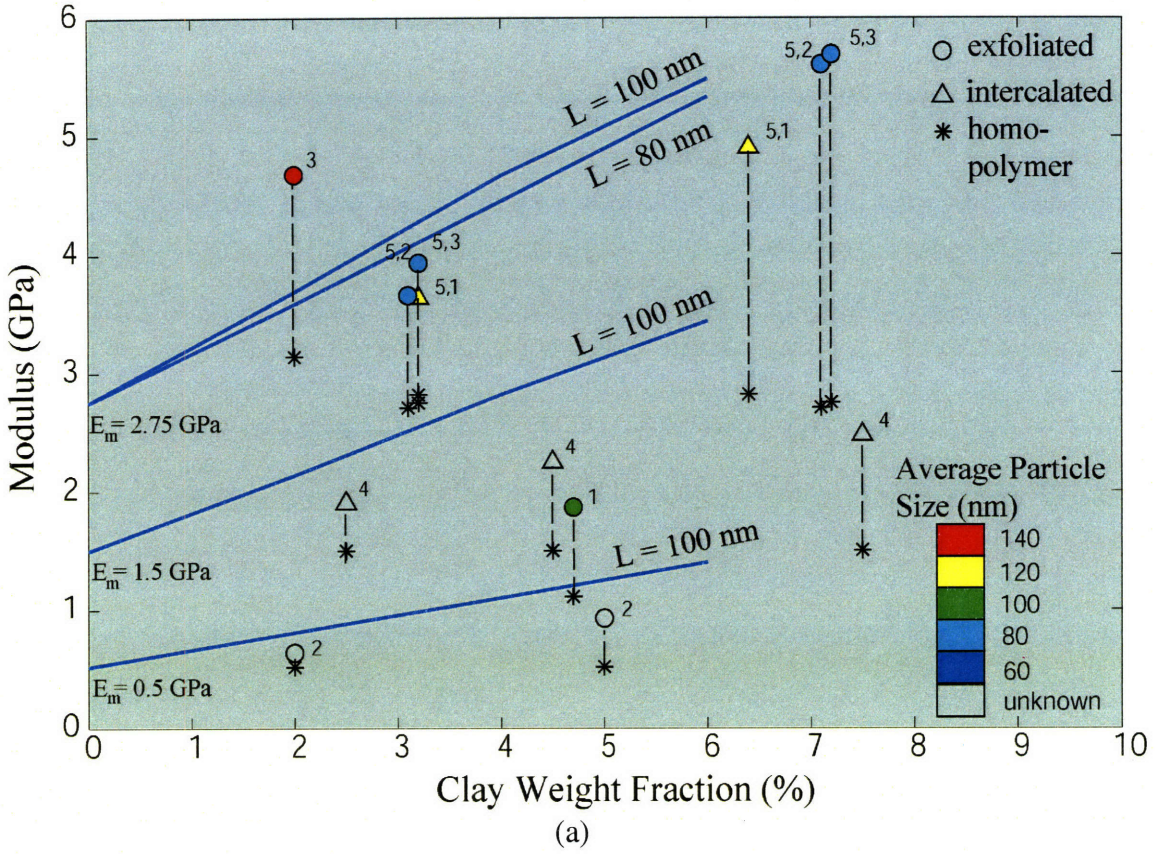

(a)

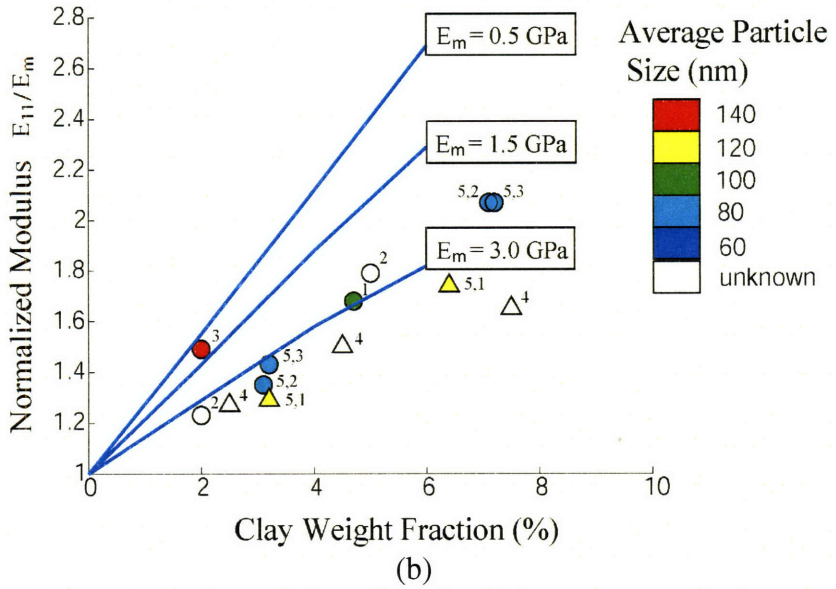

(b)

Figure 5.20: (a) Collected experimental data (for nylon 6/clay nanocomposites) superposed with 3D simulation results; each composite strength data point is tied to its homo-polymer strength marked with '*'; exfoliated (including partially exfoliated) and intercalated morphologies are marked with circles and triangles, respectively; average in-plane clay size is distinguished by color spectrum; data points with unknown particle length are left as open circles/triangles. (b) Normalized composite modulus (E_{11}/E_m).

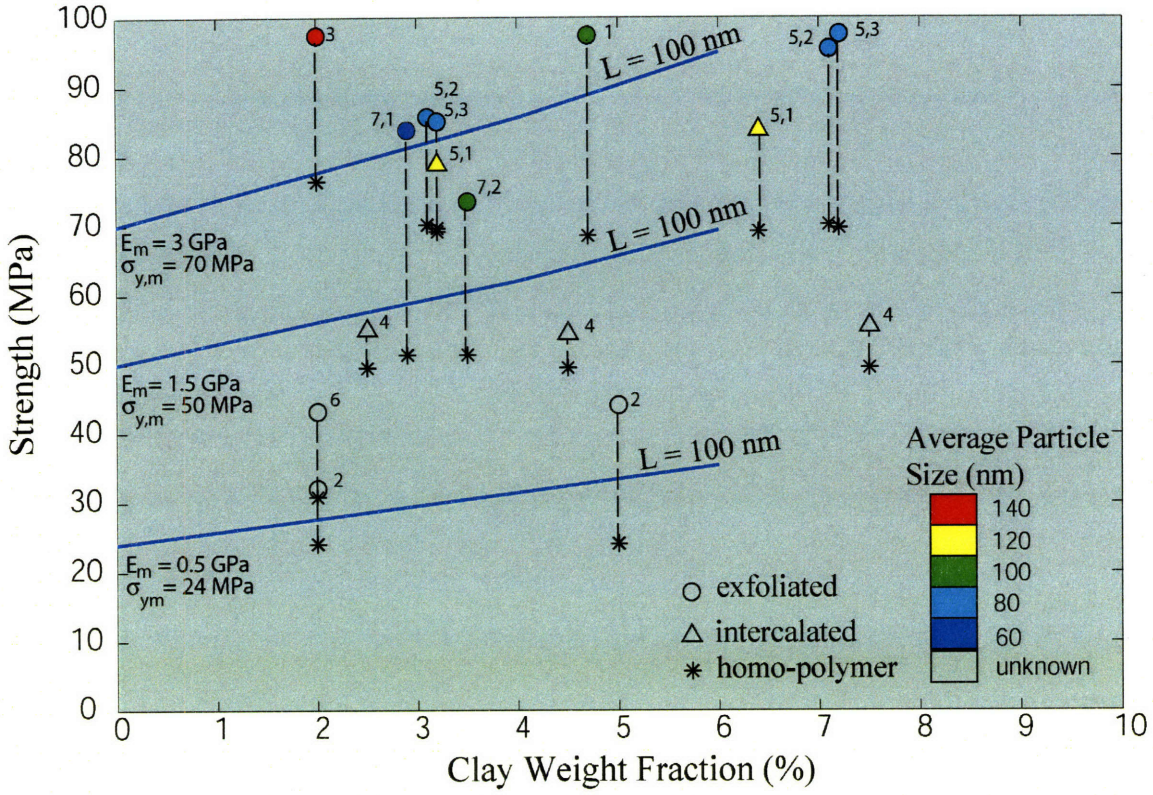

(a)

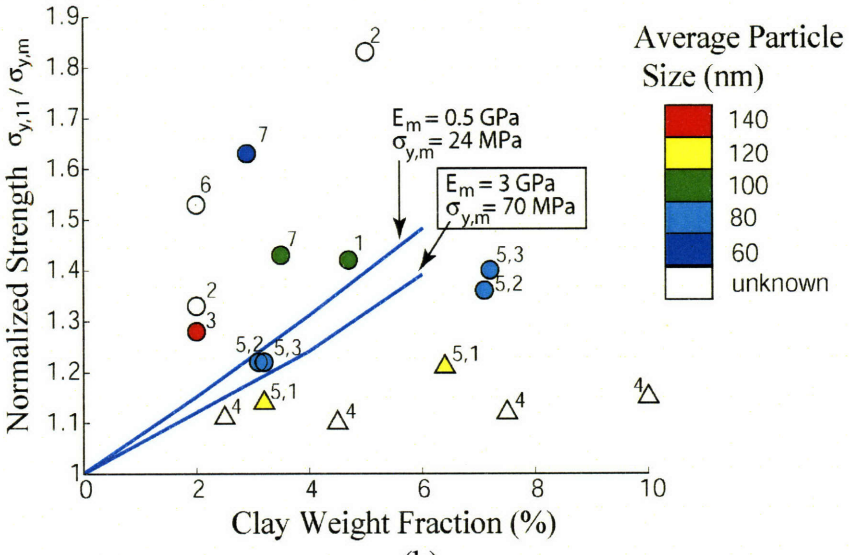

(b)

Figure 5.21: (a) Collected experimental data (for nylon 6/clay nanocomposites) superposed with 3D simulation results; each composite strength data point is tied to its homo-polymer strength marked with '*'; exfoliated (including partially exfoliated) and intercalated morphologies are marked with circles and triangles, respectively; average in-plane clay size is distinguished by color spectrum; data points with unknown particle length are left as open circles/triangles. (b) Normalized composite yield strength ($\sigma_{y,11}/\sigma_{y,m}$).

Table 5.4: Morphology and properties of referenced nylon 6/clay nanocomposites in Fig. 5.10 and Fig. 5.11

Ref		Wt %	Morphology	Mean Length L (nm)	Matrix (nylon 6)		Composite	
					E_m (GPa)	$\sigma_{y,m}$ (MPa)	E/E_m	$\sigma_y/\sigma_{y,m}$
1		4.7	exfoliated	100	1.11	68.6	1.68	1.42
2		2.0	partially exfoliated		0.518	24.1	1.23	1.33
		5.0					1.79	1.83
3		2.0	exfoliated	132	3.14	76.4	1.49	1.28
4		2.5	intercalated $d_{(001)}$ ~ 2.2 nm		1.50	49.5	1.27	1.11
		4.5					1.50	1.10
		7.5					1.65	1.12
5	1	3.2	intercalated N: 2.2 ~ 24	110 ~ 120	2.82	69.2	1.29	1.14
		6.4					1.74	1.21
	2	3.1	partially exfoliated	78 ~ 82	2.71	70.2	1.35	1.22
		7.1					2.07	1.36
	3	3.2	partially exfoliated	75 ~ 77	2.75	69.7	1.43	1.22
		7.2					2.07	1.40
6		2.0	exfoliated			30.86		1.53
7		2.9	exfoliated			51.4	*4.19*	1.63
		3.5					*5.0*	1.43

1. "Mechanical Properties of nylon 6-clay hybrid". Kojima, et al. J Mater Res Vol. 8, No. 5, 1993: 1185.
2. "Uniaxial Deformation of Nylon 6-Clay Nanocomposites by In-Situ Synchrotron X-Ray Measurements". Medellin-Rodriguez, et al. J Macromolecular Sci Part B Phys Vol. B42, No. 1, 2003: 201.
3. "Effects of clay orientation and aspect ratio on mechanical behavior of nylon-6 nanocomposite". Weon and Sue. Polymer 46, 2005: 6325.
4. "Morphology, thermal and mechanical behavior of polyamide 6/layered-silicate nanocomposites". Liu, et al. Composite science and technology 63, 2003:331.
5. "Nylon 6 nanocomposites: the effect of matrix molecular weight". Fornes, et al. Polymer 42, 2001: 9929.
6. "Synthesis, structure, thermal and mechanical properties of nanocomposites based on linear polymers and layered silicates modified by polymeric quaternary ammonium salts". Burmistr, et al. Polymer 46, 2005: 12226.
7. "Rheological and mechanical comparative study of in situ polymerized and melt-blended nylon 6 nanocomposites". Simon, et al. Polymer 46, 2005: 10405.

Note that these numberings are for the convenience of tracking the data plotted on Figures 5.20 and 5.21. Complete bibliography is provided at the end of the thesis.

Chapter 6

Impact of Matrix Transcrystallization on the Modulus and Yield Strength of Semi-crystalline Polymer/Clay Nanocomposites

The goal of this chapter is to assess the impact of the nanoclay-induced special matrix morphology on the tensile deformation behavior of the nanocomposites. A transversely isotropic morphology (and, accordingly, transversely isotropic elastic and yield properties) is assumed for the transcrystallized matrix material, as will be elaborated in Section 6.1. The modeling of the mechanical behavior (elastic-plastic) of the textured matrix material required idealizations and assumptions based on literature data for highly oriented semi-crystalline polymer together with models for textured materials; hence the FE-based micromechanical modeling results presented here are meant to serve as guidelines for the property enhancement that can be potentially achieved, provided that such pure and ideal matrix texture is produced by proper processing. First, the in-plane axial composite modulus and initial yield strength predicted by 3D FE simulations with the matrix modeled to be highly textured (hence highly anisotropic in both elastic and yield properties) are compared to collected experimental data, which have been previously introduced at the end of Chapter 5. Then the anisotropic elastic as well as yield properties of composites with textured matrix are determined and compared with

those of composites whose matrix morphology (and thus matrix properties) remain unchanged. Finally, influences of particle orientation distribution, as well as different loading directions with respect to the average particle orientation direction, on the composite end-properties are explored through 2D plane strain analyses.

6.1. Impact of Clay on the Morphology of Semi-crystalline Polymer

Over the past decade, the impact of nanoclay on the crystallization behavior of semi-crystalline matrices has been studied extensively. The addition of layered silicates has been observed to have profound influences on the matrix morphology, including special orientation of crystal lamellae with respect to the silicate surfaces (Kojima, et al., 1995; Kim, et al., 2001; Li and Shimizu, 2006; Weon, et al., 2005; see TEMs shown in Fig. 6.2), alteration of the crystal fraction (Kojima, et al. 1993; Nam, et al. 2001; Lincoln, et al., 2001), and alteration of chain mobility (Nam, et al., 2001). Kojima, et al. (1993) and many others found that nylon 6 crystallizes exclusively in the γ form in the nanocomposites because of the decreased chain mobility near the nanoclay surface (contrasting the predominant α-form in bulk nylon 6), but the total degree of crystallinity remains the same (typical degree of crystallinity ~ 30% for nylon 6); however, Weon, et al., (2005) also reported a ~ 10% reduction in the overall proportion of crystalline phase in nylon 6 with the addition of 2-wt % clay.

Although many investigations have demonstrated the influence of clay particles on the crystallization behavior of semi-crystalline polymers, the exact interactions between the nanoscopic arrangement of crystal lamellae (including orientation, crystal form, and overall degree of crystallization) and the distribution of the clay platelets are still not fully understood. Here we focus on the nanoclay-induced matrix transcrystallization behavior.

6.1.1. Orientation of Crystal Lamellae in the Presence of Nanoclay

The organically modified silicate surfaces are proposed to act as heterogeneous nucleation sites during polymer crystallization, similar to the well-known transcrystallization phenomenon observed in other particle-filled semi-crystalline polymer composites (e.g., Chacko, et al., 1982; Muratoglu, et al., 1995; Bartczak, et al., 1999).

The parallel arrangement of polymer chains ionically bound to the silicate surface has been suggested to favor the formation of the γ-form crystals, with the γ-(020) hydrogen-bonded planes oriented parallel to the silicate surface and the growth direction perpendicular (Lincoln and Vaia, 2004; Kojima, 1994). However, different chain (and hence lamellar) orientations have been reported as well. For example, Li and Shimisu (2006) observed a perpendicular arrangement of the chain-axis w.r.t. the silicate surface when the filler content is relatively high (8-Wt%); they attributed this phenomenon to confined crystallization in narrow nanoscale channels (less than 30 nm). In addition, Kojima, et al., (1995) discovered variation in the preferred orientation of clay and crystallites along the thickness direction of an injection-molded bar (3 mm-thick).

The orientations of both the silicate platelets and the crystal lamellae depend largely on the specific processing history. For instance, extensional flow in injection-molding and fiber extrusion and drawing may result in uniaxial alignment of macromolecular chains in the flow direction, leading to a parallel arrangement of stacked lamellae on the surfaces of the silicate, as illustrated in Fig. 6.1a; the shear flow during injection-molding tend to align the silicate plates parallel to each other and to the film surface, whereas fiber extrusion/drawing may give rise to a rather random lateral orientation of the silicate

plates, where each platelet remains parallel to the flow direction. In compression molded films, the macromolecular chains tend to be randomly oriented on the silicate surfaces; i.e., the lamellae grow perpendicular to the silicate platelets without any order in the lateral plane, as illustrated in Fig. 6.1b. As will be discussed later, the orientation of lamellae illustrated in Fig. 6.1a and b indicate, respectively, orthotropic and transversely isotropic matrix structure and properties.

Evidence of such processing – orientation correlations are well demonstrated via TEMs of *injection-molded* nylon-12/2-wt% clay nanocomposite by Kim, et al. (Fig. 6.2a) and *compression-molded* nylon-6/4-wt% clay nanocomposite by Li and Shimisu (Fig. 6.2b). Kim, et al., found the nylon-12 lamellae oriented perpendicular to the silicate surfaces; moreover, the lamellae appear to be laterally parallel to each other, indicating a uniaxial alignment of stacked lamellae as illustrated in Fig. 6.1a. A similar perpendicular orientation of nylon-6 lamellae with respect to silicate surfaces is observed by Li and Shimisu; however, they did not detect any preferred orientation of the polymer chains in the plane parallel to the silicate platelets from WAXD, suggesting a laterally random crystalline morphology as illustrated in Fig. 6.1b.

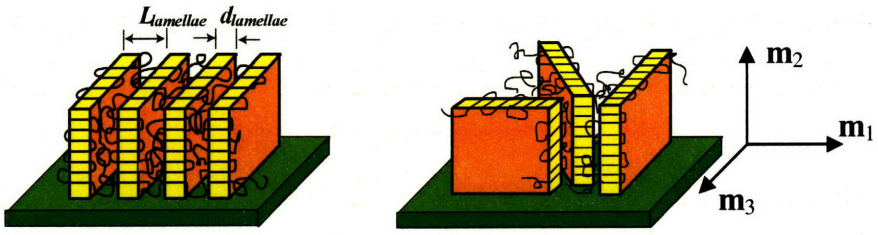

(a) Oriented fine lamellae orthotropic

(b) Transversely random lamellae transversely isotropic

Figure 6.1: Schematics of the orientation of the clay platelets and the crystal lamellae under different processing conditions: (a) clay aligned in the flow direction, orthotropic matrix; (b) clay planes parallel to the flow direction, transversely isotropic matrix.

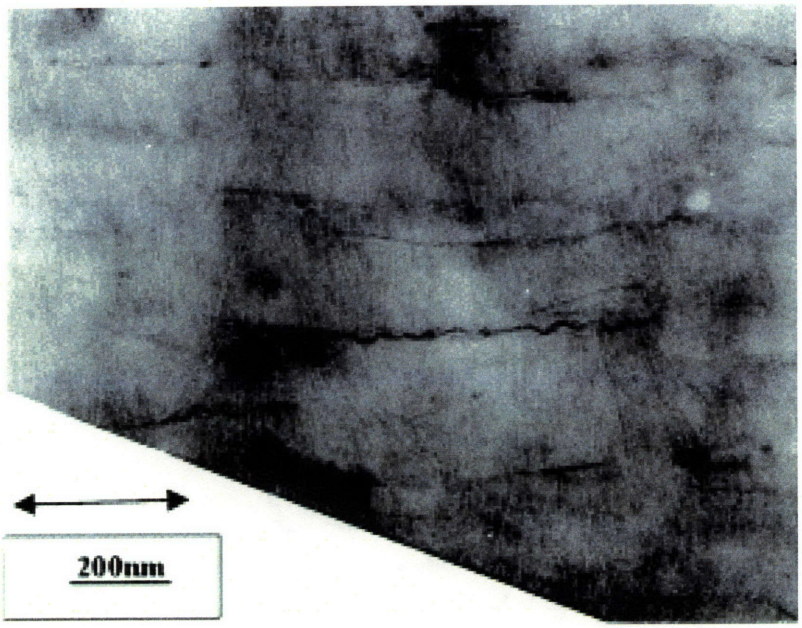

(a)

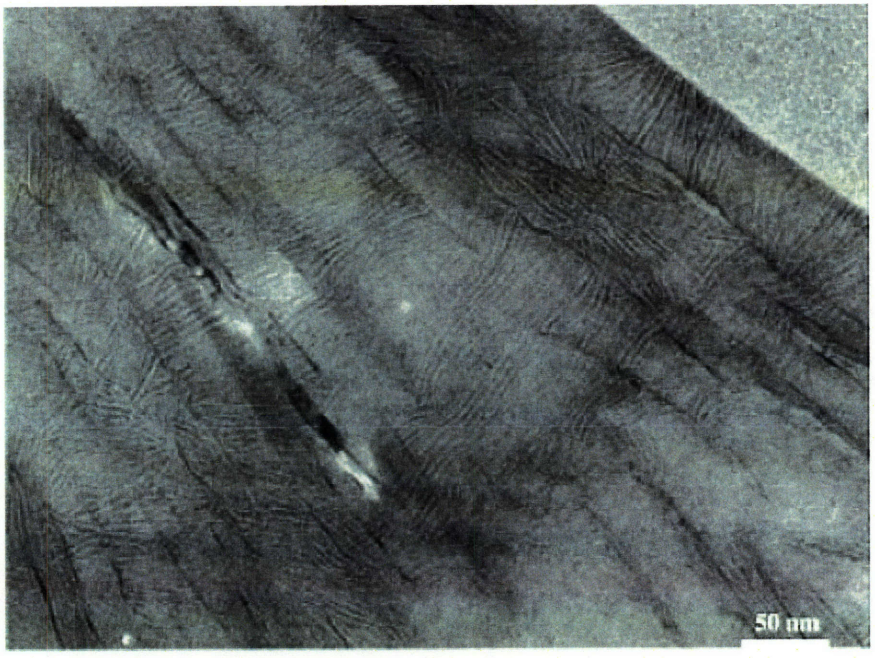

(b)

Figure 6.2: (a) 2-wt% exfoliated nylon-12/clay nanocomposite; polycondensation and injection-molded (Kim, et al, 2001). (b) 4-wt% exfoliated nylon-6/clay nanocomposite; melt-mixed and compression-molded (Li and Shimuzu, 2006).

6.2. Modeling of the nanoclay-induced special matrix morphology

Model Assumptions

Our primary goal is to investigate changes in the elastic and yield properties as well as the underlying miromechanical behavior of the nanocomposites ensuing alterations in the matrix morphology. Idealizations regarding the matrix morphology have to be made to enable probing of such a complicated subject through FE simulation. In this work, we focus on the transversely isotropic matrix morphology, as illustrated in Fig. 6.1b, with the lamellae growing perpendicular off the clay surface without any order in the lateral plane; the orthotropic matrix texture as depicted in Fig. 6.1a is not the primary concern here; however, its potential impact on the composite deformation behavior as compared with the transversely isotropic texture (e.g., higher degree of anisotropy) will be discussed in later text. Considering the fact that the inter-particle spacing is relatively small in comparison with the dimensions of the crystal lamellae in bulk, due to the high aspect ratio of the clay (the inter-layer spacing for a perfectly aligned and exfoliated system with $W_c = 2\%$ is calculated to be merely 100 nm, Sheng, et al., 2004), we assume the oriented material is percolated throughout the matrix. In addition, the matrix anisotropy is modeled as constant everywhere except for changes in the local orientation direction resulting from particle orientation distributions; i.e., possible dependence of the extent of matrix anisotropy on the inter-particle spacing is not taken into account in this work.

6.2.1. Anisotropic Elasticity and Yield Surface

While direct experimental characterization of the mechanical behavior of the crystalline phase in semi-crystalline polymer is prohibited by the small size of polymer crystals, an alternative approach is to produce highly-textured materials that macroscopically

resemble single crystals and test these "quasi-single" crystals instead. Lin and Argon (1992) developed such "quasi-single" crystal nylon-6 samples containing both α and γ crystal forms and used them to derive a complete set of elastic constants and slip system resistances. They established that the easiest slip process occurs along the hydrogen-bonded planes and in the direction of the chain, with a shear resistance of $g_0 = 16$ MPa; the shear strengths of the other two slip processes are about $1.5g_0$. The considerable difference in the slip system resistances makes the nylon-6 crystallites mechanically highly anisotropic. While such strong anisotropy is evened out by the random spherulitic texture in the bulk polymer, the anisotropic crystalline component plays a crucial role when a special order of the crystal lamellae is established (e.g., transcrystallization at heterogeneous interfaces often observed in particle-filled polymer composites, or orientation induced by large plastic deformation such as cold drawing).

Tzika, Boyce, and Parks (2000) used Lin and Argon's results as guidance in determining the elastic constants and anisotropic yield surface of transcrystallized nylon 6 induced by the inclusion of rubber particles; the transcrystalline matrix material was modeled as transversely isotropic with the plane of isotropy parallel to the polymer/particle interface. Here, we, too, model the oriented matrix with transverse isotropy, taking the crystal growth direction to be the axis of isotropy (direction $\mathbf{m}_2$ in Fig. 6.1b), and the hydrogen-bonded plane to be the plane of isotropy ($\mathbf{m}_1$-$\mathbf{m}_3$-spanned plane). We describe the anisotropy of the textured material in terms of the ratio between the property (both elastic constants and yield strength) of the textured material and that of the bulk polymer; these ratios are adopted directly from what Tzika, et al. (2000) derived for the transcrystallized nylon-6 near the surface of rubber particles. It should be noted that such treatment does

not take into account any change in the total degree of crystallinity or change in the ratio of crystal forms, as indicated by some experimental observations.

Elasticity

The "quasi-single" nylon-6 crystal, produced by large strain, plane strain compression (Lin and Argon, 1992), is a highly textured material, with the macromolecular chains aligned in the flow direction and the hydrogen-bonded planes oriented perpendicular to the loading direction. The coexistence of α and γ crystal forms in the bulk polymer results in a dual orientation of the $\{100\}$ planes with respect to the loading axis, and consequently, in orthotropic symmetry. Lin and Argon measured the complete nine elastic constants to fully describe the elastic behavior of the "quasi-single" crystal. Tzika, et al. (2000) used these results as a guide in determining the elastic properties of the transcrystallized nylon-6 near the surface of micron-sized rubber particles. The engineering elastic constants of transcrystallized nylon 6 used by Tzika, et al., normalized by the isotropic matrix modulus, E_m, are listed in Table 6.1. These ratios will be used in this work to model the elastic response of the transcrystallized polymer, based on the transversely isotropic model illustrated in Fig. 6.1b.

Note that the moduli of the transcrystallized material in the directions parallel to the hydrogen-bonded planes, E_{11} and E_{33}, were taken to be ~30% above E_m, but sufficiently lower than what Lin and Argon had found for the 'quasi-single' material in the direction of chain alignment to account for the random orientation of chains in the plane of isotropy. The in-plane Poisson ratio, ν_{13}, was taken to be the Poisson ratio of the bulk polymer since it characterizes the plane of transverse isotropy. Other elastic constants were directly taken from Lin and Argon.

Yield

Lin and Argon's study of the 'quasi-single' crystal (i.e., highly-oriented) of nylon 6 established that its plastic deformation is primarily derived from three crystallographic slip processes consisting of the (001)[010] and (100)[010] chain slip systems, and the (001)[100] transverse slip system. Moreover, they determined that the easiest slip process occurs along the hydrogen-bonded planes, in the direction of the chain. Here the plastic response of the oriented material is modeled in terms of the anisotropic yield criterion developed by Hill (1947), as introduced in Chapter 5. Particularly, the anisotropy of the yield behavior of the textured material is characterized by the so-called Hill ratios (R_{ij}), defined to be the ratio of the directional yield strength of the textured material to σ_y of the isotropic bulk material. The Hill yield criterion and physical interpretations for the Hill ratios can be found in Chapter 5, Section 5.4 (Eq. 5.4, 5.5), thus are not included here. Tzika, et al. numerically obtained a complete set of Hill ratios through the employment of the Constrained Hybrid (CH) model, initially proposed by Parks and Ahzi (1990) for polymer crystals of lower symmetry. The four independent ratios Tzika, et al., used to model the yield behavior of the transcrystallized nylon-6 with transverse isotropy are listed in Table 6.2. For detailed description of the CH procedure, refer to Tzika, et al., 2000 and Tzika, 1999.

Table 6.1: Elastic constants of transcrystalline nylon 6, normalized with E_m (Tzika, et al., 2000).

$(E_{11} = E_{33}) / E_m$	E_{22} / E_m	$\nu_{12} = \nu_{32}$	ν_{13}	$(G_{12} = G_{23}) / G_m$
1.29	0.99	0.53	0.33	0.30

Table 6.2: Hill ratios used for anisotropic yield (Tzika, et al., 2000)

$R_{11} = R_{33}$	R_{22}	$R_{12} = R_{23}$	R_{13}
1.6	3.0	0.5	1.0

6.2.2. Local Material Orientation

The constitutive description of the anisotropic matrix material requires a set of Cartesian basis vectors ($\mathbf{m}_1$, $\mathbf{m}_2$, $\mathbf{m}_3$ in Fig. 6.1b), locally aligned with the principal axes of anisotropy. As mentioned previously, the axis of transverse isotropy (base vector $\mathbf{m}_2$) coincides with the lamellar growth direction. Thus, the determination of the local orientation at any material point with respect to the global frame essentially becomes the task of identifying the underlying texture of the matrix, which is ultimately dictated by the orientation distribution of the nanoclay since the transcrystallized lamellae are assumed to grow perpendicular off the surface of the clay. When the clay platelets are aligned parallel to each other, the lamellae (hence the local base vector $\mathbf{m}_2$) is everywhere normal to the clay planes. Complication occurs in the presence of particle misalignment — presumably, the lamellae emanating perpendicularly from the surface of one particle rotate gradually away from its original trajectory to meet with lamellae emanating from the nearest neighbors without forming orientation kinks (the base vector changes direction accordingly); the spatial randomness of the particle distribution adds to the complexity, as different parts of the particle surface may be 'seeing' their own nearest neighbors, and consequently, possess trajectories of lamellar growth paths different from one another. Fig. 6.3 shows schematically the development of the lamellae initiating from one particle under the influence of its surrounding particles.

Inspired by the work of Tzika, et al., we, too, employ an assisting heat transfer analysis as an analogue for describing the local matrix orientation. The idea is to set up an appropriate heat transfer problem to generate isotherms inter-connecting particles which will mimic the lamellar growth path. This procedure is briefly outlined in the following

text. As illustrated in Fig. 6.4, the RVE is subjected to a macroscopic temperature gradient ∇T, the prescribed macroscopic heat flux coinciding with the preferred particle orientation direction (i.e., the average of the particle orientation distribution). The clay particles are modeled so that no heat flux is allowed across the particle surface, and therefore the isotherms emanate normally from the particle surfaces, just like the crystal lamellae. The heat flux vector, which is perpendicular to the isotherm, is then used to define the base vectors of the local orientation at the integration points of each element. The high resemblance borne by the isotherms to the trajectories of the crystal lamellae, as evidenced in Fig. 6.4, demonstrates our approach to be efficient and feasible.

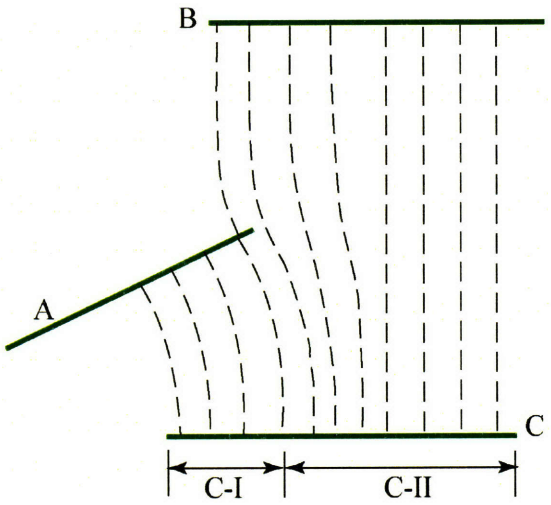

Figure 6.3: Schematic illustration of the influences of surrounding particles on the lamellae development from a particular particle: part-I and part-II of particle C see the influence of particles A and B, respectively. Dashed lines represent the lamellae.

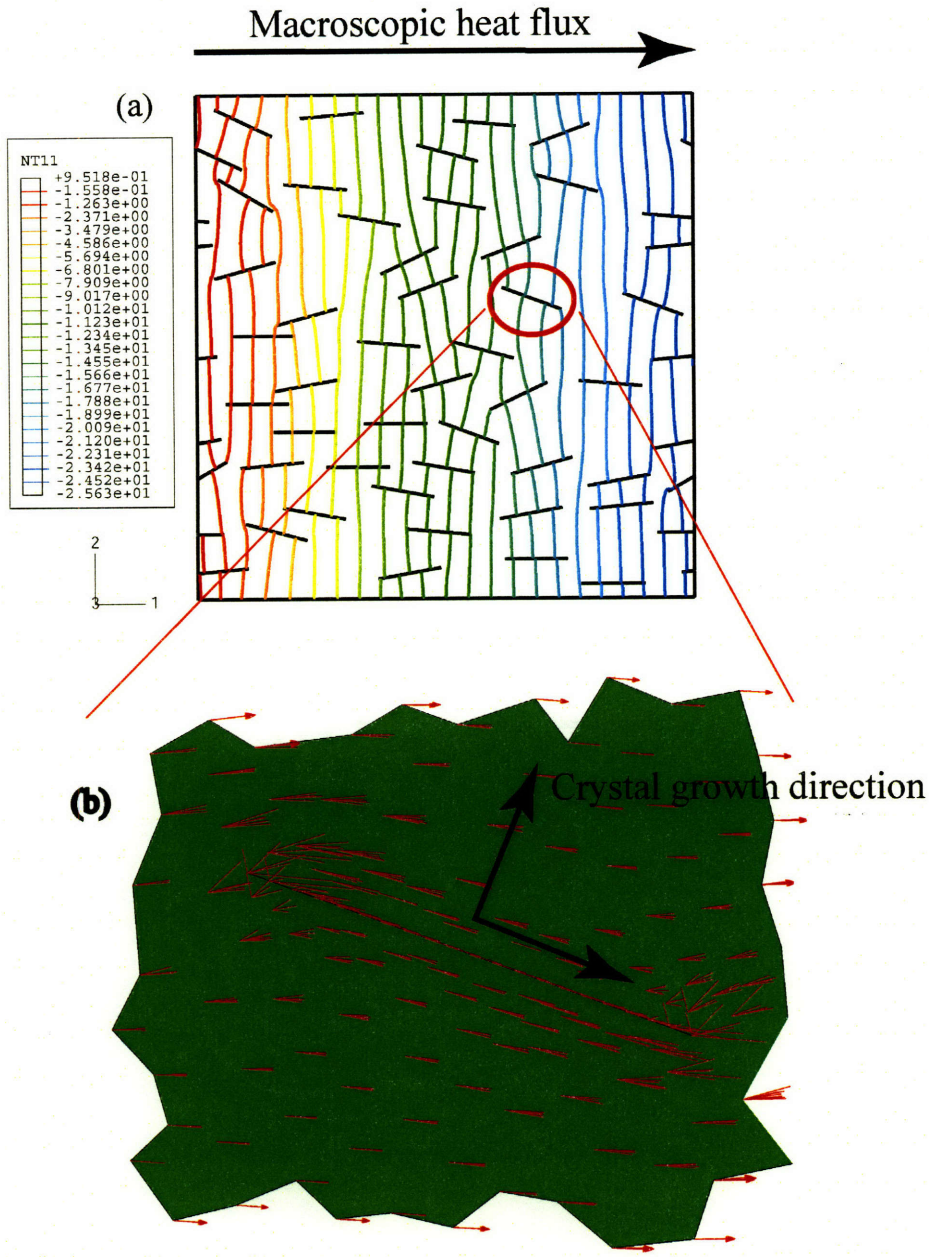

Figure 6.4: (a) Isotherms of RVE subjected to macroscopic heat flux in direction-1; (b) local heat flux vector.

6.3. Axial Composite Modulus and Initial Yield Strength

3D RVEs of composites filled with well-aligned, exfoliated clay particles are subjected to tensile loading in the 1-direction (parallel to the particle planes, as shown in Fig. 6.5a). Two types of matrices are considered: (1) isotropic matrix, whose elastic and plastic properties remain the same as the bulk homo-polymer, and (2) transcrystallized matrix, which is highly textured and mechanically highly anisotropic. The isotropic matrix properties are assigned to be E_m = 3 GPa, $\sigma_{y,m}$ = 70 MPa; the anisotropic elastic and yielding constants used to model the textured matrix are listed in Table 6.1 and Table 6.2 from Section 6.1.2.1, respectively. The clay particles are assumed to be exfoliated, with in-plane dimension of 100 nm and (thickness, modulus) pair of (0.678 nm, 370 GPa).

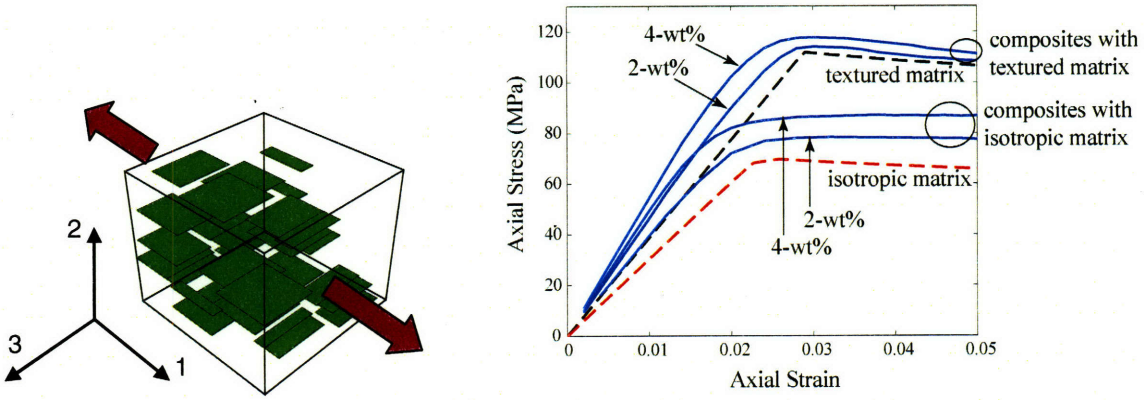

(a) (b)

Figure 6.5: (a) RVE with perfectly aligned platelet particles subjected to uniaxial tension in 1-direction. (b) Axial tension behaviors of the isotropic matrix, textured matrix, and 2-wt%, 4-wt% clay composites modeled with isotropic matrix, and with textured matrix, respectively.

The overall composite modulus and yield strength predicted by 3D FE simulations modeled with isotropic and textured matrices are plotted as functions of W_c in Fig. 6.6 and 6.7, respectively; also plotted are the collected experimental data quoted earlier in

Chapter 5 (Fig. 5.20, Fig. 5.21, and Table 5.3). Both experimental and simulation results are normalized with respect to the corresponding property of the isotropic homo-polymer.

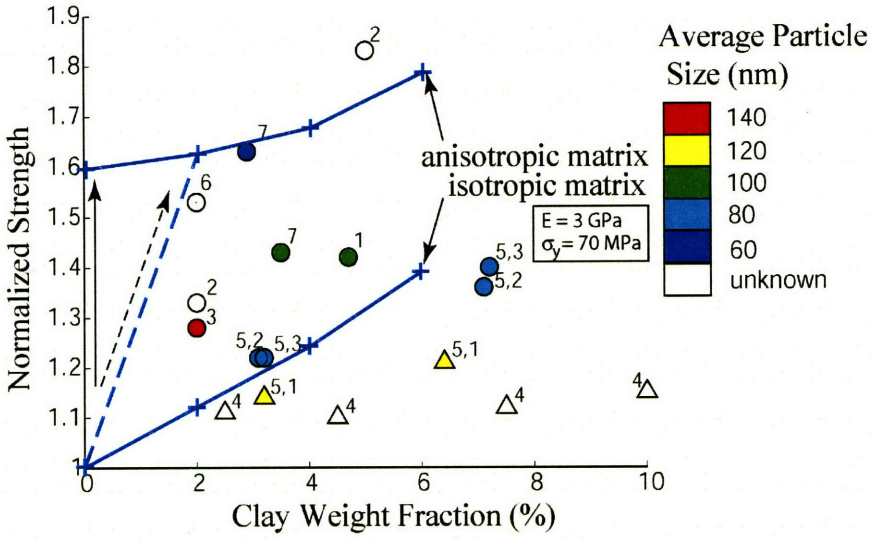

Figure 6.6: 3D simulation results of the composite in-plane tensile yield strength using isotropic, and anisotropic, matrix models, respectively, superposed with collected experimental data as depicted in Fig. 5.20.

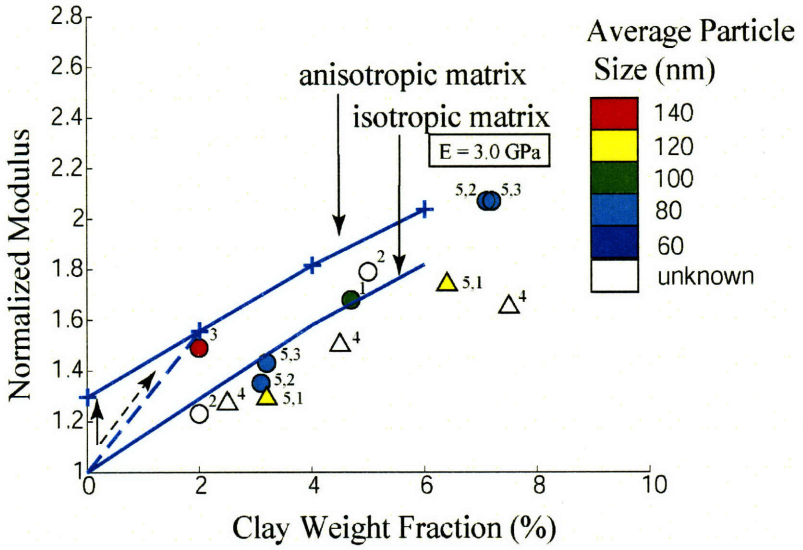

Figure 6.7: 3D simulation results of the composite modulus using isotropic, and anisotropic matrix, respectively, superposed with collected experimental data as depicted in Fig. 5.21.

The experimental data are well-bounded from above by FE predictions based on the transversely isotropic matrix model except for a few outliers. Note that $\sigma/\sigma_{y,m}$ and E/E_m

are marked to start from 1.6 and 1.3, respectively, rather than 1.0, at zero percent clay; these values correspond to the anisotropic elastic and yield ratios used to describe the textured matrix material (from Table 6.1, we have $E_{11}/E_m = 1.29$; from Table 6.2, we have $R_{11} = 1.6$). Such expressions demonstrate clearly that the enormous enhancement in σ_y and E (especially, σ_y) is essentially achieved through increases in the induced matrix properties accompanying the morphological transition.

In fact, the overall effect of property enhancement S/S_m (where S represents any material property including E and σ_y) achieved at a given weight fraction, W_c, can be hypothetically broken down into two successive steps, as illustrated in Fig. 6.8. First, the property of the isotropic homo-polymer is increased by a ratio of R_o due to the anisotropy of the textured material ($R_o \equiv S_{textured}/S_m$)[1]. Then the textured matrix material is further reinforced by the addition of stiff clay; the reinforcing efficiency depends on parameters such as the aspect ratio of the particle and the particle/matrix property ratio. Such a conceptual decomposition enables separation of the dual roles played by the nanoclay in the reinforcement of the nanocomposite: Step-1, the increase of S_m by a ratio of R_o, is attributed to the heterogeneous matrix crystal nucleation function of the nanoclay; Step-2, the steady increase of S/S_m with increasing W_c, is attributed to the 'stiff filler' role of the nanoclay, which has been discussed earlier in Chapter 3, regarding the composite modulus, and in Chapter 5, regarding the composite initial yield strength.

One can evaluate the relative importance of the two roles of the nanoclay by comparing the property enhancements achieved via Step-1 and Step-2, respectively. Observation of

[1] For instance, R_o can be thought of as E_{11}/E_m when examining the axial modulus of the composite, or as $R_{11} = \sigma_{y,11}/\sigma_{y,m}$ when studying the axial yield strength.

Fig. 6.6 and Fig. 6.7 reveals significant difference in the underlying mechanisms responsible for the enhancements of the composite strength and modulus: while the former mainly lies in the improvement of a matrix property achieved through the matrix transcrystallization induced by nanoclay as the 'nucleation site', the latter can be well explained by the conventional role of the nanoclay as a 'stiff filler'.

Note that in reality the percolation of the transcrystallized morphology, and therefore the increase of the matrix property from S_m to S_m*R_o, does not occur at zero-percent clay, as indicated by 'Step-1' in Fig. 6.8 (also solid arrows in Fig. 6.6 and Fig. 6.7); rather, it is an accumulating process which saturates at a critical clay content, $W_{c,c}$, as illustrated by the dashed-arrow denoted as 'Step-1*' in Fig. 6.8 (also dashed-arrows in Fig. 6.6 and Fig. 6.7). Here we approximate Step-1* by Step-1 since $W_{c,c}$ should be very small for polymer/clay nanocomposites, due to the high aspect ratio of the nanoclay and the large distances at which the special morphology extends from the clay surface. A TEM of nylon 12-clay (Figure 6.2a, Kim, et al, 2001) shows that this transcrystallized morphology has percolated throughout the entire matrix at a clay content of $W_c = 2\%$. Kojima (1994) has observed that the degree of crystallite orientation increases linearly till $f_p = 0.008$ (which corresponds to $W_c = 2\%$, given L = 100 nm, t = 1 nm); together with Figure 6.2(a), it is not unreasonable to assume that $W_c = 2\%$ is a critical point above which transcrystallization percolates. Previous work of the author (Sheng, et al, 2004) utilized $W_{c,c}$ to obtain an estimation of the thickness of the transcrystallized matrix layer protruding from the silicate surfaces.

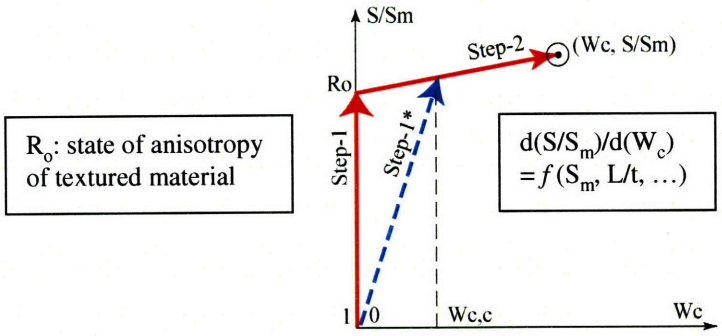

Figure 6.8: Schematic illustration of the two-steps to achieve composite property enhancement S/S_m with clay content, W_c; S is the composite property under investigation, S_m is the corresponding property of the isotropic bulk matrix. R_o characterizes the state of anisotropy of the textured material; the slope of 'Step-2' characterizes the reinforcing efficiency of the clay.

Discussion on the orthotropic matrix morphology

When the orientation of the crystal lamellae adopt in-plane order, as illustrated in Fig. 6.1(a), where the macromolecules are aligned in the the flow direction ($\mathbf{m}_1$), the resulting transcrystallized matrix material becomes essentially orthotropic, rather than transversely isotropic, as is considered here. Consequently, the axial properties in the $\mathbf{m}_1$-direction (E_{11}/E_m, $\sigma_{y,11}/\sigma_{y,m}$) corresponding to the orthotropic matrix texture are much higher compared to those for the transversely isotropic morphology. For example, Lin and Argon (1992) measured the Young's modulus of the quasi-single nylon 6 crystal in the direction of chain alignment to be twice as much as the typical modulus of bulk nylon 6; in addition, the tensile yield strength of oriented polyethylene terephthalate (PET), with draw ratio 5:1, in the original draw direction (the direction of chain alignment) is found to be nearly four times that of bulk PET (Brown, Duckett and Ward, 1968). Therefore composites based on such orthotropic transcrystalline matrix morphology are expected to possess extremely high axial modulus and yield strength (provided that the silicate platelets are aligned with their planes parallel to the flow direction); the property enhancements are mainly ascribed to the high axial properties of the transcrystallized

matrix (refer to Fig. 6.8, the value $R_o >> 1.0$ and the slope of 'Step-2' can be considered negligible compared to R_o).

6.4. Anisotropic Elastic Properties and Yield Surface of the Composite

Previously in Chapter 3 and Chapter 5, we have assessed the complete set of elastic and yield properties of composites with isotropic (un-textured) matrix and demonstrated the anisotropy of the composite brought by the unidirectional, high aspect ratio, stiff fillers. Such material anisotropy can be increased considerably when the matrix itself is a highly textured (hence highly anisotropic) material, such as the oriented transcrystallized polymer under discussion here. Following the procedure employed in the previous chapters, we calculate the anisotropic elastic and yield properties of composites with a textured matrix and well-aligned exfoliated clay by stretching and shearing the RVE in mutually orthogonal directions. Orientations of axes are defined in Fig. 6.5: axis-2 is normal to the particle planes, and plane 1-3 is parallel to the particle planes (axis-2 coincides with the axis of isotropy of the transversely isotropic matrix material). The matrix anisotropy is characterized by Table 6.1 (elasticity) and Table 6.2 (yield surface), with reference isotropic matrix properties of E_m = 3.0 GPa and $\sigma_{y,m}$ = 70 MPa. Exfoliated clay has in-plane dimension L = 100 nm and (modulus, thickness) pair of (370 GPa, 0.678 nm), which yields a f_p/W_c ratio of 0.25.

6.4.1. Anisotropic Elastic Properties

Fig. 6.9 depicts the 3D FE-based micromechanical predictions of the anisotropic elastic properties of composites as functions of the clay weight fraction; open rectangles and closed diamonds are used to distinguish between results with matrix modeled to be highly textured and isotropic. The effects of clay on the elastic properties of composites with isotropic matrix have been studied in Chapter 3 and will not be repeated here.

Comparison between the property enhancement ratio (e.g., E_{11}/E_m) vs. W_c curves for composites with an isotropic matrix and those with a textured matrix reveals that these two curves possess nearly identical slopes except the one taking into account matrix texture is shifted to a certain value at "0-wt%" clay, depending on the specific property of the textured material under investigation.

Again, the property enhancement achieved by clay together with textured matrix induced by the presence of nanoclay can be interpreted by the 2-step procedure illustrated in Fig. 6.8, where the ratio R_o can be thought of as a constant characterizing the state of anisotropy of the textured matrix material (R_o = 1.29 for E_{11}/E_m, 0.99 for E_{22}/E_m, 1.31 for G_{13}/G_m, 1.51 for ν_{12}/ν_m, and 0.94 for ν_{13}/ν_m). The reinforcing effect of clay on the textured matrix (Step-2) can simply be approximated by the effect of clay on the isotropic matrix, given the same W_c, L/t and isotropic matrix properties. Such approximation greatly reduces the complexity involved in the evaluation of properties of composites with special matrix morphology, since composite properties with isotropic matrix can be studied with relative ease through numerical micromechanical modeling (such as FE-based simulations employed in this work) as well as closed-form analytical models (e.g., Mori-Tanaka model for anisotropic elastic properties in Chapter 3, and Chow's model for anisotropic thermal expansion in Chapter 4).

Note that this is if the particles are high aspect ratio — assuming load is transferred to the particles over a relatively small length so that is not a changing factor whether or not the matrix is anisotropic. When the particle is spherical (as in rubber-modified nylon 6), the matrix texture is found to have very limited impact on the macroscopic composite elastic

and yield properties (Tzika, et al., 2002) due to the isotropic radial distribution of the crystal lamellae.

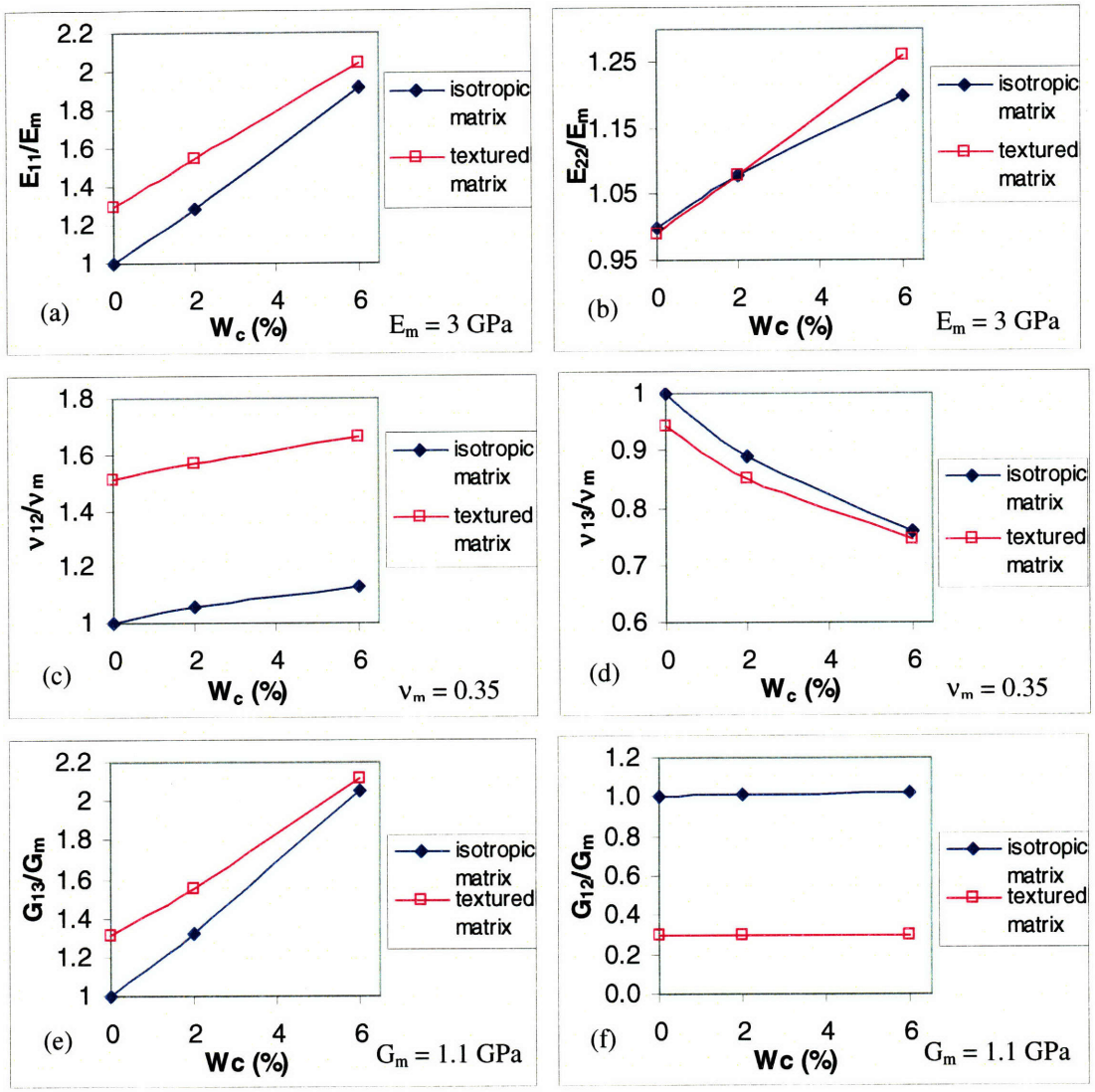

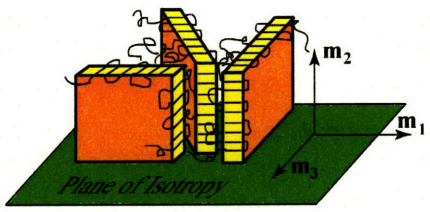

Transversely random lamellae
transversely isotropic

Figure 6.9: Anisotropic elastic properties of composites with and without textured matrix predicted by 3D FE-based micromechanical modeling. Exfoliated clay platelets are well aligned with their planes normal to axis-2, as illustrated in Fig. 6.5. L = 100 nm, t = d_s = 0.678 nm. E_m = 3 GPa, ν_m = 0.35.

6.4.2. Anisotropic Yield Properties

Fig. 6.10 depicts the 3D FE-based micromechanical predictions of the anisotropic yield properties of composites as functions of the clay weight fraction; open rectangles and closed diamonds are used to distinguish between results with the matrix modeled to be highly textured and isotropic. Hill ratios (R_{ij}, refer to Section 6.1.2.1 for definition) of the composites with isotropic matrix and with textured matrix, together with Hill ratios of the textured material, are listed in Table 6.4. Interestingly, unlike the anisotropic elastic properties, results for composite yield properties with and without matrix texture exhibit rather different trends, except for $\sigma_{y,11}$.

Table 6.3 Elastic constants of textured matrix (Tzika et al, 2000) and composite filled with 6-wt% exfoliated clay with particle plane aligned normal to the 2-direction, modeled with isotropic matrix and with textured matrix, respectively (data plotted in Fig. 6.9). L = 100 nm.

		$(E_{11} = E_{33}) / E_m$	E_{22} / E_m	$\nu_{12} = \nu_{23}$	ν_{13}	G_{13}/G_m	$(G_{12} = G_{23}) / G_m$
textured matrix		1.29	0.99	0.53	0.33	1.31	0.30
6-wt% composite	isotropic matrix	1.92	1.20	0.40	0.27	2.05	1.01
	textured matrix	2.05	1.26	0.58	0.26	2.12	1.02

Table 6.4 Hill ratios used for anisotropic yield of the textured matrix (Tzika et al, 2000) and composite filled with 6-wt% exfoliated clay with particle plane aligned normal to the 2-direction, modeled with isotropic matrix and with textured matrix, respectively (data plotted in Fig. 6.10).

		$R_{11} = R_{33}$	R_{22}	$R_{12} = R_{23}$	R_{13}
textured matrix		1.6	3.0	0.5	1.0
6-wt% composite	isotropic matrix	1.4	1.2	1.0	1.4
	textured matrix	1.8	2.8	0.5	1.2

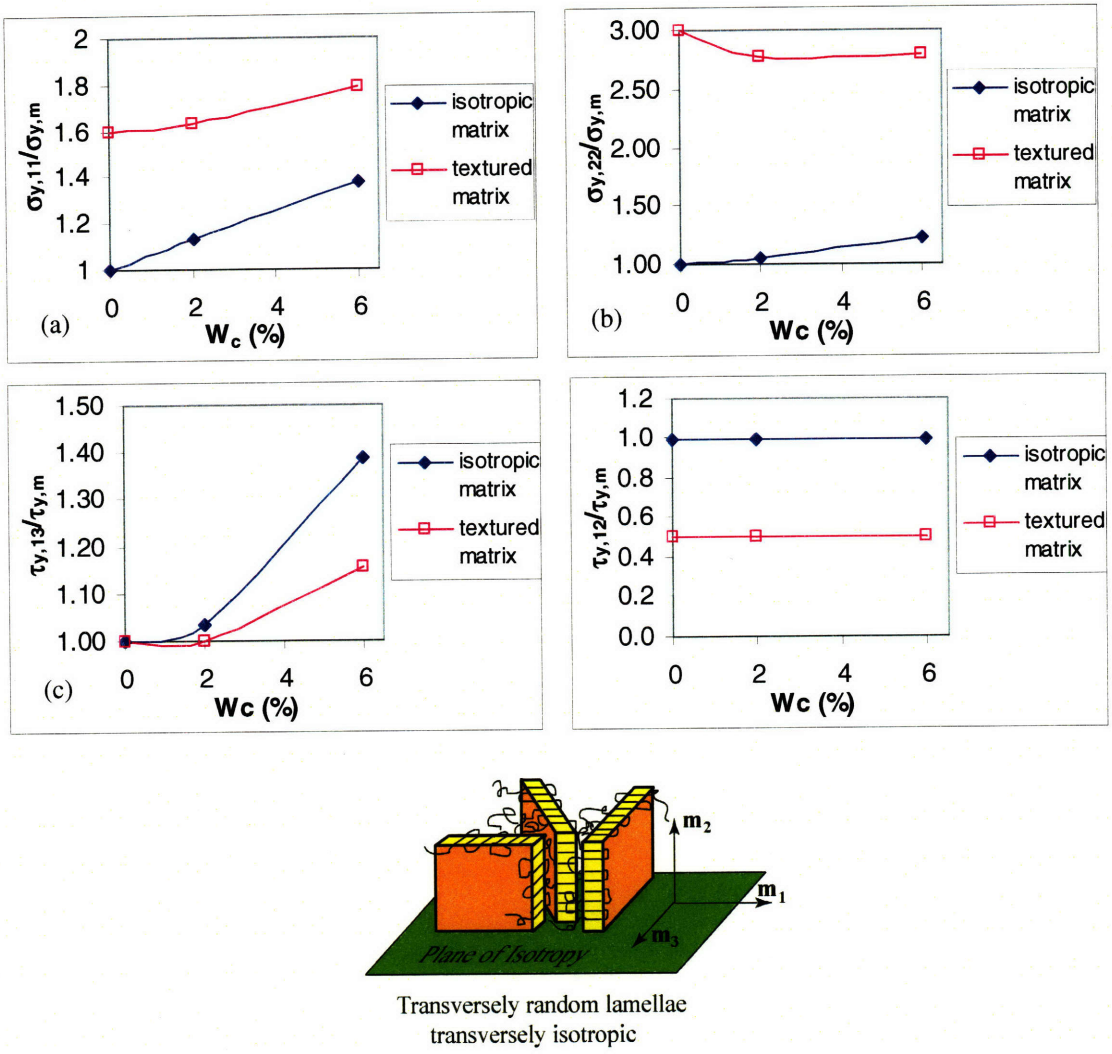

Figure 6.10: Anisotropic yield properties of composites with and without textured matrix predicted by 3D FE-based micromechanical modeling. Exfoliated clay platelets are well aligned with their planes normal to axis-2, as illustrated in Fig. 6.5. L = 100 nm, t = d_s = 0.678 nm. E_m = 3 GPa, ν_m = 0.35, $\sigma_{y,m}$ = 70 MPa. Refer to Fig. 6.9 for anisotropic elastic properties of the composite.

6.4.2.1. Effect of Matrix Texture on Composite $\sigma_{y,11}$

The impact of matrix transcrystallization on the axial composite yield strength has been assessed in Section 6.2, and is shown here in Fig. 6.10(a) for completeness. The elevated tensile yield strength of the transcrystallized matrix in the 1-direction greatly improves

the overall $\sigma_{y,11}$ of the composite; the reinforcing effect of the particles as "stiff fillers" is relatively small compared to enhancement resulting from the textured matrix.

Another aspect to study, other than the tensile strength, is the composite post-yield behavior. As mentioned in Section 6.2, the highly oriented trancrystallized material has a weak transverse shear resistance (captured by the low Hill ratio $R_{12} = 0.5$); such weak slip process, once triggered, can facilitate the formation of dramatic shear bands across the entire composite, and consequently, tremendous localization along the easy shear plane, which macroscopically manifests as steep drop in the overall stress over nearly unchanged overall strain.

An interesting contrast is made between 3D and 2D plane strain simulations of uniaxial tensile deformation of RVEs containing initially perfectly-aligned exfoliated clay particles (tensile loading along axis-1, parallel to the particle planes); in both cases the matrices are modeled to be highly textured (e.g., Hill ratios $R_{11} = 1.6$, $R_{22} = 2.0$, $R_{12} = 0.5$, as described in Table 6.1 and 6.2). The tensile stress-strain curves of the composite and contours of the post-yield equivalent plastic strain extracted from the 3D and 2D plane-strain FE simulations are depicted in Fig. 6.11 and 6.12, respectively. While both simulation results show significant increases in the composite axial yield strength $\sigma_{y,11}$ due to the high axial slip resistances of the textured matrix, the 2D curve[2] (Fig. 6.12 a) exhibits considerate strain softening shortly after initial yielding. Such a phenomenon is a combined result of the easy transverse slip and the 2D nature of the simulation: the 2D confinement of the plastic deformation pathways (as opposed to free venturing of

[2] The 2D plane-strain simulations have their inherent limitations due to the plane strain constraint. However, these are the topics of Section 6.4, where effects of particle orientation distribution on the composite yield strength are investigated employing 2D RVEs. Here we focus on the strain softening phenomenon exhibited in the 2D simulations.

pathways in 3D space shown in Fig. 6.11 b) together with the preferred easy transverse shear of the anisotropic matrix greatly increase the chance of dramatic shear banding. Neither cause alone is sufficient to induce such post-yield softening — it is observed neither for the 3D simulation with textured matrix (Fig. 6.11a) nor for the 2D plane strain simulation with isotropic matrix (Fig. 5.12 a).

It should be noted that, in addition to the physical mechanisms discussed above, we may also be seeing some effects due to the special ways that the finite element tool handles the rotation of material axes[3]. We have not follow the evolution of crystal axes due to localized plastic shearing (plastic spin), but are merely updating the local material axes based on total spin (the finite element tool treatment). Specific effects such treatment might have on the post-yield softening phenomena observed both here and later in Section 6.4.2.2.3 have yet to be accessed with further investigation.

[3] Recall in Chapter 2, Section 2.2.4, we have mentioned that modeling of the intercalated particle with anisotropic elasticity in large-deformation finite element analysis can result in unphysical particle behavior due to erroneous rotation of material axes.

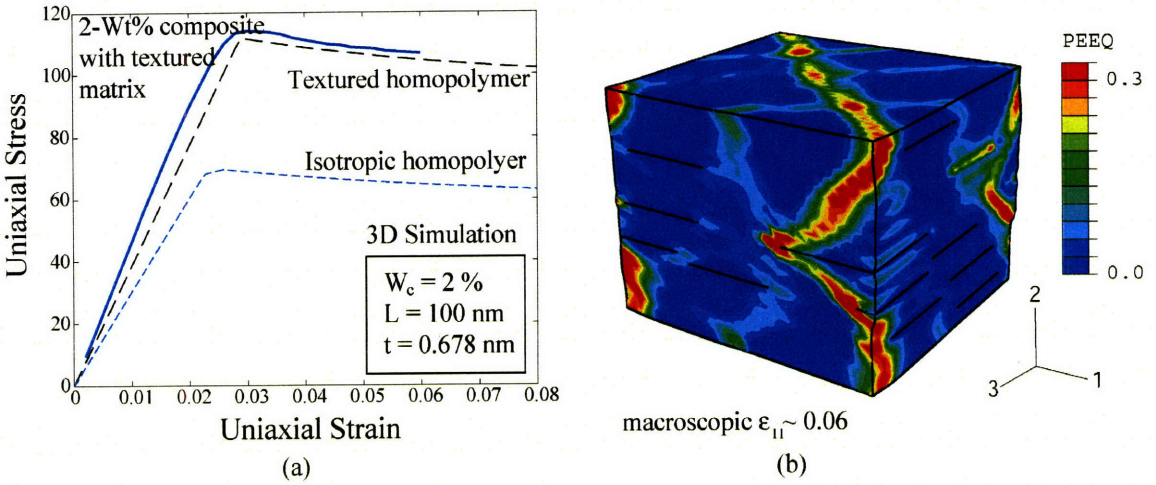

Figure 6.11: (a) 3D FE simulated stress-strain curve of 2-Wt% composite with textured matrix, uniaxially loaded in the 1-direction. (b) Contour of the equivalent plastic strain in the matrix at macroscopic axial strain of ~ 0.06 (in the 1-direction).

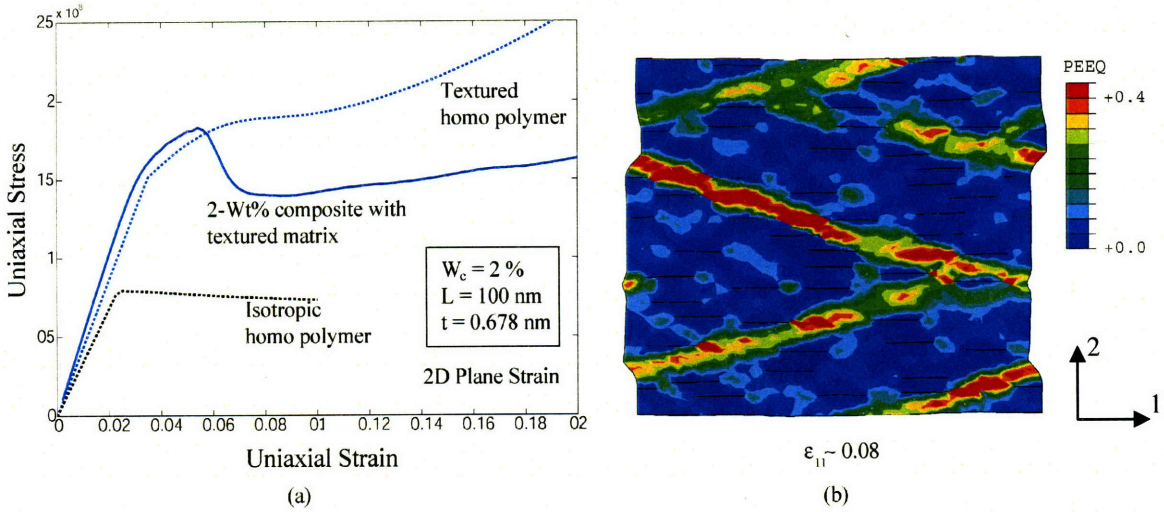

Figure 6.12: (a) 2D plane strain stress-strain curve of 2-Wt% composite with textured matrix, uniaxially loaded in the 1-direction. (b) Contour of the equivalent plastic strain in the matrix at macroscopic axial strain of ~ 0.08 (in the 1-direction).

6.4.2.2. Effect of Matrix Texture on Composite $\sigma_{y,22}$

6.4.2.2.1. Local Particle Buckling

$\sigma_{y,22}$ of the composite with textured matrix is lower than that of the pure textured material ($R_{22} \equiv \sigma_{y,22}/\sigma_{y,m} = 3.0$) and does not depend strongly on W_c, as shown in Fig. 6.10(b), suggesting a different role of the clay, other than a reinforcing agent. Careful examination of the stress state in the matrix and in the particle when the composite is tensile-loaded in the 2-direction (i.e., normal to the particle planes) reveals that macroscopic yielding is triggered by local instability events (specifically, local buckling of the particles); therefore $\sigma_{y,22}$ of the composite is dominated by the critical buckling stress, which occurs at a σ_{22} value that is less than the $\sigma_{y,22}$ of the textured material and is not sensitive to W_c. This mechanism is well illustrated in Fig. 6.13. When the composite is loaded under tension in the 2-direction, the matrix material in the vicinity of particle platelets is subjected to tensile in-plane stresses (σ_{11} and σ_{33}) due to the plane strain constraint of the stiff, planar particle; meanwhile, the particles are under in-plane compression to balance the tensile stress in the matrix, as shown in Fig. 6.13(b). The compressive stress in the particle increases as the macroscopic deformation (ε_{22}) proceeds until the critical buckling stress is reached[4], when local instability occurs and the composite undergoes macroscopic yielding, as demonstrated in Fig. 6.13(c).

[4] For composite with isotropic matrix, the matrix yield stress ($\sigma_{y,m}$) is not sufficient to generate compressive stress in the clay platelets that can trigger local buckling; thus the presence of the clay does provide some enhancement to $\sigma_{y,22}$ of the composite, as shown in Fig 10 (b).

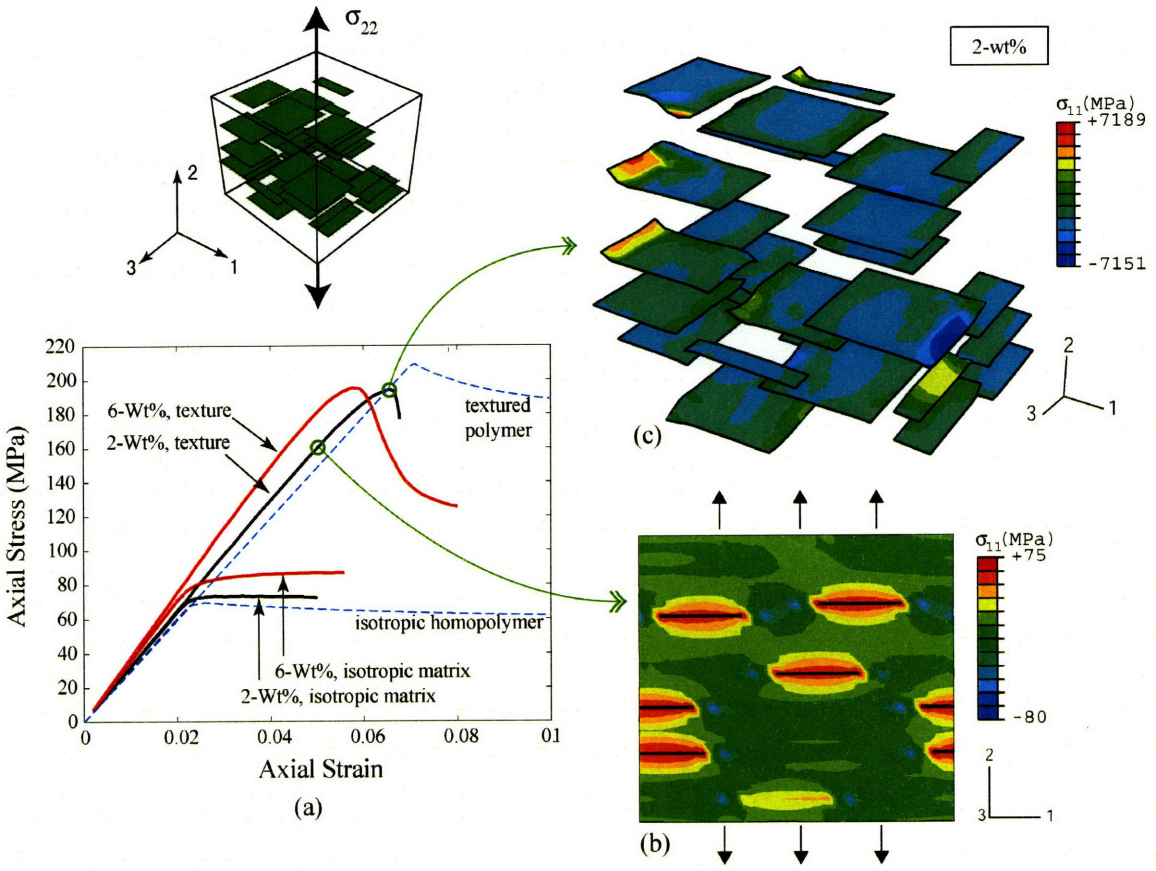

Figure 6.13: (a) Tensile curves of 2-Wt% and 6-Wt% composites with textured matrix (refer to Fig. 6.10b) loaded along 2-direction (normal to particle planes). (b) Contour of σ_{11} in the matrix at ε_{22} ~ 0.05 (elastic regime): matrix material in the vicinity of particles (marked as dark lines) is subjected to tensile in-plane stress due to the plane-strain constraint of the stiff particles, while particles are under in-plane compression. (c) Deformed shape of particles at the yield point, demonstrating local buckling of the clay plateles under in-plane compression (the deformation scale factor is set to 1.5 for clearer demonstration).

Fig. 6.13(c) also demonstrates the easy bendable nature of exfoliated single layer silicates resulting from the atomic-level small thickness. When the clay is intercalated instead, the "particle" bending stiffness is increased; however, the layered structure is highly prone to transverse shear due to the low shear modulus of the inter-layer gallery material. Therefore, when larger deformation scale is considered, the primary deformation modes for the exfoliated and the intercalated clay particles are bending and transverse shearing, respectively. The large deformation behavior of intercalated nanocomposites will be an interesting topic for future investigation.

6.4.2.2.2. Tension vs. Compression

It is interesting to compare transverse tension and compression behaviors of the composite. We have demonstrated earlier that when the composite is loaded under transverse tension, the particles experience in-plane compressive stress, which results in local buckling and, in turn, triggers macroscopic yielding; therefore it is reasonable to assume that $\sigma_{y,22}$ of the composite acquired under uniaxial compression is higher than that acquired under tension, since the macroscopic transverse compressive loading imposes in-plane tensile stresses in the particles and thus do not induce any local instability. However, micromechanical simulations give rather opposite results.

Fig. 6.14(a) depicts the uniaxial tension and compression stress-strain curves of 6-Wt% composites with textured matrix and exfoliated, well-aligned particles with L = 100 nm, as shown in Fig. 6. 13 (curves of composites with isotropic matrix are also plotted for reference). Clearly, the compressive yield strength, $\sigma_{y,22}|_{compression}$, is considerably lower than the tensile yield strength, $\sigma_{y,22}|_{tension}$; in addition, the compression curve has a fairly steep strain softening after yield (the softening phenomenon is discussed in Section 6.4.2.2.3). Analyses of the contours of the equivalent plastic strain at various stages of deformation (Fig. 6.14b and c for compression, Fig. 6.14d, e, f for tension) reveal that the difference in $\sigma_{y,22}|_{tension}$ and $\sigma_{y,22}|_{compression}$ directly results from the distinct deformation pathways developed under transverse tension and compression loadings. A significant difference between tensile and compressive loading (both in the 2-direction) is that the transverse tension tends to close up inter-particle gaps (lateral contraction), whereas the transverse compression broadens up these gaps (lateral expansion), as

illustrated in Fig. 6. 15. Even though this is at relatively modest strain[5] ($\varepsilon_{11} \sim 0.06$), it is enough of an effect at 6-Wt% clay to significantly alter yield in tension vs. yield in compression: transverse uniaxial compression acts to broaden the inter-particle gaps and to facilitate the formation of percolating shear bands, as shown in Fig. 6. 14b and c; in contrast, transverse uniaxial tension acts to close up the inter-particle gaps and to hinder the inter-connection of local shear bands, as shown in Fig. 6.14d, e and f, where more tortuous pathways has to be formed (as opposed to the one primary shear band throughout the matrix in the *compression* case) in order to achieve percolation.

Figure 6.16 compares the transverse uniaxial (tension and compression) curves of 6 and 2-Wt% composites with textured matrix; in both cases the particles are assumed to the exfoliated and well-aligned with particle planes normal to the loading direction, L = 100 nm; isotropic matrix properties are E_m = 3 GPa, $\sigma_{y,m}$ = 70 MPa, matrix anisotropy is characterized by Table 6.1 and 6.2. Again, the difference between $\sigma_{y,22}|_{tension}$ and $\sigma_{y,22}|_{compression}$ is observed for the 2-Wt% composite; however, the difference is smaller compared to that observed for the 6-Wt% composite. When W_c is small (e.g., 2 %), the particles are much farther away from each other, consequently, the impact of tension vs. compression on the formation of percolating shear bands is not as critical as for a heavier-filled composite (e.g., 6-Wt%). Note that the compressive $\sigma_{y,22}$ for the 2-Wt% composite is even higher than that for the 6-Wt% composite.

[5] The constrained regions on top/below the stiff particles in both cases means that the unconstrained matrix material must be deformed to levels much larger than the macroscopic strain, thus accounting for the very large spread/approach effects seen in the particle positions

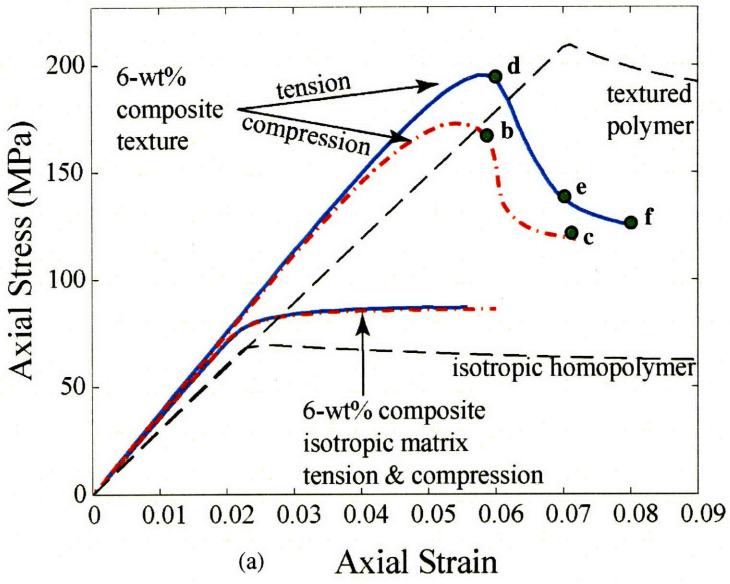

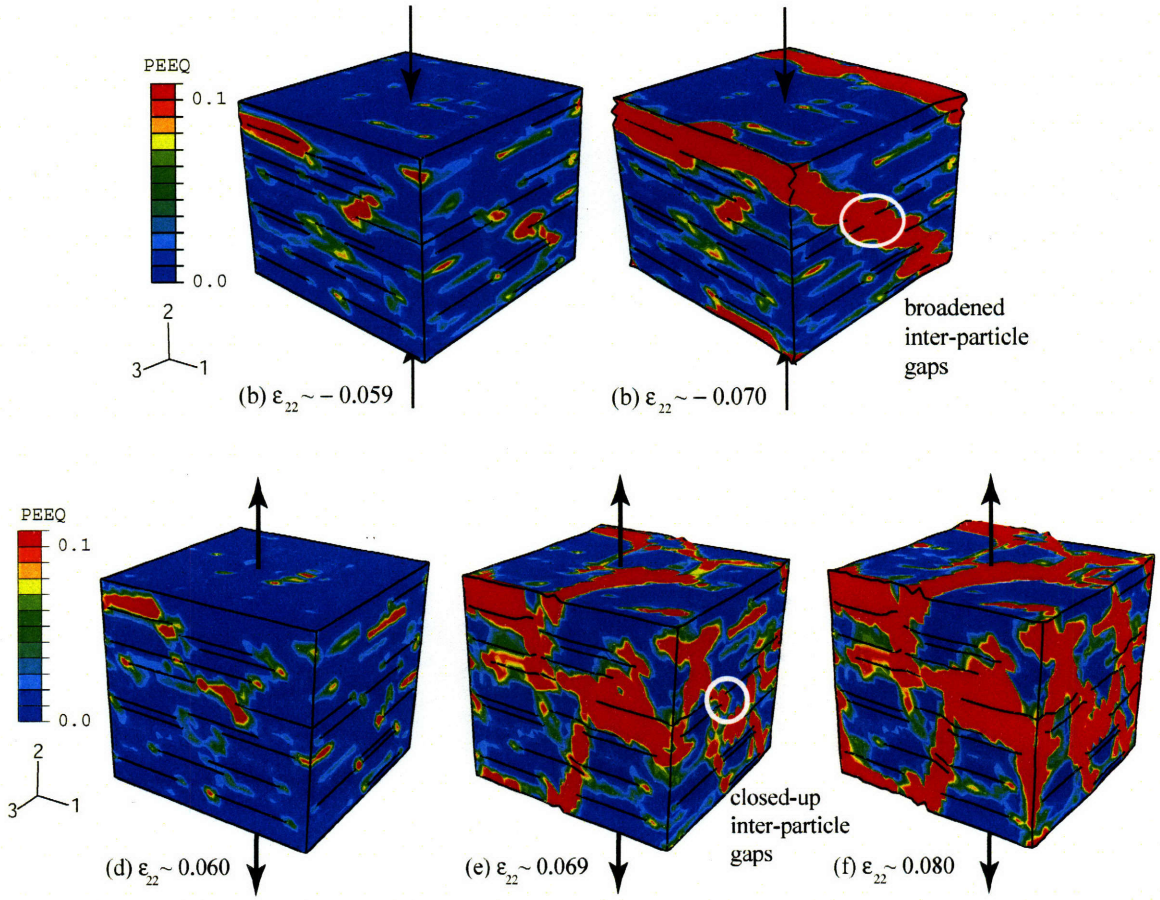

Figure 6.14: (a) Uniaxial tension and compression curves in the transverse (2) direction for 6-wt% composites (exfoliated, L = 100 nm) with and without matrix texture, markers indicate the various deformation stages when contours of the equivalent plastic strain are captured; contours of the equivalent plastic strain of composite under transverse compression at macroscopic compressive strain of ~ -0.059 (b) and ~ -0.070 (c); contours of the equivalent plastic strain of composite under transverse tension at macroscopic tensile strain of ~ 0.060 (d), 0.069 (e), and 0.080 (f).

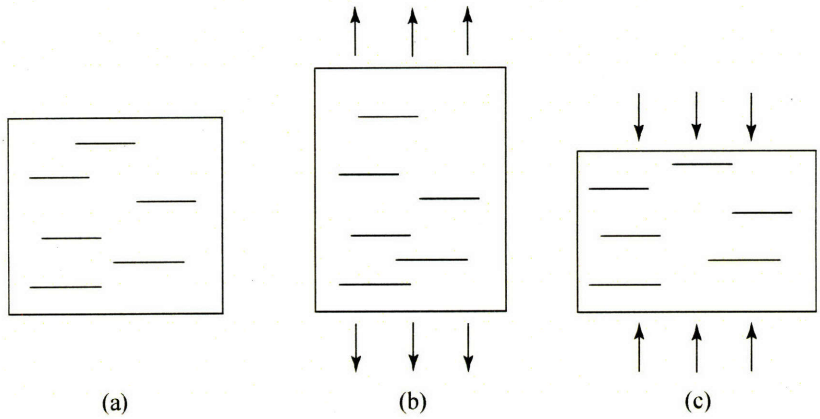

Figure 6.15: Schematics of (a) undeformed composite, (b) composite under transverse uniaxial tension with closed-up inter-particle gaps, and (c) composite under transverse uniaxial compression with broadened inter-particle gaps.

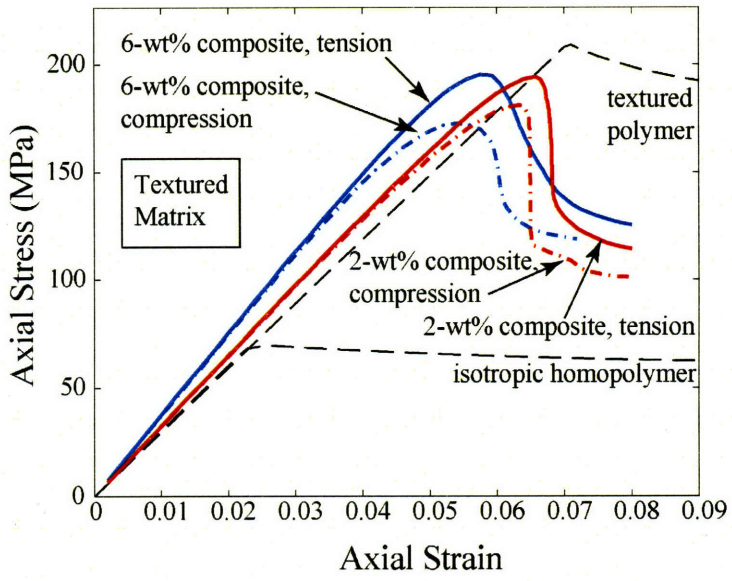

Figure 6.16: Uniaxial tension and compression curves in the transverse (2) direction for 6-wt% and 2-wt% composites (exfoliated, L = 100 nm, E_m = 3 GPa, $\sigma_{y,m}$ = 70 MPa) with textured matrix.

It should be noted that these phenomena are based upon a highly anisotropic matrix with high axial slip resistances and low transverse slip resistance; composites with isotropic matrix have nearly identical tension and compression behaviors, as shown in Fig. 6.14(a), also as discussed previously in Chapter 5 (Section 5.4).

6.4.2.2.3. Post-yield Softening

The composite exhibits significant post-yield softening under transverse uniaxal loading (in the 2-direction, normal to the particle planes), whether loaded in tension or in compression, as depicted in Fig. 6.14a and Fig. 6.16. Recall in Section 6.4.2.1, the softening of the 2D RVE when subjected to axial tension was attributed to the weak transverse slip resistance as well as the 2D restriction of plastic deformation pathways. Here the easy transverse shear mode remains as a critical factor responsible for inducement of the post-yield softening; however, additional player is needed in order to facilitate the formation of dramatic shear bands that percolate through the entire composite (for instance, the 2D spatial restriction imposed upon the development of the deformation pathways in plane strain simulations, as discussed in Section 6.4.2.1).

Observations of the deformation contours of the 6-Wt% composite, shown in Fig. 6.14, reveal rather different mechanisms responsible for the post-yield softening phenomenon of the composite when subjected to transverse tension (Fig. 6.14b and c) and to transverse compression (Fig. 6.14d, e and f). The assisting player (in addition to the easy shear of the anisotropic matrix) is identified for each loading condition: (a) the broadening of inter-particle gaps in the case of compressive loading, and (b) the local buckling of the particles in the case of tensile loading. While the former may be self-evident from the contour shown in Fig. 6.14c (in compression, the broadened inter-particle gaps favor the formation of percolating shear band rather than a more tortuous pathway), the latter needs further explanation: once the particles undergo local buckling under macroscopic tension in the transverse direction, they no longer act as obstacles to the plastic deformation pathways; instead, the curved portions of the buckled particles

become inter-connecting bridges where shear bands can percolate right through, as demonstrated in Fig. 6.17. As particle buckles, the curved portions misalign with the loading direction; the easy shear plane (45 degrees off the particle plane) of adjacent anisotropic matrix becomes exposed to the loading direction and consequently large shear deformation ensues. The effect of particle orientation on composite yielding is the topic of Section 6.5.

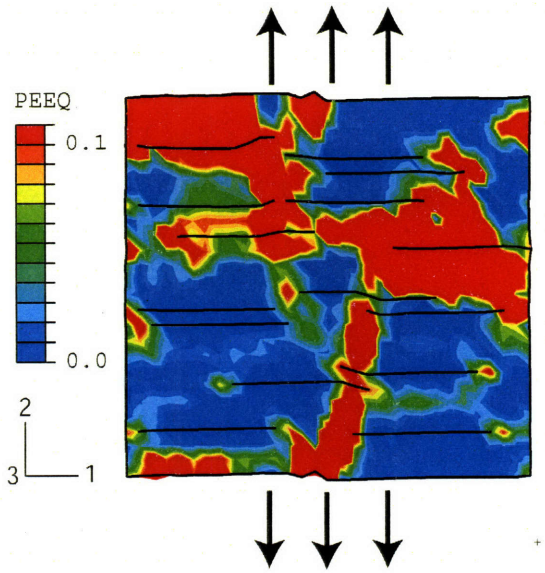

Figure 6.17: Contour of the equivalent plastic strain of 6-wt% composite (exfoliated, L = 100 nm; textured matrix) under transverse tension at macroscopic tensile strain of ~ 0.069 (zoom-in of Fig. 6.14e, 1-2 view of 3D FE simulation).

6.4.2.3. Effect of Matrix Texture on Composite $\tau_{y,12}$

Fig. 6.10(d) plots the composite $\tau_{y,12}$, with isotropic matrix and with textured matrix, as functions of the clay content. As discussed previously in Chapter 3 and Chapter 5, the transverse shear properties (G_{12} and $\tau_{y,12}$) of the composite are not affected by the addition of clay particles, provided no change in the matrix morphology occurs. Once the matrix transcrystalliztion is taken into account, the transverse shear resistance of the textured matrix material is reduced to ½ of that of the bulk homo-polymer ($R_{12} = R_{23} = 0.5$, reflecting the easy slip process along the hydrogen-bonded planes, parallel to the 1-3 plane); consequently, the composite has a low transverse shear yield strength, with Hill ratio $R_{12} = 0.5$.

6.4.2.4. Effect of Matrix Texture on Composite $\tau_{y,13}$

Sampling of weaker slip resistances

It has been shown in Chapter 5 that, with an isotropic matrix, the in-plane shear yield strength of the composite, $\tau_{y,13}$, is well-reinforced by the stiff clay particles aligned parallel to the 1-3 plane (40% increase in the composite $\tau_{y,13}$ is achieved with 6-wt% aligned, exfoliated clay). Presumably, matrix texture should not have much influence on the composite $\tau_{y,13}$, since the Hill ratio of the textured matrix is $R_{13} = 1.0$. Surprisingly, $\tau_{y,13}$ of composites with textured matrix turns out to be considerably lower than that of composites with isotropic matrix, as shown in Fig. 6.10(c). Such result can be ascribed to the weak out-of-plane slip resistances of the textured material ($R_{12} = R_{23} = 0.5$ as opposed to $R_{13} = 1.0$, as listed in Table 6.3), as will be shown in the following.

When the composite is subjected to macroscopic in-plane shearing, as illustrated in Fig. 6.18(a), severe out-of-plane shear deformation can develop locally due to the presence of

the nearly rigid clay platelets, as evidenced by contour of ε_{23} of 6-Wt% isotropic-matrix-composite shown in Fig. 6.18(d)[6]. When the matrix material is isotropic, slip resistance is the same for both in-plane and out-of-plane shearing; however, when the matrix has weaker out-of-plane slip resistances, as is the case here, the existence of such out-of-plane distortions will trigger the weaker slip systems ($R_{12} = R_{23} = 0.5$), and act to substantially reduce the overall composite yield strength, $\tau_{y,13}$.

[6] Note that the elements used in FE simulations are originally cubic-shaped, thus shear deformation can be directly demonstrated through the distortion of the elements.

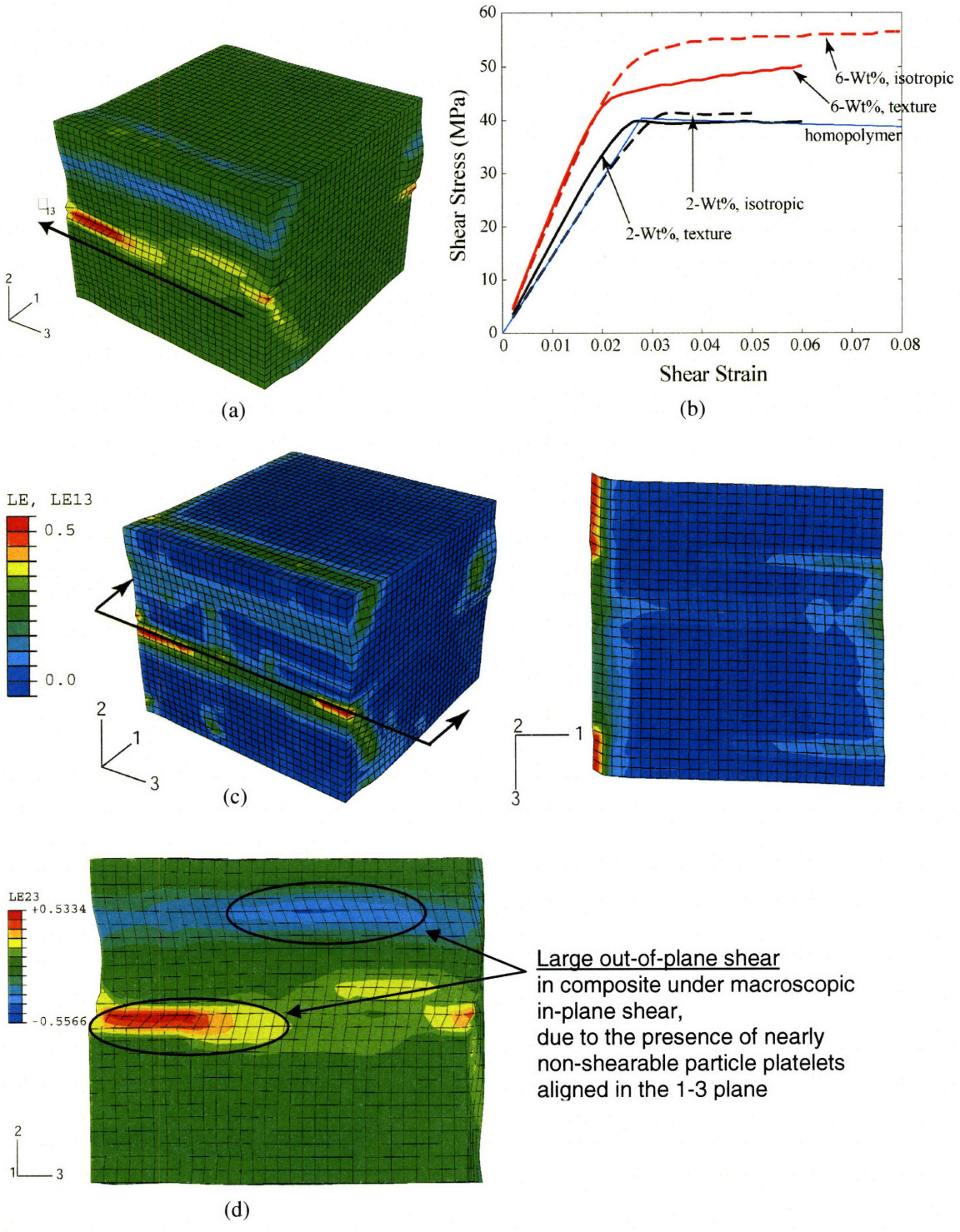

Figure 6.18: (a) Schematic of 3D RVE subjected to in-plane shearing. (b) Shear stress-strain curves of 2-Wt% and 6-Wt% composites modeled with isotropic matrix and with textured matrix (refer to Fig. 6.10c). (c) Contour of ε_{13} of 6-Wt% composite with anisotropic matrix, at ~ 0.06 macroscopic in-plane shear strain. (d) Contour of ε_{23} of 6-Wt% composite with isotropic matrix, at about 0.08 macroscopic in-plane shear strain, showing presence of large out-of-plane shear deformation (note that the elements are originally cubic-shaped, shear deformation is direction demonstrated through element distortions).

6.5. Effect of Particle Orientation Distribution on Axial Yielding of Composite

6.5.1. Anisotropic matrix behavior under off-axial loading (3D and 2D)

Before investigating influences of particle orientation as well as off-axial loading on the tensile properties of nanocomposites, it is helpful to establish a thorough understanding of the off-axial tensile behavior of the anisotropic matrix. Fig. 6.19(a) and (b) depict the 3D and 2D stress-strain responses of the anisotropic homo-polymer subjected to uniaxial tensile loadings in various directions; the loading axis resides in the plane spanned by the material base vectors $\mathbf{m}_1$ and $\mathbf{m}_2$ (recall that base vector $\mathbf{m}_2$ is the axis of isotropy for the material transverse isotropy) and the off-axial loading angle θ, are measured with respect to the base vector $\mathbf{m}_1$. Schematics of the transversely isotropic crystalline morphology as well the orientation of base vectors $\{\mathbf{m}_i\}$ are illustrated in Fig. 6.19(d).

As shown in Fig. 6.19(a), the material exhibits the highest modulus and yield strength when loaded in the two axial directions (0° and 90°); the ratios E_θ/E_m, $\sigma_{y,\theta}/\sigma_{y,m}$, where $\theta = 0^\circ$ or 90°, depend on the anisotropic elastic and yield material constants prescribed in Table 6.1 and Table 6.2:

$$E_0 / E_m = E_{11} / E_m = E_{33} / E_m = 1.29; \quad E_{90} / E_m = E_{22} / E_m = 0.99$$
$$\sigma_{y,0} / \sigma_{y,m} = R_{11} = R_{33} = 1.6; \quad \sigma_{y,90} / \sigma_{y,m} = R_{22} = 3.0$$

Off-axial loading triggers sampling of the more compliant and weaker slip systems (G_{12}/G_m = 0.11, R_{12} = 0.5), and consequently, substantial decrease in modulus and strength; in fact, with as little as 10 degrees of deviation from the material axis $\mathbf{m}_1$, the anisotropic material no longer exhibits an advantage over the isotropic material.

Note that the discrepancy between 0 and 90 degree axial behaviors almost vanished in the 2D plane strain simulations (Fig. 6.19b), due to the biaxial-loading nature resulting from the plane strain constraint, as discussed earlier in Chapter 5 (Section 5.2). To demonstrate the plane-strain effect on the tensile behavior of the anisotropic matrix material, we also plotted results from 3D plane strain simulations (loaded in the $\mathbf{m}_1$-$\mathbf{m}_2$ plane, zero-strain in the $\mathbf{m}_3$ direction) in Fig. 6.19(c); comparison of Fig. 6.19(b) and (c) shows that the 2D and 3D plane strain tensile responses are nearly identical. In summary, comparing with 3D uniaxial tension results, the 2D plane-strain simulation predicts much higher axial tensile properties (0^o), and exaggerates the effect of off-axial loading.

6.5.2. Effect of particle orientation distribution on $\sigma_{y,11}$

Similarly as in Section 5.2 for isotropic matrix, 2D RVEs with different degrees of particle orientation distributions are constructed to study the effect of particle misalignment on the composite end properties at the presence of textured matrix: (a) perfectly aligned, (b) Orientation-1 (SDV~6^o), (c) Orientation-2 (SDV~14^o), and (d) Orientation-3 (SDV~32^o). In all cases particles are assumed to be exfoliated with L = 100 nm and t = 0.678 nm; matrix anisotropy is modeled as described earlier in Section 6.2 (following Tzika, et al., 1999) with reference isotropic matrix properties E_m = 3 GPa, $\sigma_{y,m}$ = 70 MPa. RVEs are subjected to uniaxial tension loading with the loading axis aligned in the direction of average particle orientation (in the case of perfect particle alignment, the loading axis is parallel to the particle planes). Corresponding stress-strain curves are plotted in Fig. 6.20, together with the uniaxial tension behaviors of the isotropic and anisotropic homo-polymers. Apparently, with relatively small degrees of particle

misalignment (e.g., SDV of 6^{o} in Orient-1, and SDV of 14^{o} in Orient-2), the effect of particle orientation on the macroscopic stress-strain behavior is almost negligible. However, the misaligned particles can bring about significant alteration in the underlying deformation development, which is well illustrated via comparison of the contours of the equivalent plastic strain for case (a) (perfectly aligned), case (b) (orientation distribution with SDV-14^{o}), and case (d) (orientation distribution with SDV-32^{o}) at various stages of deformation, as shown in Fig. 6.21. Clearly, when particles are well aligned, plasticity initiates at particle ends due to stress concentration; as macroscopic strain increases, these local deformation pathways interconnect with each other and form into shear bands that percolate though the entire RVE. Once a shear band is formed, the material within the band undergoes excessive shear deformation due to the anisotropic yield of the matrix ($R_{12} = 0.5 << R_{11} = 1.6 < R_{33} = 3.0$), which explains the steep drop in axial stress that occurs at ~ 0.06 axial strain in the stress-strain response shown in Fig. 6.21 a.3 (the post-yield softening phenomenon has been discussed earlier in Section 6.4.2.1). However, when particles take on a wider distribution of orientation (e.g., SVD-32^{o}, as shown in Fig. 6.21c), plasticity initiates at regions where large shear strain occurs rather than exclusively at particle ends, as in case (a); these regions usually are near a particle or a cluster of particles (hence the local material base vector $\mathbf{m}_1$, which lies in the particle plane) oriented at ~ $\pm$ 45 degrees with respect to the loading direction, where the weak slip process (R_{12}) is triggered. In addition, no apparent shear band is formed until a much later stage of deformation. For the intermediate cases, such as SDV-14^{o} shown in Fig. 6.21b, initiation of plasticity triggered by stress concentration as well as by large shear has been observed to coexist.

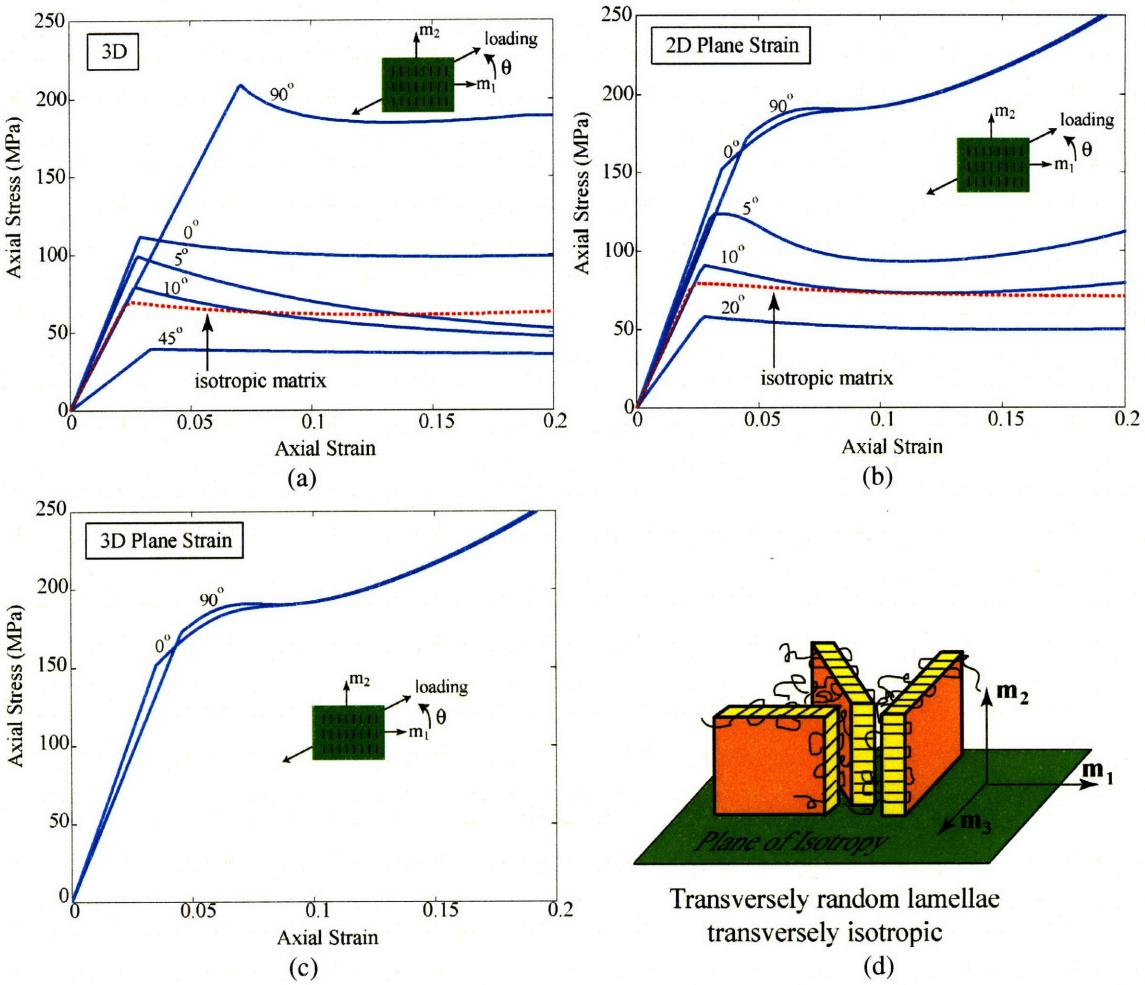

Figure 6.19: Tensile behaviors of transversely anisotropic matrix loaded at various angles with respect to the material base vector m_1 (m_1 parallel to the plane of isotropy): (a) 3D uniaxial, loaded in the m_1-m_2 plane; (b) 2D plane strain; (c) 3D plane strain: loaded in the m_1-m_2 plane, plane strain condition in the m_3 direction; (d) Schematic of the transversely isotropic morphology of the crystalline structure and the base vectors {m_1, m_2, m_3}. Dotted line denotes the uniaxial tensile behavior of the isotropic matrix

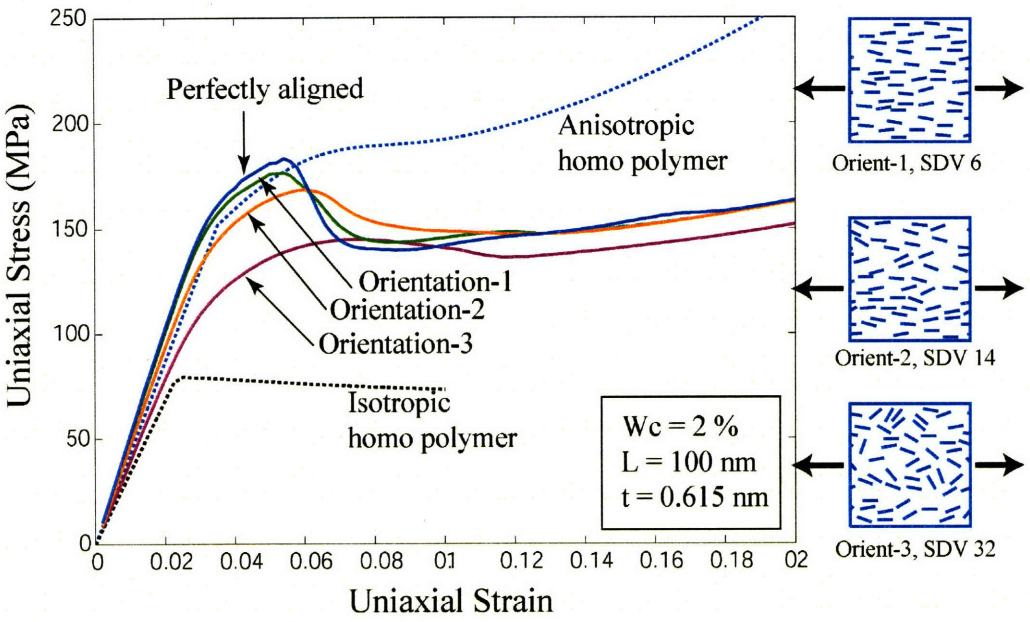

Figure 6.20: Uniaxial tension behaviors of nanocomposites with various particle orientation distributions (W_c = 2%, E_m = 3 GPa, $\sigma_{y,m}$ = 70 MPa): perfect alignment, Orientation -1 (SDV~6°), Orientation-2 (SDV~14°), and Orientation-3 (SDV~32°).

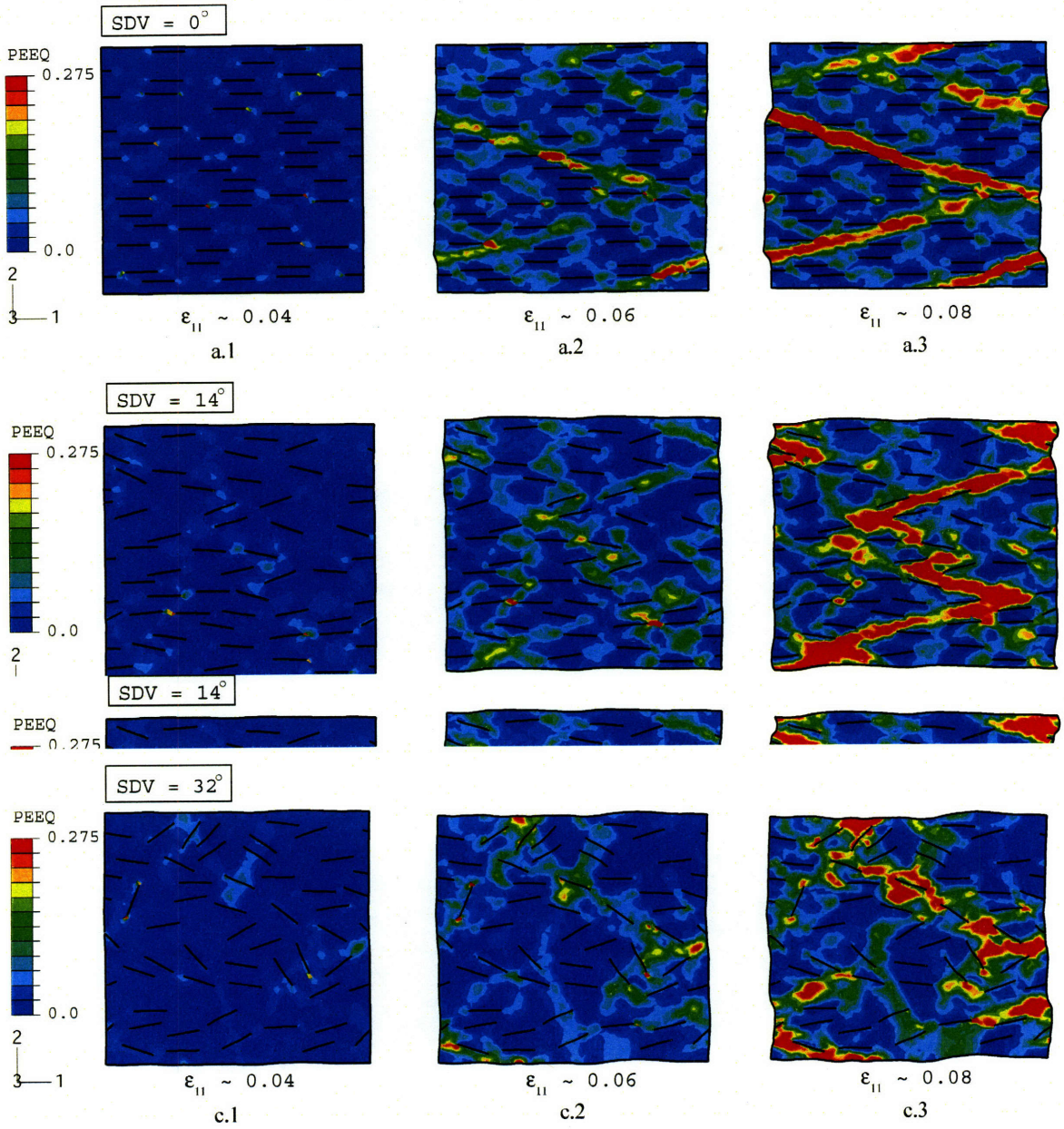

Figure 6.21: Contours of the equivalent plastic strain at various stages of deformation: (a), perfect particle alignment; (b), Orientation-2, SDV~ 14°; (c), Orientation-3, SDV~ 32°; macroscopic axial strain at 0.04 (1), 0.06 (2), and 0.08 (3).

6.6. Summary

In semi-crystalline polymer nanocomposites, the nanoclay plays a dual-role in the mechanical property enhancement — first, as an efficient filler with high stiffness and high aspect ratio; secondly, as a nucleation site that induces changes in the morphology of the matrix polymer, which in turn results in remarkable enhancements in the end composite properties. The enhancements of composite modulus and strength are found to rely on different functions of the clay: while the modulus enhancement can be explained by the conventional role of "stiff filler", the strength enhancement of the nanocomposite mainly lies in the improvements of the matrix property achieved through the matrix transcrystallization induced by the nanoclay "nucleation site". The degree of anisotropy in the composite elastic and yield properties results from both the nanoclay and the textured matrix. Due to the high axial yield strength of the textured material, local buckling of the nanoclay can be triggered when the composite is subjected to axial compression or transverse tension. In addition, the uniaxial tension and compression behaviors of the composite can bear considerable difference as a result of the formation of distinctive percolating deformation pathways under tension vs. compression. The weak transverse slip resistance of the oriented matrix polymer, under certain circumstances that favor the formation of percolating shear bands (such as 2D plane-strain condition, or change in local particle orientation resulted from particle buckling), can lead to significant post-yield softening. The effect of initial particle orientation on the macroscopic stress-strain behavior of the composite is almost negligible; however, the misaligned particles can bring about significant alteration in the underlying plastic deformation development.

Chapter 7

Conclusions and Future Work

Continuum-based micromechanical models can provide robust predictions of the overall thermal/mechanical properties of polymer/clay nanocomposites, provided that a reliable method is employed to account for the intrinsically hierarchical morphology of intercalated nanoclay, and for the special matrix morphology and properties adjacent to the nanoclay. The intercalated nanoclay, idealized as a multi-layer stack with N silicate sheets and inter-layer spacing of $d_{(001)}$, can be effectively represented as a homogeneous "particle", which comprises the same spatial domain occupied by both the silicate layers and the inter-layer galleries. Transcrystallization behavior in a semi-crystalline polymer matrix, induced by the presence of nanoclay, is taken into account by defining highly-anisotropic matrix layers around the particles. A careful mapping between the characteristic clay structural parameters (N, $d_{(001)}$) and clay weight fraction (W_c) and the conventional micromechanical model parameters (particle volume fraction f_p, particle aspect ratio L/t, and anisotropic thermal/mechanical properties of the particle) is established. Various three-dimensional and two-dimensional representative volume elements (RVEs) of the underlying structure of polymer/clay nanocomposite are constructed and utilized in finite element simulations, enabling the assessment of the effect of morphological features of different lengthscales on the end composite properties. The model prediction of the overall axial modulus and anisotropic thermal expansion behavior of well-characterized amorphous (MXD 6) and semi-crystalline (nylon 6)

polymer/clay nanocomposites are in good agreement with experimental data. In addition, the complete sets of anisotropic elastic properties as well as the anisotropic yield surface of the nanocomposite are determined by stretching and shearing the RVE in all three orthogonal directions. An idealized "upper-bound" model is proposed to investigate the effects of special matrix morphology induced by the addition of nanoclay in semi-crystalline polymers on the anisotropic elastic and yield properties of the nanocomposite. The impact of clay structural parameters (N, $d_{(001)}$), as well as properties of the matrix homopolymer, on the overall thermal/mechanical properties of the nanocomposite are probed through systematic parametric studies. Important results and observations regarding elastic, thermal expansion, and yielding behavior of the nanocomposites are summarized in the following:

1. Elastic Properties

The elastic behavior of polymer/clay nanocomposite (with clay particles aligned in the 1-direction) is rather anisotropic. While the in-plane properties ($E_{11}= E_{33}$ and G_{13}), are well reinforced by the stiff fillers, the influence of clay on the out-of-plane counterparts, (E_{22} and G_{12}, especially G_{12}), are rather limited. Two mechanisms are found to play important roles in the stiffness enhancement of the nanocomposite: the load transfer mechanism and the "plane-strain" constraint mechanism. Load transfer from surrounding matrix to the particle through interface shearing is the governing mechanism for the well-observed enhancement in the composite axial modulus E_{11}; large particle aspect ratio and high relative matrix shear modulus are desired for efficient load transfer. On the other hand, the high aspect ratio high stiffness particles create a nearly plane-strain constraint on the in-plane deformation of surrounding matrix; such constraint acts to increase the

composite transverse modulus (E_{22}) and the out-of-plane Poisson ratio (ν_{12}), but to decrease the in-plane Poisson ratio (ν_{13}). There is a strong dependence of the overall elastic properties on the degree of particle exfoliation (characterized by the number of silicate sheets in a primary "particle", N): at a fixed W_c, exfoliated clay morphology is found to be most efficient in the composite stiffness enhancement; however, no dramatic transition occurs as N goes from 2 → 1 (i.e., intercalated → exfoliated) due to the counteracting effects of increased particle aspect ratio and decreased particle volume fraction. The stiffness enhancement efficiency also depends on the base matrix modulus: elastomer nanocomposites in general see much more dramatic improvement in the stiffness compared to thermoplastic nanocomposites, due to the large particle/matrix stiffness ratio (E_p/E_m). A direct consequence of the E_p/E_m effect on soft matrices is the much-improved Heat Distortion Temperature (HDT) of thermoplastic polymer nanocomposites.

2. Thermal Expansion

Like the elastic properties, thermal expansion of well-aligned polymer/clay nanocomposite is highly anisotropic as well — while the in-plane coefficient of thermal expansion (CTE) of the composite is sufficiently reduced by the addition of the nanoclay, the transverse CTE of the composite is increased substantially due to the in-plane constraint imposed by the low-CTE, planar-shaped nanoclay inclusion, giving an additional Poisson-effect expansion normal to the particle plane. For a given clay weight fraction, the effect of clay exfoliation vs. intercalation on CTE is found to be rather trivial for thermoplastic polymer nanocomposites. When the matrix is elastomer, the degree of

anisotropy in the composite thermal expansion is enhanced due to the high Poisson ratio of the elastomer polymer and also due to the high E_p/E_m stiffness ratio.

3. Initial Yield Strength

In amorphous polymer nanocomposites, where no change in the matrix morphplogy occurs, the enhancement in the composite axial initial yield strength ($\sigma_{y,11}$) is less prominent compared to the composite axial modulus. The strain shielding effect of the particle proves to be a crucial mechanism for the increase in the composite $\sigma_{y,11}$: the stiff particles cause the formation of low-strain zones in their vicinity; materials in these regions bear load, but remain elastically stiff; the shear bands percolate around these regions, finding a continuous path across a net section, giving macroscopic yield. Composite $\sigma_{y,11}$ is found to increase with increasing clay weight fraction, since the addition of clay particles raises the proportion of the constrained elastic regions in the matrix and increases the degree of the tortuosity of the plastic deformation pathways. Unlike for the composite modulus, the impact of the clay morphology on composite $\sigma_{y,11}$ is rather significant: $\sigma_{y,11}$ experiences a steep jump when the morphology transits from intercalation to exfoliation. Such phenomenon can be attributed to the considerably higher volume of the "constrained region" and degree of tortuosity of an exfoliated nanocomposite as opposed to an intercalated one with the same clay fraction. The impact of particle misalignment on the composite modulus and yield strength is found to be negligible when the SDV of the orientation angle is less than 14^o; only when the orientation distribution widens and approaches randomness is the clay reinforcement efficiency noticeably impaired. The anisotropic initial yield surface of the nanocomposite

can be characterized in terms of the so-called Hill ratios; the degree of anisotropy for low $\sigma_{y,m}$ matrices are observed to be higher than for typical thermoplastics.

4. Matrix Transcrystallization Effects

In semi-crystalline polymer nanocomposites, the nanoclay plays a dual-role in the mechanical property enhancement — first, as an efficient filler with high stiffness and high aspect ratio; secondly, as a nucleation site that induces changes in the morphology of the matrix polymer, which in turn results in remarkable enhancements in the end composite properties. The enhancements of composite modulus and strength are found to rely on different functions of the clay: while the modulus enhancement can be explained by the conventional role of "stiff filler", the strength enhancement of the nanocomposite mainly lies in the improvements of the matrix property achieved through the matrix transcrystallization induced by the nanoclay "nucleation site". The degree of anisotropy in the composite elastic and yield properties results from both the nanoclay and the textured matrix. Due to the high axial yield strength of the textured material; local buckling of the nanoclay can be triggered when the composite is subjected to axial compression or transverse tension. In addition, the uniaxial tension and compression behaviors of the composite can bear considerable difference as a result of the formation of distinctive percolating deformation pathways under tension vs. compression. The weak transverse slip resistance of the oriented matrix polymer, under certain circumstances that favor the formation of percolating shear bands (such as 2D plane-strain condition, or change in local particle orientation resulted from particle buckling), can lead to significant post-yield softening. The effect of initial particle orientation on the macroscopic stress-strain behavior of the composite is almost negligible; however, the

misaligned particles can bring about significant alteration in the underlying plastic deformation development.

Future Work

1. Model Construction

Particle Orientation Distribution

In this work, 3D RVEs with well-oriented particles that possess a random spatial distribution are constructed for FE-based simulations of thermal/mechanical properties of the nanocomposite. However, 2D RVEs are employed when accessing the effects of particle orientation distribution for simplification. Such a treatment, while computationally efficient, introduces numerous restrictions due to the two-dimensional nature of the simulation (e.g., the plane-strain constraint imposed by 2D plane strain simulations and the neglect of the 3D nature of the orientation distribution as well as the 3D nature of the particle geometry). Therefore it is desirable to develop 3D RVEs containing particles that follow a specific orientation pattern (the orientation distribution information can be obtained through various microscopy techniques, Loo and Gleason, 2004). Preliminary attempts made by the author suggest that automatic mesh-generating tools such as *Tetgen* can be used to facilitate the RVE construction process.

Particle Geometry

So far the clay particles in the model adopt a simplified planar geometry with the particle aspect ratio, defined to be the in-plane size/thickness ratio, as the characteristic parameter. In reality, nanoclay platelets are often observed to possess certain curvature since the

slender particles (especially exfoliated single-layer silicate sheets) are highly prone to bending or shear deformations. In the future work, particle models should be extended to include the particle curvature as a geometrical parameter in addition to the particle aspect ratio (in fact, the introduction of curviness reduces the effective particle aspect ratio); effects of the particle curviness on the nanocomposite properties need to be investigated parametrically.

2. Large Deformation Behavior and Failure Mechanism

This work focuses on the thermal/mechanical behavior of nanocomposites under relatively small deformation (less than 10% strain). The micromechanics involved in larger scale deformation as well as failure mechanisms for different nanocomposite systems prove to be extremely interesting and challenging topics. One of the challenges lies in the lack of systematic experimental results — rather contradicting tensile behaviors of various polymer/clay nanocomposites have been reported (e.g., 5-Wt% MXD6 nylon/clay nanocomposite behaves in a rather brittle manner, whereas McNally et al. (2003) observed improvements in both strength and elongation at break for 4-Wt% nylon 12/fluoromica nanocomposite) — careful treatment of the literature data, such as the complete recording of the nanocomposite morphology/material/processing features performed in Section 5.5, is needed for a comprehensive understanding of the underlying mechanism as well as the identification of the key player among material parameters of various lengthscales.

In the modeling of the large deformation behavior or even failure events of the nanocomposite, special attention should be given to the deformation modes of the nanoclay particle. The particle model needs to be extended to properly account for large

bending (exfoliated clay platelets) and large shearing (intercalated stacks with low inter-layer shear modulus); in addition, proper criteria for possible delamination and cavitation processes during deformation need to be developed. Systematic experiments that capture the anisotropic tension/compression behaviors of the nanocomposite as well as characterization of the microstructure evolution at various stages of the deformation are critical for micromechanical modeling of the proper physics.

Appendix A

MATLAB Codes for the Generation of 2D RVEs with Triangular Meshes

A series of MATLAB codes is employed for the automatic generation of ABAQUS input files of 2D RVEs containing particles with a prescribed orientation distribution. Triangular mesh generator *Triangle*[1] is used to create triangular meshes for the desired particle spatial distribution. The procedure leading to the final generation of the *.inp file are described in the following (indivial MATLAB codes are well-commented and are not repeated here):

- Run T1_geo.m. This code will ask for generic information (e.g., particle geometry, volume fraction, and orientation distribution) and generate an initial input file (*test.poly*) for the mesh generator *Triangle*.
- Copy *test.poly* to the work directory of Triangle and run. Successful triangulation will generate node file test.1.node and element file test.1.ele. Note that the nodes on periodic boundaries might not fall into periodic pairs. Copy the Triangle output files to the MATLAB work directory. Example of Triangle command line:

  triangle -pq25La4A test.poly

- Run T2_new.m. A new input file (*test.new.poly*) for Triangle is generated, in which the periodic boundaries consist only of well-matching node-pairs.

[1] http://www.cs.cmu.edu/~quake/triangle.html

- Copy *test.new.poly* to the Triangle work directory and run. Repeat the previous command line, only adding option 'Y' in the end to prohibit additional node generation on the boundaries. Copy output files test.new.1.node and test.new.1.ele to the MATLAB work directory. Command line example:

  triangle -pq25La4AY test.new.poly

- Run T3_par.m. Boundary nodes are paired and recorded into files.

- Run T4_final.m. ABAQUS input file with period boundary conditions is finally generated.

1. T1_geo.m

```
% ##################################################
% T1_geo.m
% GENERATE TRIANGLE INPUT FILE
% SUBROUTINE:     test_new.m
% OUTPUT FILE:    test.poly
% ##################################################

clear all

test_new;     % Create New Particle Info

dL1 = 10; dL2 = 10;          % delta_X and delta_Y for the matrix
dPL = 5; dPT = GeoParThMean/3;  % delta_X and delta_Y for the particle
% Number of subdivisions for the matrix
N1 = GeoMatWidth/dL1; N2 = GeoMatHeight/dL2;
% Number of subdivixsions for the particle
PN1 = GeoParLMean/dPL; PN2 = GeoParThMean/dPT;

NSeg = 4*(1 + Np1);     % Total number of segments

% Total number of holes -- this corresponds to the number of the particles
NHole = 0;          % Zero holes: if particles are modeled as beams

% Number of attributes = total number of particles
NAttrib = 0;

nl = 0;nl = nl + 1;
M(nl, 1) = 0; M(nl,2) = 2; M(nl,3) = 0; M(nl,4) = 1; nl = nl + 1;

% Write Matrix vertices
% M(i,1) -- Vertex #; M(i,2:3)-- Vertex coordinates;
% M(i,4)-- boundary marker;
```

```
M(nl,1) = 1; M(nl,2) = 0; M(nl,3) = 0; M(nl,4) = 200; nl = nl+1;
M(nl,1) = 2; M(nl,2) = GeoMatWidth; M(nl,3) = 0; M(nl,4) = 200; nl = nl+1;
M(nl,1) = 3; M(nl,2) = GeoMatWidth; M(nl,3) = GeoMatHeight; M(nl,4) = 200;
nl = nl+1;
M(nl,1) = 4; M(nl,2) = 0; M(nl,3) = GeoMatHeight; M(nl,4) = 200;
nl = nl+1;

% particle segment indices
s = 1;
% Write Particle Vertices
for i = 1:Np1
   for j = 1:2
      M(nl,1) = M(nl-1,1)+1;     % node number
      M(nl,2) = ParInfo(j,1,i);  % x-coordinate
      M(nl,3) = ParInfo(j,2,i);  % y-coordinate

      % record the first particle node number
      if M(nl,2)==0                          % on the LEFT edge
         M(nl,4) = 4;
      elseif M(nl,2)==GeoMatWidth            % on the RIGHT edge
         M(nl,4) = 2;
      elseif M(nl,3)==0                      % on the BOTTOM edge
         M(nl,4) = 1;
      elseif M(nl,3)==GeoMatHeight           % on the TOP edge
         M(nl,4) = 3;
      else
         M(nl,4) = 100 + i;                  % node marker
      end
      nl = nl + 1;
   end
   ParInfo(5,1,i) = M(nl-2,1);  % record the first particle node number

   PN2_temp = GeoParThMean/dPT;

   % BOTTOM EDGE
   PN1_bot = round(norm(ParInfo(1,:,i)-ParInfo(2,:,i))/dPL);
   for j = 1:(PN1_bot-1)              % interior bottom edge nodes
      M(nl,1)=M(nl-1,1)+1;
      M(nl,2)=ParInfo(1,1,i)+j*(ParInfo(2,1,i)-ParInfo(1,1,i))/PN1_bot;
      M(nl,3)=ParInfo(1,2,i)+j*(ParInfo(2,2,i)-ParInfo(1,2,i))/PN1_bot;
      M(nl,4)=100+i;
      % Create segments
      Par_seg(s,1) = s;
      if j==1
         Par_seg(s,2) = ParInfo(5,1,i);
         Par_seg(s,3) = M(nl,1);
      else
         Par_seg(s,2) = M(nl-1,1);
         Par_seg(s,3) = M(nl,1);
      end
      Par_seg(s,4) = 10000 + i;
      s = s + 1;
      nl=nl+1;
   end
   Par_seg(s,1) = s;
   Par_seg(s,2) = M(nl-1,1); Par_seg(s,3) = ParInfo(5,1,i)+1;
```

```
   Par_seg(s,4) = 10000 + i; s = s+1;

end
Par_seg(:,1) = Par_seg(:,1)+4;

% Write additional Matrix Vertices
for i = 1:(N1-1)
   temp(1,1)=M(nl-1,1)+1; temp(1,2)=i*dL1; temp(1,3)=0; temp(1,4)=1;
   new = 1;
   for p = 6:(nl-1)
      if temp(1,2:3)==M(p,2:3) new=0; break; end
   end
   if new
      M(nl,:)=temp; nl = nl + 1;
   end
end
for i = 1:(N1-1)
   temp(1,1)=M(nl-1,1)+1; temp(1,2)=i*dL1; temp(1,3)=GeoMatHeight;
   temp(1,4)=3;
   new = 1;
   for p = 6:(nl-1)
      if temp(1,2:3)==M(p,2:3) new=0; break; end
   end
   if new
      M(nl,:)=temp; nl=nl+1;
   end
end
for i = 1:(N2-1)
   temp(1,1)=M(nl-1,1)+1; temp(1,2)=0; temp(1,3)=i*dL2; temp(1,4) = 4;
   new = 1;
   for p = 6:(nl-1)
      if temp(1,2:3)==M(p,2:3) new=0; break; end
   end
   if new
      M(nl,:)=temp; nl=nl+1;
   end
end
for i = 1:(N2-1)
   temp(1,1)=M(nl-1,1)+1; temp(1,2)=GeoMatWidth; temp(1,3)=i*dL2;
   temp(1,4) = 2;
   new = 1;
   for p = 6:(nl-1)
      if temp(1,2:3)==M(p,2:3) new=0; break; end
   end
   if new
      M(nl,:)=temp; nl=nl+1;
   end
end

% correct total number of nodes
M(1,1) = M(nl-1,1);

M(nl,1) = 4 + (s-1) + nV; M(nl,2) = 1; nl = nl + 1;

% Write Matrix Segments
M(nl,1)=1; M(nl,2)=1; M(nl,3)=2; M(nl,4)=1; nl=nl+1;    % BOTTOM
```

```
M(nl,1)=2; M(nl,2)=2; M(nl,3)=3; M(nl,4)=2; nl=nl+1;   % RIGHT
M(nl,1)=3; M(nl,2)=3; M(nl,3)=4; M(nl,4)=3; nl=nl+1;   % TOP
M(nl,1)=4; M(nl,2)=4; M(nl,3)=1; M(nl,4)=4; nl=nl+1;   % LEFT

nl = 1;
M1(nl,1) = NHole; nl=nl+1;  % zero holes

M1(nl,1) = NAttrib; nl=nl+1;

dlmwrite('test.poly',M,'delimiter','\t','precision',10);
dlmwrite('test.poly', Par_seg, '-append', 'delimiter', '\t');
dlmwrite('test.poly', M1, '-append', 'delimiter', '\t','precision',10);

save ParInfo ParInfo ParGeoList ParAngDist ParAngVar;
```

2. T2_new.m

```
% ########################################################
% T2_new.m
% GENERATE NEW TRIANGLE INPUT FILE
% INPUT FILE:  test.poly
%              test.1.node
% OUTPUT FILE: test.new.poly
% ########################################################

clear all
L1 = 665; L2 = L1;  % RVE size

M = dlmread('test.poly','\t');
[N1, M1] = ReadNode('test.1.node');

N = M(1,1);

k = 1;
for i = 2:(1+N1)
   a = M1(i,4);
   if a==1 | a==2 | a==3 | a==4
      new = 1;
      for j = 2:(1+N)
         if M1(i,2:3) == M(j,2:3)
            new = 0; break
         end
      end
      if new==1
         X(k,1)=k; X(k,2)=M1(i,2); X(k,3)=M1(i,3); X(k,4)=M1(i,4);k=k+1;
         if M1(i,2)==0   Y(1,1)=k; Y(1,2)=L1; Y(1,3)=M1(i,3); Y(1,4)=2;
         elseif M1(i,2)==L1
            Y(1,1)=k; Y(1,2)=0; Y(1,3)=M1(i,3); Y(1,4)=4;
         elseif M1(i,3)==0
            Y(1,1)=k; Y(1,2)=M1(i,2); Y(1,3)=L2; Y(1,4)=3;
         elseif M1(i,3)==L2
            Y(1,1)=k; Y(1,2)=M1(i,2); Y(1,3)=0; Y(1,4)=1;
         end
         new1 = 1;
         for p = 2:(1+N1)
            if Y(1,2:3)==M1(p,2:3)  new1=0; break; end
```

```
        end
        if new1
          for p = 2:(1+N)
            if Y(1,2:3)==M(p,2:3) new1=0; break; end
          end
        end

        if new1  X(k,:)=Y; k=k+1; end
      end
    end
end

A = M(1:(1+N), :);
B = M((N+2:size(M,1)), :);

X(:,1)=X(:,1) + N;
A(1,1) = N + size(X,1);

dlmwrite('test.new.poly', A, '\t');
dlmwrite('test.new.poly', X, '-append', 'delimiter', '\t');
dlmwrite('test.new.poly', B, '-append', 'delimiter', '\t');
```

3. T3_par.m

```
% ##########################################################
% T3_par.m
% IDENTIFY BOUNDARY NODE SETS: LEFT, RIGHT, TOP, BOTTOM
% INPUT FILE:     test.new.1.node
%                 test.new.1.ele
% OUTPUT FILE:    left.node, right.node
%                 bottom.node, top.node
% ##########################################################

clear all

L1 = 665; L2 = L1;                    % width and height of the 2D RVE

[NNode, M] = ReadNode('test.new.1.node');
[NEle, Q] = ReadEle('test.new.1.ele');

% O -- higher order element flag: O=1 -> linear; O=2 -> quadratic
O = 1;

dPL = 0.2; dPT = 0.2;  % delta_X and delta_Y for the particle

%Match boundary nodes
nL = 1; nR = 1; nB = 1; nT = 1;
for i = 6:(NNode+1)
  if M(i,4) == 1
    MB(nB,1)=M(i,1); MB(nB,2:3)=M(i,2:3); nB=nB+1;   %bottom
  elseif M(i,4) == 2
    MR(nR,1)=M(i,1); MR(nR,2:3)=M(i,2:3); nR=nR+1;   %right
  elseif M(i,4) == 3
    MT(nT,1)=M(i,1); MT(nT,2:3)=M(i,2:3); nT=nT+1;   %top
  elseif M(i,4) == 4
```

```
      ML(nL,1)=M(i,1); ML(nL,2:3)=M(i,2:3); nL=nL+1;   %left
   end
end

% number of nodes at left, right, bottom and top
nL = nL-1; nR = nR-1; nB = nB-1; nT=nT-1;

% sort ML/MR and MB/MT to match the nodes
for i = 1:nL
   found = 0;
   for j = i:nL
      if MR(j,3)==ML(i,3)
         temp = MR(i,:);
         MR(i,:) = MR(j,:);
         MR(j,:) = temp;
         break
      end
   end
end

for i = 1:nB
   found = 0;
   for j = i:nB
      if MT(j,2)==MB(i,2)
         temp = MT(i,:);
         MT(i,:) = MT(j,:);
         MT(j,:) = temp;
         break
      end
   end
end

dlmwrite('Left.node', ML(:,1));
dlmwrite('Right.node', MR(:,1));
dlmwrite('Bottom.node', MB(:,1));
dlmwrite('Top.node', MT(:,1));
```

4. T4_final.m

```
% ######################################################################
% T4_final.m
% GENERATE ABAQUS INPUT FILE
% OUTPUT FILE:     *.inp
% ######################################################################
clear all

L1 = 665; L2 = L1; D = 10;
O = 1; % O = 1 -> linear element; O = 2 -> quadratic element
load ParInfo ParInfo;
Np1 = size(ParInfo,3);

% $$$$$$$$$$$$$$$$$$  INPUT MATERIAL PROPERTIES $$$$$$$$$$$$$$$$$$

clear title prompt def answer1 answer data
title = 'Input material properties';
```

```
prompt = {'Clay tensile modulus (GPa):', 'Clay Poisson ratio :',...
        'Polymer tensile modulus (GPa):', 'Polymer Poisson ratio :'};
def = {'250','0.2','3.37','0.33'};
lines= 1;
answer1  = inputdlg(prompt,title,lines,def);
answer=char(answer1);
data=str2num(answer);

EClay = data(1);
NuClay = data(2);
EPolymer = data(3);
NuPolymer = data(4);

% $$$$$$$$$$$$$$$$$$  MATERIAL PROPERTIES OVER $$$$$$$$$$$$$$$$$$$$

% material property -- polymer matrix
mater = zeros(1,12);
mater(1) = EPolymer*1e9;     %  Yong
mater(2) = NuPolymer;        %      Nu
mater(3) = 1.7e-5;           %      Talf
mater(4) = 5.4e7;            % (1/s) Strain rate
mater(5) = 2.5e-19;          % (nN*nM) G0
mater(6) = 95e6;             %  S_ss
mater(7) = 65e6;             %  S_0
mater(8) = 150e6;            %  H
mater(9) = 3e6;              %  CR
mater(10) = 4.5;             %      N
mater(11) = 298.0;           % (K)  Temp
mater(12) = 0.075;           %      Alf
% Number of DEP var
depvar = 19;
E1 = EPolymer*1e9;
nu1 = NuPolymer;

% material property -- clay particle
E2 = EClay*1e9;
nu2 = NuClay;

% $$$$$$$$$$$$$$$$$$  INPUT LOADING CONDITION $$$$$$$$$$$$$$$$$$$$
clear title prompt def answer1 answer data
title = 'Input loading precondition';
prompt = {'Global E11 [type n/N to disable]',...
        'Global E22 [type n/N to disable]',...
        'Gloabl E12 [type n/N to disable]'};
def = {'0.005','N','0.0'};
lines= 1;
answer1  = inputdlg(prompt,title,lines,def);
answer=char(answer1);
%data=str2num(answer);
EnableFlag = ones(1,3);
temp1 = answer(1,:);temp = deblank(temp1);
if(strcmp(temp,'n')|strcmp(temp,'N')) EnableFlag(1)=0;
else LoadE11=str2num(answer(1,:));end
temp1 = answer(2,:);temp = deblank(temp1);
if(strcmp(temp,'n')|strcmp(temp,'N')) EnableFlag(2)=0;
else LoadE22=str2num(answer(2,:));end
```

```
temp1 = answer(3,:);temp = deblank(temp1);
if(strcmp(temp,'n')|strcmp(temp,'N')) EnableFlag(3)=0;
else LoadE12=str2num(answer(3,:));end
% $$$$$$$$$$$$$$$  LOADING PRECONDITIONING OVER $$$$$$$$$$$$$$$$$$$



% $$$$$$$$$$$$$$$$$$$$$$$ INPUT FILE NAME $$$$$$$$$$$$$$$$$$$$$$$$$

% DISPLAY 'SAVE FILE' DAILOG BOX
[filename, newpath]=uiputfile('*.inp','Save As');

% $$$$$$$$$$$$$$$$$$$ INPUT FILE NAME DECIDED $$$$$$$$$$$$$$$$$$$$

% $$$$$$$$$$$$$$$$$$$$$$$$$$$$$$$$$$$$$$$$$$$$$$$$$$$$$$$$$$$$$$$$$$$$$$$
% START WRITING ABAQUS INPUT FILE

% generate abaqus input file -- test.inp
fid = fopen(filename, 'w+');

fprintf(fid, '*HEADING\n');
fprintf(fid, 'periodic polymer matrix with uniforml\n');

CNode1 = 900000;
CNode2 = 900001;
Extra1 = 900002;
Extra2 = 900003;

fprintf(fid, '*NODE, NSET=CNode1\n');
fprintf(fid, '%6d,  -100,  -100,  0.0\n', CNode1);
fprintf(fid, '*NODE, NSET=CNode2\n');
fprintf(fid, '%6d,  -200,  -100,  0.0\n', CNode2);
fprintf(fid, '*NODE, NSET=Extra1\n');
fprintf(fid, '%6d,  -10,   -10,   0.0\n', Extra1);
fprintf(fid, '*NODE, NSET=Extra2\n');
fprintf(fid, '%6d,  -11,   -11,   0.0\n', Extra2);

[NNode, temp] = ReadNode('test.new.1.node');
NODE = temp(2:size(temp,1),1:3);
NODE(:,4) = 0;


fprintf(fid, '*NODE, NSET = ALL\n');
fprintf(fid, '%6d,   %4.2f,   %4.2f,   %2.1f\n', NODE');
%fprintf(fid, '%6d,   %4.2f,   %4.2f,   %2.1f\n', NODE_INT(:,1:4)');


% corner nodes
fprintf(fid, '*NSET, NSET = A\n');
fprintf(fid, '%6d\n', 1);
fprintf(fid, '*NSET, NSET = B\n');
fprintf(fid, '%6d\n', 2);
fprintf(fid, '*NSET, NSET = C\n');
fprintf(fid, '%6d\n', 3);
fprintf(fid, '*NSET, NSET = D\n');
fprintf(fid, '%6d\n', 4);
```

```
% print edges
clear temp;
temp = dlmread('Left.node');
fprintf(fid, '*NSET, NSET = LEFT, UNSORTED\n');
fprintf(fid, '%6d\n', temp);
clear temp;
temp = dlmread('Right.node');
fprintf(fid, '*NSET, NSET = RIGHT, UNSORTED\n');
fprintf(fid, '%6d\n', temp);
clear temp;
temp = dlmread('Bottom.node');
fprintf(fid, '*NSET, NSET = BOTTOM, UNSORTED\n');
fprintf(fid, '%6d\n', temp);
clear temp;
temp = dlmread('Top.node');
fprintf(fid, '*NSET, NSET = TOP, UNSORTED\n');
fprintf(fid, '%6d\n', temp);

% $$$$$$$$$$$$$$$$$$$$$$$$$ DEFINE ELEMENTS $$$$$$$$$$$$$$$$$$$$$$

% Matrix -- 8-node Continuum ele
% Particle :  FlagParEle == 1 -- 3-node Beam ele
%             FlagParEle == 2 -- 8-node Continuum ele

% define matrix elements: 6-node triangule elements

clear temp;
[NEle, temp] = ReadEle('test.new.1.ele');
ELE = temp(2:size(temp,1),:);


% Generate Silicate Sheet --> Beam Elements
[num, EDGE] = ReadEdge('test.new.1.edge');

for i = 1:Np1
   SHEET(1,1,i) = 0;
end

for i = 1:num
   temp = EDGE(i+1,:);
   marker = temp(4);  % Edge Marker
   if marker > 10000   % Particle Top/Bot edge
      particle = marker - 10000;      % ASSOCIATED PARTICLE #
      index = SHEET(1,1,particle);   % total # of edgeswhos

      index = index + 1;
      SHEET(1,1,particle) = index;
      SHEET(index+1,1,particle) = index;  % edge #
      SHEET(index+1,2:3,particle) = temp(2:3);    % edge nodes
      SHEET(index+1,4,particle) = particle;       % associated particle #
   end
end


temp = 0;
for i = 1:Np1
```

```
   num = SHEET(1,1,i);
   SHEET(2:num+1,1,i) = SHEET(2:num+1,1,i) + temp;
   temp = temp + num;
end

%num = ELEM(1,1);
ELE(:,1) = ELE(:,1) + temp;


% Particle Elements:
for i = 1:Np1
   num = SHEET(1,1,i);
   fprintf(fid, '*ELEMENT, TYPE=B21, ELSET=PARTICLE%1d\n', i);
   fprintf(fid, '%6d, %6d, %6d\n', SHEET(2:(num+1),1:3,i)');
end

fprintf(fid, '*ELSET, ELSET=PARTICLE\n');
for i = 1:Np1
          fprintf(fid, 'PARTICLE%1d, \n', i);
end

if O == 1   % linear element
   fprintf(fid, '*ELEMENT, TYPE = CPE3H, ELSET = MATRIX\n');
   fprintf(fid, '%6d, %6d, %6d, %6d\n', ELE(:,1:4)');
else    % quadratic element
   ELE(:,5) = temp1(:,7);
   ELE(:,6) = temp1(:,5);
   ELE(:,7) = temp1(:,6);
   fprintf(fid, '*ELEMENT, TYPE = CPE6H, ELSET = MATRIX\n');
   fprintf(fid, '%6d, %6d, %6d, %6d, %6d, %6d, %6d\n', ELE');
end

% $$$$$$$$$$$$$$$$$$$$ ELEMENT DEFINITION OVER $$$$$$$$$$$$$$$$$$$$


% material property -- polymer

%fprintf(fid, '*MATERIAL, NAME = POLYMER\n');
%fprintf(fid, '*USER MATERIAL,CONSTANTS=12\n');
%for i=1:8
%    fprintf(fid, '%4.2e,', mater(i));
%end
%fprintf(fid, '\n');
%for i=9:12
%    fprintf(fid, '%4.2e, ', mater(i));
%end
%fprintf(fid, '\n');
%fprintf(fid, '*DEPVAR\n');
%fprintf(fid, '%2d\n', depvar);

fprintf(fid, '*MATERIAL, NAME = POLYMER\n');
fprintf(fid, '*ELASTIC\n');
fprintf(fid, '%3.2e, %3.2f\n', E1, nu1);

% material property -- clay
fprintf(fid, '*MATERIAL, NAME = CLAY\n');
```

```
fprintf(fid, '*ELASTIC\n');
fprintf(fid, '%3.2e, %3.2f\n', E2, nu2);

% matrix el section property
fprintf(fid, '*SOLID SECTION, ELSET = MATRIX, MATERIAL = POLYMER\n');
fprintf(fid, '%2.1f, %2.1f, %2.1f\n', 10, 0, 0);

% particle el section property
 fprintf(fid, '*SOLID SECTION, ELSET=PARTICLE, MATERIAL=CLAY\n');
 fprintf(fid, '%2.1f, %2.1f, %2.1f\n', 10, 0, 0);

% periodic boundary
fprintf(fid, '*EQUATION\n');

fprintf(fid, '%1d\n', 3);
fprintf(fid, 'RIGHT, 1, 1.0, LEFT, 1, -1.0, CNode1, 1, %6.1f\n', -L1);

fprintf(fid, '%1d\n', 3);
fprintf(fid, 'TOP, 2, 1.0, BOTTOM, 2, -1.0, CNode1, 2, %6.1f \n', -L2);

fprintf(fid, '%1d\n', 3);
fprintf(fid, 'RIGHT, 2, 1.0, LEFT, 2, -1.0, CNode2, 1, %6.1f\n',-L1);

fprintf(fid, '%1d\n', 3);
fprintf(fid, 'TOP, 1, 1.0, BOTTOM, 1, -1.0, CNode2, 2, %6.1f\n', -L2);

fprintf(fid, '3\n');
fprintf(fid, 'C, 1, 1.0, B, 1, -1.0, D, 1, -1.0\n');

fprintf(fid, '3\n');
fprintf(fid, 'C, 2, 1.0, D, 2, -1.0, B, 2, -1.0\n');

fprintf(fid, '3\n');
fprintf(fid, 'B, 1, 1.0, A, 1, -1.0, CNode1, 1, %6.1f\n', -L1);

fprintf(fid, '3\n');
fprintf(fid, 'B, 2, 1.0, A, 2, -1.0, CNode2, 1, %6.1f\n', -L1);

fprintf(fid, '3\n');
fprintf(fid, 'D, 2, 1.0, A, 2, -1.0, CNode1, 2, %6.1f\n', -L2);

fprintf(fid, '3\n');
fprintf(fid, 'D, 1, 1.0, A, 1, -1.0, CNode2, 2, %6.1f\n', -L2);


% $$$$$$$$$  INPUT PARAMETERS FOR STANDARD ANALYSIS $$$$$$$$$$$$$
clear title prompt def answer1 answer data
title = 'Input parameters for Standard Annalysis';
prompt = {'[ANALYSIS] total analysis time',...
        '[ANALYSIS] starting increment',...
        '[ANALYSIS] minmum increment','[ANALYSIS] maximum increment',...
        '[OUTPUT] restart file writing frequency'};
def = {'1.0','0.001','0.0001','0.05','2'};
lines= 1;
answer1  = inputdlg(prompt,title,lines,def);
answer=char(answer1);
```

```
data=str2num(answer);
AnaTotalTime = data(1);
AnaStInc = data(2);
AnaMinInc = data(3);
AnaMaxInc = data(4);
AnaResFreq = data(5);
% $$$$$$$$$$  STANDARD ANALYSIS PARAMETERS INPUT OVER $$$$$$$$$

% process
fprintf(fid, '*STEP\n');
fprintf(fid, '0.03 global strain e11\n');

fprintf(fid, '*STATIC\n');
%fprintf(fid, '%6.5f, %6.5f, %6.5f, %6.5f\n',AnaStInc, AnaTotalTime,...
%           AnaMinInc, AnaMaxInc);

%fprintf(fid, '*CONTROLS,PARAMETERS=FIELD\n');
%fprintf(fid, '%3.2f, %3.2f\n', 0.02, 0.02);

%%%
% boundary
fprintf(fid, '*BOUNDARY\n');
if(EnableFlag(1)) fprintf(fid, 'CNode1, 1, 1, %5.4f\n', LoadE11);end
if(EnableFlag(2)) fprintf(fid, 'CNode1, 2, 2, %5.4f\n', LoadE22);end
if(EnableFlag(3)) fprintf(fid, 'CNode2, 1, 1, %5.4f\n', LoadE12);
          fprintf(fid, 'CNode2, 2, 2, %5.4f\n', LoadE12);end
fprintf(fid, 'A, ENCASTRE\n');

% output
fprintf(fid, '*NODE PRINT, NSET = CNode1\n');
fprintf(fid, 'U, RF\n');
fprintf(fid, '*END STEP\n');
%fprintf(fid, '*USER SUBROUTINES,INPUT=umat.f');2
fclose(fid);

% print post processing file init.p

fid = fopen('init.p', 'w+');
fprintf(fid, '*set, d title=off\n');
fprintf(fid, '*set, c title=off\n');
fprintf(fid, '*set, axes=off\n');
fprintf(fid, '*set, c border=on\n');
fprintf(fid, '*set, outline=off\n');
fprintf(fid, '*set, fill=on\n');
fprintf(fid, '*color set,elset=particle,c=red\n');
fclose(fid);

% print post processing file curve.p

fid = fopen('curve.p', 'w+');
fprintf(fid, '*delete curve, name=all curves\n');
fprintf(fid, '*read c,name=e11,node=CNode1,var=u1\n');
fprintf(fid, '*read c,name=force1,node=CNode1,var=rf1\n');
vol = L1*L2*D;
fprintf(fid, '*define curve, name=s11, op=multiply, const=%3.1e\n', ...
          1.0/vol);
```

```
fprintf(fid, 'force1\n\n');

fprintf(fid, '*define c, name=ss_1, op=comb\n');
fprintf(fid, 'e11\n');
fprintf(fid, 's11\n\n');

fprintf(fid, '*graph axes, x title=STRAIN_11\n');
fprintf(fid, '*graph axes, y title=STRESS_11\n');
fprintf(fid, '*display curve\n');
fprintf(fid, 'ss_1\n\n');
fprintf(fid, '*set, xy print file=ss.rpt\n');
fprintf(fid, '*print curve\n');
fprintf(fid, 'ss_1\n\n');

fclose(fid);
```

5. test_new.m

```
% ############################################################
% GENERATE PARTICLE GEOMETRIC DISTRIBUTION
% SUBROUTINE:    parGeo.m
%                par.m
%                draw.m
% OUTPUT VARIABLE:  ParGeoList
%           ParLenDist, ParLenMean, ParLenVar
%           ParThDist, ParThMean, ParThVar
%           ParAngDist, ParAngMean, ParAngVar
%           ParInfo, Np1
% ############################################################

clear all
close all

% $$$$$$$$$$$$$$$$$$$$  INPUT GENERAL INFO  $$$$$$$$$$$$$$$$$
title = 'General Info';
prompt = {'Number of particles','Clay volume fraction (%)'};
def = {'50', '1'};
lines = 1;
answer1  = inputdlg(prompt,title,lines,def);
answer=char(answer1);
data=str2num(answer);
Np = data(1);
ParVF = data(2)*0.01;
% $$$$$$$$$$$$$$$$$$$$  INPUT GENERAL INFO OVER  $$$$$$$$$$$$$$$$$$$

% $$$$$$$$$$$$$$$ INPUT PARTICLE GEOMETRY DISTRIBUTION  $$$$$$$$$$
% ParGeoList -- [Np * 3] matrix storing length & thickness of each particle
%               & morphology of each particle:0/1 = exf./int.
% ParLenDist -- particle length distribution
% ParLenVar -- particle length variance
% ...
[ParGeoList,ParLenDist,ParLenMean,ParLenVar,ParThDist,ParThMean,...
   ParThVar,ParAngDist,ParAngMean,ParAngVar] = parGeo(Np);
```

```
ParLenMin = min(ParLenDist(1,:));
ParLenMax = max(ParLenDist(1,:));
ParThMin = min(ParThDist(1,:));
ParThMax = max(ParThDist(1,:));
% $$$$$$$$$$$$$$$$$ INPUT PARTICLE GEOMETRY OVER  $$$$$$$$$$$$$$$$$


% $$$$$$$$$$$$$$$$$$$$  CALCULATE RVE SIZE  $$$$$$$$$$$$$$$$$$$$$
ParVol = sum(ParGeoList(:,1).*ParGeoList(:,2));
RVEVol = ParVol/ParVF;
%RVEL1 = 10 * ParLenMean;
%RVEL2 = round(RVEVol/RVEL1);
RVEL1 = round(sqrt(RVEVol));
RVEL2 = RVEL1;

FlagNew = 1;
h1 = 0;
while FlagNew
  title = 'Input RVE size';
  prompt = {'RVE width', 'RVE height'};
  def = {num2str(RVEL1), num2str(RVEL2)};
  lines = 1;
  answer1  = inputdlg(prompt,title,lines,def);
  answer=char(answer1);
  data=str2num(answer);
  RVEL1 = data(1);
  RVEL2 = data(2);

  % display particle and RVE size info
  str1 = 'Particle Dimensions :';
  str2 = strcat('  mean particle length : ',num2str(ParLenMean));
  str3 = strcat('  mean particle thickness : ',num2str(ParThMean));
  str4 = 'RVE Dimensions :';
  str5 = strcat('  width : ',num2str(RVEL1));
  str6 = strcat('  height : ',num2str(RVEL2));
  msg = char(str1,str2,str3,str4,str5,str6);
  %h1 = msgbox(msg);

  % display question dialog box
  button = questdlg(msg, 'Do you want to change RVE size?',...
        'No','Yes','Cancel','No');
  if strcmp(button,'No')
    FlagNew=0;
  elseif strcmp(button,'Cancel')
    disp('Program is terminated'); break;return;
  end
end
% $$$$$$$$$$$$$$$$$$ CALCULATE RVE SIZE OVER  $$$$$$$$$$$$$$$$$$$$$$

GeoMatWidth = RVEL1;
GeoMatHeight = RVEL2;
GeoParLMean = ParLenMean;
GeoParThMean = ParThMean;
GeoVF = ParVF;

% $$$$$$$$$$$$$$$$$$$ SELECT PARTICLE ELEMENT $$$$$$$$$$$$$$$$$$$$
```

```
list = {'Beam','Continuum'};
prompt = 'Choose particle element type';
size = [150 50];

%[FlagParEle, s] = listdlg('ListString',list, 'SelectionMode','single',...
%                'ListSize',size, 'PromptString',prompt);

% FlagParEle = 1 : Beam element
% FlagParEle = 2 : Continuum element
FlagParEle = 2;

% $$$$$$$$$$$$$$$$$$ PARTICLE ELEMENT CHOSEN $$$$$$$$$$$$$$$$$$$$$


% subroutines par.m, parcheck.m, draw.m

% PARTICLE INFO
%  content
vf = GeoVF; % volume fraction (%)
%  Particle Size
%  asp = GeoParAsp; % aspect = Length/Thickness
%  cross-section -- Pd, Pt
%  length        -- Pl
Pd = 10;
Pt = GeoParThMean;
Pl = GeoParLMean;

% Matrix (RVE) size -- L1, L2, T
L1 = GeoMatWidth;
L2 = GeoMatHeight;
D = Pd;  % depth of matrix

list = {'Pattern','Random'};
prompt = 'Choose a particle distribution mode';
size = [150 50];

%[FlagDistMode, s] = listdlg('ListString',list, 'SelectionMode',...
%                'single','ListSize',size, 'PromptString',prompt);
% FlagDistMode -- 1: pattern
%              -- 2: random
FlagDistMode = 2;


CellSize = [0 0];
% CellSize(1) -- Cell Width
% CellSize(2) -- Cell Height

if FlagDistMode==1

  CellArea = Area/Np;
  CellBMax = CellArea/GeoParLen;

  title = strcat('CellArea = ', num2str(CellArea), ...
            'ParLength = ', num2str(GeoParLen));
  StrProp = strcat('Center-to-center (direction 2) (Less than: ',...
        num2str(CellBMax), ')');
```

```
  prompt = {StrProp};
  def = {'10'};
  lines = 1;
  answer1  = inputdlg(prompt,title,lines,def);
  answer=char(answer1);
  data=str2num(answer);
  CellSize(2) = data(1);
  CellSize(1) = CellArea/CellSize(2);

end


% DECIDE PARTICLE DISTRIBUTION
FlagNew = 2;
h2 = figure('Name','Geometrical Particle Distribution');
while(FlagNew==2)
  clear ParInfo
  %partdist = ParTDist;
  %partdist(1,:) = partdist(1,:)/deltaY;
  [ParInfo, Np1, ParInfo_TOT] = par(GeoMatWidth,GeoMatHeight,Np,...
                          ParGeoList,FlagParEle,FlagDistMode);
  % now Np1 is the real num of particles

  % display the particle spacing distribution
  if(h2~=0) close(h2);end   % close the old figure
  h2 = figure('Name','Geometrical Particle Distribution');
  draw(ParInfo, Np1, L1, L2)

  % display question dialog box
  button = questdlg('Do you want to continue?','Particle Distribution',...
              'Yes','New','Cancel','Yes');
  if strcmp(button,'Yes')
    disp('Creating ABAQUS input file...');FlagNew=1;
  elseif strcmp(button,'Cancel')
    disp('Job canceled, no input file created');FlagNew=3;
  elseif strcmp(button,'New')
    FlagNew=2;
  end
end
% $$$$$$$$$$$$ PARTICLE DISTRIBUTION DECIDED $$$$$$$$$$$$$$$$$$$$$$
if(FlagNew==3) return;end
```

6. par_Geo.m

```
% ######################################################################
% SUBROUTINE:  parDist.m
% ######################################################################

function [ParGeoList,ParLenDist,ParLenMean,ParLenVar,ParThDist,...
      ParThMean,ParThVar,ParAngDist,ParAngMean,ParAngVar] = parGeo(Np)
% Np: number of particles

% ParGeo: Np*2   particle geometry info
ParGeoList = zeros(Np,3);
```

```
title = 'Particle Geometry Parameters';
prompt = {'Mean Particle Length:', 'Length Variance', 'Variance Inc',...
      'Length Min:', 'Length Max:', 'Length Inc:',...
      'Mean particle Thickness', 'Thickness Variance', 'Variance Inc',...
      'Thickness Mean', 'Thickness Max', 'Thickness Inc'};

def = {'130','1000','10','70','200','10','0.615','0','0.1','1','5','1'};
lines = 1;
answer1  = inputdlg(prompt,title,lines,def);
answer=char(answer1);
data=str2num(answer);
Lmean = data(1);
Lvar = data(2);
LvarInc = data(3);
Lmin = data(4);
Lmax = data(5);
Linc = data(6);
Tmean = data(7);
Tvar = data(8);
TvarInc = data(9);
Tmin = data(10);
Tmax = data(11);
Tinc = data(12);


% UNIFORM LENGTH AND UNIFORM THICKNESS
if Lvar==0 & Tvar==0
 ParLenDist(1,:) = Lmean;   % value of length
 ParLenDist(2,:) = Np;              % number of particles in the range
 ParLenVar = 0;

 ParThDist(1,:) = Tmean;     % value of thickness
 ParThDist(2,:) = Np;       % number of particles in the range
 ParThVar = 0;

% LENGTH DISTRIBUTION AND UNIFORM THICKNESS
elseif Lvar~=0 & Tvar==0
 [ParLenDist, ParLenVar] = parDist(Np,Lmean,Lvar,LvarInc,Lmax,Lmin,Linc);
 ParThDist(1,:) = Tmean;
 ParThDist(2,:) = Np;
 ParThVar = 0;

% UNIFORM LENGTH AND THICKNESS DISTRIBUTION
elseif Lvar==0 & Tvar~=0
 ParLenDist(1,:) = Lmean;
 ParLenDist(2,:) = Np;
 ParLenVar = 0;

 [ParThDist, ParThVar] = parDist(Np,Tmean,Tvar,TvarInc,Tmax,Tmin,Tinc);

 now = 1;
 for i = 1:length(ParThDist(1,:))
  T = ParThDist(1,i);
  for j = 1:ParThDist(2,i)
   ParGeo(now,1) = Lmean;
   ParGeo(now,2) = T;
```

```
    now = now+1;
   end
  end

  % LENGTH DISTRIBUTION AND THICKNESS DISTRIBUTION
elseif Lvar~=0 & Tvar~=0
  subplot(2,1,1);
  [ParLenDist, ParLenVar] = parDist(Np,Lmean,Lvar,LvarInc,Lmax,Lmin,Linc);
  subplot(2,1,2);
  [ParThDist, ParThVar] = parDist(Np,Tmean,Tvar,TvarInc,Tmax,Tmin,Tinc);
end

title = 'Particle Geometry Parameters';
prompt = {'Mean particle Orientation Angle', 'Angle Variance',...
        'Variance Inc', 'Angle Min', 'Angle Max', 'Angle Inc'};
def = {'0','130','10','-45','45','5'};
lines = 1;
answer1  = inputdlg(prompt,title,lines,def);
answer=char(answer1);
data=str2num(answer);
Amean = data(1);
Avar = data(2);
AvarInc = data(3);
Amin = data(4);
Amax = data(5);
Ainc = data(6);

ParLenMean = Lmean;
ParThMean = Tmean;
ParAngMean = Amean;

if Avar~=0
   [ParAngDist, ParAngVar]=parDist(Np,Amean,Avar,AvarInc,Amax,Amin,Ainc);
   ParAngDist(2,8:12) = ParAngDist(2,8:12)+1;
else
   ParAngDist(1,:) = Amean;
   ParAngDist(2,:) = Np;
   ParAngVar = 0;
end

now=1;
for i = 1:length(ParLenDist(1,:))
  L = ParLenDist(1,i);
  for j = 1:ParLenDist(2,i)
    A(now) = L; now = now+1;
  end
end
now = 1;
for i = 1:length(ParThDist(1,:))
  T = ParThDist(1,i);
  for j = 1:ParThDist(2,i)
    B(now) = T; now = now+1;
  end
end

now = 1;
```

```
for i = 1:length(ParAngDist(1,:))
 theta = ParAngDist(1,i);
 for j = 1:ParAngDist(2,i)
  C(now) = theta; now = now+1;
 end
end
a = randperm(Np); b = randperm(Np); c = randperm(Np);
for i = 1:Np
  ParGeoList(i,1) = A(a(i)); % particle length
  ParGeoList(i,2) = B(b(i)); % particle thickness
  ParGeoList(i,3) = C(c(i)); % particle orientation angle
end

return
```

7. parDist.m

```
function [M, v] = parDist(Np, Mean, Var, VarInc, Max, Min, Inc)

x = Min:Inc:Max;
n = zeros(1,length(x));
Variance = Var;
FlagNew = 1;
while FlagNew
 sdv = sqrt(Variance);
 y = randn(10000,1)*sdv + Mean;
 p = hist(y,x)/10000;  % p -- weight percentage
 n = round(Np*p);  % n is the number of particles in each length range bar(x,n)
 % display question dialog box
 button = questdlg('Do you want to change variance?',...
       'Orientation Distribution','No','Inc','Dec','No');
 if strcmp(button,'No')
   FlagNew=0;
 elseif strcmp(button,'Inc')
   disp('Variance increased by one'); Variance = Variance+VarInc;
 elseif strcmp(button,'Dec')
   disp('Variance decreased by one'); Variance = Variance-VarInc;
 end
end

% find the true Max and Min
indexMin = 1;
indexMax = length(x);
for i=1:length(x)
  if n(i)~=0  MinTrue=x(i);indexMin=i;break;end
end

k = 1;
for i=1:length(x)
  if n(i)~=0
    A(1,k) = x(i);
    A(2,k) = n(i);
    k = k+1;
  end
end
```

```
if sum(A(2,:))~=Np
  i = (Mean - MinTrue)/Inc + 1;
  A(2,i) = A(2,i) + Np - sum(A(2,:));
end

M = A;
v = Variance;
```

8. par.m

```
% ######################################################################
% SUBROUTINE:      parcheck.m
% ######################################################################

function [ParInfo, Np1, ParInfo_TOT] = par(L1, L2, Np, ParGeo, flag, DMode)
% L1 -- Width of the RVE
% L2 -- Height of the RVE
% Np
% ParGeo -- Particle Geometry Distribution
% ParGeo(1,:) -- Length, ParGeo(2,:) -- Thickness, ParGeo(3,:)--Orientation
% flag -- beam/continuum
% DMode -- Particle Distribution Mode: pattern/random
% CSize -- Cell Size (1,2)

pos = zeros(4,2,Np);
now = 1;
now_1 = 1;

delta_x = 15;
delta_y1 = 10;
delta_y2 = 10;

for i = 1:size(ParGeo,1)
 % % continuum ele
 L = ParGeo(i,1);     % Particle Length
 t = ParGeo(i,2);     % Particle Thickness
 theta = ParGeo(i,3)* (pi/180);  % Particle Orientation Angle
 % Rotation matrix
 Q = [cos(theta) -sin(theta);
     sin(theta) cos(theta)];
 % use 4*2 matrix 'temp' to record the particle vertex coordinates in
 % the rotated local frame
 temp = [0 0; L 0; L t; 0 t];
 temp = Q * temp';
 temp = temp';
 valid = 0;
 xbisect = 0; ybisect = 0;
 while valid == 0
   % generate a new pair of coordinates (x,y)
   bisect = 0;
   xbisect = 0;
   ybisect = 0;
   %x1 = floor(rand(1)*N1)+1;  % col
   %y1 = floor(rand(1)*(N2-TD(1,j)))+1;  % row
   x1 = rand(1)*(L1-2*delta_x)+delta_x;
   y1 = rand(1)*(L2-delta_y1-delta_y2)+delta_y1;
```

```
% Coordinates of the Vertices (4 by 2 matrix)
Vertex = temp + [x1 y1; x1 y1; x1 y1; x1 y1];
endX = Vertex(2,1); endY = Vertex(2,2);
% Not Bisected at all
if endX<=(L1-delta_x) & endY<=(L2-delta_y2) & endY>=(delta_y1)
   valid = parcheck(Vertex,now,pos);
% Only bisected by Right edge
elseif endX>=(L1+delta_x) & endY<=(L2-delta_y2) & endY>=(delta_y1)
   bisect = 1;
   % Y-coordinate of intersection point 1
   Y_1 = Vertex(1,2) + (L1-Vertex(1,1))*tan(theta);
   % Y-coordinate of intersection point 2
   Y_2 = Vertex(4,2) + (L1-Vertex(4,1))*tan(theta);
   Vertex_a = Vertex;
   Vertex_b = Vertex;
   Vertex_a(2,1) = L1; Vertex_a(2,2) = Y_1;
   Vertex_a(3,1) = L1; Vertex_a(3,2) = Y_2;
   Vertex_b(1,1) = 0; Vertex_b(1,2) = Y_1;
   Vertex_b(2,1) = Vertex_b(2,1)-L1;
   Vertex_b(3,1) = Vertex_b(3,1)-L1;
   Vertex_b(4,1) = 0; Vertex_b(4,2) = Y_2;
   valid = parcheck(Vertex_a,now,pos);
   if(valid)  valid=parcheck(Vertex_b,now,pos);
   end
% Only bisected by Bottom edge
elseif endY<=(0-delta_y2) & endX<=(L1-delta_x) & endX>=(0+delta_x)
   bisect = 1;
   % X-coordinate of intersection point 1
   X_1 = Vertex(1,1) + Vertex(1,2)/abs(tan(theta));
   % X-coordinate of intersection point 2
   X_2 = Vertex(4,1) + Vertex(4,2)/abs(tan(theta));
   Vertex_a = Vertex;
   Vertex_b = Vertex;
   Vertex_a(2,1) = X_1; Vertex_a(2,2) = 0;
   Vertex_a(3,1) = X_2; Vertex_a(3,2) = 0;
   Vertex_b(1,1) = X_1; Vertex_b(1,2) = L2;
   Vertex_b(2,2) = Vertex_b(2,2)+L2;
   Vertex_b(3,2) = Vertex_b(3,2)+L2;
   Vertex_b(4,1) = X_2; Vertex_b(4,2) = L2;
   valid = parcheck(Vertex_a,now,pos);
   if(valid)  valid=parcheck(Vertex_b,now,pos);
   end
% Only bisected by Top edge
elseif endY>=(L2+delta_y1) & endX<=(L1-delta_x) & endX>=(0+delta_x)
   bisect = 1;
   % X-coordinate of intersection point 1
   X_1 = Vertex(1,1) + (L2-Vertex(1,2))/tan(theta);
   % X-coordinate of intersection point 2
   X_2 = Vertex(4,1) + (L2-Vertex(4,2))/tan(theta);
   Vertex_a = Vertex;
   Vertex_b = Vertex;
   Vertex_a(2,1) = X_1; Vertex_a(2,2) = L2;
   Vertex_a(3,1) = X_2; Vertex_a(3,2) = L2;
   Vertex_b(1,1) = X_1; Vertex_b(1,2) = 0;
   Vertex_b(2,2) = Vertex_b(2,2)-L2;
   Vertex_b(3,2) = Vertex_b(3,2)-L2;
```

```
      Vertex_b(4,1) = X_2; Vertex_b(4,2) = 0;
      valid = parcheck(Vertex_a,now,pos);
      if(valid)  valid=parcheck(Vertex_b,now,pos);
      end
   else
      % Both x-bisected and y-bisected
      valid = 0;
   end
 end

 if bisect == 0       % not bisected
    pos(:,:,now) = Vertex; now = now+1;
 else
    pos(:,:,now) = Vertex_a; now = now+1;
    pos(:,:,now) = Vertex_b; now = now+1;
 end

 pos_1(:,:,now_1) = Vertex; now_1 = now_1 + 1;

end

% new particle-start-postion in ParInfo(Np1, 3)
% data structure of ParInfo:
% Np1 : actural num of particles ( a bisected is now 2)
% ParInfo(:, 1) -- length of the particle (in terms of grids)
% ParInfo(:, 2) -- thickness of the particle
% ParInfo(:, 3) -- lowest-left col#
% ParInfo(:, 4) -- lowest-left row#

Np1 = now - 1;
ParInfo = pos;
ParInfo_TOT = pos_1;
% now Np1 is the real num of particles
```

9. parcheck.m

```
function [valid] = parcheck(Vertex,n,M)

% x,y -- coordinate to be checked
% n   -- current indice
% M   -- the info matrix for (n-1) particle pos's
% L   -- length of particle
% T   -- thickness of particle
% flag-- beam/continuum

valid = 1;  % flag of validity

%Vertex = zeros(4,2);

X_space = 20;
Y_space = 35;
t = 0.615;            % particle thickness

A = Vertex(1,:);
B = Vertex(2,:);
e1 = (B-A)/norm(B-A); e1C = e1(1) + e1(2)*i;    % e1C -- complex of e1
```

```
e2C = e1C*i; e2(1) = real(e2C); e2(2) = imag(e2C);  % e2C -- complex of e2
L = norm(B-A);
Q = [e1' e2'];

if n==1 valid = 1;return;end

if L<3 valid = 0; return; end

for j = 1:(n-1)
   temp = M(:,:,j);
   n1 = temp(2,:) - temp(1,:); L1 = norm(n1); n1 = n1/L1;
   n1C = n1(1) + n1(2)*i;      % complex form of vector n1
   n2C = n1C*i;                % complex of vector n2
   n2(1) = real(n2C); n2(2) = imag(n2C);
   V1_G = temp(1,:) - X_space*n1 - Y_space*n2;
   V2_G = V1_G + (2*X_space+L1)*n1;
   V3_G = V2_G + (2*Y_space+t)*n2;
   V4_G = V1_G + (2*Y_space+t)*n2;
   V1 = Q'*(V1_G' - A'); V1 = V1';
   V2 = Q'*(V2_G' - A'); V2 = V2';
   V3 = Q'*(V3_G' - A'); V3 = V3';
   V4 = Q'*(V4_G' - A'); V4 = V4';

   flag = [0 0 0 0];
   if V1(2)>0 flag(1) = 1;end
   if V2(2)>0 flag(2) = 1;end
   if V3(2)>0 flag(3) = 1;end
   if V4(2)>0 flag(4) = 1;end
   mark = size(find(flag==1),2);
   if mark == 3
      flag = [1 1 1 1] - flag;
   end

   if (V1(2)>0&V2(2)>0&V3(2)>0&V4(2)>0)|(V1(2)<0&V2(2)<0&V3(2)<0&V4(2)<0)
      valid = 1;
   else
      p = find(flag == 1);
      if size(p,2)==1
         if p == 1
            x1=V1(1);y1=V1(2); x2=V2(1);y2=V2(2); x3=V4(1);y3=V4(2);
         elseif p == 2
            x1=V2(1);y1=V2(2); x2=V1(1);y2=V1(2); x3=V3(1);y3=V3(2);
         elseif p == 3
            x1=V3(1);y1=V3(2); x2=V2(1);y2=V2(2); x3=V4(1);y3=V4(2);
         elseif p == 4
            x1=V4(1);y1=V4(2); x2=V3(1);y2=V3(2); x3=V1(1);y3=V1(2);
         end
         S1 = -(x1*y2-x2*y1)/(y1-y2);
         S2 = -(x1*y3-x3*y1)/(y1-y2);
         if (S1>L & S2>L)|(S1<0 & S2<0)
            valid = 1;
         else
            valid = 0; return;
         end
      elseif size(p,2)==2
%           if j==49
```

```
%            warning('error about to occur!')
%          end
        if (p(1)==1 & p(2)==2)|(p(1)==3 & p(2)==4)
           x1=V1(1);y1=V1(2);x2=V4(1);y2=V4(2);
           x3=V2(1);y3=V2(2);x4=V3(1);y4=V3(2);
        elseif (p(1)==1 & p(2)==4)|(p(1)==2 & p(2)==3)
           x1=V1(1);y1=V1(2);x2=V2(1);y2=V2(2);
           x3=V4(1);y3=V4(2);x4=V3(1);y4=V3(2);
        elseif (p(1)==1 & p(2)==3)|(p(1)==2 & p(2)==4)
           warning('Error Parcheck line 80!');
        end
        %
        if y1==y2
           warning('Error Parcheck Y1=Y2! n=%d, p=[%d %d]',...
                 n, p(1),p(2));
        end
        S1 = -(x1*y2-x2*y1)/(y1-y2);
        if y3==y4
           warning('Error Parcheck Y3=Y4! n=%d, j=%d, p=[%d %d]',...
                 n,j,p(1),p(2));
        end
        S2 = -(x3*y4-x4*y3)/(y3-y4);
        if (S1>L & S2>L)|(S1<0 & S2<0)
           valid = 1;
        else
           valid = 0; return;
        end
     end
  end
end
```

10. draw.m

```
function draw(Par, n, L1, L2)

Vx = [0 L1 L1 0];
Vy = [0 0 L2 L2];
fill(Vx,Vy,'w');
hold on
axis equal
axis([0 L1 0 L2])

for i=1:n
  clear x y;
  x = [Par(1,1,i) Par(2,1,i) Par(3,1,i) Par(4,1,i)];
  y = [Par(1,2,i) Par(2,2,i) Par(3,2,i) Par(4,2,i)];
  fill(x,y,'r');
  hold on
end
```

Bibliography

J. D. Eshelby. The determination of the elastic field of an ellipsoidal inclusion and related problems. *Proc. Roy. Soc. A*, **241**:376-396, 1957.

J. E. Ashton, J. C. Halpin, and P. H. Petit. Primer on composite materials: analysis. Technomic, Stamford, Conn, 1969.

Z. Bartczak, A. S. Argon, R. E. Cohen, and T. Kowalewski. Toughness mechanism in semi-crystalline polymer blends: I. High-density polyethylene toughened with rubbers. *Polymer*, **40**:2331-2346, 1999.

J. S. Bergström and M. C. Boyce. Mechanical behavior of particle filled elastomers. *Rubber Chem. Technol.*, **72**:633-656, 1999.

J. M. Brown, D. Curliss, R. A. Vaia. Thermoset-layered silicate nanocomposites. quaternary ammonium montmorillonite with primary diamine cured epoxies. *Chem. Mater.*, **12**:3376-3384, 2000.

D. A. Brune and J. Bicerano. Micromechanics of nanocomposites: comparison of tensile and compressive elastic moduli, and prediction of effects of incomplete exfoliation and imperfect alignment on modulus. *J. Polymer*, **43**:369-387, 2002.

M. V. Burmistr, K. M. Sukhyy, V. V. Shilov, P. Pissis, A. Spanoudaki, I. V. Sukha, V. I. Tomilo, and Y. P. Gomza. Synthesis, structure, thermal and mechanical properties of nanocomposites based on linear polymers and layered silicates modified by polymeric quaternary ammonium salts. Polymer 46:12226-12232, 2005.

S. D. Burnside SD and E. P. Giannelis. Nanostructure and properties of polysiloxane-layered silicate nanocomposites. *J. Polym. Sci. Pol. Phys.*, **38**:1595-1604, 2000.

V. P. Chacko, F. E. Karasz, R. J. Farris, and E. L. Thomas. MORPHOLOGY OF CACO3-FILLED POLYETHYLENES. *J. Polym. Sci. Polym. Phys.*, **20**:2177-2195, 1982.

M. Danielsson, D. M. Parks, and M. C. Boyce. Three-dimensional micromechanical modeling of voided polymeric materials. *J. Mech. Phys. Solids*, **50:**351-379, 2002.

H. R. Dennis, D. L. Hunter, D. Chang, S. Kim, J. L. White, J. W. Cho, and D. R. Paul. Effect of melt processing conditions on the extent of exfoliation in organoclay-based nanocomposites. *Polymer*, **42**:9513-9522, 2001.

J. D. Eshelby. The determination of the elastic field of an ellipsoidal inclusion and related problems. *Proc. Roy. Soc. A*, **241:**376-396, 1957.

T. D. Fornes, P. J. Yoon, H. Keskkula H, and D. R. Paul. Nylon 6 nanocomposites: the effect of matrix molecular weight. *Polymer*, **42**:9929-9940, 2001.

E. P. Giannelis, R. Krishnamoorti, and E. Manias. Polymer-silicate nanocomposites: model systems for confined polymers and polymer brushes. *Adv. Polym. Sci.*, **138**:107-147, 1999.

J. W. Gilman. Flammability and thermal stability studies of polymer layered-silicatre (clay) nanocomposites. *Appl. Clay Sci.*, **15**:31-49, 1999.

A. A. Gusev. Numerical identification of the potential of whisker- and platelet-filled polymers. Macromolecules, **34**:3081-3093, 2001.

E. Hackett, E. Manias, and E. P. Giannelis. Molecular dynamics simulations of organically modified layered silicates. *J. Chem. Phys.*, **108**:7410-7415.

J. C. Halpin. Stiffness and expansion estimates for oriented short fiber composites. *J. Compos. Mater.*, **3:**732-734, 1969.

J. C. Halpin and J. L. Kardos. The Halpin-Tsai equations: a review. *Polym. Eng. Sci.*, **16:**344-352, 1976.

J. J. Hermans. The elastic properties of fiber reinforced materials when the fibers are aligned. *Proc. K. Ned. Akad. Wet., Ser. B*, **65:**1-9, 1967.

R. Hill. Theory of mechanical properties of fiber-strengthened materials: I elastic behavior. *J. Mech. Phys. Solids*, **12:**199-212, 1964.

G. M. Kim, D. H. Lee, B. Hoffmann, J. Kressler, and G. Stoppelmann. Influence of nanofillers on the deformation process in layered silicate/polyamide-12 nanocomposites. *Polymer*, **42**:1095-1100, 2001.

Y. Kojima, A. Usuki, M. Kawasumi, A. Okada, Y. Fukushima, T. Kurauchi, and O. Kamigaito. Synthesis of nylon 6-clay hybrid. *J. Mater. Res.*, **8**(5):1179-1184, 1993a.

Y. Kojima, A. Usuki, M. Kawasumi, A. Okada, Y. Fukushima, T. Kurauchi, and O. Kamigaito. Mechanical properties of nylon 6-clay hybrid. *J. Mater. Res.*, **8**(5):1185-1189, 1993b.

Y. Kojima, A. Usuki, M. Kawasumi, A. Okada, T. Kurauchi, O. Kamigaito, and K. Kaji. Fine structure of nylon-6-clay hybrid. *J. Polym. Sci. Part B Polym. Phys.*, **32**:625-630, 1994.

Y. Kojima, A. Usuki, M. Kawasumi, A. Okada, T. Kurauchi, O. Kamigaito, and K. Kaji. Novel preferred orientation in injection-molded nylon 6-clay hybrid. *J. Polym. Sci., Part B, Polym. Phys.*, **33**:1039-1045, 1995.

Lee H and McKinley GH. Rheology and Processing of PMMA/clay and Nylon/clay Nanocomposites. J Rheology (in preparation).

Y. J. Li and H. Shimizu. Effect of spacing between the exfoliated clay platelets on the crystallization behavior of polyamide-6 in polyamide-6/clay nanocomposites. *J. Polym. Sci. Part B Polym. Phys.*, **44**:284-290, 2006.

L. Lin and A. S. Argon. DEFORMATION RESISTANCE IN ORIENTED NYLON-6. *Macromolecules*, **25**:4011-4024, 1992.

D. M. Lincoln and R. A. Vaia. Isothermal crystallization of nylon-6/montmorillonite nanocomposites. *Macromolecules*, **37**:4554-4561, 2004.

L. M. Liu, Z. N. Qi, X. G. Zhu. Studies on nylon 6 clay nanocomposites by melt-intercalation process. *J. Appl. Polym. Sci,*, **71**:1133-1138, 1999.

T. X. Liu, Z. H. Liu, K. X. Ma, L. Shen, K. Y. Zheng, and C. B. He. Morphology, thermal and mechanical behavior of polyamide 6/layered-silicate nanocomposites. *Compos. Sci. Technol.*, **63**:331-337, 2003.

L. S. Loo and K. K. Gleason. Fourier transform infrared investigation of the deformation behavior of montmorillonite in nylon-6/nanoclay nanocomposite. *Macromolecules*, **36**:2587-2590, 2003.

L. S. Loo and K. K. Gleason. Investigation of polymer and nanoclay orientation distribution in nylon6/montmorillonite nanocomposite. *Polymer*, **45**:5933-5939, 2004.

F. W. Maine and P. D. Shepherd. Mica reinforced plastics: a review. *Composites*, September:193-200, 1974.

P. Maiti, P. H. Nam, and M. Okamoto. Influence of crystallization on intercalation, morphology, and mechanical properties of polypropylene/clay nanocomposites. *Macromolecules*, **35**:2042-2049, 2002.

O. L. Manevitch and G. C. Rutledge. Elastic Properties of a Single Lamella of Montmorillonite by Molecular Dynamics Simulation. *J. Phys. Chem. B*, 108:1428-1435, 2004.

F. J. Medellin-Rodriguez, B. S. Hsiao, B. Chu, and B. X. Fu. Uniaxial Deformation of Nylon 6-Clay Nanocomposites by In-Situ Synchrotron X-Ray Measurements. *J. Macromolecular Sci. Phys.*, **B42**:201-214, 2003.

P. B. Messersmith and E. P. Giannelis. Synthesis and characterization of layered silicate-epoxy nanocomposites. *Chem. Mater.*, **6**:1719-1725, 1994.

P. B. Messersmith and E. P. Giannelis. Synthesis and barrier properties of poly(epsilon-caprolactone)-layered silicate nanocomposites. *J. Polym. Sci., Part A, Polym. Chem.*, **33**:1047-1057, 1995.

T. Mori and K. Tanaka. Average stress in matrix and average elastic energy of materials with misfitting inclusions. *Acta Metall.*, **21:**571-574, 1973.

O. K. Muratoglu, O. S. Argon, and R. E. Cohen. CRYSTALLINE MORPHOLOGY OF POLYAMIDE-6 NEAR PLANAR SURFACES. *Polymer*, **36**:2143-2152, 1995.

O. K. Muratoglu, O. S. Argon, and R. E. Cohen. TOUGHENING MECHANISM OF RUBBER-MODIFIED POLYAMIDES. *Polymer*, **36**:921-930, 1995.

S. S. Nair and C. Ramesh. Studies on the crystallization behavior of nylon-6 in the presence of layered silicates using variable temperature WAXS and FTIR. Macromolecules, 38:454-462, 2005.

P. H. Nam, P. Maiti, M. Okamoto, T. Kotaka, N. Hasegawa, and A. Usuki. A hierarchical structure and properties of intercalated polypropylene/clay nanocomposites. *Polymer*, **42**:9633-9640, 2001.

A. Pantano, D. M. Parks, and M. C. Boyce. Mechanics of deformation of single- and multi-wall carbon nanotubes. *J. Mech. Phys. Solids*, **52**:789-821, 2004.

D. Ratna, N. R. Manoj, R. Varley, R. K. S. Raman, and G. P. Simon. Clay-reinforced epoxy nanocomposites. *Polym. Int.*, **52**:1403-407, 2003.

W. B. Russel. On the effective moduli of composite materials: effect o fiber length and geometry at dilute concentrations. *J. Appl. Math. Phys. (ZAMP)*, **24**:581-600, 1973.

G. P. Tandon and G. J. Weng. The effect of aspect ratio of inclusions on the elastic properties of unidirectionally aligned composites. *Polym. Compos.*, **5:**327-333, 1984..

C. S. Triantafillidis, P. C. LeBaron, and T. J. Pinnavaia. Thermoset epoxy-clay nanocomposites: The dual role of alpha,omega-diamines as clay surface modifiers and polymer curing agents. *J. Solid. State. Chem.*, **167**:354-362, 2002.

C. L. Tucker and E. Liang. Stiffness predictions for unidirectional short-fiber composites: review and evaluation. *Compos. Sci. Technol.*, **59**:655-671, 1999.

P. A. Tzika, M. C. Boyce, and D. M. Parks. Micromechanics of deformation in particle-toughened polyamides. *J. Mech. Phys. Solids*, **48**:1893-1929, 2000.

P. A. Tzika. Micromechanical Modeling of the Toughening Mechanisms in Particle-Modified Semicrystalline Polymers, Thesis (S. M.), Massachusetts Institute of Technology, Dept. of Mechanical Engineering, 1999.

R. A. Vaia, K. D. Jandt, E. J. Kramer, and E. P. Giannelis. Kinetics of polymer melt intercalation. *Macromolec.*, **28**:8080-8085.

R. A. Vaia, G. Price, P. N. Ruth, H. T. Nguyen, and J. Lichtenhan. Polymer/layered silicate nanocomposites as high performance ablative materials. *Appl. Clay Sci.*, **15**:67-92, 1999.

R. A. Vaia. Structural characterization of polymer-layered silicate nanocomposites. *Polymer-clay nanocomposites* ed. T. J. Pinnavaia and G. W. Beall, pp. 229-265, 2000.

van Es M, Xiqiao F, van Turnhout J, van der Giessen E. Comparing Polymer-Clay Nanocomposites with Conventional Composites using Composite Modeling. In: Al-Malaika S, Golovoy A, Wikie CA, editors. Specialty Polymer Additives. Malden, MA: Blackwell Science, 2001.

Z. Wang, T. J. Pinnavaia. Nanolayer reinforcement of elastomeric polyurethane. *Chem. Mater.*, **10**:3769, 1998.

J. I. Weon and H. J. Sue. Effects of clay orientation and aspect ratio on mechanical behavior of nylon-6 nanocomposite. *Polymer*, **46**:6325-6334.

J. I. Weon, Z. Y. Xia, and H. J. Sue. Morphological characterization of nylon-6 nanocomposite following a large-scale simple shear process. *J. Polym. Sci. Part B Polym. Phys.*, **43**:3555-3566, 2005.

S. B. Xie, S. M. Zhang, H. J. Liu, G. M. Chen, M. Feng, H. L. Qin, F. S. Wang, and M. S. Yang. Effect of processing history and annealing on polymorphic structure of nylon-6/montmorrillonite nanocomposites. *Polymer*, **46**:5417-5427, 2005.

B. I. Yakobson, C. J. Brabec, and J. Bernholc. Nanomechanics of carbon tubes: Instabilities beyond linear response. *Phys. Rev. Lett.*, **76**:2511-2514, 1996.

K. Yano, A. Usuki, A. Okada, T. Kurauchi, and O. Kamigaito. Synthesis and properties of polymide clay hybrid. *J. Polym. Sci., Part A, Polym. Chem.*, **31**:2493-2498, 1993.

P. J. Yoon, T. D. Fornes, and D. R. Paul. Thermal expansion behavior of nylon 6 nanocomposites. *Polymer*, **43**:6727-6741, 2002.

J. Yung, R. K. Gupta, G. P. Simon, G. H. Edward, S. N. Bhattacharya. Rheological and mechanical comparative study of in situ polymerized and melt-blended nylon 6 nanocomposites. Polymer, 46:10405-10418, 2005.